University of Southampton

FACULTY OF ENGINEERING AND PHYSICAL SCIENCES
School of Physics and Astronomy

Vibrational and Electronic Excitations in TMD Monolayers and Heterostructures Probed by Resonance Raman Spectroscopy

by

Jacob John Scotchford Viner

MPhys

ORCiD: 0000-0002-2436-2992

A thesis for the degree of
Doctor of Philosophy

March 2022

University of Southampton

Abstract

FACULTY OF ENGINEERING AND PHYSICAL SCIENCES
School of Physics and Astronomy

Doctor of Philosophy

Vibrational and Electronic Excitations in TMD Monolayers and Heterostructures Probed by Resonance Raman Spectroscopy

by Jacob John Scotchford Viner

This thesis presents the results of a resonance Raman study of TMD monolayers and heterostructures. These measurements allow the 2s Rydberg excitons to be characterised in heterostructures for the first time. This data is used in conjunction with a model of the Coulomb potential in heterostructures to allow the effects of exciton binding energy and the single particle band gap to be measured in the monolayers and heterostructures. This showed shifts in single particle band gap of -25 ±5 meV and -31 ±5 meV for WSe_2 and $MoSe_2$ respectively and with corresponding changes in exciton binding energy of -8 ±0.5 meV and -19 ±1 meV on formation of a heterostructure. Hyperbolic phonon polariton (HPP) states are also probed in hBN encapsulating TMD layers via resonance Raman spectroscopy. Excitons in the TMD layers excite HPPs in the hBN. The high resolution Raman measurements of the lineshape of the HPP modes were compared with a model of the dispersion relation. This revealed large momenta were being accessed, >50 000 cm^{-1} which requires a breaking of momentum conservation in the HPP Raman scattering process.

Contents

List of Figures **ix**

List of Tables **xiii**

Declaration of Authorship **xv**

Acknowledgements **xvii**

1 Introduction **1**
1.1 Organisation . . . 2

2 Theoretical Background **3**
2.1 TMDs . . . 3
2.1.1 Physical Properties . . . 3
2.1.2 Electronic Band Structure . . . 6
2.1.3 Excitons . . . 7
2.1.3.1 Keldysh Potential . . . 7
2.1.4 Bilayers and Heterostructures . . . 11
2.1.5 Encapsulation in hBN . . . 12
2.2 Phonons . . . 12
2.3 Hyperbolic Materials . . . 14
2.4 Raman Spectroscopy . . . 15
2.4.1 Resonance Raman Spectroscopy . . . 18
2.5 Reflectivity and Photoluminescence Spectroscopy . . . 20

3 Experimental Methods **21**
3.1 Sample Fabrication . . . 21
3.1.1 Mechanical Exfoliation . . . 22
3.1.2 Stamp Transfer . . . 23
3.2 Resonance Raman System . . . 24
3.2.1 Laser Sources . . . 24
3.2.2 Polarisation Control . . . 26
3.2.3 Sample Positioning and Temperature Control . . . 26
3.2.4 Acquiring Spectra . . . 27
3.2.5 Spot Size Measurements . . . 28
3.3 Data Analysis and Fitting . . . 29
3.3.1 Resonance Raman . . . 29
3.3.1.1 Background Subtraction . . . 29

3.3.1.2 Calibration of Raman Shift . . . 31
3.3.1.3 Absolute Scattering Cross Section . . . 32
3.3.1.4 Fitting Raman Spectra . . . 32
3.3.1.5 Fitting Resonance Profiles . . . 33
3.3.2 Photoluminescence . . . 34
3.3.3 Reflectivity . . . 35

4 Resonance Raman Spectroscopy of Exciton Rydberg States in WSe_2 / $MoSe_2$ Heterostructures 37
4.1 Literature Review . . . 37
4.2 Results . . . 38
4.2.1 Sample Characterisation . . . 38
4.2.1.1 Monolayer WSe_2 Photoluminescence and Reflectivity . . 38
4.2.1.2 Monolayer $MoSe_2$ Photoluminescence and Reflectivity . . 41
4.2.1.3 57° Twist Heterostructure Photoluminescence and Reflectivity . . . 43
4.2.1.4 20° Twist Heterostructure Photoluminescence and Reflectivity . . . 46
4.2.2 Characterisation of Excited State Raman Peaks in Monolayer WSe_2 48
4.2.2.1 WSe_2 A1s . . . 48
4.2.2.2 WSe_2 A2s . . . 50
4.2.2.3 WSe_2 B1s . . . 54
4.2.3 Characterisation of Excited State Raman Peaks in Monolayer $MoSe_2$ 56
4.2.3.1 $MoSe_2$ A1s . . . 56
4.2.3.2 $MoSe_2$ A2s and B1s . . . 59
4.2.3.3 $MoSe_2$ B2s . . . 62
4.2.3.4 Conclusions . . . 65
4.2.4 Identification of Excited States in $MoSe_2$/WSe_2 Heterostructures . 65
4.2.4.1 57° Twist Heterostructure $MoSe_2$ A1s . . . 65
4.2.4.2 57° Twist Heterostructure WSe_2 A1s . . . 67
4.2.4.3 57° Twist Heterostructure $MoSe_2$ A2s and B1s . . . 69
4.2.4.4 57° Twist Heterostructure WSe_2 A2s . . . 72
4.2.4.5 57° Twist Heterostructure $MoSe_2$ B2s . . . 74
4.2.4.6 57° Twist Heterostructure WSe_2 B1s . . . 76
4.2.4.7 20° Twist Heterostructure $MoSe_2$ A1s . . . 79
4.2.4.8 20° Twist Heterostructure WSe_2 A1s . . . 81
4.2.4.9 20° Twist Heterostructure $MoSe_2$ A2s . . . 83
4.2.4.10 20° Twist Heterostructure $MoSe_2$ B1s . . . 85
4.2.4.11 20° Twist Heterostructure WSe_2 A2s . . . 86
4.2.4.12 20° Twist Heterostructure $MoSe_2$ B2s . . . 88
4.2.4.13 20° Twist Heterostructure WSe_2 B1s . . . 90
4.2.4.14 Summary of Exciton Energies . . . 91
4.3 Comparison with Theoretically Calculated Exciton Binding Energies . . . 92
4.3.1 Theoretical Model . . . 93
4.3.2 Energy Comparison . . . 95
4.4 Conclusions . . . 96

5 Resonance Raman Spectroscopy of Hyperbolic Phonon Polaritons in hBN Encapsulated TMDs **97**
5.1 Literature Review 97
5.2 Results 98
5.2.1 hBN Modes Identification 99
5.2.2 WSe_2 hBN Resonance Behaviour 102
5.2.3 $MoSe_2$ hBN Resonance Behaviour 109
5.2.4 T-Matrix Modelling of HPPs 113
5.3 Conclusions 116

6 Conclusions **117**
6.1 Perspectives and Outlook 119

References **121**

List of Figures

2.1 TMD atomic structure. 4
2.2 TMD stacking structures. 5
2.3 TMD Brillouin zone diagram. 6
2.4 TMD band diagram. 7
2.5 TMD band diagram showing dark excitons. 10
2.6 TMD energy diagram showing hybrid excitons. 12
2.7 Phonon vibrations for monolayer TMDs. 13
2.8 Parallel and perpendicular permittivity of hBN. 14
2.9 Isofrequency surfaces of HPP in hBN. 15
2.10 Feynman diagram of Raman scattering. 16
2.11 Feynman diagram of additional Raman scattering processes. 17
2.12 Mechanism for resonance Raman enhancement. 18
2.13 Examples of resonance Raman profiles. 19

3.1 Stacking diagram and optical microscope images of the heterostructure samples. 23
3.2 Schematic of the stamp transfer technique for assembling a TMD vdW heterostructure. 24
3.3 Diagram of the setup of the laser sources. 25
3.4 Diagram of the Raman spectroscopy system. 27
3.5 Measurement of the spot size on the sample. 28
3.6 Polarised Raman spectra of $MoSe_2$ at 1.652 eV 30
3.7 Raman spectra of $MoSe_2$ at 1.652 eV before and after background subtraction 31

4.1 WSe_2 monolayer differential reflectivity spectrum. 39
4.2 WSe_2 monolayer PL spectrum. 40
4.3 $MoSe_2$ monolayer differential reflectivity spectrum. 42
4.4 $MoSe_2$ monolayer PL spectrum. 43
4.5 HS57 heterostructure differential reflectivity spectrum. 44
4.6 HS57 heterostructure PL spectrum. 45
4.7 HS20 heterostructure differential reflectivity spectrum. 46
4.8 HS20 heterostructure PL spectrum. 47
4.9 Monolayer WSe_2 A1s Raman colour-map. 49
4.10 Monolayer WSe_2 A1s resonance Raman profile. 50
4.11 Monolayer WSe_2 A2s Raman colour-map. 51
4.12 Monolayer WSe_2 A2s Raman waterfall plot. 52
4.13 Monolayer WSe_2 A2s resonance Raman profiles. 53

4.14 Energy diagram for 2s associated two-phonon Raman scattering. 54
4.15 Monolayer WSe_2 B1s Raman colour-map. 55
4.16 Monolayer WSe_2 B1s resonance Raman profiles. 56
4.17 Monolayer $MoSe_2$ A1s Raman colour-map. 57
4.18 Band diagrams for intervalley two-phonon Raman scattering. 58
4.19 Monolayer $MoSe_2$ A1s resonance Raman profile. 58
4.20 Monolayer $MoSe_2$ A2s/B1s Raman colour-map. 60
4.21 Monolayer $MoSe_2$ A2s/B1s resonance Raman single and two state fits. . . 61
4.22 Monolayer $MoSe_2$ A2s/B1s resonance Raman profiles. 61
4.23 Monolayer $MoSe_2$ B2s Raman colour-map. 63
4.24 Monolayer $MoSe_2$ B2s resonance Raman profiles. 64
4.25 57° twist $MoSe_2/WSe_2$ heterostructure resonance Raman colour-map. . . 66
4.26 57° twist $MoSe_2/WSe_2$ heterostructure $MoSe_2$ A1s resonance Raman profiles. 67
4.27 57° twist $MoSe_2/WSe_2$ heterostructure resonance Raman colour-map. . . 68
4.28 57° twist $MoSe_2/WSe_2$ heterostructure WSe_2 A1s resonance Raman profiles. 69
4.29 57° heterostructure resonance Raman colour-map at the $MoSe_2$ B1s / A2s. 70
4.30 57° twist $MoSe_2/WSe_2$ heterostructure $MoSe_2$ A2s resonance Raman profiles. 71
4.31 57° twist $MoSe_2/WSe_2$ heterostructure $MoSe_2$ B1s resonance Raman profile. 72
4.32 57° heterostructure resonance Raman colour-map at the WSe_2 A2s. 73
4.33 57° twist $MoSe_2/WSe_2$ heterostructure WSe_2 A2s resonance Raman profile. 74
4.34 57° heterostructure resonance Raman colour-map at the $MoSe_2$ B2s. . . . 75
4.35 57° twist $MoSe_2/WSe_2$ heterostructure $MoSe_2$ B2s resonance Raman profiles. 76
4.36 57° heterostructure resonance Raman colour-map at the WSe_2 B1s. 77
4.37 57° twist $MoSe_2/WSe_2$ heterostructure WSe_2 B1s resonance Raman profile. 78
4.38 20° heterostructure resonance Raman colour-map at the $MoSe_2$ A1s. . . . 79
4.39 20° twist $MoSe_2/WSe_2$ heterostructure $MoSe_2$ A1s resonance Raman profiles. 81
4.40 20° heterostructure resonance Raman colour-map at the WSe_2 A1s. 82
4.41 20° twist $MoSe_2/WSe_2$ heterostructure WSe_2 A1s resonance Raman profile. 83
4.42 20° heterostructure resonance Raman colour-map at the $MoSe_2$ A2s. . . . 84
4.43 20° twist $MoSe_2/WSe_2$ heterostructure $MoSe_2$ A2s resonance Raman profile. 84
4.44 20° heterostructure resonance Raman colour-map at the $MoSe_2$ B1s. . . . 85
4.45 20° twist $MoSe_2/WSe_2$ heterostructure $MoSe_2$ B1s resonance Raman profile. 86
4.46 20° heterostructure resonance Raman colour-map at the WSe_2 A2s. 87
4.47 20° twist $MoSe_2/WSe_2$ heterostructure WSe_2 A2s resonance Raman profile. 87
4.48 20° heterostructure resonance Raman colour-map at the $MoSe_2$ B2s. . . . 89
4.49 20° twist $MoSe_2/WSe_2$ heterostructure $MoSe_2$ B2s resonance Raman profiles. 89
4.50 20° heterostructure resonance Raman colour-map at the WSe_2 B1s. 91
4.51 20° twist $MoSe_2/WSe_2$ heterostructure WSe_2 B1s resonance Raman profile. 91
4.52 Comparison of Rytova-Keldysh and Coulomb potentials. 94

5.1 First report of hBN modes in WSe_2. 98
5.2 Monolayer WSe_2 hBN Raman spectrum. 99

5.3 Monolayer $MoSe_2$ hBN Raman spectrum. 100
5.4 hBN permittivity in the infrared. 100
5.5 Monolayer WSe_2 hBN Raman lineshapes. 101
5.6 Monolayer $MoSe_2$ hBN Raman lineshapes. 102
5.7 Monolayer WSe_2 hBN Raman colour-map. 103
5.8 Zoom of monolayer WSe_2 hBN Raman colour-map. 104
5.9 Monolayer WSe_2 hBN HPP Raman resonance profiles. 105
5.10 Monolayer WSe_2 hBN Raman HPP + phonon resonance profiles. 105
5.11 Monolayer WSe_2 hBN Raman 815 cm^{-1} lineshapes. 107
5.12 Monolayer WSe_2 hBN Raman 1050 cm^{-1} lineshapes. 108
5.13 Resonance adjusted HPP Raman at different resonance conditions. 109
5.14 Monolayer $MoSe_2$ hBN Raman colour-map. 110
5.15 Monolayer $MoSe_2$ hBN Raman resonance profile. 111
5.16 Parameter correlation matrix for $MoSe_2$ hBN fit. 112
5.17 First 3 HPP modes H field vs depth 114
5.18 Dispersion relation and Raman lineshape of HPPs in hBN 114
5.19 Dispersion relation and Raman lineshape of HPPs in hBN 115

List of Tables

4.1 Monolayer WSe_2 PL fit coefficients. 41
4.2 $MoSe_2$ PL fit coefficients. 43
4.3 HS57 PL fit coefficients. 45
4.4 HS20 PL fit coefficients. 47
4.5 $MoSe_2$ A2s B1s resonance Raman fit coefficients. 62
4.6 $MoSe_2$ B2 resonance Raman fit coefficients. 64
4.7 57° heterostructure WSe_2 A1s resonance Raman fit coefficients. 69
4.8 57° heterostructure $MoSe_2$ A2s resonance Raman fit coefficients. 71
4.9 57° heterostructure $MoSe_2$ B2s resonance Raman fit coefficients. 76
4.10 HS57 WSe_2 IX* and A2s resonance Raman fit coefficients. 78
4.11 HS20 WSe_2 A1s resonance Raman fit coefficients. 81
4.12 20° heterostructure $MoSe_2$ A2s resonance Raman fit coefficients. 85
4.13 20° heterostructure $MoSe_2$ B2s resonance Raman fit coefficients. 90
4.14 Table of resonance Raman exciton energies. 92
4.15 Model parameters used to calculate the exciton energies. 95
4.16 Measured and theoretical 1s-2s exciton energy spacings. 96

5.1 WSe_2 hBN HPP resonance profile fit parameters. 106
5.2 $MoSe_2$ 800 cm^{-1} resonance parameters. 113

Declaration of Authorship

I declare that this thesis and the work presented in it is my own and has been generated by me as the result of my own original research.

I confirm that:

1. This work was done wholly or mainly while in candidature for a research degree at this University;
2. Where any part of this thesis has previously been submitted for a degree or any other qualification at this University or any other institution, this has been clearly stated;
3. Where I have consulted the published work of others, this is always clearly attributed;
4. Where I have quoted from the work of others, the source is always given. With the exception of such quotations, this thesis is entirely my own work;
5. I have acknowledged all main sources of help;
6. Where the thesis is based on work done by myself jointly with others, I have made clear exactly what was done by others and what I have contributed myself;
7. None of this work has been published before submission

Signed:..... Date:.....

Acknowledgements

First of all, I would like to first thank my PhD supervisor Prof. David C. Smith, whose patience and breadth of theoretical and practical knowledge were an invaluable help during my PhD. I am greatful for his support and direction over the past few years. I want to also give thanks to Kath Leblanc for her help and training in the cleanroom as well as Justin Harris and Cameron Murray for supplying the liquid helium and nitrogen needed to run the experiments at a moment's notice.

I would also like to thank Dr Liam McDonnell, who recently complted his PhD and left the group, for training me in the operation of the resonance Raman system, especially for his help at the times where the dye laser needed realignment. I would also like to thank him for his help in developing the code and procedures for correcting and fitting the reflectivity and resonance Raman data. I also want to aknowledge the other students and academics in the QLM group for all of our interesting physics discussions during my PhD.

I would also like to thank my friends Ben Allen, Darren and Cris for their support and excellent sense of humour. Finally I want to thank my parents Nigel and Sue, and my brother Sam for all of their help and support over the years.

To my family...

Chapter 1

Introduction

Transition metal dichalcogenides (TMDs) have been the subject of great interest recently after the reports of the graphene [1] had brought the technique of mechanical exfoliation to popular attention. This same technique has been applied to a variety of layered materials including phosphorene [2], hexagonal boron nitride (hBN) [3] and TMDs [4]. One of the reasons for the interest in TMDs is the large exciton binding energies, which results in excitons dominating the optical properties. Unusually, excitons have been observed all across the band structure, not just at the band gap [5, 6]. The main reason for the strength of excitons in monolayer TMDs is the reduction in dielectric screening of the Coulomb interaction in the system as a result of the 2D nature of the layers. This leads to a greatly enhanced Coulomb interaction which is significantly different in form from a standard potential in a 3D system [7, 8]. The direct band gap nature of monolayer TMDs also means that the excitons are bright. This combined with the fact that the band gap is in the visible range makes TMD monolayers particularly interesting for optoelectronic devices. Symmetry breaking in the monolayer case also leads to a coupling between valley and polarisation [9] which allows for exciting excitons in a chosen valley [10]. This could be applied in 'valleytronics' which involves the optical control of charge carrier momentum [11].

The weak van der Waals forces between the layers of these materials allow more complex samples to be made by picking up and placing down flakes of multiple different 2D materials [12]. This creates a multitude of additional effects. These can be as simple as a modification of the dielectric environment tuning the binding energies. Stacking of two layers with similar lattice constants with a twist angle between the two layers can create moiré patterns which add another level of periodicity. This can lead to zone folded moiré phonons [13, 14]. Moiré superlattice minibands and hybrid excitonic states [15, 16] are also possible in TMD heterostructures. Excitons trapped in the moiré potentials are also observed [17].

1.1 Organisation

This thesis reports on resonance Raman measurements made on hBN encapsulated WSe_2 and $MoSe_2$ monolayers and two van der Waals heterostructures made from stacks of those monolayers. The first experimental chapter discusses the range of excitonic states that are identified using resonance Raman, most notably the energies of the 2s excitons are determined in the heterostructures for the first time. The second experimental chapter explores the behaviour of hyperbolic phonon polaritons in the hBN layer created by the TMD excitons.

Before these chapters, an overview of the required theory is given with a review of the relevant literature. This thesis also details the experimental methods which were used to ensure the Raman spectra were repeatable and could be corrected to absolute Raman scattering rate, including correction for differences in electric field in different layers in the sample stack.

Chapter 2

Theoretical Background

This chapter will provide an overview of the theory required to understand the experimental results and interpretations in this thesis. The main focus is the physics of transition metal dichalcogenides (TMDs) and their electronic and optical properties. The most widely used optical techniques for studying TMDs are also discussed alongside the more specialised resonance Raman spectroscopy which is the main technique utilised in this work. The physics of hyperbolic phonon polaritons is also discussed which becomes relevant in the second experimental chapter.

2.1 TMDs

TMDs are semiconductor crystals of the form MX_2 where M is a transition metal and X is a chalcogen (group 16 of the periodic table). The most commonly discussed of these is $MoSe_2$, which is naturally occurring but TMDs made with Mo or W as the metal and S, Se or Te as the chalcogen also feature significantly in the literature.

2.1.1 Physical Properties

Similarly to graphite, TMDs are made up of covalently bonded atoms in layers which are held together by Van der Waals interactions. Each of these layers is a hexagonal lattice which is three atoms thick. In one of these layers, the centre plane of transition metal atoms is flanked by two planes of chalcogen atoms as shown in Figure 2.1. Each metal atom is bonded to six chalcogen atoms a trigonal prismatic configuration. This means that the monolayers belong to the D_{3h} space group [18–21].

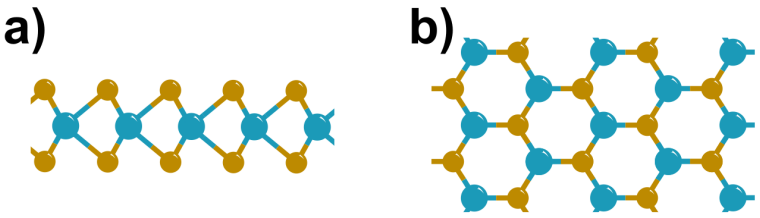

FIGURE 2.1: Sketches of the crystal structure of a TMD monolayer. The chalcogen atoms (e.g. Se) are shown in gold and the transition metal atoms (e.g. Mo) are shown in blue. These are shown as observed from a) the side (as seen from within the plane) and b) top-down.

In addition to the trigonal prismatic structures, an octahedral structure is possible [22]. In this case the chalcogen atoms are not directly above each other in the monolayers and this has D_{3d} point group. However, none of the TMDs discussed in this thesis are stable in this 1T structure [23].

If a second layer is introduced to the stack to form a bilayer, it can be rotated in-plane relative to the first layer by any angle from 0 to 60°. Angles greater than 60° are equivalent under reflection to those less than 60°, with 120° being the same as 0° thanks to the three-fold rotational symmetry of the individual layers. Examples of stacking configurations are shown in Figure 2.2. The 0° AA stacking in a) is the least energetically favourable. AC and AB stacking shown in b) and c) are more favourable in samples with 0° twist and are also referred to in literature as 3R structure. The most energetically favourable configuration is AA' stacking which occurs at 60° and is shown in Figure 2.2d). This is also called 2H structure and is what is observed in 'natural' bilayers, which are those produced directly from bulk TMD crystals. Bulk crystals of TMDs belong to the D_{6h} space group and have 2H structure where each layer is rotated 60° from the layer below [18–21].

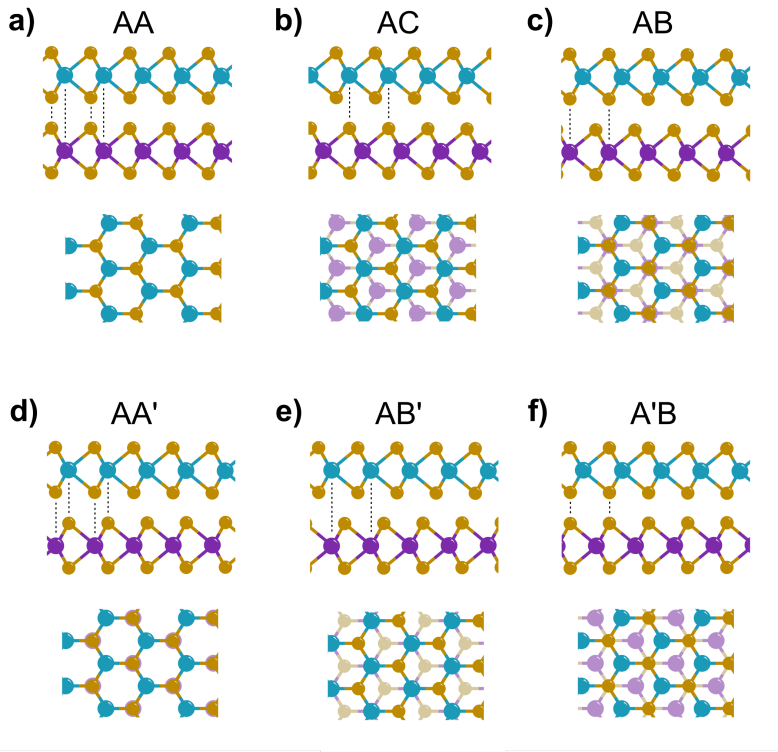

FIGURE 2.2: Sketches of the crystal structure of different stacking in TMD bilayers. The chalcogen atoms (e.g. Se) are shown in gold and the transition metal atoms (e.g. Mo) are shown in blue for the top layer and purple for the bottom layer. A side and top-down view are given for each configuration. Different in-plane offsets between the two layers are shown and labelled. a)-c) have a twist angle of 0° and d)-f) have a twist angle of 60° between the two layers. Dashed lines between the layers indicate the atoms that are aligned vertically in each case [21, 24, 25].

The layers are weakly held together by Van der Waals forces. This fact means that mechanical exfoliation techniques such as ultrasonication in a solvent [26] or the 'sticky-tape method' [27, 28] can be used to separate the layers and produce monolayers and bilayers with areas on the order of 100 square microns. More complex techniques can be used to synthesize larger area monolayers. However, these usually result in lower quality flakes than those produced with the sticky-tape method [29]. These monolayers can be identified using a standard optical microscope if the substrate is chosen correctly. Using a smooth Si wafer with 90 or 290 nm thick SiO_2 produces enough contrast under the microscope to allow monolayers, bilayers and bulk crystals to be distinguished [30].

With a mechanically exfoliated TMD monolayer, hot pick-up techniques [12] can be used to manipulate individual flakes as discussed in section 3.1. The flakes can be stacked to produce heterostructures with different TMDs or homobilayers with any desired twist angle between the layers. The twist angles can be estimated under a microscope by the angles of the edges of the crystals or more accurately determined through polarised second harmonic scattering measurements [31–33].

The different symmetry of various TMD stacking configurations can lead to different interlayer scattering [34]. Additionally, inversion symmetry, which is present in natural bilayers, can be broken by different bilayer stacking [35]. This alters the optical selection rules and leads to the notable spin-valley-locking effect which is also present in the monolayer case, as discussed in the following section.

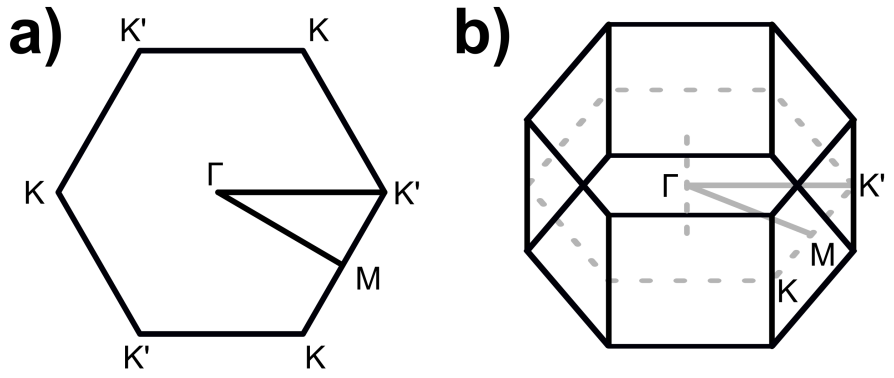

FIGURE 2.3: Sketches of the Brillouin zone of a TMD. a) 2D Monolayer case and b) 3D bulk case. The notable high symmetry points are labelled.

2.1.2 Electronic Band Structure

The hexagonal 2D lattice gives a corresponding hexagonal Brillouin zone, as shown in Figure 2.3a). Density-functional theory (DFT) calculations [36–38] and direct ARPES measurements [39–42] have been used to study the TMD band structures. These have shown that bulk TMDs have indirect band gaps, with band edges at the Γ point and at the Q point, half way between the Γ and K. Additionally, tight binding models, which consider the contributions from the electron orbitals, have shown that the p orbitals, which contribute more to the bands near the centre of the Brillouin zone, are much more affected than the d electron orbitals by the adjacent layers. Confinement to the plane of the monolayer then results in an increase in the band gap around the Brillouin zone centre [43]. This means the conduction band minima and valence band maxima both fall at the K points in monolayers [4, 44].

In addition to confinement effects, the inversion symmetry that is present in bulk TMDs and natural TMD bilayers is broken in the monolayer case. This inversion symmetry breaking makes the K and K' points no longer equivalent [9, 20, 45], which is made more significant by the large valence band spin-splitting [20]. For example, in WS_2 the bottom of the conduction band has a splitting on the order of 30 meV and the top of the valence band is split by 450 meV [46]. Figure 2.4 shows a sketch of the spin splitting at the band edges for the K points, with the associated spin marked with an up or down arrow. At the K' points, the spin splitting is the opposite, such that spin up and spin down are swapped.

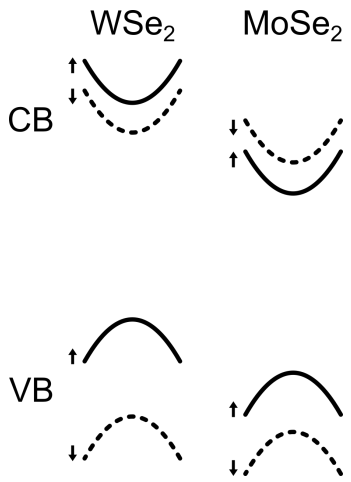

FIGURE 2.4: Sketch of the valence band (VB) maxima and conduction band (CB) minima for monolayers of $MoSe_2$ and WSe_2 at the K high symmetry points. The solid parabolas indicate the bands associated with spin up and the dashed parabolas indicate spin down - as marked with arrows.

The inversion symmetry breaking also results in transitions at the K and K' points coupling to right and left circular polarisations respectively [9, 28, 45]. This means states can be excited in a chosen valley. Circularly polarised photoluminescence emission has been observed with polarisation predominantly in the same direction as the excitation polarisation [10, 28, 34, 47, 48]. This shows that the states excited in one valley are long lived enough to make these TMD monolayers promising candidates for use in valleytronics [11, 49].

2.1.3 Excitons

An exciton is an excited state consisting of an electron and a hole. They are generally divided into Wannier-Mott or Frenkel exitons. The latter corresponding to excitons with sizes smaller than the atomic spacing in the material and therefore high binding energies. Excitons in crystalline semiconductors are usually of the Wannier-Mott type. Wannier-Mott excitons are larger, on the scale of several times the atomic spacing with a smaller binding energy [50]. The excitons observed in TMDs are of the Wannier-Mott type and generally follow Wannier-Mott models [36].

2.1.3.1 Keldysh Potential

Excitons in monolayer (and few layer) TMDs experience reduced screening of the Coulomb interaction compared to bulk crystals as the charge carriers which are present in the adjacent layers in the bulk TMD case, are not present in the monolayer case. This reduced screening results in an enhanced electron-hole interaction which gives both a larger quasiparticle band gap and a greatly enhanced exciton binding energy [51]. Exciton binding

energies on the order of 300 meV are commonly observed in TMD monolayers, which is much greater than the 15 meV of more typical Wannier-Mott excitons in Si [52]. This means excitons dominate the optical properties of TMDs, being observed at more than just the band gap. The high binding energy has also allowed for observation of excitons by optical spectroscopy even at room temperature [53].

The simplest model of an exciton in a TMD monolayer follows that of a hydrogen atom, in which the Coulomb interaction between two charges is considered. For a hydrogen atom, the electron mass is a factor of approximately 2000 less than the proton mass. The case of the exciton differs in that the masses of the electron and hole are on the same scale, so the same approximations cannot be used. A reduced mass for the electron and hole must be used and the dielectric screening from only the environment is considered [54]. When considering the possible excitonic states, Like the hydrogen atom, in addition to the 'ground state' 1s excitons, excited exciton states (2s, 3s, etc.) are also present, in a Rydberg series. Such a series of excited states has been observed in bulk MoS_2 crystals as early as 1967 [22, 55]. The hydrogenic nature of the Rydberg series does not hold for the few layer and monolayer cases however, due to the confinement and reduced dielectric screening modifying the effective Coulomb interaction [51, 56, 57]. Instead, the Coulomb interaction is better modelled by a Rytova-Keldysh potential, which was developed 1967 and describes the interaction of a pair of point charges in an infinite thin semiconductor sheet of known polarizability [7, 51, 58, 59]. This Rytova-Keldysh potential takes the form:

$$U_\lambda(\rho) = -\frac{\pi e^2}{2r_*^\lambda}\left[H_0\left(\frac{\rho}{r_*^\lambda}\right) - Y_0\left(\frac{\rho}{r_*^\lambda}\right)\right] \tag{2.1}$$

Where $r_*^\lambda = 2\pi\kappa_\lambda/\varepsilon$ is the the screening length for the excitons. This is defined by the in-plane polarizability of the TMD layer κ_λ. As the layer is thin, the electric field associated with the exciton exists entirely in the environment outside the TMD layer, with permittivity ε. H_0 is the zeroth Struve function and Y_0 is the zeroth Bessel function of the second kind. The simpler Coulomb potential has the form:

$$U_\lambda(\rho) = -\frac{e^2}{\varepsilon\rho} \tag{2.2}$$

The Coulomb potential gives predicted binding energies for the TMD monolayer excitonic states that overestimate the values by around 20% vs experiment for the higher order (4s, 5s) states, but for the more tightly bound 1s exciton, the model overestimates by a factor of five. This is because the energies of the most tightly bound excitons are much more affected by the polarizability of the TMD layer rather than the dielectric environment further from the layer. The Keldysh potential gives much better agreement, with only a few percent deviation from experiment for all states in monolayer TMDs [51, 60, 61]. The form of this potential is discussed in more specific detail in section 4.3 of this thesis.

Reflectivity measurements of TMD monolayers have shown that the oscillator strength of the excited excitonic states drops by about an order of magnitude for each increase in principal quantum number [57, 62, 63]. The reduction in oscillator strength is a result of the increased size of the dipole in excitons with larger quantum number, resulting in a reduced overlap of the electron and hole wave-functions. Measurements at 4 K of the widths of the excitonic states, which are inversely proportional to their lifetimes, show that the WSe_2 A1s is broader than the A2s. This is despite the fact that the A2s and higher states can non-radiatively decay to the A1s, whereas the A1s does not have an equivalent non-radiative decay channel. This increased width of the A1s is a result of the very strong dipole interaction, which allows it to rapidly radiatively decay and produce intense photoluminescence [64–66]. For example, in WSe_2 at 4 K, A1s and A2s line widths of 5 and 3 meV respectively have been reported [65]. Reports of the lifetimes of the A1s excitons are on the order of a few ps at 4 K [64, 67].

The spin splitting of the conduction and valence bands at the K points leads to the formation of two classes of bright direct excitons. The lower energy of these, called 'A' excitons correspond to a hole in the the highest energy branch of the valence band and an electron in the conduction band of the same spin. The 'B' excitons are then resulting from a hole in the lower energy of the split valence bands and an electron in the conduction band of the same spin [68]. In addition, broader, higher energy excitonic states are also observed. These are 'C' excitons and are due to nested bands nearer to the gamma point [5, 6]. The energies at which the excitons are observed are the single particle band gap energy minus the exciton binding energy.

An exciton can also be composed of an electron and hole in the bands associated with different spins as is shown in Figure 2.5a). Photons do not couple directly to these excitons as it is spin-forbidden. Since they cannot directly be optically accessed, they are called 'dark' excitons. The same is also true of the momentum-dark intervalley exciton shown in Figure 2.5b). Both of these dark excitons can be lower or higher in energy than the bright A exciton, depending on the band alignment [66]. Dark excitons can still impact the lifetimes of the bright excitonic states as scattering with phonons can provide the momentum required to scatter between valleys [53, 69–71]. The dark states themselves can be very long-lived as they cannot radiatively decay [72].

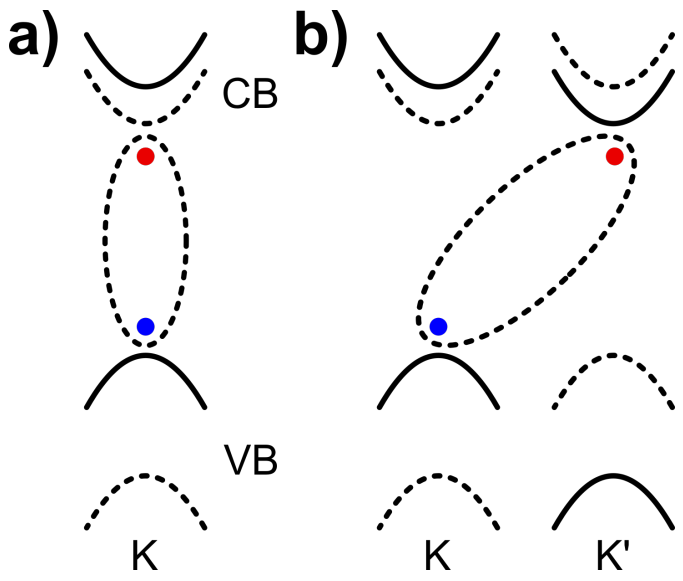

FIGURE 2.5: Sketch of the electron (shown in red) and hole (blue) configurations of a) A spin-dark exciton. b) A momentum-dark exciton. The the valence band (VB) maxima and conduction band (CB) minima are shown for a WSe_2 monolayer at the K high symmetry points. The solid parabolas indicate the bands associated with spin up and the dashed parabolas indicate spin down.

In addition to excitons, states with three charge carriers called trions have been observed in TMD monolayers [73, 74]. These can be both positively and negatively charged and their relative population can be manipulated by charging the TMD layer [75, 76]. The trion states typically fall 20-40 meV below the A1s exciton as their binding energies are less than those of excitons. In addition, states with four (biexcitons) or more charge carriers have also been observed with populations that can be tuned by charging the TMD monolayers [77–79]. Further adding to the complexity of these trion states that are observed below the A1s exciton, trions can have one of the charges in a different K/K' valley to the other two, forming intervalley and intravalley versions of the trions [75, 80]. In addition to states associated with 1s excitons, 2s trions have been observed in WS_2 22 meV below the 2s exciton [81].

As well as interactions of individual particles, interaction between excitons and a Fermi sea of charges are possible [82, 83]. At the limit of higher charge density, the interaction of excitons with the Fermi sea follows an exciton-polaron model rather than a trion model. This leads to an attractive and a repulsive polaron, where the cloud of screening electrons are either attracted or repulsed repulsed from an exciton respectively [84, 85]. These polaronic states can be identified in electrically gated measurements by a shift in their energy with charge density [84, 86].

2.1.4 Bilayers and Heterostructures

In TMD bilayers and heterostructures, interlayer excitons can form with a hole in one layer and an electron in the other. These have lower binding energy and much lower dipole matrix element than the intralayer excitons due to the physical separation of the charges. Despite these facts, interlayer excitons have been observed in TMD bilayers at room temperature [87]. In homobilayers, the lower binding energy means that the interlayer excitons fall above the intralayer excitons in energy. In heterostructures however, the band alignment can allow for interlayer excitons with much lower energies than the intralayer excitons [88, 89]. The interlayer excitons in TMD heterostructures have long lifetimes, on the order of 10 times that of monolayers [90]. Interlayer excitons also show the valley polarisation effects that are present in monolayers [88].

Whilst natural TMD bilayers with a twist angle of 60° do not have broken inversion symmetry, the symmetry is broken for bilayers with other twist angles, and heterostructures made from stacked different monolayers. This means that the spin splitting and valley polarisation effects from monolayers are also present. The misalignment between the layers creates a moiré pattern, with a periodically varying potential. This can create additional trapped excitonic states [91, 92]. The moiré potential has a corresponding wavevector in reciprocal space, the moiré wavevector. This leads to additional Raman peaks in the spectrum of TMD heterostructures [13, 93].

The stacked TMD layers are not entirely rigid so do not hold their shape perfectly when stacked. The twisted stacked layers can relax into a more energetically favourable arrangement. This reconstruction process creates domains of different stacking arrangements with size dependant on twist angle. The domains can be are orders of magnitude larger than a unit cell and are largest near 0° and 60° of twist [94, 95]. These can lead to strain induced shifts of existing Raman peaks [96].

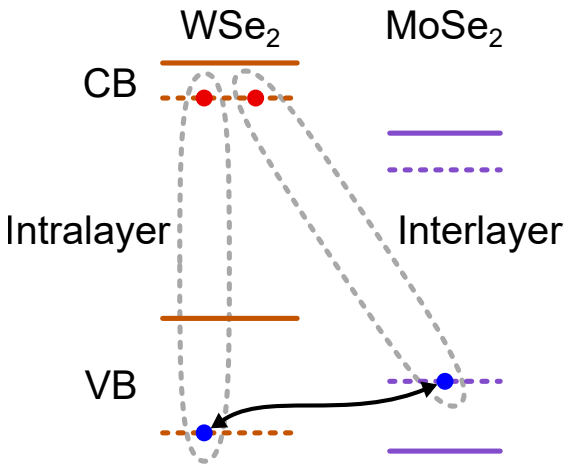

FIGURE 2.6: Sketch of the electron (shown in red) and hole (blue) configuration of the hybrid excitons in a TMD heterostructure resulting from the tunnelling of holes (double headed arrow) between inter- and intra- layer excitons. The energies of the valence band (VB) maxima and conduction band (CB) minima are marked with solid and dashed horizontal lines which correspond to opposite spins.

Hybridisation of inter- and intra- layer excitons states can occur in TMD heterostructures with certain twist angles [97]. This works by tunnelling of electrons or holes between the layers as shown in Figure 2.6. This kind of hybridisation has been observed for both A and B excitons in different heterostructures [16, 97, 98]. The excitons which hybridise are dependant on the band alignment of the two constituent layers which is affected by twist angle and chosen monolayer materials.

2.1.5 Encapsulation in hBN

TMDs can oxidise in air [99]. This is a significant concern for monolayers, as they have a large surface area. Encapsulation of the monolayers can prevent this by providing a physical barrier. Hexagonal boron nitride is the most commonly used material for this as it has a large band gap of 6 eV which prevents the hBN from strongly interacting with light in the visible range [100]. Encapsulation in hBN also narrows the exciton linewidths due to exclusion of molecules at the surface which lead to inhomogeneities in unencapsulated layers. The reduced inhomogeneities lead to fewer trapped states and localised defects in the TMD [62, 65, 101–103]. In addition, hBN encapsulation adds additional dielectric screening as compared to unencapsulated TMD samples which leads to lower exciton binding energies and a smaller single particle band gap.

2.2 Phonons

Phonons are quantized modes of vibration of an elastic structure. Physically, phonons are collective oscillations of atoms in a material about their equilibrium positions. They

contribute strongly to the thermal and electrical properties of materials [50, 104–106]. For materials with more than one atom in the unit cell, such as TMDs, phonons can be grouped into acoustic and optical. Acoustic phonons involve the adjacent atoms in the lattice vibrating in-phase and show a characteristic linear dependence of frequency on wavevector near zero momentum. Optical phonons involve adjacent atoms in the lattice vibrating out of phase (in opposite directions) from each other. These are at higher frequencies than acoustic phonons and their frequency does not tend to zero at zero momentum.

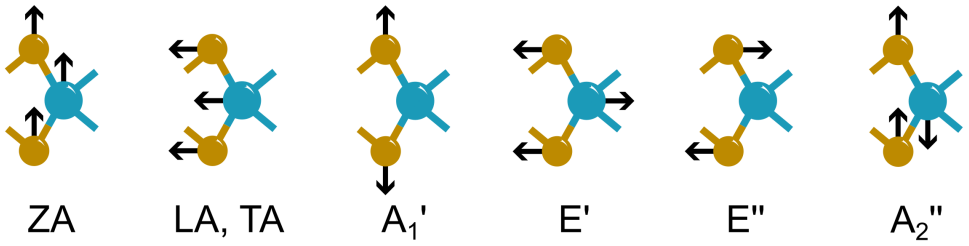

FIGURE 2.7: Sketch of the displacements of the atoms in a TMD monolayer for each of the different vibrational modes near the gamma point [107, 108].

To understand the phonons in TMD monolayers, the crystal symmetry is considered. The reduction of the D_{3h} symmetry group of the TMD monolayers gives the symmetries of the different TMD phonons [19, 109]. A sketch of these is shown in Figure 2.7. The lowest frequency phonons are the acoustic phonons LA, TA and ZA. The LA and TA are longitudinal and transverse in-plane waves and the ZA is an out of plane vibration. The rest of the phonons are optical. Of these, the A_1' and A_2'' are both out of plane vibrational modes. The E' and E'' are both in-plane, where each of the E phonons has both a transverse or longitudinal variant, e.g. $E_L'O$ and $E_T'O$ which are equivalent at zero momentum. Phonon dispersion relations, calculated using DFT, are available in literature which show the frequencies of all the TMD phonons at the various high symmetry points for $MoSe_2$ [110] and WSe_2 [111] amongst other TMDs [112, 113].

2.3 Hyperbolic Materials

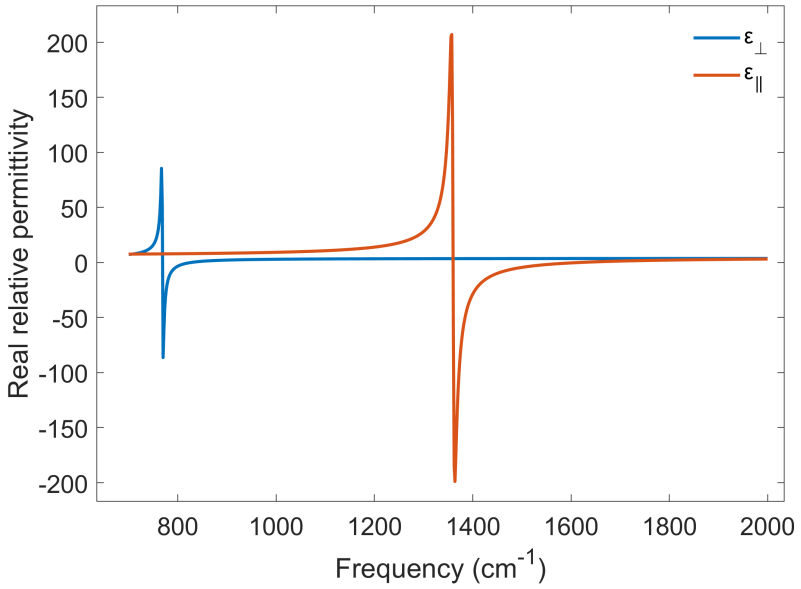

FIGURE 2.8: The real part of the permittivity of hBN in the parallel and perpendicular directions, using two Lorentzian oscillators. hBN is hyperbolic in the lower Reststrahlen band between the TO frequency of $\sim 760cm^{-1}$ and the LO frequency of $\sim 825cm^{-1}$. hBN is also hyperbolic in the opposite sense in the higher Reststrahlen band which ranges from $1360 - 1620cm^{-1}$.

Birefringent materials are those with a different values of dielectric permittivity along different crystal axes. Hyperbolic materials go beyond this by having permittivity with a different sign in different directions. One example of this is hBN, which has two bands in which the permittivity in-plane and out-of-plane are of opposite sign [114]. These are called the reststrahlen bands and fall in the infrared range as shown in Figure 2.8. Within these bands, hyperbolic phonon polaritons (HPP) can be excited in the hBN. Polaritons are mixed states arising from electromagnetic waves strongly coupled with matter. For these phonon polaritons, the oscillating dipoles from the acoustic phonons in hBN can couple strongly to photons. The 'hyperbolic' name comes from the shape of the isofrequency surface of the HPPs in k space, which takes the form of a hyperbola as shown in Figure 2.9. The figure shows three different surfaces for different frequencies, increasing from red to green to blue. The angle of the surface to the z axis tends to a constant value as momentum increases, with different frequencies tending to different angles. The angle is defined by the ratio of the in-plane and out-of-plane permittivity at that frequency and defines the out-of-plane propagation angle of the HPP through the hBN. This means, assuming the momentum is large, the angle of propagation depends only on the frequency. In contrast, for a simple isotropic medium the equivalent isofrequency surfaces would be concentric spherical shells, allowing propagation in any

direction. For HPPs, the hyperbola extend to infinity with increasing k, meaning an excitation with a set frequency can have arbitrarily large momentum and propagate through the hBN (provided there are no losses). Arbitrarily large momentum also corresponds to arbitrarily small photonic confinement. This has allowed for volume confinement of radiation in the infrared range by a factor of 86 smaller than in free space [114–116]. This means hyperbolic materials can be used for subdiffractional imaging [117]. They are also of interest as the confinement can lead to strong-coupling effects [118] such as second-harmonic generation [119–121].

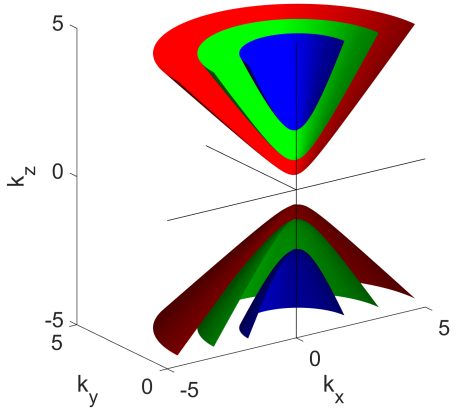

FIGURE 2.9: Cross-section of the isofrequency surfaces of HPP of three different frequencies, increasing going from red to green to blue, in the lower reststrahlen band in hBN. The three axes are wavevector in each direction (in arbitrary units).

Generating and measuring these HPP with high momentum is not trivial. The standard methods are Fourier transform infrared spectroscopy (FTIR) which has limited accessible momentum. This can be augmented with prism coupling or gratings to allow access to higher momenta [122, 123]. Scattering-type scanning near-field optical microscopy (s-SNOM) can be used to measured HPP with even higher momenta. It involves scanning a sharp point across the sample and illuminating it with infrared of the energy of interest. This allows an image of the HPPs to be built up in real space. The spacing of the peaks in intensity of the signal can then be used to calculate the momentum [124–126].

2.4 Raman Spectroscopy

In contrast to the elastic Rayleigh scattering of light, Raman scattering is the inelastic scattering of a photon by a material. This results in the scattered photon being of a different energy to the incoming photon. The Raman process involves the creation (Stokes) or absorption (anti-Stokes) of a low energy excitation in that material. This can be any state such as a polariton, magnon or plasmon, but in literature Raman scattering is generally via phonons [104].

The Raman scattering processes depend on the phonon population of the material, N. The scattering rate for Stokes Raman is proportional to $N+1$ whereas for anti-Stokes the rate is proportional to N. The phonon population is related to temperature by the Bose-Einstein distribution. This means that as temperature (and therefore N) becomes small, only Stokes Raman is observed.

Raman spectroscopy is the main technique used in this thesis. It is a non-destructive technique which probes the phonons and electronic states in a material [127]. Raman spectroscopy involves exciting the sample with light of a narrow wavelength distribution (i.e. from a laser) and measuring the spectrum of scattered light. Since the Raman scattering rate is generally less than 10^{-6} the rate for Rayleigh scattered light, the Rayleigh-scattered light must be filtered out for the signal from Raman scattered light to be observed. This results in a Raman spectrum with peaks shifted by different amounts from the excitation energy. The Raman shifts then correspond to the energies of the phonons in the material. Strain in materials effects the phonons. As a result, Raman spectroscopy can probe strain in 2D materials [128]. Shifts in TMD associated phonons have been reported due to strain in the TMD layer [129].

Since phonons and visible photons couple so weakly that they cannot directly scatter at any reasonable rate, Raman scattering occurs via intermediate electronic states [104, 105]. A Feynman diagram of a Raman scattering process is shown in Figure 2.10. In this TMD case, the incoming photon excites an electron to create an exciton in the TMD. The excitonic state then propagates and scatters creating a phonon. The lower energy excitonic state propagates until it recombines to emit a photon. This is a coherent process which means that the polarisation of the Raman scattered light is the same as the incoming beam.

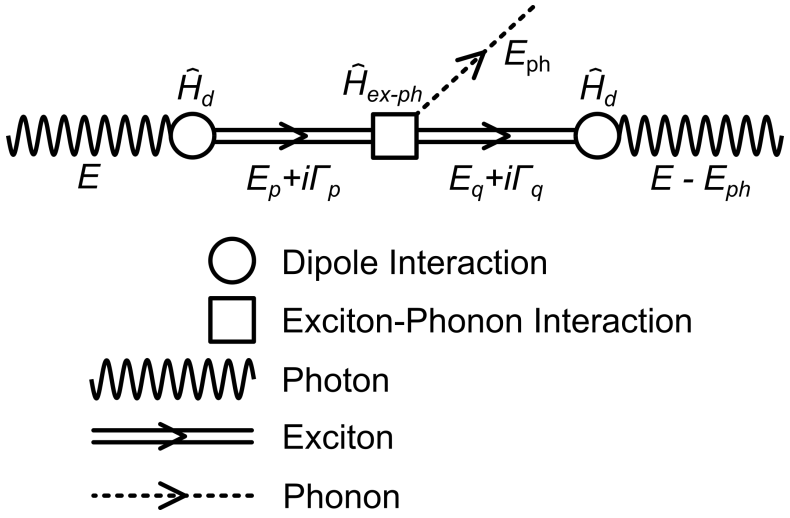

FIGURE 2.10: Feynman diagram of a Stokes Raman scattering process with 1 phonon. The scattering process proceeds from left to right. The labels below each of the propagating states are their energies. The interaction Hamiltonians are also marked above each of the three scattering events.

In addition to the simplest case shown in Figure 2.10, Raman scattering processes are possible in which two phonons are emitted. This can involve simultaneous or sequential Raman scattering as shown in Figure 2.11. Generally in single phonon Raman, only phonons with little momentum (ie near the Γ point) can be created due to conservation of the small momentum provided by the photon. By contrast, two phonon Raman allows scattering to phonons with much greater momentum. This is because two phonons with higher momentum can be emitted in opposite directions, such that the total momentum is still conserved. This creates additional peaks in the Raman spectra at Raman shifts equal to the sum of the shifts of the two phonons. In warm samples, combinations of Stokes and anti-Stokes can also occur, leading to Raman peaks at shifts equal to the difference between the two phonon energies. Single phonon Raman scattering with large momentum is also possible in the case where a defect is present in the crystal lattice of the material. The first excited state can elastically scatter from such a defect, providing additional momentum which then allows for emission (or absorption) of a large wavevector single phonon [71, 130].

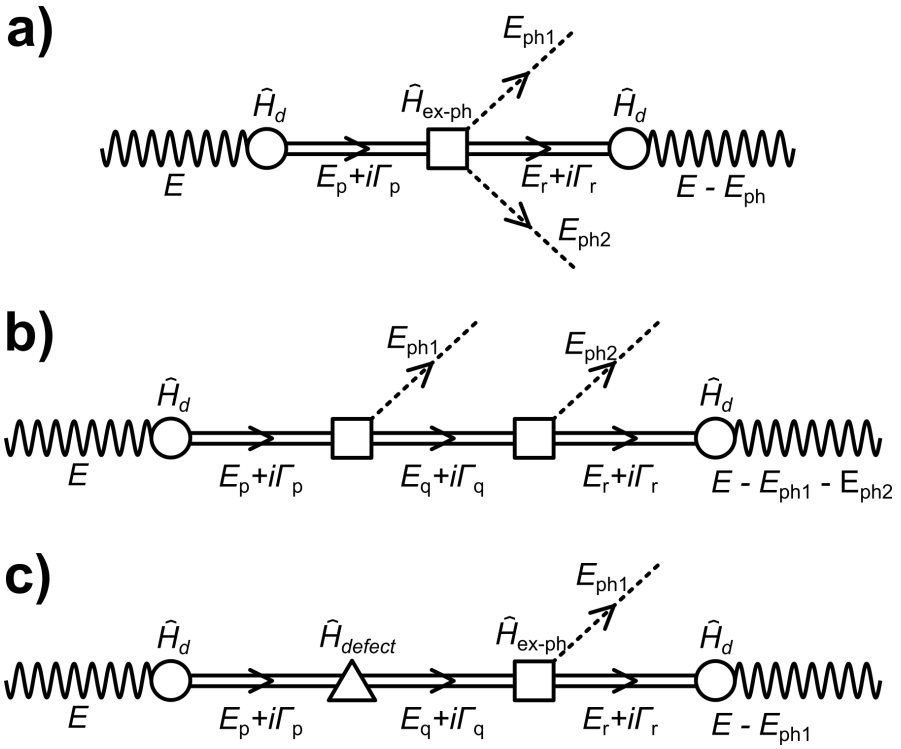

FIGURE 2.11: Feynman diagram of Stokes Raman processes. a) Simultaneous 2 phonon emission. b) Sequential 2 phonon emission. c) Single phonon Raman with defect scattering. The labels below each of the propagating states are their energies.

Raman spectroscopy can be used to identify TMD monolayers from bilayers or bulk flakes by changes in the shifts of the main single phonon A_1' and E' optical Raman modes [113, 131–134] or by measuring low frequency layer breathing phonon modes [127]. Other than these more common uses of Raman spectroscopy of TMDs, Raman measurements have also been used to identify moiré phonons in twisted bilayers [13, 14],

probe hybrid excitonic states in TMD heterostructures [98] and access dark excitonic states [71]. The latter reports make use of resonance Raman spectroscopy, which gives additional information about the excitonic states. This more complex technique has had less use in literature, and is discussed in the following section.

2.4.1 Resonance Raman Spectroscopy

Resonance Raman spectroscopy involves taking multiple Raman spectra with the exciting photons at different energies. This is usually achieved using wavelength-tunable laser sources. The variations in intensity of the Raman scattering from each of the phonons can then be analysed to give extra information about the electronic states involved in the Raman scattering processes. This is possible as the Raman scattering rate is enhanced when the incoming or outgoing photon energy matches the exciton energy. These are called the incoming and outgoing resonances respectively. These two conditions are sketched in Figure 2.12.

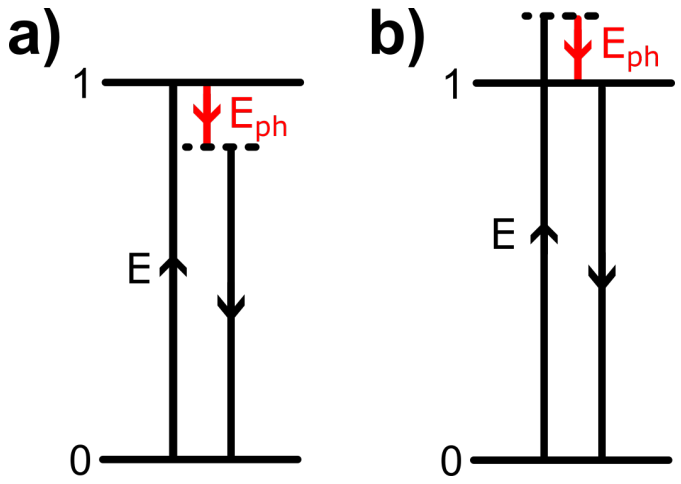

FIGURE 2.12: Diagram of the conditions for resonant Raman scattering with an electronic state. The horizontal line for 0 marks the ground state and for 1 marks the energy of the excited state. The dashed horizontal lines are virtual excited states. The black arrows indicate the absorbed (up) and emitted (down) photons and the red arrow indicates the emitted phonon energy. a) Shows the incoming resonance. b) Shows the outgoing resonance.

In order to understand these resonances and the response of the Raman scattering over the energy range of an electronic state, a functional form for the intensity of the scattering is needed. This can be found using third order perturbation theory by considering the Feynman diagram in Figure 2.10 [105, 135]. The Fermi golden rule shows that the matrix elements for the three scattering events contribute to the numerator of the fraction. Examining Equation 2.3, the right-most term in the numerator comes from the first scattering event in the Feynman diagram, where the ground state (with no phonons) $|0\rangle$ is excited to the state $|p\rangle$. The middle term is then from scattering from

the excitonic states $|p\rangle$ to $|q\rangle$ and the left term from scattering from $|q\rangle$ to the electronic ground state with 1 phonon $|1\rangle$. The $\hat{H}_d$ is the electric dipole Hamiltonian and $\hat{H}_{ex-ph}$ the exciton-phonon interaction Hamiltonian.

$$A_{Raman}(E) \propto \left| \frac{\langle 1|\hat{H}_d|q\rangle\langle q|\hat{H}_{ex-ph}|p\rangle\langle p|\hat{H}_d|0\rangle}{(E - E_p - i\Gamma_p)(E - E_q - E_{ph} - i\Gamma_q)} \right|^2 \tag{2.3}$$

The denominator of the equation comes from the energy differences between the initial state and the states present after each interaction [105]. The left term in the denominator of Equation 2.3 comes from the first interaction, where the photon of energy E scatters to the first excitonic state with energy E_p and linewidth $\Gamma_p = \hbar/\tau_p$ where τ_p is the lifetime of the state. The right term in the denominator is from the difference between E and the phonon of energy E_{ph} plus the second excitonic state with energy E_q and width Γ_q. The third interaction contributes a delta function which enforces conservation of energy, such that the outgoing photon energy to be equal to $E - E_p$. When either of the two terms in the denominator approaches zero, the scattering rate becomes large. This gives rise to the incoming and outgoing resonances.

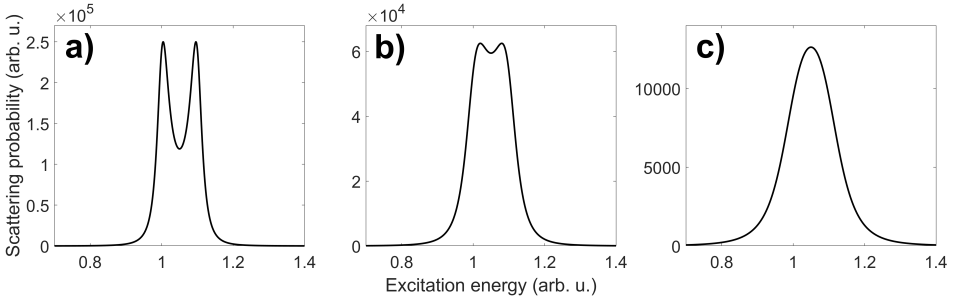

FIGURE 2.13: Plot of Equation 2.3 for a phonon ($E_{ph} = 0.1$) scattering with a single excitonic state of energy 1.0 with different excitonic linewidths. a) $\Gamma_p = 0.02$. b) $\Gamma_p = 0.04$. c) $\Gamma_p = 0.08$.

The numerator in Equation 2.3 does not change with energy so can be replaced with a constant amplitude term proportional to the product of oscillator strength of the excitonic states squared and exciton phonon coupling for each of the Raman peaks of interest. Plots of this function for the simplest case of a single excitonic state ($E_p = E_q$ and $\Gamma_p = \Gamma_q$) are given in Figure 2.13. Two clearly separated resonance peaks are visible in a) near to $E = E_p$ and $E - E_p h = E_p$. When the exciton linewidth is larger, the two resonance peaks move closer together and merge into a single peak at the midpoint of the two resonance energies. In addition to the lineshape changes, the peak amplitude of the Raman scattering signal drops significantly with increasing linewidth.

Resonance Raman spectroscopy has been used to observe resonances at A, B and C excitonic states in multiple TMDs [136–138]. The observation of Raman peaks that shift with excitation energy has revealed inter-valley scattering in TMDs [139]. Resonance Raman has also revealed scattering with dark excitons [71] and excited excitonic

states in few-layer and bulk TMDs [140]. Resonance Raman scattering is therefore a technique that can provide deep insights into the physics of the excitonic states in TMD monolayers.

2.5 Reflectivity and Photoluminescence Spectroscopy

A mode direct probe of the oscillator strengths of the electronic states is reflectivity [105]. This has been used extensively in TMDs to identify the excitonic states [62, 87, 141–143]. Reflectivity allows for the determination of the dielectric function of TMDs [144].

Photoluminescence (PL) spectroscopy has also been widely used to probe the excitonic states in TMDs [60, 145]. This technique involves exciting states in the material of interest with light of higher energy than the states to be probed. This creates excited electronic states which repeatedly scatter non-radiatively towards the lowest energy states before radiatively recombining, emitting light. The spectrum of the emitted PL then has peaks corresponding to the excitonic states [104]. Since PL is incoherent, it is generally not polarised. This is however, not true for samples with valley-spin locking such as TMD monolayers for which the emitted PL maintains the sense of circular polarisation of the exciting beam [28, 48, 146].

In addition to the oscillator strength of the electronic states, the PL signal is sensitive to the population of the states. This means that generally PL gives the strongest signal from the lower energy exciton states, leading to significantly stronger A exciton PL than that from the B [147] despite their similar oscillator strengths. This also enables the detection of lower oscillator strength trions, biexcitons and other multi-particle states [79] as well as detection of interlayer excitons, which have near zero dipole matrix element but still show significant PL [17].

Chapter 3

Experimental Methods

This chapter details the methods used in fabrication of the samples in this thesis, as well as all of the measurement techniques and apparatus used. All of the corrections applied to the experimental data are then discussed for each of the techniques followed by an explanation of the data fitting and analysis methodology.

3.1 Sample Fabrication

The samples used in this thesis were produced by Pasqual Rivera and Xiaodong Xu at the Nanoscale Optoelectronics laboratory in the University of Washington and can be considered as 'state of the art', featuring in previous publications by that group [63, 91]. The heterostructures were assembled bottom-up using a dry stamp-transfer technique from mechanically exfoliated monolayer flakes. Whilst the fabrication of these samples was not performed by me, the procedure that was used is detailed in the following two sections.

Figure 3.1a) and d) show schematics of the stacked layers in the van der Waals (vdW) heterostructure samples discussed in this thesis. The substrates used to hold these samples were 280 nm SiO_2 coated Si wafer chips. This oxide thickness is chosen because it gives the best contrast when examining monolayer flakes of graphene or TMDs [30, 148]. The $MoSe_2$ and WSe_2 layers are encapsulated within exfoliated flakes of hBN. The hBN acts as a dielectric insulator allowing for electrical gating by charging the graphite or TMD layers independently. Figure 3.1b) and d) show microscope images of the samples with the constituent exfoliated flakes outlined in black, dark blue, light blue and red for graphite, hBN, WSe_2 and $MoSe_2$ respectively. Where multiple flakes of the same material are present, dashed outlines indicate the upper layers in the stack.

The position of the laser spot for optical measurements on the vdW heterostructure areas are indicated by white stars in Figure 3.1b) and d). These heterostructures have

twist angles of 57 ° ± 1 ° and 20 ° ± 1 ° respectively and are referred to as HS57 and HS20. These twist angles were determined during fabrication via polarisation-resolved second harmonic generation (SHG) spectroscopy of the constituent monolayers prior to stacking [31–33, 149–151] and confirmed via phase-resolved second harmonic generation spectroscopy of the resultant heterostructures [152, 153]. The phase resolved SHG is needed as the polarisation resolved measurement can not distinguish angles near 60 ° from those near 0 °. The blue and red stars in Figure 3.1b) and d) indicate respectively the positions upon which the laser was focussed for optical measurements of the hBN encapsulated monolayer WSe_2 and $MoSe_2$ areas.

In addition to the exfoliated flakes, the sample shown in Figure 3.1b) has gold electrical contacts, visible at the top and bottom of the image. The two at the bottom of the image are attached to the two few layer graphite layers and the one at the top of the image is attached to the WSe_2 monolayer. One of these became disconnected and they were not used in the main measurements reported this thesis. The contacts were fabricated using standard e-beam lithography and are gold atop a vanadium layer to aid adhesion to the sample surface.

3.1.1 Mechanical Exfoliation

Mechanical exfoliation is the technique by which graphene was first famously synthesised in 2004 [1, 27]. A high quality single crystal of the desired material is brought into contact with adhesive tape and peeled away, leaving flakes of a range of thicknesses adhered onto the tape. The tape is then folded onto its self and peeled back repeatedly to thin the flakes and increase the likelihood of producing a monolayer. Finally the flake-covered tape is stuck down onto the desired substrate and then peeled off to deposit the flakes. Heat can be applied to the substrate before peeling at this step to increase the number of flakes deposited. The final stage is identification of monolayers which can be achieved by atomic force microscopy (AFM) or more rapidly by optical microscopy with thicknesses determined from their contrast.

Mechanical exfoliation can be applied for any material which is composed of layers bound only by weak van der Waals (vdW) forces and was first applied to TMDs in 2010 [4, 44]. Despite its simplicity, this technique can produce monolayers of excellent optical quality from a range of TMDs thanks to the availability of high quality single crystals grown by chemical vapour transport (CVT) [154] or flux growth methods [155]. It is only in the most recent reports that bottom up techniques such as molecular beam epitaxy (MBE) [156–158] or chemical vapour deposition (CVD) [29, 159] have been able to produce monolayer TMD flakes with optical quality approaching the level of mechanical exfoliation.

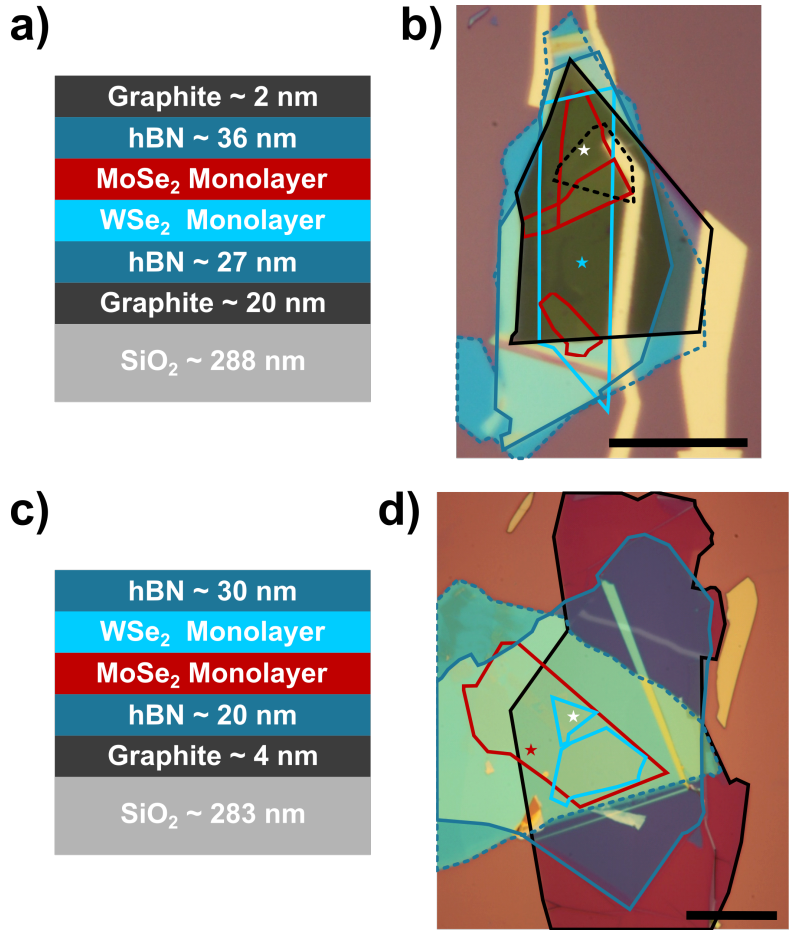

FIGURE 3.1: a) Illustration of the cross section of the 57° twist heterostructure. c) Illustration of the cross section of the 20° twist heterostructure. Layer thickness are given for each of the layers in the stack as determined by fitting reflectivity spectra taken at multiple positions on the sample. b) Microscope image of the sample containing a large WSe_2 monolayer and the 57° twist heterostructure. The position of the laser spot for the spectra taken on those areas are marked with blue and white stars respectively. d) Microscope image of the sample containing a large $MoSe_2$ monolayer and the 20° twist heterostructure. The position of the laser spot for the spectra taken on those areas are marked with red and white stars respectively. The black scale bars in b) and d) are 20 µm.

3.1.2 Stamp Transfer

Whilst exfoliating monolayer TMD flakes can be achieved without too much difficulty, assembling them to create van der Waals (vdW) heterostructures requires the ability to accurately pick up and place down flakes without introducing contamination. There are two widely used methods for this in literature. The first is a wet technique in which potassium hydroxide (KOH) is used to etch away the SiO_2 substrate, which allows the flakes to be picked up and transferred by a PMMA stamp [129]. The second is a dry stamp transfer [12, 40, 160], which was used to produce the samples in this thesis. Each of the layers that make up the stack are individually exfoliated from bulk crystals onto their own SiO_2 coated Si chips.

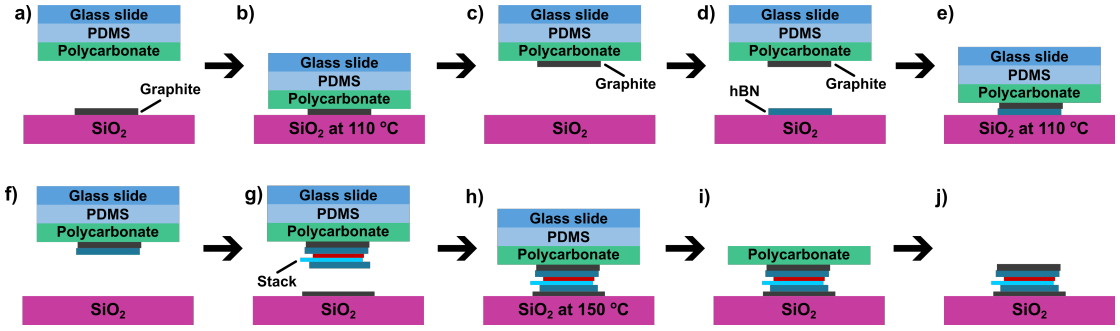

FIGURE 3.2: Schematic of the stamp transfer technique for assembling a TMD vdW heterostructure in order from a) to j). A stamp, consisting of a glass slide with a flexible PDMS layer and a thin polycarbonate film is used to pick up flakes that have been exfoliated onto SiO_2 coated Si substrates, forming the heterostructure stack. h) Finally, the stack is deposited on the bottom graphite layer, i) the stamp is detached, and j) the polycarbonate is dissolved with chloroform.

Figure 3.2 Illustrates the steps in the stamp transfer process; first the stamp is formed, which consists of a polycarbonate (PC) layer on an elastic polydimethylsiloxane (PDMS) layer (∼1 mm) atop a glass slide. This is used to pick up the layers that make up the sample in turn. For the sample in Figure 3.1a) and b) the first layer to be picked up is the top graphite layer. The SiO_2 coated Si chip is held in a temperature controlled stage, above which is the stamp in a translation stage. A microscope looking through the stamp aids in positioning the flake for pickup. Figure 3.2b) illustrates the how stamp is brought into contact with the flake which is then heated to 110 °C, causing the flake to adhere to the PC. The stamp is then lifted away, picking up the flake. This is repeated with the next layers which adhere to the previous layer (or the PC if they extend past the edge of the previous layers) to form the stack on the stamp. The stack is positioned on top of the bottom graphite layer as shown in Figure 3.2h) and heated to a higher temperature of 150 °C which releases the glass slide and PDMS layer, leaving the stack with the PC layer on top. The PC is removed with a 6 hour wash in chloroform followed by 1 hour in acetone.

3.2 Resonance Raman System

The experimental setup discussed here was used for all of the optical measurements on the samples discussed in this thesis, including PL, resonance Raman and reflectance spectroscopy.

3.2.1 Laser Sources

Resonance Raman spectroscopy requires a sharp, background free CW laser source which is continuously tunable over the range of energies of the excitonic states in the samples. A

Coherent Mira 900 Titanium Sapphire laser, optically pumped by a 15W Laser Quantum Finesse 532nm diode laser, was used to cover 1.240 eV to 1.766 eV. Its output was filtered by a Photon etc. laser line tunable filter to remove the unwanted Ti:Sapphire photoluminescence. The filter has a passband width of <0.45 nm over its full range, corresponding to 9.2 cm^{-1} at worst. A Coherent CR-599, pumped by an 8W 532nm Coherent Verdi, with three different dyes was used to cover the rest of the accessible range (DCM: 2.033 - 1.734 eV; Rhodamine 6G: 1.968 - 2.175 eV; Rhodamine 110: 2.101 - 2.275 eV). The photoluminescence background from the dye laser is filtered from the beam by reflecting it off of an Optigrate volume Bragg grating, with the angle adjusted to control the reflected wavelength as shown in Figure 3.3. Multiple gratings were required to cover the full range of the dye laser and these all have passband widths of <10 cm^{-1}. For the reflectivity spectra, a Fianium WhiteLase supercontinuum fiber laser (0.564 - 2.755 eV) is used. Figure 3.3 Illustrates how all three of these sources are coarsely aligned down the path at the top of Figure 3.4 and are selectable via flipper mirrors. For each of these sources a telescope, consisting of a pair of lenses, is used to expand the beam such that it covers the whole of the back of the microscope objective. These telescopes are set such that they also minimise divergence (or convergence) of the beam. An achromatic half wave plate and polariser were used to control the power of the beam. For the dye laser, a noise eater (Thorlabs NEL01) was used to remove fluctuations in beam power over time. The power of the beam transmitted by the cube beamsplitter was measured by a Newport 2832-C power meter and is used to define the power incident on the sample. For all measurements, the incident power on the sample was kept below 100 µW, to avoid any laser heating [161, 162].

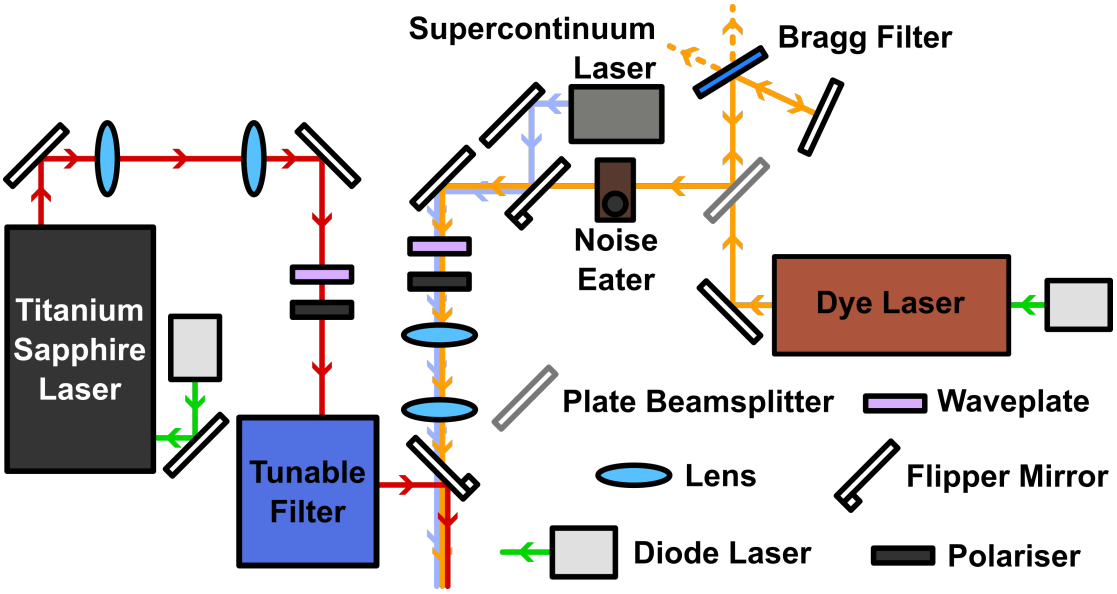

FIGURE 3.3: An illustration of the three laser sources in the resonance Raman setup used to take the resonance Raman, PL and reflectivity spectra. All of the beams are aligned such that they end up down the same path.

3.2.2 Polarisation Control

A diagram of the measurement section of the setup is given in Figure 3.4. The laser beam enters from the top of the diagram with a coarse alignment. Two piezoelectrically driven mirrors (Newport AG-M100N) are used to align the beam under computer control in conjunction with a pair of broadband monochrome cameras. The cameras image the beam with beam samplers and proper alignment is achieved only when the beam is in the centre of the sensor for both cameras. This corrects for any deviation in both angle and offset of the beam, isolating any changes in alignment of the laser source from the experiment, such as those from changing source or tuning the wavelength. After passing the beam sampler for the second alignment camera, the beam enters a linear polariser (Thorlabs LPVIS100) which is adjusted to set the polarisation to either vertical, defined as being normal to the surface of the optical bench, or horizontal. The beam is then directed onto the sample in backscattering geometry with a (Thorlabs BS019) 30:70 cube beamsplitter and onto the 50x 0.5 NA microscope objective. The returning beam passes through a second polariser which controls the polarisation measured by the spectrometer. A broadband superachromatic half wave plate (Thorlabs SAHWP05M-700) after this second polariser is used to rotate the polarisation such that the light entering the spectrometer always has the same polarisation, thus eliminating any effects from the spectrometer. With this set-up the polarisation purity, measured by the ratio of the desired polarization component to the undesired component, was 3000:1. Exciting with, or measuring, circular polarisation was achieved by inserting a superachromatic quarter wave plate (Thorlabs SAQWP05M-700) with its fast axis at 45 ° in between the polariser and cube beamsplitter for the laser, or spectrometer, side of the cube beamsplitter respectively. When exciting with *and* measuring circular polarisation the quarter wave plate is placed in between the microscope objective and cube beamsplitter. The sense of circular polarisation is controlled by the direction of the linear polarisers. The polarisation purity for the circular case was measured at 90%

3.2.3 Sample Positioning and Temperature Control

The sample was attached by silver conductive paint to the copper cold finger of a (Oxford Instruments MicrostatHires) liquid helium flow cryostat and kept under high vacuum (10^{-7} mbar) by a turbomolecular pump (Pffeifer HiCube). During the measurements the sample was held at 4K and the temperature was monitored via a RhFe sensor in the cold finger. The temperature varied by no more than 0.4 K during an experimental run after the cryostat reached equilibrium. The laser was focussed on the sample by a long working distance (Olympus LMPLFLN50X) 50x 0.5 NA microscope objective placed outside the cryostat's sapphire window. When the flipper mirror is in place as shown in Figure 3.4 it directs light from the tungsten halogen lamp (Thorlabs SLS301) to illuminate the sample. This produces an image the of the sample and the laser spot

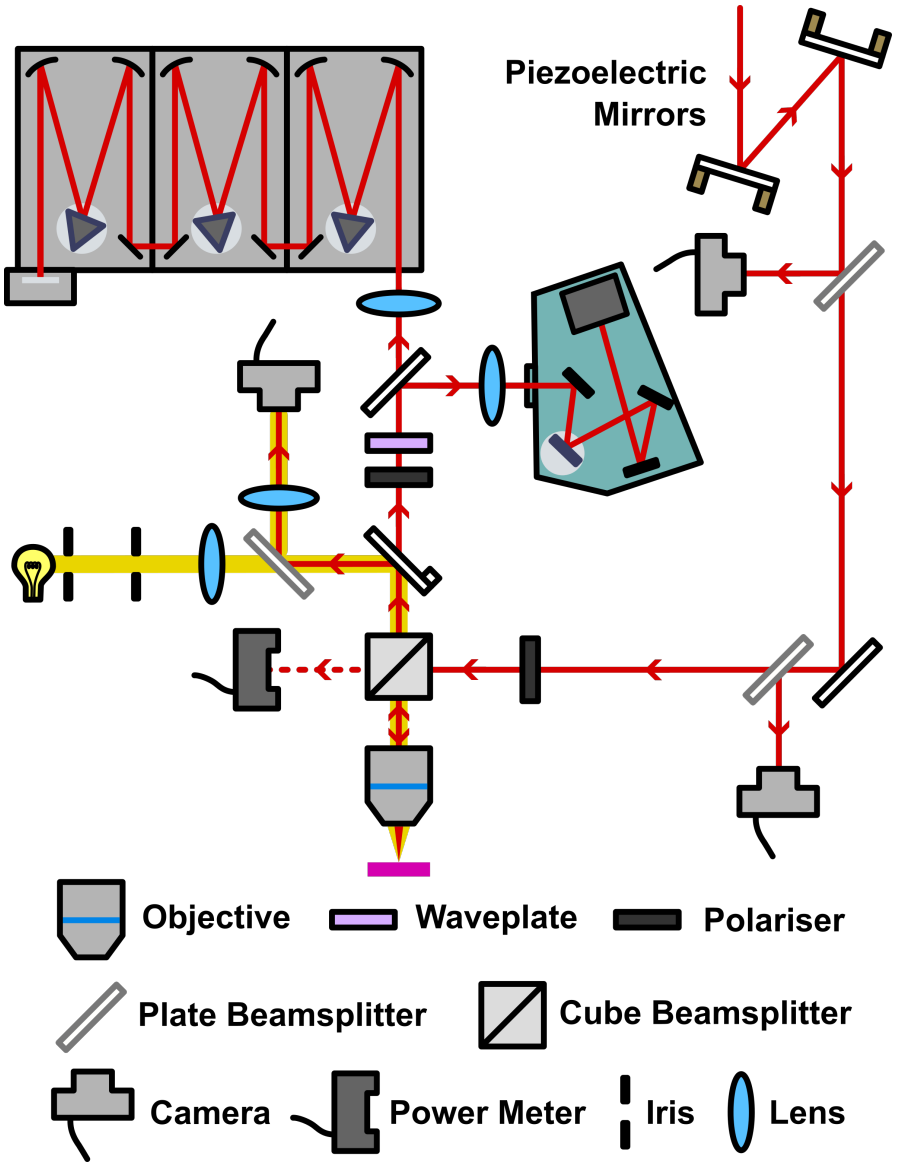

FIGURE 3.4: An illustration of the spectroscopy setup used to take the resonance Raman, PL and reflectivity spectra as well as image the sample.

on the final camera via a tube lens. The cryostat is mounted on translation stages which provide motion in X, Y and Z, aided by motorised linear actuators (Newport LTA-HL). This allows positioning of the laser spot on the sample with a precision of 0.2 µm.

3.2.4 Acquiring Spectra

The Raman spectra were taken with a liquid nitrogen cooled CCD (Roper Scientific PyLoN LN/400 BR) and a triple spectrometer system (TriVista 555) as illustrated in Figure 3.4. Light from the sample is coupled into the entrance slit of the spectrometer by a lens. The first two stages were operating in subtractive mode, where they act as a highly selective tunable bandpass filter. The first stage disperses the incident light

onto the wide slit at the entrance of the second stage. This slit acts as a bandpass filter, passing only the desired spectral window. The second stage, using and identical 900 l/mm grating to the first, recombines the dispersed light onto the narrow slit at the entrance to the third stage, which rejects any stray scattered light. The final stage then disperses the light onto the CCD to produce the spectrum. This configuration allowed for Raman spectra to be taken to within 15 cm^{-1} of the laser energy. The final stage uses a 1500 l/mm grating for wavelengths longer than 700 nm (<1.77 eV) and 1800 l/mm otherwise. For PL spectra, the same setup was used, with multiple spectra taken and stitched together to cover the desired energy range. Reflectivity spectra were taken using an alternate spectrometer (Princeton Instruments FERGIE) shown in teal in Figure 3.4, with the flipper mirror in place. This spectrometer covers 460 - 800 nm (1.55 - 2.71 eV) without the need for stitching.

3.2.5 Spot Size Measurements

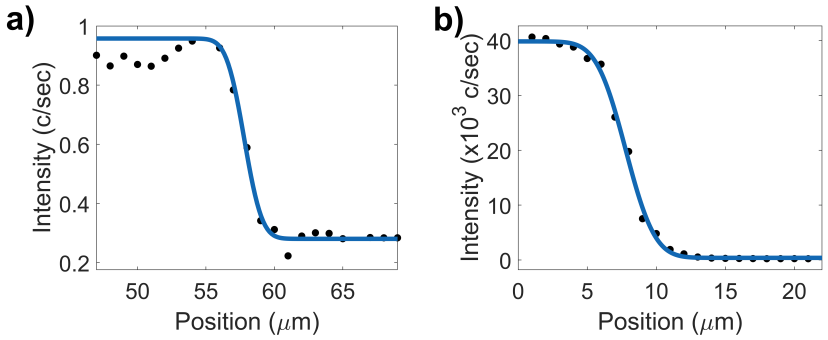

FIGURE 3.5: Spot size was determined from knife-edge intensity profiles for a) single wavelength and b) broadband illumination of the sample. The fitted Gaussian step functions are shown in blue.

The spatial resolution of the system is ultimately limited by the size of the laser spot on the sample. It was characterised independently for excitation by a single wavelength, as used in Raman and PL measurements, and by the broadband spectrum as used for reflectivity. For the former case, the intensity of the 520 cm^{-1} Si Raman peak was measured at a series of positions as the beam was translated off of the sharp cleaved edge of a Si chip, moving normal to the edge. A laser wavelength of 702 nm (1.766 eV) was used. For the broadband spectrum provided by the Fianium, the mean intensity of the reflected spectrum was taken while translating off the edge of a Si chip in the same way. For both cases, the intensity profile was fitted to a Gaussian step function, as shown in Figure 3.5. This function corresponds to the integral of the intensity distribution of a single mode Gaussian beam with intensity I given by:

$$I(r) = I_0 \exp\left(\frac{-2r^2}{{r_0}^2}\right) \tag{3.1}$$

to find the beam radius r_0. This gave beam widths ($2r_0$) of 2.0 ± 0.2 µm and 3.3 ± 0.2 µm for single wavelength and broadband illumination respectively.

3.3 Data Analysis and Fitting

This section details all of the processing of resonance Raman, PL and reflectivity spectra. For the Raman case, this includes the corrections applied to the spectra for uncertainties in Raman shift, removal of unwanted background signals and conversion of the spectra to absolute Raman scattering probability. The procedure for fitting the spectra and extracting intensity profiles of the Raman peaks as a function of excitation energy is then presented. Finally, the methods used for fitting these resonance profiles to extract the energies, widths and scattering rates of the excitonic states of interest is discussed, along with the simpler PL and reflectivity cases.

3.3.1 Resonance Raman

The following sections describe, in the order in which they are applied, all of the methods and corrections used to avoid the pitfalls of unwanted background signal in the Raman spectra as well as uncertainties in spectrometer throughput and calibration.

3.3.1.1 Background Subtraction

Due to the low-strength nature of Raman scattering, especially when off-resonance, a significant exposure time is required to achieve a good signal to noise ratio. The exposure time used for each Raman spectra was typically between one and five minutes. During the exposure, cosmic rays can strike the CCD and create additional peaks in the spectrum. These peaks are sharp, in most cases being a single pixel wide which is narrower than the diffraction limited resolution of the spectrometer. These are manually identified by both their width and by observing that they are not present in both spectra when comparing Raman spectra taken with the same or similar laser energies. Any pixels found to be associated with cosmic rays were excluded from the spectra.

In addition to cosmic rays, unwanted signal was present from photoluminescence from the sample as well as stray light from the lab can appear in the spectra. This was mitigated by always taking pairs of alternately polarised Raman spectra. The sample was illuminated with light polarised horizontally (H), i.e. with the electric field parallel to the plane of the optical bench. Two spectra were taken, one with the spectrometer measuring the scattered light with H polarisation and the other with vertical (V) polarisation (with the electric field normal to the optical bench). This produced a crossed polarised spectrum (HV) and a parallel polarised spectrum (HH), equivalent to $z(xy)\bar{z}$

and $z(xx)\bar{z}$ respectively in Porto's notation. The two orthogonal principal polarisation directions to excite an exciton in the TMD samples are right and left circular. These are notably associated with the K and K' valleys in the Brillouin zone due to inversion symmetry breaking in monolayers [9, 10, 28, 146]. The incoming linearly polarised photons are equivalent to a coherent superposition of right and left handed circular polarisations which then excite an equal amount of states in the K and K' valleys. The emission of a Raman scattered photon occurs before these states have time to decohere, so the resultant Raman scattered light has the same polarisation as the incoming beam. Photoluminescence emission occurs after the the coherence has been lost, so for this case of linear excitation the emission is unpolarised. Thus, the HH and HV spectra should contain equal photoluminescence background and only the HH spectra should contain Raman scattering.

This was found to be true as expected [163–165] the majority of the time, with some exceptions. For Raman scattering, some peaks were observed in the both the HH and HV spectra. A $MoSe_2$ peak at 584 cm^{-1} was found to have the greatest depolarisation ratio, defined as the intensity in the HV spectrum over that in the the HH spectrum [164, 166]. This was measured at 0.22 at 1.93 eV, which is at the B1s outgoing resonance in monolayer $MoSe_2$. It is likely that this is a result of scattering between valleys changing the phase difference between the emitted left and right circular polarisations. Only multi-phonon processes allow enough momentum for intervalley scattering and a peak at 584 cm^{-1} must be multi-phonon as phonon dispersion calculations show that single phonons in $MoSe_2$ can only have shift up to 350 cm^{-1} [110].

To extract only the Raman signal, the HV were subtracted from the HH spectra as shown in Figure 3.6. In cases where the signal from the photoluminescence was multiple orders

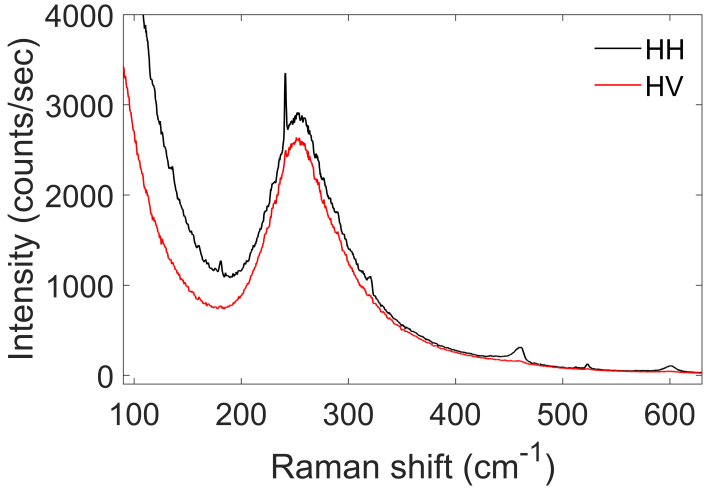

FIGURE 3.6: Raman spectra of $MoSe_2$ at 1.652 eV taken with parallel (HH) and perpendicular (HV) illumination and measurement polarisation. A strong photoluminescence background makes the Raman peaks difficult to resolve.

of magnitude greater than the Raman signal, such as those when exciting just above the A1s exciton, residual PL signal remained at the 8% level. A significant amount of this was likely from the fluctuations in laser power between taking the HH and HV spectra, however there was a tendency for the PL to be slightly co-linear, more so nearer the laser energy. In addition, some signal from Rayleigh scattered laser light was also present at Raman shifts below 30 cm^{-1}. This was present even when exciting away from the exciton energies, where minimal PL is expected. These broad undesired signals were removed by fitting the spectra to a series of Gaussian peaks taking the form in Figure 3.7, with the spectral data containing Raman peaks was excluded from the fitting. Any Raman peaks appear on top of this background and therefore the Gaussians were subtracted to leave the Raman peaks with minimal undesired background as shown in Figure 3.7.

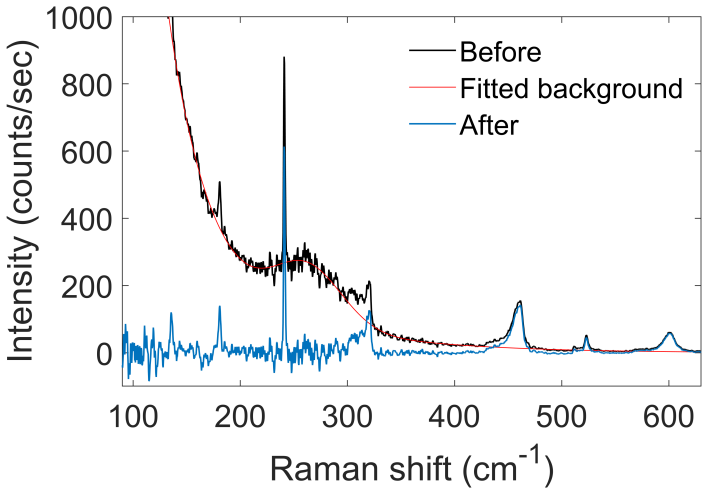

FIGURE 3.7: Raman spectra of $MoSe_2$ at 1.652 eV before and after background subtraction shown in black and blue. The fitted background composed of Gaussian peaks is shown in red. The remaining photoluminescence background is eliminated with this subtraction.

3.3.1.2 Calibration of Raman Shift

The Raman spectrometer is not perfectly calibrated for all wavelengths and the laser energy is not precisely fitted while taking the spectra. This leads to uncertainties in the measured Raman shift of the peaks in the spectra. As the samples are all on Si substrates, the 520 cm^{-1} Si LO phonon Raman peak is present in the spectra and was used as an internal reference to calibrate the shift of the Raman spectra. The use of this peak as a standard reference in studies of TMDs is widespread [133, 134, 138, 167, 168]. Before correcting for the shift of the Si peak, the spectra were offset by an average value of 2.2 cm^{-1} with a repeatability of 0.64 cm^{-1}. After calibrating to the Si peak shift, the offset was eliminated and the repeatability of the measured Raman shift was reduced

to 0.13 cm^{-1}. These values were determined from fitting the same Raman peak in five repeat spectra taken at points throughout an experimental run.

3.3.1.3 Absolute Scattering Cross Section

In addition to giving a standard reference for Raman shift, the 520 cm^{-1} Si peak also allows determination of the absolute Raman scattering rate, using resonance Raman data of Si from Aggarwal et al. [169]. However, this correction is more complex than the previous section as the layered structure of the sample forms a Fabry-Perot cavity, enhancing or diminishing the electric field differently across each layer. Fortunately, the enhancement of the electric field can be determined from the reflectivity spectra, following the methodology of Yoon et al. [170]. The transfer matrix code used for fitting the reflectivity spectra in subsection 3.3.3 provides an electric field strength at any depth z in the layer stack. For the SiO_2 layer and the TMD layer, this is integrated over the layer thickness d:

$$R_{layer} = \int_0^d |E_{laser}(z) E_{scattered}(z)|^2 dz \tag{3.2}$$

This gives a Raman enhancement factor R_{layer} for scattering with an electric field strength of $E_{laser}(z)$ at the laser energy and an electric field strength of $E_{scattered}(z)$ at the scattered photon energy. The final scaling factor is therefore the ratio of the Raman enhancement factors for the Si and TMD layers R_{TMD}/R_{Si}.

To summarise the correction to absolute scattering cross section, the spectra were first divided by the fitted intensity of the 520 cm^{-1} Si peak. They were then multiplied by the absolute scattering cross section of the Si Raman peak [169] and finally by the ratio of the Raman enhancement factors R_{TMD}/R_{Si}.

3.3.1.4 Fitting Raman Spectra

In order to extract the Raman shift c_i, width b_i and amplitude a_i of the peaks in each of the Raman spectra, the corrected and background-subtracted spectra were fitted to a sum of n Lorentzian lineshapes of the form:

$$I(x) = \sum_{i=1}^{n} \frac{a_i \, {b_i}^2}{(x - c_i)^2 + {b_i}^2} \tag{3.3}$$

Where $I(x)$ is the intensity of the Raman spectrum at a shift of x cm^{-1}. MATLAB's non-linear least squares fitting was used to fit the spectra with the start points for the coefficients in the fit and the number of peaks used determined by inspection of the spectra.

3.3.1.5 Fitting Resonance Profiles

As discussed in subsection 2.4.1, for first order Raman scattering it is possible to use the Fermi golden rule to define a standard time-dependent third-order perturbation expansion prediction for the dependence of the Raman scattering on the resonance energies of the available electronic states. This class of model is used by many people, including DelCorro et al. [140] who applied it to unencapsulated monolayer WSe_2. The most general case allows scattering with N states and it takes the form:

$$A_{Raman}(E) \propto \left| \sum_{p=1,\,q=1}^{N} \frac{\boldsymbol{\sigma}_{sc} \cdot \langle 1|\hat{H}_d|q\rangle\langle q|\hat{H}_{ex-ph}|p\rangle\langle p|\hat{H}_d|0\rangle \cdot \boldsymbol{\sigma}_{in}}{(E - E_p - i\Gamma_p)(E - E_q - E_{ph} - i\Gamma_q)} \right|^2 \tag{3.4}$$

Here $|0\rangle$, $|1\rangle$, $|p\rangle$ and $|q\rangle$ are the initial, final and intermediate excitonic states respectively, with $\hat{H}_d$ being the electric dipole Hamiltonian and $\hat{H}_{ex-ph}$ the exciton-phonon interaction Hamiltonian. $\boldsymbol{\sigma}_{in}$ and $\boldsymbol{\sigma}_{out}$ are the unit polarisation vectors of the incoming and outgoing photons in the scattering process. The energies of the pth and qth intermediate states are E_p and E_q with broadening factors Γ_p and Γ_q defined as $\Gamma_p = \hbar/\tau_p$ where τ_p is the lifetime of the state. E_{ph} is the phonon energy and i is the imaginary unit.

The resonance profiles extracted in the previous section, give absolute Raman scattering probability $A_{Raman}(E)$ as a function of laser energy E, for each of the Raman peaks of interest. For the simplest case when only a single state is involved, the fitting function used is:

$$A_{Raman}(E) = \left| \frac{A_1}{(E - E_1 - i\Gamma_1)(E - E_1 - E_{ph} - i\Gamma_1)} \right|^2 \tag{3.5}$$

As was also used by Carvalho et al. and Du et al. [136, 171]. Here, the numerator of the fraction in the sum of Equation 3.4 becomes the fitted constant A_1, representing the amplitude of the scattering with the excitonic state. This simplest case produces a symmetric profile with two peaks of equal height and width separated by the phonon energy, corresponding to the incoming and outgoing resonances as discussed in 2.4.1. For the cases where multiple excitonic states overlapped, which was not uncommon in the data, a different fitting function was needed. For two excitonic states, the following form was used:

$$\begin{aligned} A_{Raman}(E) = \Bigg| & \frac{A_1}{(E - E_1 - i\Gamma_1)(E - E_1 - E_{ph} - i\Gamma_1)} + \frac{A_{12}\, e^{i\pi\phi_{12}}}{(E - E_1 - i\Gamma_1)(E - E_2 - E_{ph} - i\Gamma_2)} \\ & + \frac{A_{12}\, e^{-i\pi\phi_{12}}}{(E - E_2 - i\Gamma_2)(E - E_1 - E_{ph} - i\Gamma_1)} + \frac{A_2\, e^{i\pi\phi_2}}{(E - E_2 - i\Gamma_2)(E - E_2 - E_{ph} - i\Gamma_2)} \Bigg|^2 \end{aligned} \tag{3.6}$$

Here the first of the four terms, with amplitude A_1, represents scattering involving only with the first excitonic state. The second term corresponds to the process where the incoming photon scatters with the first excitonic state and the outgoing photon scatters

with the second excitonic state. The third term has the incoming photon scatter with the second and the outgoing with the first excitonic state. The last term is from scattering via only the second excitonic state. A phase difference $e^{i\pi\phi}$ between the scattering channels was taken out of the amplitude terms to keep them real valued, with the phase of A_1 set to zero as in the single state case. The inter-state scattering terms share the same amplitude A_{12} but have conjugate phase. For any fits with multiple excitonic states, the state with amplitude A_1 defined zero phase. As such, the order of the states was always chosen to avoid the case where the first state had very low scattering amplitude as that would create a large uncertainty in phases and hinder the fitting process.

In the few cases where only the incoming or outgoing resonance of the Raman peak of interest was visible and the full profile could not be fitted with the above model, a Lorentzian peak was used to fit the profile with the form:

$$A_{Raman}(E) = \left| \frac{A_1}{(E - E_1 - i\Gamma_1)} \right|^2 \tag{3.7}$$

This enabled extraction of the amplitude, width and energy of the excitonic state involved in the scattering process.

3.3.2 Photoluminescence

There are multiple potential lineshapes that could be used to fit the photoluminescence, such as Gaussian or Lorentzian, as well as the more complex Voigt and the asymmetric Breit-Wigner Fano. For the photoluminescence spectra, as well as for the subtraction of any unwanted PL background in subsubsection 3.3.1.1, a summation of Gaussian peaks was used. Gaussians were chosen as, in addition to producing fits of quality on par with that of Lorentzians, MATLAB has a built in 'Gaussians' fitting model which converges to a good fit much more quickly than using custom fitting functions. This was especially beneficial for the background subtraction of the large number of spectra in a resonance Raman run. The summation of Gaussians has the form:

$$I_{PL}(E) = \sum_{i=1}^{n} a_i \, exp\left(-\left(\frac{(E - c_i)}{b_i} \right)^2 \right) \tag{3.8}$$

For the PL spectra, the fitted amplitude A_i is in counts per second so it cannot be directly compared with other work, but the energy c_i and width b_i of the states provided by the fit are more useful.

3.3.3 Reflectivity

When taking reflectivity spectra of the sample, one spectrum was taken on the sample area of interest and a second was taken in quick succession on an adjacent area of bare SiO_2. The SiO_2 spectrum provides a constant reference which takes into account all other components in the optical system. The sample spectrum is divided by the Si spectrum to give the fractional reflectivity which was used in the fitting. In order to fit the reflectivity spectra, the permittivity of the TMD layer $\varepsilon(E)$, at energy E, was modelled as a sum of n Lorentz oscillators:

$$\varepsilon(E) = 1 + \sum_{k=1}^{n} \frac{a_k}{{E_k}^2 - E^2 - 2iE\Gamma_k} \tag{3.9}$$

Each excitonic state contributes one oscillator; with a_k, E_k and Γ_k corresponding to the amplitude, energy and width of the kth Lorentz oscillator. This permittivity is then used with standard permittivity data from literature for the Si [172], SiO_2 [173], hBN [174] and graphite [175] layers. The sample was modelled as a stack of infinitely wide and smooth layers in a transfer matrix approach described in [105]. Before fitting the spectrum of the whole sample stack, the thicknesses of the graphite and hBN layers were determined. This was achieved by fitting reflectivity spectra taken of different areas of the sample where the individual layers could be accessed separately. For this fitting, start points for the thickness of the layers was determined from AFM values and the SiO_2 thickness was allowed to vary with a start point of 300 nm. Between these measurements, the SiO_2 thickness was found to be 286 ± 0.8 nm and 288 ± 0.4 nm for the samples containing HS57 and HS20 respectively. The underlying Si was treated as having infinite thickness. When fitting the full sample stack spectrum, the graphite and hBN thicknesses were fixed at the previously found values and the TMD layer thickness was fixed at 0.67 nm which is the expected interlayer distance for bilayer $MoSe_2$ and WSe_2. Once the fit had converged, the modelled permittivity and layer thicknesses could be used for the correction to absolute scattering probability described in subsubsection 3.3.1.3.

Chapter 4

Resonance Raman Spectroscopy of Exciton Rydberg States in WSe_2 / $MoSe_2$ Heterostructures

This chapter presents the results of resonance Raman spectroscopy measurements on two different hBN encapsulated WSe_2 / $MoSe_2$ vdW heterostructures with twist angles of 20 °and 57 °between the two constituent monolayers. These are referred to as HS20 and HS57 respectively. In addition to the heterostructures, the same measurements were performed on hBN encapsulated WSe_2 and $MoSe_2$ monolayers, allowing for comparison. Laser energies from 1.59 to 2.26 eV were used, which allowed observation of the WSe_2 A1s, A2s & B1s and the $MoSe_2$ A1s, A2s, B1s & B2s intralayer excitons. This constitutes the first observation of the 2s excitonic states in hetero-bilayers, allowing measurement of their energies and linewidths. In addition, this chapter covers the characterisation of the monolayer and heterostructure samples with PL and reflectivity.

4.1 Literature Review

2014 saw the first report of excited Rydberg states in TMDs [56], after predictions in 2013 [176] and since then many reports of these states have been made for several TMD monolayers [51, 56, 57, 177–179]. Zeeman splitting of these states has been measured via magneto-absorption and magneto-photoluminescence in monolayers, allowing the unambiguous identification of the Rydberg states up to the A4s in WSe_2 and $MoSe_2$ [60, 61, 180]. Despite this, measurements of the 2s or higher states have not been reported in van der Waals TMD heterostructures.

Raman spectroscopy has been widely used on TMD monolayers, with many single phonon and multi-phonon peaks observed [113, 130, 134, 156, 181]. Under most conditions, the most intense of these peaks are the zone centre $A_1'(\Gamma)$ and $E'(\Gamma)$ modes. These are also notable because they, or their multilayer equivalents (A_{1g}, E_{1g}), shift in frequency with the number of TMD layers [132–134, 182, 183]. Davydov splitting of these peaks, as well as low frequency acoustic phonons, is also observed with layer number [181, 184].

The more comples resonance Raman spectroscopy is a less common technique, but resonances with the A, B and C excitons in TMD monolayers have been reported [136–138, 185]. Resonance Raman measurements also have probed trions [186] and revealed dark excitonic states [71]. Raman peaks that change frequency with excitation energy have been observed [139], resulting from large wavevector phonons scattering between valleys. Most resonance Raman studies are limited by the number or range of exciting photon energies, where too few Raman spectra result in under-sampled resonance profiles, such that extracting precise information on the excitonic states involved, like their widths, in the resonances is not possible [187].

4.2 Results

4.2.1 Sample Characterisation

In addition to the main resonance Raman measurements discussed in this chapter, photoluminescence and reflectivity spectra were taken of the sample areas of interest. These techniques are used much more commonly in the study of TMD samples in literature than resonance Raman measurements as they give the energies of the excitonic states in a single spectrum. Before getting into the identification of the 2s states in the heterostructures, this section first compares features observed in the reflectivity, PL and resonance Raman for all of the sample areas. This provides a concrete identification of the main excitonic states in these samples which are essential to understand before probing further.

4.2.1.1 Monolayer WSe_2 Photoluminescence and Reflectivity

To characterise the monolayer WSe_2 sample area, a reflectivity spectrum was taken as described in subsection 3.2.4. Figure 4.1 shows a plot of the differential reflectivity spectrum, given by:

$$R(E) = \frac{dI}{dn_{px}} \frac{dn_{px}}{dE} = \frac{dI}{dE} \tag{4.1}$$

Where I is intensity at a pixel in the spectrum, n_{px} is pixel number and E is the energy associated with that pixel. Four absorption features are observed, with the lowest energy

and most intense around 1.74 eV. The spectrum was fitted using the thin film transfer matrix model as described in subsection 3.3.3, with the fitted curve shown on the figure in red. Four states were used in the fit, giving fitted energies of 1.737 ± 0.001, 1.867 ± 0.001, 1.887 ± 0.002 and 2.171 ± 0.003 eV. The corresponding widths were 6.5 ± 0.1, 8 ± 2, 4 ± 2 and 100 ± 10 meV. The errors given are the standard deviation determined from the fitting process. The energies of the states observed by resonance Raman scattering, as described later in subsection 4.2.2, are also shown on the same figure for comparison. These fall at energies of 1.740 ± 0.001, 1.871 ± 0.001, 1.891 ± 0.002 and 2.166 ± 0.001 eV, with respective widths of 5.6 ± 0.3, 3.5 ± 0.2, 10.5 ± 2.2 and 32.6 ± 2.2 meV. The highest energy of these features appears in the reflectivity above the resonance Raman energy and with a significantly greater width. In this area of the spectrum, the reflectivity fit does not properly capture the data. This is likely due a broad higher lying state such as the C exciton which was not included in the fitting function. The two other states appear lower in energy than their resonance Raman counterparts at the few meV level, which is comparable to their linewidth. The reason for this small down-shift in energy in this spectrum compared to the resonance Raman data is not known. However, the fact that this shift is 3-4 meV for all of the excitonic states suggests an error in wavelength calibration of this spectrum rather than a change in exciton energies.

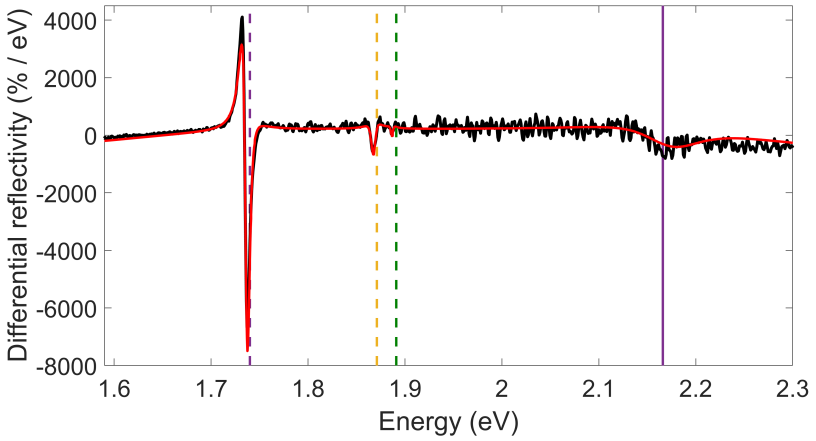

FIGURE 4.1: A differential reflectivity spectrum of the hBN encapsulated monolayer WSe_2 sample area (black) at 4 K. The fitted transfer matrix model is shown in red. The energies of the WSe_2 A1s and A2s exciton energies are indicated with purple and yellow dashed vertical lines, with the B1s energy shown with a purple solid line.

A PL spectrum of the hBN encapsulated WSe_2 monolayer sample area was acquired with an incident power of 100 µW and a laser energy of 2.33 eV. The spectrum is presented in Figure 4.2 in black. As with the reflectivity spectrum, the energies from the resonance Raman data are shown on the plots with vertical dashed lines. In Figure 4.2a) a strong peak in the photoluminescence around 1.74 eV is observed, with a series of peaks of similar intensity and width at lower energies. A zoomed-in subsection of the PL spectrum

in a) is shown in Figure 4.2b), where a peak around 1.87 eV is visible with a broader higher energy shoulder. The spectrum was fitted to a summation of 17 Gaussian peaks, shown in red, with the coefficients of the fit given in Table 4.1

For the first of the 3 states observed in both the reflectivity (1.7351 eV) and resonance Raman (1.740 eV), a strong feature was also observed in the PL and fitted to a group of 3 peaks with the biggest contribution being at 1.7344 eV. This is assigned to the A1s exciton and falls within the range of 1.723 - 1.747 eV from measurements of similar samples in literature [80, 188–190]. The second of the 3 features at 1.871 eV (Raman), 1.8665 eV (reflectivity) and 1.869 eV (PL) is assigned to the A2s exciton. This gives an A1s-A2s exciton energy difference which falls within the range of 130 - 133 meV in literature [60, 61, 189, 191]. This peak appears in the PL with broad underlying feature centred at 1.879 eV, which has also been reported in literature but not identified [189, 191]. The final broader feature in the reflectivity spectrum at 2.171 eV and 2.166 eV in Raman is assigned to the B1s exciton. This falls in line with the expected A1s-B1s separation of 430 meV from literature [189]. All of the features in the PL spectrum that are not observed in the resonance Raman and Reflectivity measurements must have weak oscillator strength [61, 177, 189] and there are many possible assignments, including defect induced bound excitonic states [142]. This is the case for the numerous strong peaks in the PL observed below 1.72 eV. The peaks at 1.6983 and 1.7061 eV can be assigned to the inter- and intra- valley negative trions respectively, where the sample is too negatively doped for the positive trion to be visible, which is expected at just over 21 meV below the neutral exciton peak [78, 80, 190]. In addition, gated PL measurements have reported a negatively charged biexciton 14 meV below the inter-valley negative trion [78, 79] which can explain the peak observed at 1.6841 eV. None of the peaks in Table 4.1 at energies below this were assigned.

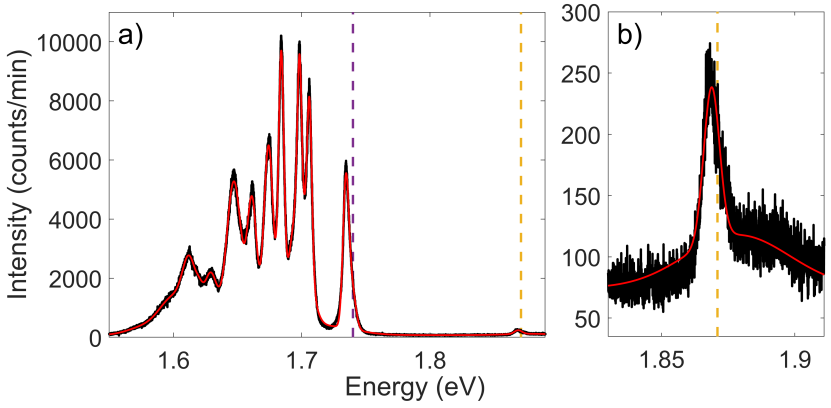

FIGURE 4.2: a) A PL spectrum of the hBN encapsulated monolayer WSe_2 sample area at 4 K. The spectrum is fitted to a summation of Gaussian peaks. Energies of the A1s and A2s excitonic states determined from fitting the resonance Raman data are marked with purple and yellow lines respectively. b) A subsection of a) showing the lineshape of the A2s PL peaks.

Energy (eV)	Width (meV)	Amplitude (c/min)
1.576 ± 0.006	18 ± 3	250 ± 90
1.601 ± 0.001	16 ± 3	1300 ± 100
1.6128 ± 0.0002	7.5 ± 0.4	1900 ± 200
1.6203 ± 0.0002	3.9 ± 0.4	480 ± 80
1.6292 ± 0.0001	7.4 ± 0.2	2000 ± 70
1.6472 ± 0.0001	8.20 ± 0.04	5196 ± 8
1.6614 ± 0.0001	5.26 ± 0.03	4410 ± 10
1.6742 ± 0.0001	5.26 ± 0.02	6360 ± 10
1.6841 ± 0.0001	2.893 ± 0.009	8550 ± 30
1.6980 ± 0.0009	11.1 ± 0.5	4400 ± 600
1.6983 ± 0.0001	2.34 ± 0.02	5070 ± 40
1.7061 ± 0.0001	2.60 ± 0.02	5390 ± 40
1.71 ± 0.04	10 ± 20	100 ± 600
1.7344 ± 0.0001	2.63 ± 0.04	4100 ± 200
1.735 ± 0.005	9.5 ± 0.2	1080 ± 40
1.7380 ± 0.0003	3.4 ± 0.2	1300 ± 100
1.8690 ± 0.0003	4.6 ± 0.5	130 ± 10
1.879 ± 0.005	53 ± 8	33 ± 4

TABLE 4.1: Coefficients for fitting the monolayer WSe_2 PL spectrum presented in Figure 4.2. Errors given are the standard deviations from the fitting process.

4.2.1.2 Monolayer $MoSe_2$ Photoluminescence and Reflectivity

The differential reflectivity spectrum of the $MoSe_2$ monolayer area is shown in Figure 4.3, with a fitted transfer matrix model curve plotted in red. Three fitted features are observed in the spectrum, with energies of 1.647 ± 0.001 eV, 1.803 ± 0.003 and 1.865 ± 0.003 eV. With widths of 7.1 ± 0.2, 30 ± 10 and 74 ± 9 meV respectively. The first of these features appears by far the largest, with a fitted amplitude of 1.22 ± 0.05 eV^2, followed by 0.3 ± 0.2 and 2.2 ± 0.5 eV^2 for the other two in ascending energy order. The energies of the states observed by resonance Raman scattering, as described later in subsection 4.2.3, are also shown on the same figure for comparison. The energy of the $MoSe_2$ A1s exciton determined from the Raman scattering is indicated on the spectrum with a blue dashed line and it falls in the middle of the most intense feature of the spectrum. The energy extracted from the Raman fitting is 1.648 ± 0.001 eV which is in close agreement the 1.647 eV from the reflectivity. The $MoSe_2$ A2s energy from the Raman is marked by the dashed orange at an energy of 1.803 ± 0.002 eV which also closely matches the reflectivity value of 1.803 ± 0.003 from the smallest fitted peak in the spectrum. Above the A2s exciton, the B1s is also visible in the reflectivity spectrum and yields a fitted energy of 1.865 ± 0.003 eV. The B2s energy (2.021 eV) is also marked

on the spectrum, with a solid orange line, but no feature near this energy is visible above the noise.

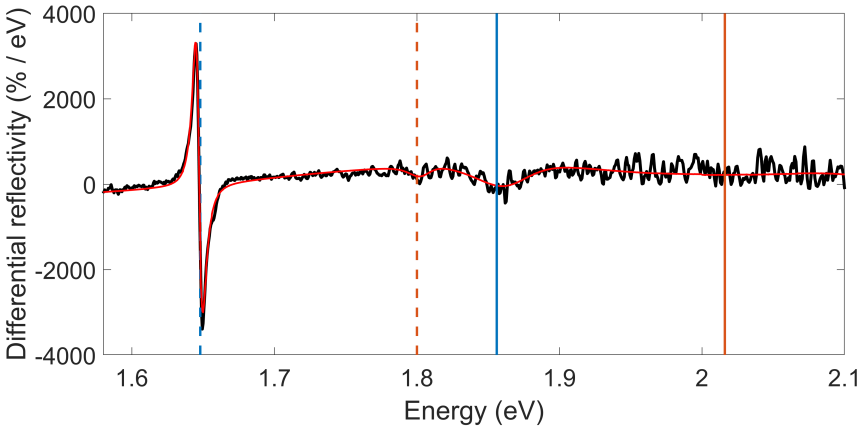

FIGURE 4.3: A differential reflectivity spectrum of the hBN encapsulated monolayer $MoSe_2$ sample area at 4 K. The fitted transfer matrix model is shown in red. Energies of the A1s and A2s excitonic states determined from fitting the resonance Raman data are marked with blue and orange dashed lines.

The PL spectrum of the $MoSe_2$ monolayer was taken with a laser energy of 1.968 eV an an excitation power incident on the sample of 100 µW. As with the WSe_2 case, strong photoluminescence signal was observed. The fitted spectrum is presented in Figure 4.4. No peaks are observed at the A2s exciton energy of 1.803 eV. A sum of four Gaussian peaks were used to fit the cluster of peaks visible around the A1s exciton, with their energies given in Table 4.2. The fitted peak in the PL spectrum with energy closest to the A1s exciton energy falls at 1.646 ± 0.002 eV, in line with the Raman and reflectivity values of 1.648 ± 0.001 and 1.647 ± 0.001 eV respectively. This peak appears as a shoulder on the low-energy side of the most intense peak at 1.6558 eV. The lowest energy peak at 1.6275 ± 0.0001 eV is then most likely a trion, 19 ± 2 meV below the exciton. This exciton-trion splitting is smaller than the typical range given in literature of 24 - 28 meV [82, 142, 192–194] below the exciton. The origin of the peaks above the A1s exciton energy is not clear. In addition to this $MoSe_2$ monolayer, PL and reflectivity measurements were performed on an additional hBN encapsulated monolayer. This sample also showed a single feature at the A1s in reflectivity as well as PL peaks above and below the A1s exciton energy determined from the reflectivity. In this case however, the PL overwhelmed the A1s Raman signal and so a resonance profile could not be measured therefore the main $MoSe_2$ monolayer sample was chosen over this additional one. Despite the presence of higher energy peaks in the PL, the excellent agreement between the reflectivity and resonance Raman values for the A1s energy for this sample, as well as the observation of similar higher energy PL peaks in another sample, mitigates any doubt about the assignment of the A1s energy.

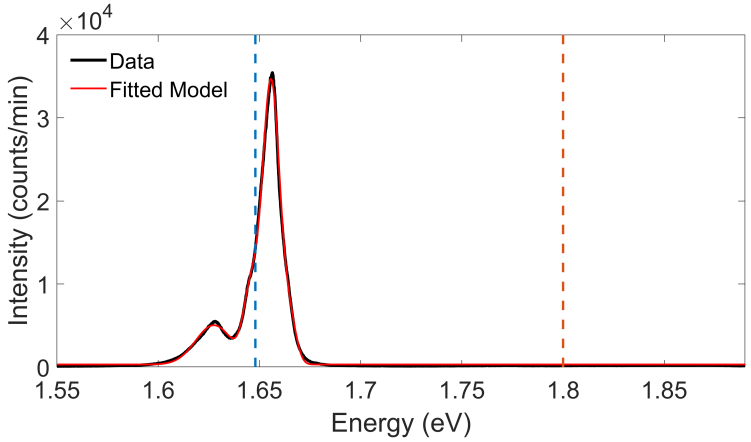

FIGURE 4.4: A PL spectrum of the hBN encapsulated monolayer $MoSe_2$ sample area at 4 K. The spectrum is fitted to a summation of Gaussian peaks. Energies of the A1s and A2s excitonic states determined from fitting the resonance Raman data are marked with blue and yellow dashed lines.

Energy (eV)	Width (meV)	Amplitude (c/min)
1.6275 ± 0.0001	12.7 ± 0.2	4730 ± 40
1.646 ± 0.002	5.01 ± 0.09	7800 ± 100
1.6558 ± 0.0001	6.24 ± 0.04	34160 ± 70
1.6654 ± 0.0002	4.5 ± 0.2	4300 ± 200

TABLE 4.2: Coefficients for fitting the monolayer $MoSe_2$ PL spectrum shown in Figure 4.4 to a summation of Gaussian peaks. Errors given are the standard deviations from the fitting process.

4.2.1.3 57° Twist Heterostructure Photoluminescence and Reflectivity

A reflectivity spectrum was taken of HS57 and the differential reflectivity shown in black in Figure 4.5 with the transfer matrix fitted curve shown in red. Three strong features appear in the spectrum below 1.9 eV. The most intense and lowest in energy was assigned to the $MoSe_2$ A1s exciton, with a fitted energy of 1.622 ± 0.001 eV. This energy falls very close to the 1.620 ± 0.001 eV resonance Raman value. The next peak in the spectrum is a more unusual case, with a fitted energy of 1.707 ± 0.001 eV. This falls 21 meV below the WSe_2 A1s exciton at 1.728 ± 0.001 eV, indicated with a purple dashed line, as determined from the resonance Raman measurements. The most likely assignment for this feature, which is also observed in the resonance Raman, is then a WSe_2 A1s positively charged trion. The strength of the WSe_2 trion can be explained if the sample is p-doped. By considering the band offsets as in Figure 2.4. The upper valence band in WSe_2 is higher in energy than for $MoSe_2$ so holes will flow into the WSe_2 layer, increasing the hole population and thus the probability of forming a positive trions. Further, the $MoSe_2$ conduction bands fall below (in energy) those of WSe_2. This means

electrons migrate to the $MoSe_2$ layer, which reduces the WSe_2 electron population and further increases the ratio of positive trions to neutral excitons for the WSe_2 case.

This means that no WSe_2 A1s exciton peak is observed in the reflectivity spectrum. There is also no feature in the reflectivity spectrum corresponding to the $MoSe_2$ A2s exciton, which is less surprising due to its low oscillator strength. The peak appearing third in energy, at 1.841 ± 0.001 eV is assigned to the $MoSe_2$ B1s exciton which was measured via resonance Raman at 1.839 ± 0.001 eV (not marked). No feature was observed in the reflectivity spectrum at the energy of the WSe_2 A2s exciton (1.857 ± 0.003 eV), marked with a yellow dashed line. As with the $MoSe_2$ A2s case, this is not unexpected due to the low oscillator strength. Additional, any WSe_2 A2s peak would be more difficult to observe as it is obscured by the $MoSe_2$ B1s exciton. At the highest energy end of the spectrum, two peaks are observed at 2.102 ± 0.001 and 2.168 ± 0.001 eV. These are assigned to hybridised states [16, 86, 97] originating from the WSe_2 B1s exciton and a bright interlayer exciton with an electron in the lower WSe_2 conduction band a hole in the upper $MoSe_2$ valence band, as discussed in our paper [98].

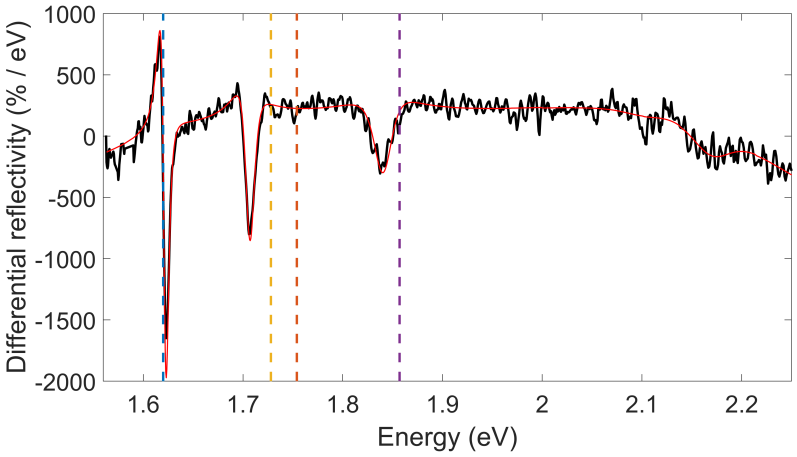

FIGURE 4.5: A differential reflectivity spectrum of the hBN encapsulated 57° twisted $WSe_2/MoSe_2$ heterostructure sample area at 4 K. The fitted transfer matrix model curve is shown in red. Energies of the A1s and A2s excitonic states associated with the WSe_2 layer determined from fitting the resonance Raman data are marked with blue and orange dashed lines. The $MoSe_2$ A1s and A2s exciton energies are marked with dashed lines in purple an yellow respectively.

Figure 4.6 shows a PL spectrum of HS57, the hBN encapsulated 57° twisted WSe_2 $MoSe_2$ heterostructure sample. The spectrum was taken with an incident power of 100 µW with an excitation energy of 2.33 eV. The spectrum was fitted to a summation of 10 Gaussian peaks, with the energies of these peaks given in Table 4.4. The $MoSe_2$ A1s exciton energy from resonance Raman measurements is indicated with a blue dashed vertical line at 1.620 ± 0.001. Whilst it is tempting to assign the PL peak at 1.6227 ± 0.0003 to this excitonic state, it is more likely to be one of the significant number of defect states associated with the WSe_2 layer. The other peaks with energies between 1.598

and 1.662 eV were also assigned to WSe_2 defect states. The peak in the PL spectrum with a fitted energy of 1.7285 ± 0.0001 eV is assigned to the WSe_2 A1s exciton and its energy matches the 1.728 ± 0.002 eV from the resonance Raman, as marked on the PL spectrum with a purple dashed line. Below this peak in energy is a broad shoulder, which is most likely from a combination of WSe_2 trions. No peak in the PL is visible corresponding to the $MoSe_2$ B1s or WSe_2 A2s exciton energies, marked in orange and yellow respectively.

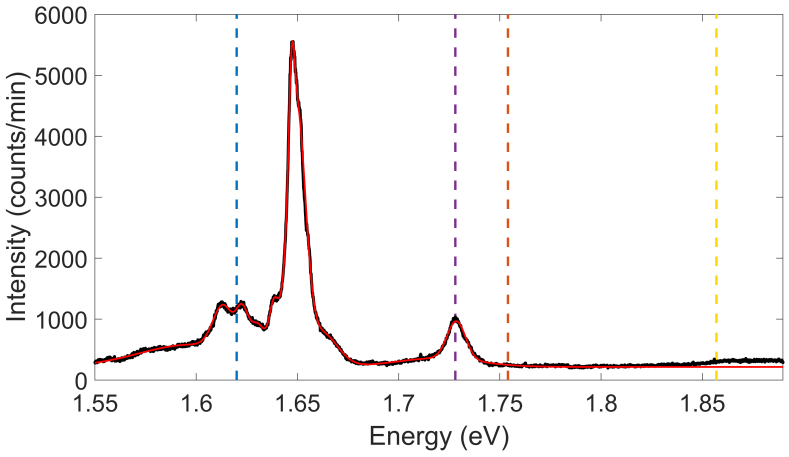

FIGURE 4.6: A PL spectrum of the hBN encapsulated 57° twisted $WSe_2/MoSe_2$ heterostructure sample area at 4 K. The spectrum is fitted to a summation of 10 Gaussian peaks, shown in red. The coefficients for the fit are given in Table 4.3 Energies of the A1s and A2s excitonic states associated with the WSe_2 layer determined from fitting the resonance Raman data are marked with purple and yellow lines. The $MoSe_2$ A1s and A2s exciton energies are similarly marked in blue and orange respectively.

Energy(eV)	Width (meV)	Intensity (c/min)
1.598 ± 0.001	37 ± 1	366 ± 6
1.6134 ± 0.0002	7.1 ± 0.3	710 ± 20
1.6227 ± 0.0003	4.1 ± 0.3	600 ± 90
1.6306 ± 0.0004	6 ± 1	530 ± 30
1.6385 ± 0.0001	3.3 ± 0.2	780 ± 50
1.6471 ± 0.0001	1.91 ± 0.03	1580 ± 30
1.6495 ± 0.0001	6.13 ± 0.04	4100 ± 30
1.6622 ± 0.0004	10.8 ± 0.4	530 ± 10
1.7193 ± 0.0007	29 ± 1	141 ± 6
1.7285 ± 0.0001	6.4 ± 0.1	622 ± 8

TABLE 4.3: Coefficients for fitting the PL spectrum of the 57° twisted WSe_2 $MoSe_2$ heterobilayer. Errors given are the standard deviations from the fitting process.

4.2.1.4 20° Twist Heterostructure Photoluminescence and Reflectivity

The reflectivity spectrum was measured of HS20 and the differential is shown in Figure 4.7. The spectrum was fitted with a transfer matrix approach to extract the amplitudes, energies and widths corresponding to 4 spectral features. The lowest energy of these is the $MoSe_2$ A1s exciton, which is observed at 1.628 ± 0.003 eV. This appears slightly below the energy for the same state as determined by the resonance Raman fitting, 1.633 ± 0.002 eV, which is marked on the spectrum with a blue dashed vertical line. The next peak in energy appears at 1.716 ± 0.001 eV, falling very close to the 1.718 ± 0.002 eV measured via resonance Raman for the WSe_2 A1s exciton. At 1.765 ± 0.002 eV, an orange dashed line indicates the energy of the $MoSe_2$ A2s exciton. No clear spectral feature is observed here, which is as expected due to the low oscillator strength of the 2s states. The same is also true of the WSe_2 A2s exciton at 1.835 ± 0.004 eV indicated in yellow, which additionally clashes with the $MoSe_2$ B1s excitonic state. This state is observed at 1.851 ± 0.001 eV in this reflectivity spectrum which is very close to the 1.849 ± 0.001 given by resonance Raman. Finally, the highest energy feature observed in the reflectivity spectrum is at 2.163 ± 0.001 eV is from the WSe_2 B1s exciton. This also closely matches the energy measured by resonance Raman of 2.164 ± 0.001 eV.

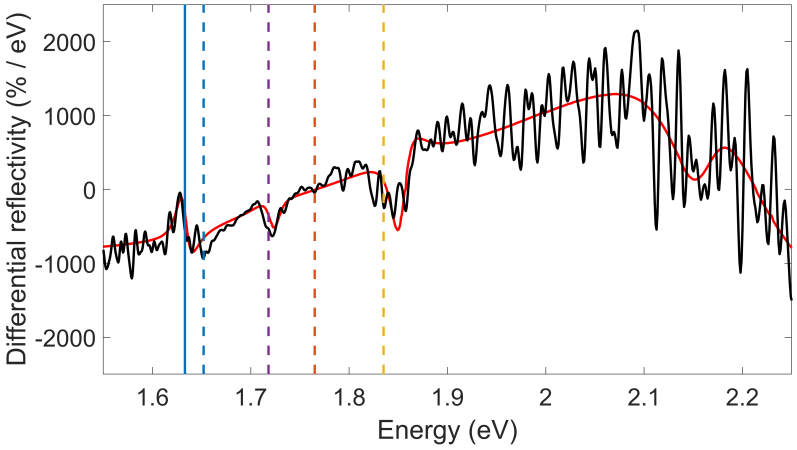

FIGURE 4.7: A differential reflectivity spectrum of the hBN encapsulated 20° twisted $WSe_2/MoSe_2$ heterostructure sample area at 4 K. The fitted transfer matrix model curve is shown in red, with the $MoSe_2$ A1s & B1s and the WSe_2 A1s & B1s features fitted. Energies of the A1s and unobserved A2s $MoSe_2$ excitonic states determined from fitting the resonance Raman data are marked with blue and orange dashed lines respectively. The resonance Raman determined WSe_2 A1s and A2s energies are also marked in purple and yellow respectively.

A PL spectrum of HS20 was taken with an excitation power of 100 µW with a laser energy of 1.968 eV. The spectrum was fitted to a summation of Gaussian peaks, shown in red in Figure 4.8, with the measured spectrum in black. The peak fitted at 1.617 ± 0.001 eV is tentatively assigned to the $MoSe_2$ A1s exciton as it appears just below the

energy determined by the resonance Raman of 1.623 ± 0.001 eV. The adjacent peaks below 1.7 eV are most likely from defect states associated with the WSe_2 A1s exciton. However, unlike the 57° heterostructure case, no PL peak is visible at the WSe_2 A1s exciton energy of 1.718 ± 0.002 eV. A peak is observed between where we would expect the WSe_2 A1s and $MoSe_2$ A2s excitons, at 1.7306 ± 0.0001 eV, but there is no clear state that it can be assigned to. Similarly to the HS57 case, the $MoSe_2$ and WSe_2 A2s energies, indicated with orange and yellow lines respectively, have no associated PL features. The peaks that appear around 1.85 eV are from Raman scattering via hBN hyperbolic phonon polariton modes as reported in literature for WSe_2 monolayers [171, 188, 195, 196] and discussed for both constituent monolayer cases in chapter 5 and our paper [197].

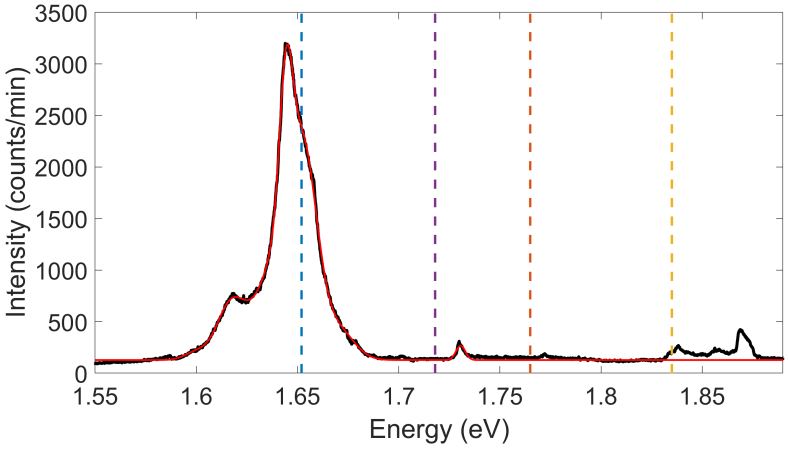

FIGURE 4.8: A PL spectrum of the hBN encapsulated 20° twisted $WSe_2/MoSe_2$ heterostructure sample area at 4 K. The spectrum is fitted to a summation of Gaussian peaks, shown in red. The coefficients for the fit are given in Table 4.4. Energies of the A1s and A2s excitonic states associated with the WSe_2 layer determined from fitting the resonance Raman data are marked with yellow and purple lines. The $MoSe_2$ A1s and A2s exciton energies are similarly marked in blue and orange respectively.

Energy (eV)	Width (meV)	Amplitude (c/min)
1.600 ± 0.001	8 ± 1	70 ± 10
1.617 ± 0.001	10 ± 1	540 ± 80
1.640 ± 0.006	13 ± 6	1000 ± 300
1.6443 ± 0.0001	4.5 ± 0.1	1370 ± 80
1.653 ± 0.001	9.8 ± 0.8	1800 ± 800
1.670 ± 0.001	11.2 ± 0.8	290 ± 20
1.7306 ± 0.0001	3.2 ± 0.2	140 ± 7

TABLE 4.4: Coefficients for fitting the 20° twisted heterostructure sample photoluminescence spectrum to a sum of Gaussian peaks. Errors given are the standard deviations from the fitting process.

4.2.2 Characterisation of Excited State Raman Peaks in Monolayer WSe_2

4.2.2.1 WSe_2 A1s

Raman spectra were taken, with the setup described in section 3.2, at 4 K of the monolayer WSe_2 area with an incident power of 100 µW. For the A1s exciton resonance, 31 spectra were taken with laser energies from 1.655 to 1.835 eV. A colour-map comprised of these spectra is shown in Figure 4.9. The strongest feature in the colour-map is the Raman peak that falls at 249.5 cm^{-1}. Incoming and outgoing resonances of this Raman peak are visible in the colour-map around 1.74 and 1.77 eV respectively. In addition to this strongest peak, a cluster of peaks is observed around 265 cm^{-1} which also show incoming and outgoing resonances. At 207 cm^{-1} a peak is visible that only shows strong resonance just above the incoming energy. In addition to this unusual resonance behaviour, this peak is observed to be dispersive, appearing at 206.3 cm^{-1} at 1.742 eV and shifting to 208.3 cm^{-1} at 1.776 eV where it is much less intense. The dispersive nature of this peak is not unprecedented, as there have been reports of dispersive peaks in $MoSe_2$ [110] and MoS_2 [138, 139]. The highest shift WSe_2 feature observed at this exciton energy is around 395 cm^{-1}. It was fitted to a peak at 399 cm^{-1} with a shoulder from another at 395 cm^{-1}. These peaks show a clear outgoing resonance but they are only visible for one Raman spectrum at the incoming resonance energy as they are not intense enough to the noise level from the strong A1s photoluminescence.

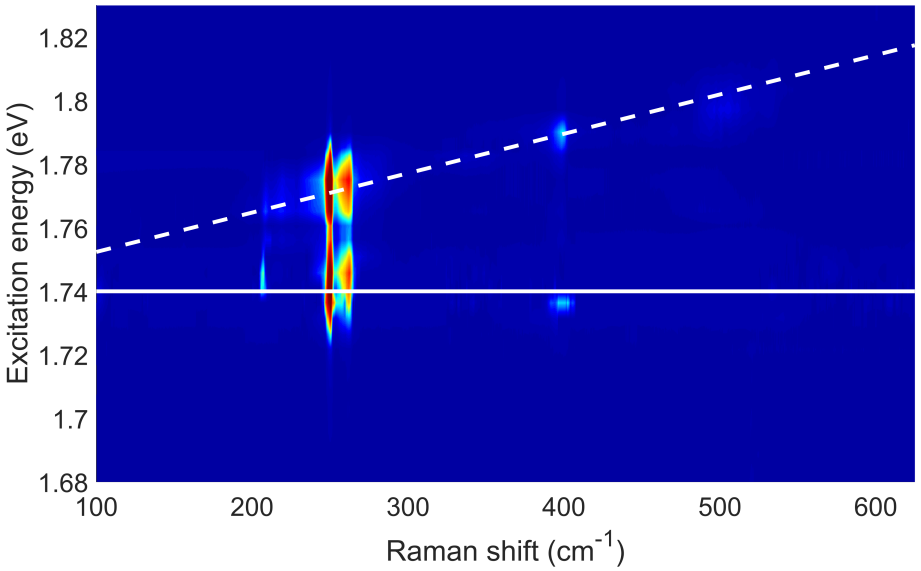

FIGURE 4.9: A colour-map of the resonance Raman data taken on the hBN encapsulated monolayer WSe_2 area covering the energy range of the A1s exciton. The intensity of the Raman scattering is indicated by the colour, with dark blue showing minimum intensity and red corresponding to maximum. The colour scale is logarithmic, which aids examination of the less intense Raman peaks. The white lines indicate the energies of the resonances associated with the A1s exciton, with the solid line and the dashed line corresponding to the incoming and outgoing resonances respectively.

The most intense peak at 249.5 cm^{-1} is also the most discussed in literature, being assigned to both the $A_1'(\Gamma)$ and $E'_{TO/LO}(\Gamma)$ (gamma point) phonons which are found to fall at the same energy by phonon dispersion calculations [113, 182]. A resonance profile of this peak was produced and fitted to a single state Raman scattering model following the procedure in subsection 3.3.1. Figure 4.10 shows this extracted resonance profile in black which features two peaks of similar width and amplitude separated by approximately 0.03 eV. These peaks correspond to the incoming and outgoing resonances, where the first falls at the exciton energy and the second falls at the exciton energy plus the phonon energy (0.03093 eV). The fitted model is shown in red in Figure 4.10 and visually it matches the data well, with the biggest discrepancy being the intensity of the pair of spectra in between the two resonance peaks falling significantly below the fitted curve. The fit yields an energy of 1.740 ± 0.001 eV with a width of 5.6 ± 0.3 meV and a squared scattering amplitude of 3.1 ± 0.2 $\times 10^{-13}\, eV^4$ for the A1s exciton.

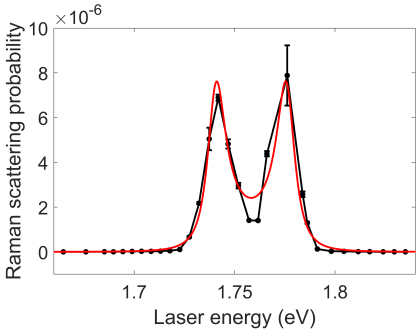

FIGURE 4.10: A resonance Raman profile of the WSe_2 monolayer 249.5 cm^{-1} Raman peak at the A1s exciton energy. The error bars on the data points are standard deviations of the amplitude of the peak determined from the fitting of the Raman spectra. The profile is fitted to a single state Raman scattering model, shown in red.

4.2.2.2 WSe_2 A2s

Above the A1s resonance, 49 Raman spectra were taken from 1.835 - 1.969 eV across the A2s exciton energy on the same WSe_2 monolayer under the same conditions. A colour-map of this data is shown in Figure 4.11 with the solid and dashed white lines indicating the energies of the incoming and outgoing resonances associated with the A2s exciton. The Raman peak at 249.5 cm^{-1} is observed once again at this energy, with distinct incoming and outgoing resonances. The signal does not go to zero below the A2s incoming resonance before it meets the tail of the A1s outgoing resonance. Adjacent weaker Raman features are observed at 234.5 cm^{-1}, 257.7 cm^{-1} and 261.9 cm^{-1}. These all similarly show distinct incoming and outgoing resonances that fall along the white lines. The same is also true of the weak signal near 400 cm^{-1}.

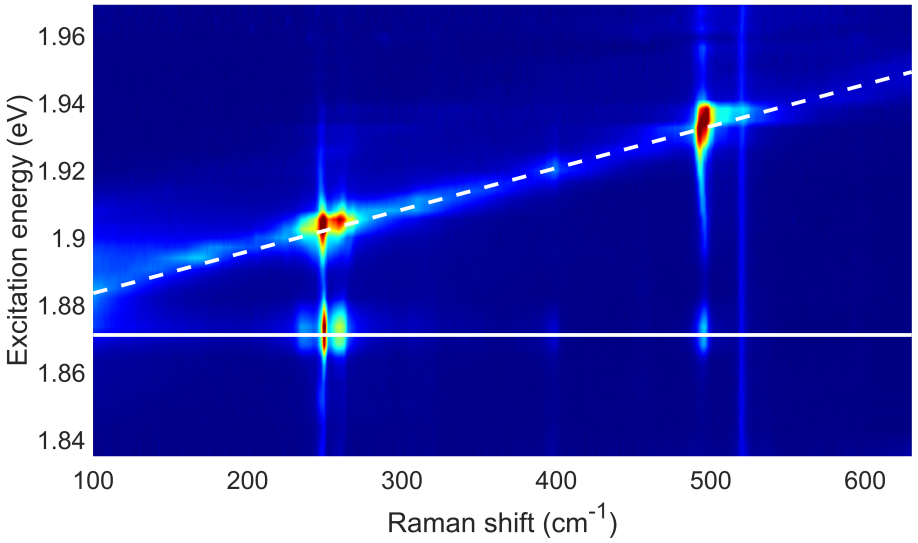

FIGURE 4.11: A colour-map of the resonance Raman spectra of the hBN encapsulated monolayer WSe_2 area with excitation energies from 1.835 - 1.969 eV, covering the A2s exciton. The intensity of the Raman scattering is indicated by the colour, with dark blue showing minimum intensity and red corresponding to maximum. The colour scale is logarithmic, which aids examination of the less intense Raman peaks. The white lines indicate the energies of the resonances associated with the A2s exciton, with the solid line and the dashed line corresponding to the incoming and outgoing resonances respectively.

An unusual feature is observed around 495 cm^{-1}. It shows resonance with the A2s exciton energy at 1.871 eV at 495.6 cm^{-1}. As the excitation energy increases, the peak reappears with the same shift at 1.902 eV and disperses to 493 cm^{-1} at 1.926 eV. The peak then splits into 3 peaks which each show different dispersion at higher energy before their intensity drops off at 1.941 eV. This behaviour is more clearly illustrated in Figure 4.12. This splitting and dispersive behaviour cannot be explained without requiring additional dark states in the exciton dispersion relation however, theoretical calculations of the full band structures are not available. A peak is visible at 520 cm^{-1} in the colour-map with no resonance behaviour. This is the Si Raman peak from the sample substrate which is used in the calibration of the spectra as discussed in subsection 3.3.1. The colour-map also shows a signal which spans across the whole spectrum, following the outgoing resonance energy and weakening as the excitation energy increases. This is the result of photoluminescence from the A2s exciton which was not entirely removed by crossed polarisation subtraction.

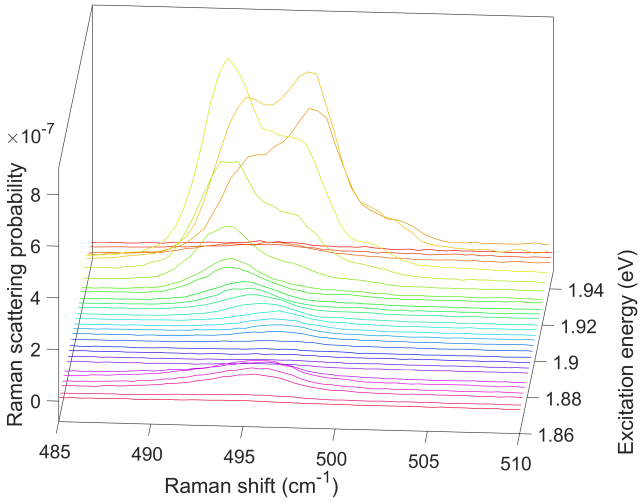

FIGURE 4.12: A waterfall plot showing Raman spectra taken with excitation energies of 1.86 - 1.95 eV, around the A2s exciton resonance in the hBN encapsulated monolayer WSe_2 sample. Only a narrow section of the spectrum around the dispersive 495 cm^{-1} Raman peak is shown.

The resonance profile of the main $A_1'(\Gamma)/E'_{TO/LO}(\Gamma)$ peak at 249.5 cm^{-1} was extracted and is shown in Figure 4.13a) and fit to a single state resonance model. As with the A1s case, the two resonance peaks have similar amplitudes however the incoming resonance peak is broader, with a full width at half maximum (FWHM) of 11 meV compared to the 6 meV of the outgoing. There is no clear explanation for this discrepancy. Also similarly to the A1s case, the fitted resonance model predicts a higher intensity than measured for the spectra between the incoming and outgoing resonances. At the energies below the incoming resonance, the model falls below the measured intensity in the spectra. This can be explained by non-resonant Raman scattering which is not included in the model or the tail end of the more intense A1s outgoing resonance. The fitted profile gives an energy of 1.8714 ± 0.0005 eV with a width of 3.5 ± 0.2 meV and a squared scattering amplitude of 3.8 ± 0.8 $\times 10^{-15}\, eV^4$. This linewidth is narrower than the 5.6 ± 0.3 meV of the A1s exciton, following the trend predicted in literature [65], which is a result of temperature independent radiative broadening in the A1s case.

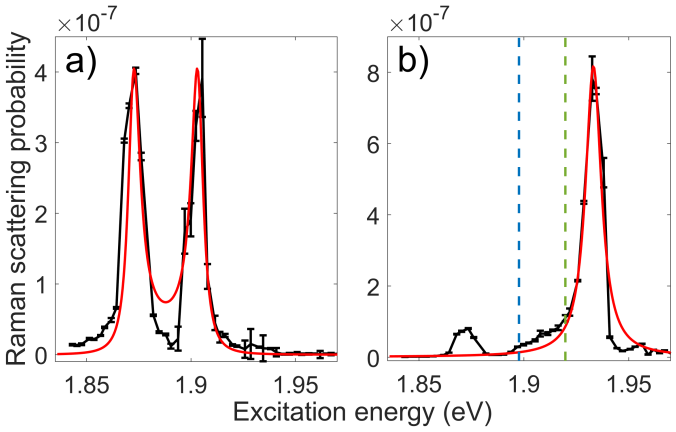

FIGURE 4.13: a) A resonance Raman profile of the WSe_2 monolayer 249.5 cm^{-1} Raman peak. The profile is fitted to a single state Raman scattering model, shown in red. b) A resonance Raman profile of the WSe_2 monolayer 495 cm^{-1} Raman peak. The fit shown in red is a Lorentzian fit to the outgoing resonance. The blue and green dashed vertical lines indicate the predicted A3s energy and the unbound continuum energy respectively. For both cases, the error bars on the data points are standard deviations of the amplitudes of the peaks determined by the spectra fitting process.

A resonance profile was also extracted for the 495 cm^{-1} peak is shown in Figure 4.13b). The profile shows an isolated peak at the incoming resonance followed by a signal that increases towards the more intense outgoing resonance peak. The outgoing resonance peak is much more intense than its incoming resonance counterpart. Above the energy of the outgoing resonance peak, the scattering rapidly drops off to zero. The predicted energies of the A3s exciton and unbound continuum energy are indicated on the plot and between these marked energies the 4s and higher order states are present. These states cover the energy range of this increasing signal. From it's shift, the 495 cm^{-1} Raman peak was identified as combination of 3 possible two-phonon scattering processes. These are $2A_1'(\Gamma)$, $A_1'(\Gamma) + E'(\Gamma)$ and $2E'(\Gamma)$, where the two phonons are degenerate in energy. Since these are gamma point phonons, they do not have enough momentum to scatter between valleys, however there is enough to scatter within a valley. It is likely that scattering via these higher order states in the same valley, as shown in Figure 4.14, contributes to both the enhancement in between the two resonance peaks and the much greater intensity of the outgoing resonance peak.

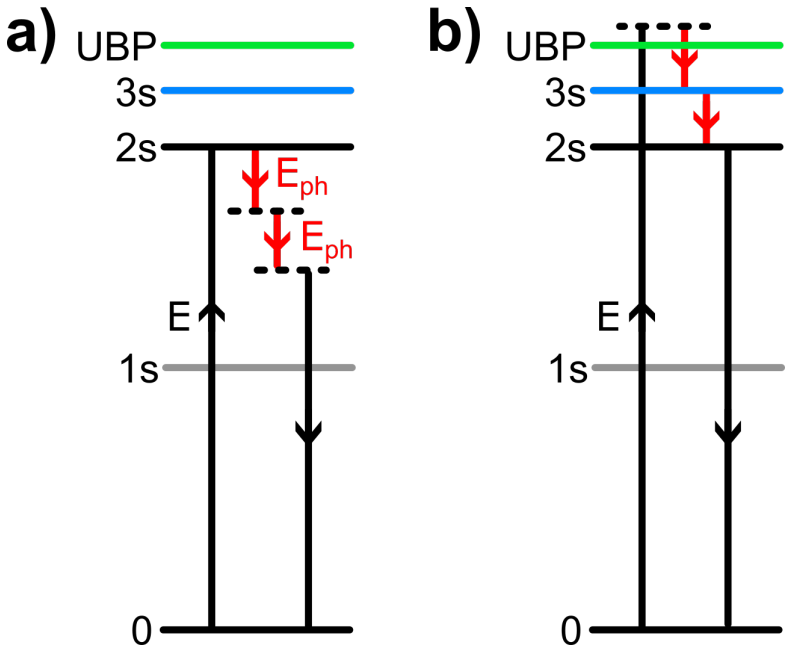

FIGURE 4.14: Energy level diagram showing the energies of the A1s A2s and A3s states as well as the unbound electron hole pair energy (UBP). The black arrows indicate the absorbed (pointing up) and emitted photon (down) energies. The pairs of red arrows indicate the pair of gamma point phonons which are emitted during the Raman scattering process to corresponding to the 495 cm^{-1} 2s associated Raman peak. The scattering process is shown at a) an incoming resonance and b) an outgoing resonance, where scattering to intermediate states enhances the Raman signal.

Both of the resonance peaks of the 495 cm^{-1} profile were fitted to Lorentzian lineshapes in order to extract the energy and linewidths, with only the fit to the outgoing resonance peak shown in red on Figure 4.13. The incoming and outgoing resonance peaks yielded linewidths of 3.6 ± 1.0 and 4.6 ± 0.3 meV respectively with A2s energies of 1.8711 ± 0.0005 and 1.8708 ± 0.0002 eV. In this case the phonon energy (495 cm^{-1} = 61.4 meV) has been subtracted from the value given for the outgoing resonance. There is excellent agreement between these three measured energies for the A2s exciton which shows that either the incoming or outgoing resonance fits can be used to accurately determine the energy of the excitonic state. However, only the width of the incident state agrees with the value determined from the 249.5 cm^{-1} peak. This is likely due to the influence on the outgoing fit of the Raman signal in between the two main resonance peaks in the profile.

4.2.2.3 WSe_2 B1s

A Raman colour-map of the WSe_2 B1s exciton is given in Figure 4.15, with 31 excitation energies from 2.048 - 2.256 eV. The solid and dashed white lines indicated the incoming and outgoing resonances with the B1s exciton which has an energy of 2.166 ± 0.001 eV. The 249.5 cm^{-1} peak is visible but, unlike the A1s and A2s cases, here it is not the

most intense of the Raman peaks. The brightest peak in the plot is at 261.6 cm^{-1}, with additional peaks visible below the $A_1'(\Gamma)/E'_{TO/LO}(\Gamma)$ peak at 217.9, 224.9, 237.9 and 241.6 cm^{-1}. The feature comprised of a pair of peaks at 395 and 399 cm^{-1} is also present with similar resonance behaviour to the lower shift peaks. A peak at 375.6 cm^{-1} is visible which was not observed at the A1s and A2s exciton energies. All of these peaks only show a single broad resonance in the colour-map. This corresponds to the case where the exciton linewidth is similar to or greater than the phonon energy, creating a broad peak centred in the middle of the incident and outgoing resonance energies. The 520 cm^{-1} Si peak can also be identified in the colour-map, but the noise level in the highest energy spectra makes it difficult to observe beyond the B1s outgoing resonance energy. No Raman peaks are observed around 495 cm^{-1} at this resonance. As the same is true of the A1s, and also as discussed later the $MoSe_2$ excitons, the 495 cm^{-1} dispersive peak can be used as a Raman fingerprint of resonance with the WSe_2 A2s exciton.

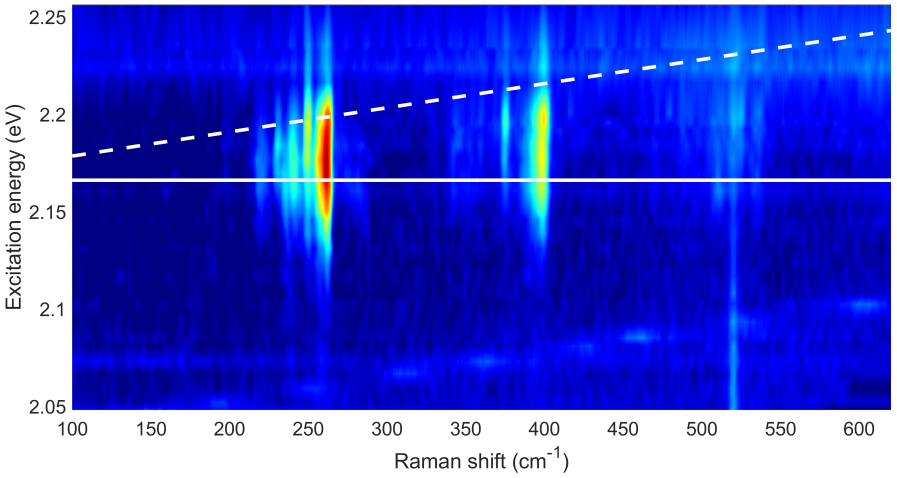

FIGURE 4.15: A colour-map of the resonance Raman spectra of the hBN encapsulated monolayer WSe_2 area with excitation energies from 2.048 - 2.256 eV, covering the B1s exciton. The intensity of the Raman scattering is indicated by the colour, with dark blue showing minimum intensity and red corresponding to maximum. The colour scale is logarithmic, which aids examination of the less intense Raman peaks. The white lines indicate the energies of the resonances associated with the A2s exciton at 2.166 eV, with the solid line and the dashed line corresponding to the incoming and outgoing resonances respectively.

Resonance Raman profiles of the 249.5 cm^{-1} $A_1'(\Gamma)/E'_{TO/LO}(\Gamma)$ peak was extracted and is shown in black in Figure 4.16. The profile shows some asymmetry which is suggestive the presence of scattering with an additional electronic state. Figure 4.16a) and b) respectively show a single state and two state fit to the resonance data, as described in subsection 3.3.1. The single state fit corresponds to an energy of 2.166 ± 0.001 eV, a width of 33 ± 2 meV and a squared scattering amplitude of 2.0 ± 0.4 $\times 10^{-12}\, eV^4$. Despite this larger amplitude than the A1s and A2s cases, the broad linewidth of this state means the measured scattering probability for the peaks in the Raman spectra is

within an order of magnitude of that for the A2s. The two state model fit shown in Figure 4.16b) involves states with energies of 2.149 ± 0.003 and 2.164 ± 0.002 eV with widths of 9 ± 3 meV and 28 ± 4 meV. Whilst this fit does more tightly fit the data, there is no other evidence of an additional state in either the PL or reflectivity spectra and, as discussed in [63], none of the resonance profiles of the other Raman peaks show evidence of an additional state.

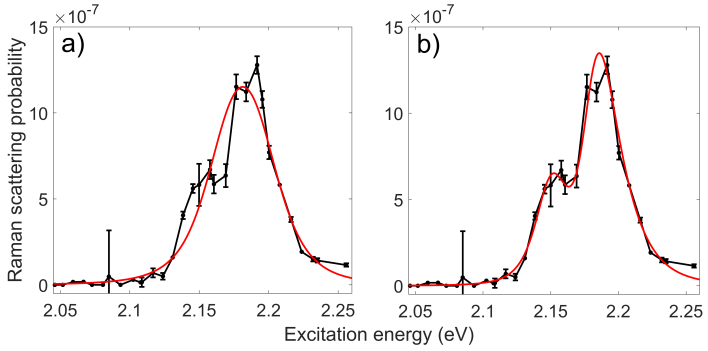

FIGURE 4.16: Resonance Raman profile of the WSe_2 monolayer 249.5 cm^{-1} Raman peak. The profile is fitted to a single state resonance model, shown in red on a) and a two state model in b). For both cases, the error bars on the data points are standard deviations of the amplitudes of the peaks determined by the spectra fitting process.

4.2.3 Characterisation of Excited State Raman Peaks in Monolayer $MoSe_2$

4.2.3.1 $MoSe_2$ A1s

Similarly to the WSe_2 case, 38 Raman spectra were taken of the $MoSe_2$ monolayer at 4 K with excitation energies between 1.597 and 1.765 eV. A colour-map of these spectra is shown in Figure 4.17, with the incoming and outgoing resonance energies of the A1s exciton indicated by solid and dashed white lines respectively. The Si Raman peak is visible in the plot at 520 cm^{-1}. The Raman peak with the most intense signal at the incoming resonance energy is at 241.5 cm^{-1}, which corresponds to the $A_1'(\Gamma)$ phonon [63, 110, 138, 198]. This peak, as well as those observed at the lower frequencies of 181.0 and 136.1 cm^{-1} all show a similar intensity at the incoming and outgoing resonances as expected for a single excitonic state. The peaks observed at higher Raman shifts however, show clear asymmetry with the outgoing resonance appearing more strongly.

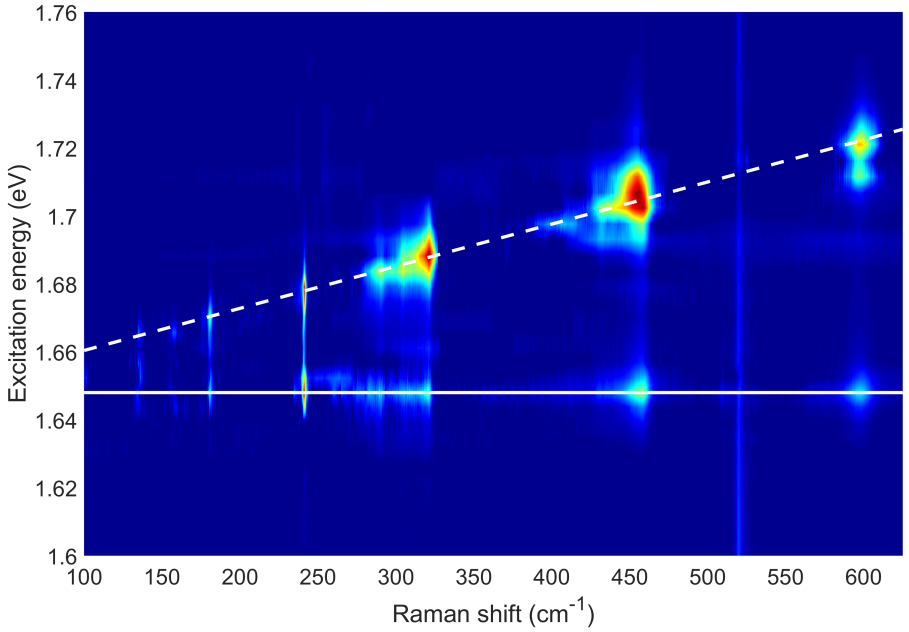

FIGURE 4.17: A colour-map of the resonance Raman spectra of the hBN encapsulated monolayer $MoSe_2$ area with excitation energies from 1.597 - 1.765 eV, covering the energy range of the A1s exciton. The intensity of the Raman scattering is indicated by the colour, with dark blue showing minimum intensity and red corresponding to maximum. The colour scale is logarithmic, which aids examination of the less intense Raman peaks. The white lines indicate the energies of the resonances associated with the A1s exciton, with the solid line and the dashed line corresponding to the incoming and outgoing resonances respectively.

These higher shift Raman peaks are necessarily multi-phonon, as the energy is too high to be explained by a single phonon process. The Raman shift of these peaks also does not match the small wavevector gamma point phonons (240 or 290 cm^{-1}) or combinations of these. The cause of the asymmetry in the resonance behaviour can be understood by examining the WSe_2 and $MoSe_2$ exciton band structures at the high symmetry K and K' points shown in Figure 4.18. The large wavevector phonons involved have enough momentum to scatter between the K and K' valleys. In the WSe_2 case a lower energy state in the opposite valley is present in both the incoming b) and outgoing a) resonance cases. In the $MoSe_2$ case, the opposite valley conduction band is higher in energy which means there are no intermediate states to scatter to at the incoming resonance d) but there is a state at the outgoing c). This results in observation of less Raman scattering at the incoming resonance than at the outgoing. A list of possible phonon assignments for these modes are given in the supplementary section of our paper [63].

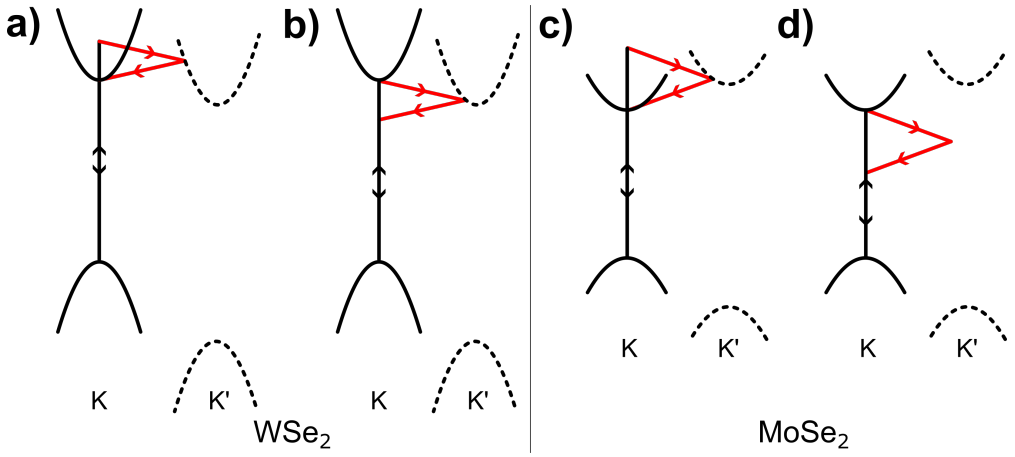

FIGURE 4.18: Electronic band structure diagram showing for the two monolayers at the K and K' high symmetry points. The black arrows indicate the absorbed (pointing up) and emitted photons (down). The pairs of red arrows indicate the pair of large wavevector phonons which are emitted during the Raman scattering process.

A resonance profile was extracted for the $A_1'(\Gamma)$ phonon at 241.5 cm^{-1} and is presented in Figure 4.19. The profile shows two well separated peaks with similar heights and widths. The profile is fitted by a single state resonance model, shown in red on the figure, which matches the data well. The biggest deviation from the data is just below the incoming resonance at 1.64 eV. This is where the PL signal was strongest and so the deviation is most likely the result of uncertainty from the background subtraction. The amplitude, width and energy of the A1s exciton from this fit are 7.1 $\pm$ 0.5 $\times 10^{-15}\, eV^4$, 3.0 $\pm$ 0.1 meV and 1.648 $\pm$ 0.001 eV respectively.

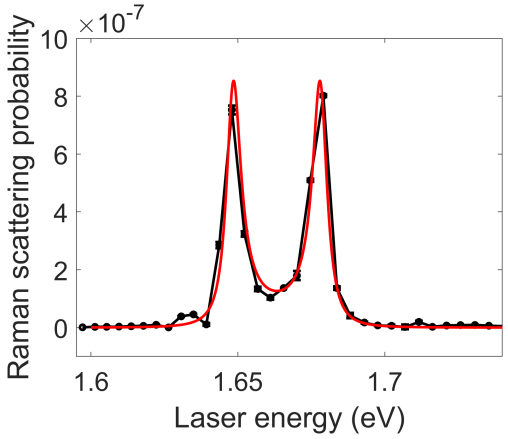

FIGURE 4.19: A resonance Raman profile of the $MoSe_2$ monolayer 241.5 cm^{-1} Raman peak at the A1s exciton. The profile is fitted to a single state Raman scattering model, shown in red. The error bars on the data points are standard deviations of the amplitudes of the peaks determined by the spectra fitting process.

4.2.3.2 $MoSe_2$ A2s and B1s

A further 32 Raman spectra were taken with excitation energies from 1.75 - 2.00 eV, covering the $MoSe_2$ A2s and B1s excitons. A Raman colour-map of the data is shown in Figure 4.20, with the resonances associated with the B1s and A2s excitons marked with white and red lines respectively. The $A_1'(\Gamma)$ 241.5 cm^{-1} Raman peak is observed across the whole energy range. Unlike the A1s case, a distinct incoming and outgoing resonance is not visible for any of the Raman peaks. This is not unexpected, as the B1s exciton already showed a significantly broader linewidth than the A1s in the reflectivity spectrum. Once again, the 520 cm^{-1} Si peak is present across the whole energy range.

Dispersive peaks are visible in the colour-map with a peak that shifts from 283.3 cm^{-1} at 1.811 eV to 278.6 cm^{-1} at 1.891 eV and another that shifts from 289.0 cm^{-1} at 1.849 eV to 283.8 cm^{-1} at 1.945 eV. In addition, a peak is visible which shifts in the opposite direction with increasing energy, going from 258.3 cm^{-1} at 1.857 eV to 260.7 cm^{-1} at 1.908 eV. As well as showing this dispersion, the peaks show different resonance behaviour, with the peak at the lowest Raman shift appearing most intense at 1.891 eV and the middle peak at 1.857 eV. These peaks are most likely the result of multi-phonon scattering between the K and K' valleys, similar to those reported in MoS_2 [139], where a model of the exciton dispersion relation is required to be able to properly fit the resonance behaviour.

In addition to the Raman peaks observed at the A1s exciton, peaks at 354.6, 480.4, 530.8 and 582.5 cm^{-1} were observed, where no Raman signal was present in the A1s case. The first of these peaks shows resonance behaviour similar to the $A_1'(\Gamma)$ and the rest of the peaks also observed at the A1s. However, the other three peaks at at 480.4, 530.8 and 582.5 cm^{-1} show distinctly different behaviour. Rather than appearing with a broad resonance centred between the B1s incoming and outgoing resonance energies, these three peaks follow the A2s outgoing resonance energy, dropping in intensity quickly above it and more slowly trailing off down towards the A2s incoming energy. The peaks are much less intense at the A2s incoming resonance, which shows that the peaks are not just resonant with the A2s alone, they are doubly resonant with the A2s and B1s excitons. Whilst the reason is unclear, the colour-map illustrates that these three peaks show clearly distinct resonance behaviour from the rest of the Raman peaks.

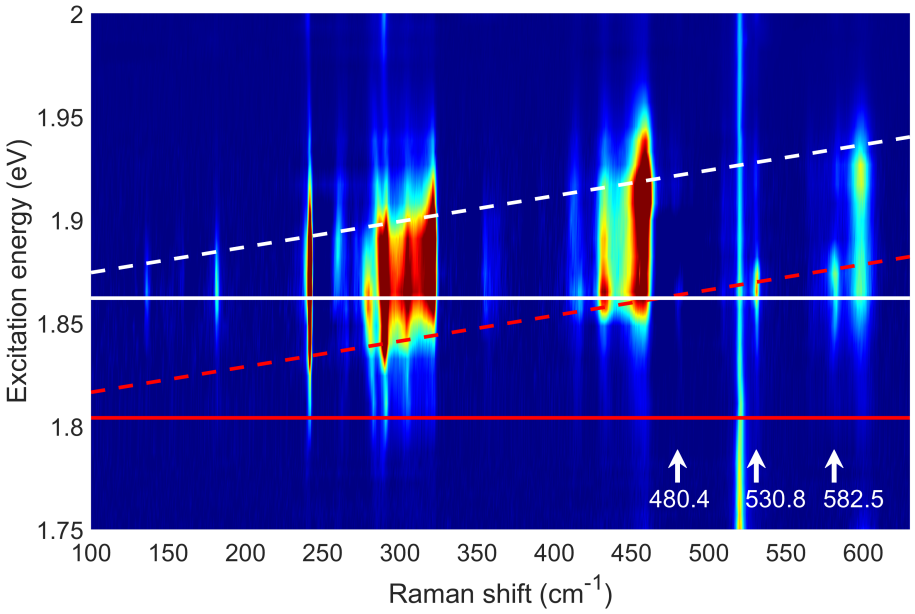

FIGURE 4.20: A colour-map of the resonance Raman spectra of the hBN encapsulated monolayer $MoSe_2$ area with excitation energies from 1.75 - 2.00 eV, covering the A2s and B1s excitons. The intensity of the Raman scattering is indicated by the colour, with dark blue showing minimum intensity and red corresponding to maximum. The colour scale is logarithmic, which aids examination of the less intense Raman peaks. The white lines indicate the energies of the resonances associated with the B1s exciton at 1.858 eV, with the solid line and the dashed line corresponding to the incoming and outgoing resonances respectively. Similarly, the red lines correspond to the A2s exciton with an energy of 1.803 eV.

Before considering the resonance profiles of these peaks, the $A_1'(\Gamma)$ case is examined. Figure 4.21 shows the resonance profile of the 241.5 cm^{-1} Raman peak across the A2s and B1s energies where plotted in red in a) is the fit to a single state resonance model. The fit captures well the data above 1.9 eV but the peak of the fit falls at a lower energy than the data appears to suggest. The two 'shoulders' on the low energy side of the peak in the data, near 1.81 and 1.84 eV are also not fit well by the curve. A two-state resonance model was used to fit the same data as shown in red in Figure 4.21b). In this case, the curve is much more successful in fitting the two 'shoulders', which correspond to the A2s incoming and outgoing resonance energies. In addition, the curve more closely follows the biggest peak and matches the data exceptionally well above 1.88 eV. The parameters for the fit are given in Table 4.5. As expected, the A2s scattering amplitude is a smaller than the B1s, in this case by a factor of 110, with the inter-state scattering falling in-between.

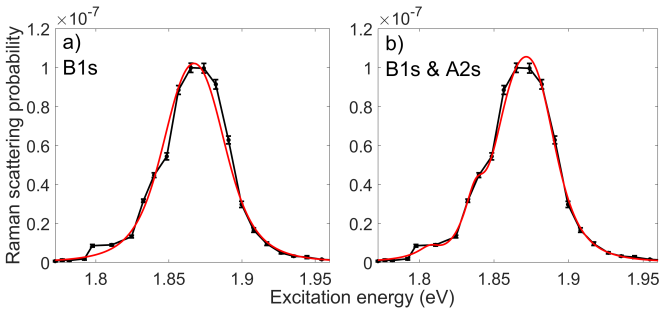

FIGURE 4.21: A resonance Raman profile of the $MoSe_2$ monolayer 241.5 cm^{-1} Raman peak. The error bars on the data points are standard deviations of the amplitudes of the peaks determined by the spectra fitting process. The profile is fitted to a single state Raman scattering model, shown in red in a) and a two state model shown in b).

The two state fitted $A_1'(\Gamma)$ is shown again in Figure 4.22a) alongside the interesting 480.4, 530.8 and 582.5 cm^{-1} peaks, shown in b) - d). These were also all fitted to two state resonance models and despite the markedly different resonance behaviour from the $A_1'(\Gamma)$ phonon, the two state model also fits these three peaks well. The fitted models yielded energies and widths for the A2s and B1s excitons given in Table 4.5. These place the A2s slightly higher in energy than the fit to the $A_1'(\Gamma)$ peak suggests, however they are still within one linewidth. The measured widths also agree with the 241.5 cm^{-1} peak value to within two standard deviations, which shows the scattering is with the same excitonic state. In contrast to the value of 110 measured for the $A_1'(\Gamma)$ peak, the ratio of the B1s to the A2s scattering amplitudes gave significantly smaller values of 4, 18 and 20 for the three peaks. This shows that whilst these peaks are scattering via the same two excitons as the $A_1'(\Gamma)$ phonon, the amplitudes associated with the A2s for the three peaks are significantly higher.

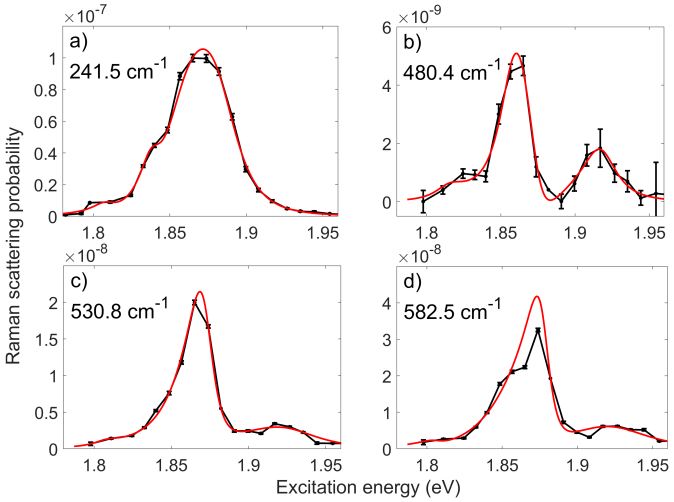

FIGURE 4.22: Resonance Raman profiles of the $MoSe_2$ monolayer sample for the A2s/B1s exciton energies and fitted two state resonance models for the Raman peaks at a) 241.5 cm^{-1}, b) 480.4 cm^{-1}, c) 530.8 cm^{-1} and d) 582.5 cm^{-1}. The error bars on the data points are standard deviations of the amplitudes of the peaks determined by the spectra fitting process.

Raman Shift (cm^{-1})	241.5	480.4	530.8	582.5
A2s Energy (eV)	1.803 ± 0.002	1.813 ± 0.010	1.806 ± 0.008	1.809 ± 0.011
B1s Energy (eV)	1.858 ± 0.001	1.859 ± 0.002	1.859 ± 0.003	1.850 ± 0.006
A2s Width (meV)	8.2 ± 0.7	10.6 ± 3.4	9.7 ± 0.8	11 ± 2.0
B1s Width (meV)	19 ± 1	14.4 ± 2.8	36.7 ± 6.7	37.4 ± 10.9
A2s Amplitude ($\times 10^{-15}\ eV^4$)	0.3 ± 0.2	0.7 ± 0.5	1.8 ± 0.8	10.65 ± 6.33
B1s Amplitude ($\times 10^{-15}\ eV^4$)	34 ± 3	2.7 ± 1.7	34 ± 16	210 ± 200
Inter-state Amplitude ($\times 10^{-15}\ eV^4$)	4 ± 0.4	0.18 ± 0.12	3.9 ± 1.3	43 ± 28

TABLE 4.5: Coefficients for fitting the two state scattering models to the resonance Raman profiles of the three $MoSe_2$ 2s associated Raman peaks for the hBN encapsulated monolayer $MoSe_2$ sample.

4.2.3.3 $MoSe_2$ B2s

An additional 33 Raman spectra were taken of the $MoSe_2$ monolayer area from 2.00 to 2.24 eV which covered the B2s exciton. Figure 4.23 shows a colour-map of the Raman spectra, with the B2s exciton incident and outgoing resonance energies marked with solid and dashed white lines respectively. The 241.5 cm^{-1} $A_1'(\Gamma)$ peak is visible, showing a single resonoance rather than distinct incoming and outgoing resonances. The tail end of the B1s resonance is visible for this peak at the bottom of the colour-map and above 2.1 eV the peak starts getting stronger towards higher energy. This is likely either non-resonant Raman scattering and the lower energy tail of the resonance with a broad C exciton which has previously been reported in resonance Raman studies of this material [138, 181]. The next most intense peak appears at 290.1 cm^{-1} and shows a more distinct incoming and outgoing resonance. The Si 520 cm^{-1} peak is also present in the colour-map, appearing more intensely as the colour scale has been adjusted to increase the visibility of the weaker peaks. The trio of A2s associated peaks are also observed at this resonance, at shifts of 480.7, 530.8 and 582.6 cm^{-1}. Here, there is also not a clear distinction between the incoming and outgoing resonances. Whilst additional Raman peaks are visible, they show minimal signal.

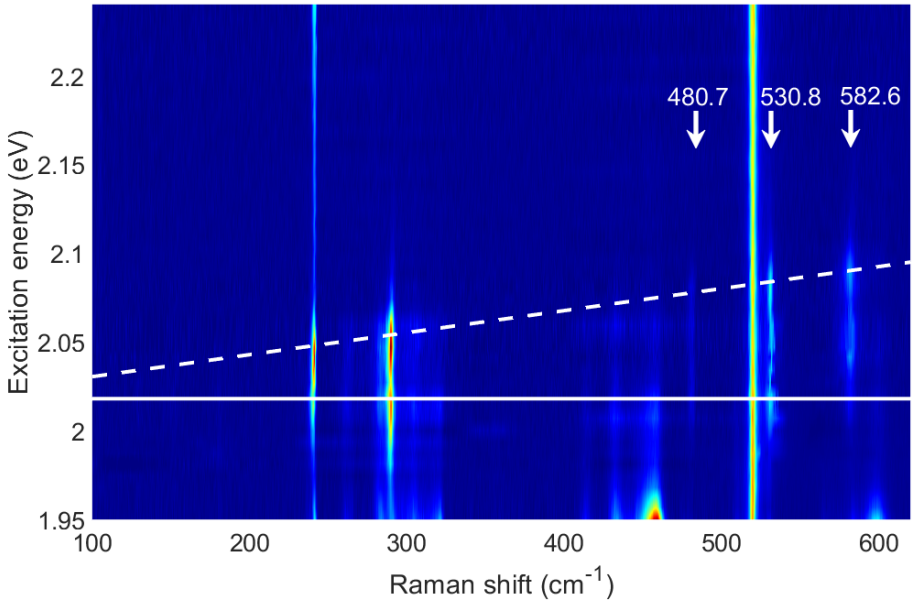

FIGURE 4.23: A colour-map of the resonance Raman spectra of the hBN encapsulated monolayer $MoSe_2$ for an energy range covering the B2s exciton. The intensity of the Raman scattering is indicated by the colour, with dark blue showing minimum intensity and red corresponding to maximum. The colour scale is logarithmic, which aids examination of the less intense Raman peaks. The white lines indicate the energies of the resonances associated with the B2s exciton, with the solid line and the dashed line corresponding to the incoming and outgoing resonances respectively.

Resonance profiles were extracted and fitted for the 241.5, 480.7, 530.8 and 582.6 cm^{-1}. These are shown in Figure 4.24, with the fitted curves shown in red corresponding to single state resonance models. The 241.5 cm^{-1} peak profile shows some asymmetry at the top, with the higher energy side more intense than the lower. The intensity also does not go to zero either side of the resonance as observed in the colour-map, due to contributions from the B1s and C excitons as well as non-resonant Raman scattering which are not included in the standard resonance model. A constant is added to the model for only this peak to prevent the background from influencing the fitted width. Without the addition of this constant, the fitted width is 39 meV, significantly higher than determined from the other B2s profiles. The 480.7 and 530.8 cm^{-1} fitted peak profiles both reveal the separate incoming and outgoing resonances and show a good fit to the data. The resonance profile of the 582.6 cm^{-1} peak however, shows more signal at 2.05 eV and less at 2.02 eV than expected, resulting in a broader and higher energy fit than the other two peaks. The widths determined and energies for the four peaks are given in Table 4.6. The 582.6 cm^{-1} peak is the outlier of the bunch, with asymmetric resonance behaviour indicative of scattering with a dark excitonic state.

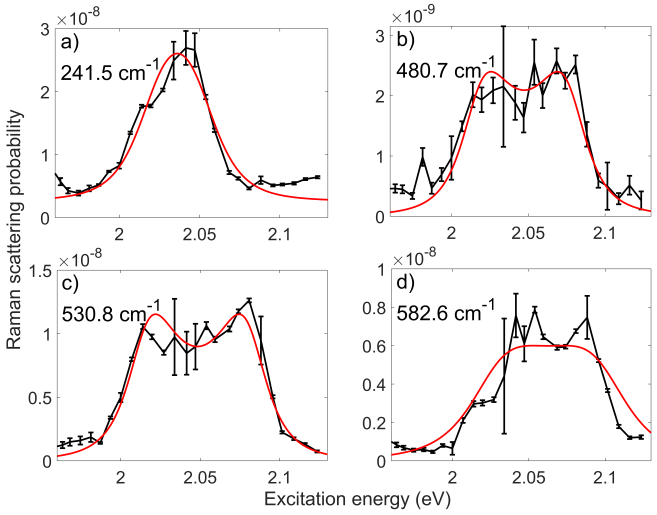

FIGURE 4.24: Resonance Raman profiles of the $MoSe_2$ monolayer sample near the energy of the B2s exciton and fitted single state resonance models for the Raman peaks at a) 241.5 cm^{-1}, b) 480.7 cm^{-1}, c) 530.8 cm^{-1} and d) 582.6 cm^{-1}. The error bars on the data points are standard deviations of the amplitudes of the peaks determined by the spectra fitting process. A constant background has been added to the resonance model for a). The coefficients for the fits are given in Table 4.6.

Raman Shift (cm^{-1})	Width (meV)	Energy (eV)
241.5	27 ± 7	2.021 ± 0.002
480.7	20 ± 3	2.018 ± 0.002
530.8	20 ± 2	2.015 ± 0.002
582.6	34 ± 10	2.027 ± 0.002

TABLE 4.6: Coefficients for fitting the single Raman state scattering models to the resonance profiles of the 241.5 cm^{-1} $A_1'(\Gamma)$ peak and the three $MoSe_2$ 2s associated Raman peaks for the hBN encapsulated monolayer $MoSe_2$ sample at the B2s exciton resonance.

As discussed in [71], the three A2s associated Raman peaks with frequencies of 480.7, 530.8 and 582.6 cm^{-1} have Raman shifts which are too high to be from single phonon Raman scattering. Theoretically modelled Raman shifts for the phonon modes in monolayer $MoSe_2$ from [113] were used to produce a list of possible combinations for multi-phonon scattering at the three Raman shifts. This included multiple combinations of phonons at the high-symmetry M, K and Γ points. At this B2s resonance, the only other peaks with strong Raman signal are the $A_1'(\Gamma)$ phonon peak at 241.5 cm^{-1} and a peak at 290.1 cm^{-1} which is assigned to the $E'_{TO}(\Gamma)$ phonon mode. This means that all 5 of these peaks observed at this resonance can be assigned to purely Γ point modes; with the 480.7 cm^{-1} corresponding to $2A_1'(\Gamma)$, the 530.8 cm^{-1} to $A_1'(\Gamma) + E'_{TO}(\Gamma)$ and the 582.6 cm^{-1} to $2E'_{TO}(\Gamma)$. This is significant as Γ point phonons are small-wavevector which means that they cannot scatter between valleys. This provides a natural explanation of why the peaks are not present in the Raman spectra at the A1s exciton energy. There

are no lower energy intra-valley dark states, however these are available at the higher energy exciton branches which allows resonant scattering between the dark states and the bright A and B excitons.

4.2.3.4 Conclusions

In summary, the resonance behaviour of the Raman peaks from monolayer $MoSe_2$ and WSe_2 have been examined and the majority of the peaks followed the behaviour of the $A_1'(\Gamma)$, or $A_1'(\Gamma)/E'(\Gamma)$ in WSe_2, single phonon peak. Behaviour that deviated from this was examined and includes peaks that scattered via dark excitonic states which showed dispersion as well as different resonance behaviour. In $MoSe_2$, the presence of a higher energy conduction band which can act as an intermediate state in multi-phonon Raman scattering can explain the asymmetric resonance behaviour of the modes with higher Raman shift. Most notably, a trio of Raman peaks have been identified in monolayer $MoSe_2$ which were only present at resonance with the 2s excitons with Raman shifts around 480, 530 and 582 cm^{-1}. In addition, a dispersive Raman peak was observed around 495 cm^{-1} in WSe_2 monolayer which similarly shows resonance at the A2s exciton only. Here the WSe_2 B2s falls at too high an energy for the Raman system to access so its presence there was not determined. These multi-phonon peaks can therefore allow identification of the 2s resonances in monolayers of WSe_2 or $MoSe_2$ where they are difficult to identify via other spectroscopic methods such as reflectivity or even resonance Raman of the often more intense $A_1'(\Gamma)$ peak. In the following sections, these 2s associated peaks are used to identify the A and B 2s excitons in $MoSe_2/WSe_2$ heterostructures.

4.2.4 Identification of Excited States in $MoSe_2/WSe_2$ Heterostructures

The next section presents the resonance Raman measurements of the excitonic states observed in the hBN encapsulated 57° heterostructure sample, presented in ascending energy order.

4.2.4.1 57° Twist Heterostructure $MoSe_2$ A1s

A colour-map of resonance Raman spectra of the HS57 heterostructure sample is given in Figure 4.25 with the energies associated with the $MoSe_2$ A1s exciton indicated with white lines. Clearly separated incoming and outgoing resonances are present with multiple Raman peaks. Similarly to the $MoSe_2$ monolayer case presented previously in Figure 4.17, the strong multi-phonon peaks observed at Raman shifts above 270 cm^{-1}

are once again significantly stronger at the outgoing resonance energy than the incoming. A resonance profile for the peak with a shift of 456.5 cm^{-1} is given in Figure 4.26c) and highlights this asymmetry which, as in the monolayer case, is a result of scattering to a higher energy conduction band at the opposite valley (K / K'). The $A_1'(\Gamma)$ peak is observed at 240.8 cm^{-1} at this resonance with distinct incoming and outgoing resonances. The resonance profile of this peak is shown in Figure 4.26b). The signal at the incoming resonance is slightly more intense than at the outgoing however, this is most likely a result of PL signal present at the outgoing resonance increasing the uncertainty in the data. This is reflected in the larger error bars around the outgoing resonance energy from the fits of the Raman spectra. Aside from the three data points at the outgoing resonance, the single state model shown in red fits the data well, and yields an energy of 1.620 ± 0.001 eV, width of 5.4 ± 0.3 meV and scattering probability of 9.2 ± 0.7 $\times 10^{-15}$ eV^4 for the $MoSe_2$ A1s exciton. This agrees with the 1.622 ± 0.001 eV and 5.0 ± 0.1 meV from the reflectivity to within the fitted errors.

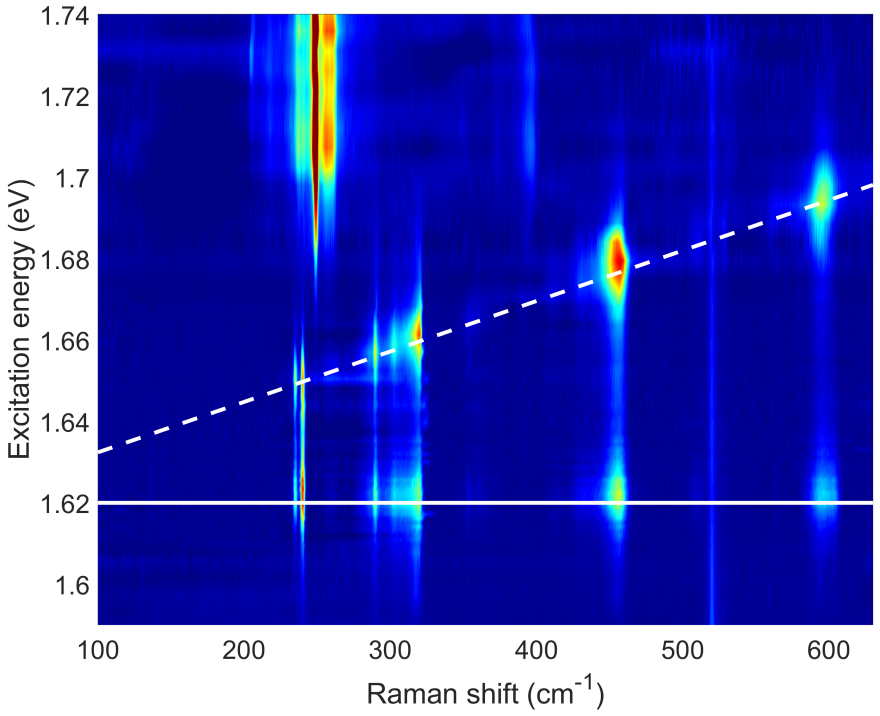

FIGURE 4.25: A colour-map of the resonance Raman spectra of the hBN encapsulated 57° twist $MoSe_2/WSe_2$ heterostructure sample for an energy range from 1.59 - 1.74 eV. The intensity of the Raman scattering is indicated by the colour, with dark blue showing minimum intensity and red corresponding to maximum. The colour scale is logarithmic, which aids examination of the less intense Raman peaks. The white lines indicate the energies of associated with the $MoSe_2$ A1s exciton, with the solid lines and the dashed lines corresponding to the incoming and outgoing resonances respectively.

The more significant difference between this heterostructure sample and the monolayer case at this resonance is the additional Raman peak at 235.2 cm^{-1}. This peak was also observed resonant at the $MoSe_2$ B1s exciton in this heterostructure and cannot

be clearly assigned to any high symmetry points of the Brillouin zone in published monolayer $MoSe_2$ phonon band structures [110, 199]. This peak was instead assigned to a Moiré zone folding of the $A_1'(\Gamma)$ phonon as we discussed in [14] which includes this sample as well as a 2° twisted heterostructure, with the same constituent monolayers, which also shows Moiré zone folded Raman peaks.

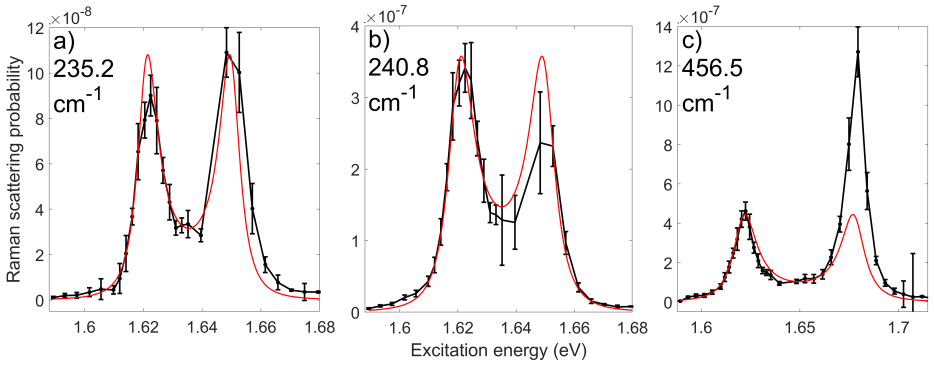

FIGURE 4.26: Resonance Raman profiles of the 57° twist $MoSe_2/WSe_2$ heterostructure sample across the $MoSe_2$ A1s exciton energy range for the $MoSe_2$ a) 235.2 cm^{-1} b) 240.8 cm^{-1} $A_1'(\Gamma)$ c) Raman peaks. The error bars on the data points are standard deviations of the amplitudes of the peaks determined by the spectra fitting process. The single state resonance model fits are shown in each case in red.

4.2.4.2 57° Twist Heterostructure WSe_2 A1s

The next highest energy feature observed in the resonance Raman data from this sample was from the WSe_2 A1s. A colour-map of the resonance Raman data is given in Figure 4.27. Similarly to the monolayer case, the most intense peak here is from the $A_1'(\Gamma)/E'(\Gamma)$ phonon, at 248.8 cm^{-1}. The resonance behaviour however does not have clearly distinct incoming and outgoing resonances. A resonance profile of this peak is shown in Figure 4.28, fitted to a single state resonance model in pannel a). Whilst this fit matches the data well below 1.73 eV, the shoulder on the higher energy side is not captured by the fit. The two state model in b) can explain this shoulder, yielding the fitted parameters given in Table 4.7. The energies from this fit are separated by 23 meV, which is closest to the 21 meV reported in WSe_2 monolayers in literature for the positively charged trion [78, 190]. The negative trions are reported with larger separations, falling at energies 29 and 36 meV below the exciton. Thus the WSe_2 A1s exciton is assigned to 1.728 eV and the positively charged trion to 1.705 eV. As discussed in subsubsection 4.2.1.3, this strong signal from the trion, which is also observed in the reflectivity, is indicative of the WSe_2 layer in this sample being p-doped resulting from charge transfer from the $MoSe_2$ layer. This charge transfer is expected as a result of the band alignment of the two constituent monolayers. The valence band of the WSe_2 layer is above that of the $MoSe_2$ layer [40], causing holes to move from the $MoSe_2$ to the

WSe_2 layer. Additionally, the WSe_2 conduction band is above the $MoSe_2$ conduction band which results in electrons flowing from the WSe_2 to the $MoSe_2$ layer.

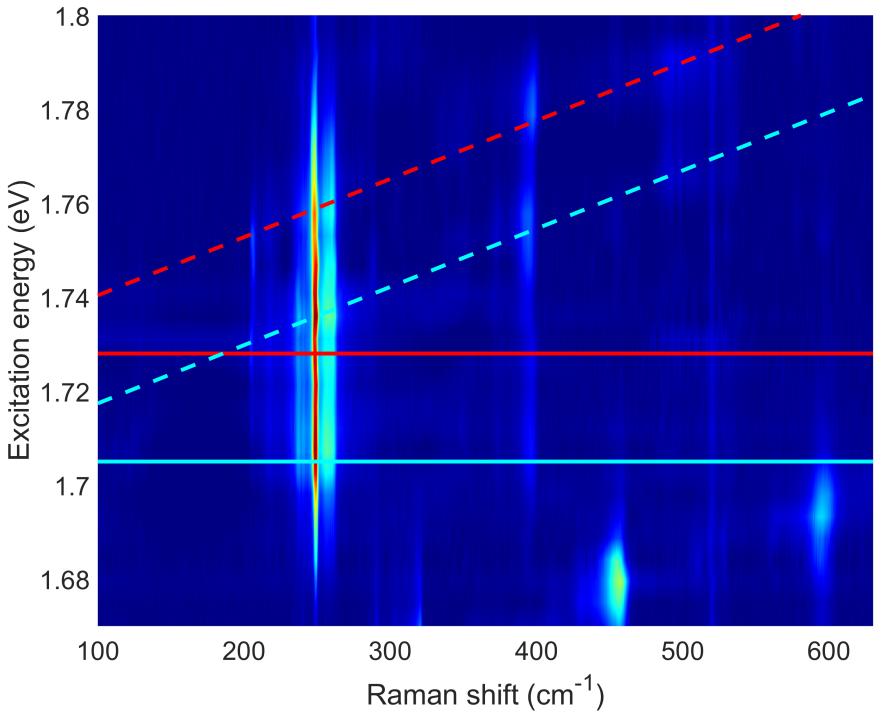

FIGURE 4.27: A colour-map of the resonance Raman spectra of the hBN encapsulated 57° twist $MoSe_2/WSe_2$ heterostructure sample for an energy range from 1.67 - 1.80 eV. The intensity of the Raman scattering is indicated by the colour, with dark blue showing minimum intensity and red corresponding to maximum. The colour scale is logarithmic, which aids examination of the less intense Raman peaks. The red lines indicate the energies of associated with the WSe_2 A1s exciton, with the solid and dashed lines corresponding to the incoming and outgoing resonances respectively. Similarly, the cyan lines correspond to the A1s trion.

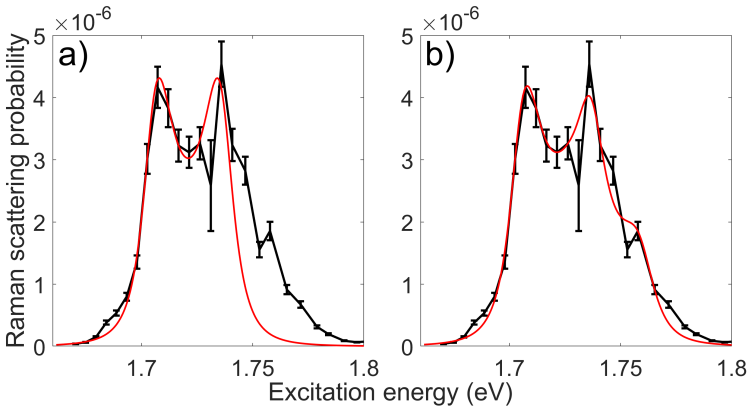

FIGURE 4.28: Resonance Raman profile of the 248.8 cm^{-1} $A_1'(\Gamma)/E'(\Gamma)$ peak for the the 57° twist $MoSe_2/WSe_2$ heterostructure sample across the WSe_2 A1s exciton energy range. a) Fitted to a single state resonance model. b) Fitted to a two state resonance model. The fits are shown in red for each case. The error bars on the data points are standard deviations of the amplitudes of the peaks determined by the spectra fitting process.

	Energy (eV)	Width (meV)	Amplitude ($\times 10^{-15}\ eV^4$)
Exciton	1.728 ± 0.002	6.5 ± 1.1	163 ± 51
Trion	1.705 ± 0.001	7.9 ± 0.7	261 ± 38

TABLE 4.7: Coefficients for fitting the two state scattering model to the resonance Raman profile of the 248.8 cm^{-1} Raman peak in the energy range of the WSe_2 A1s exciton for the 57° twist $MoSe_2/WSe_2$ heterostructure sample.

4.2.4.3 57° Twist Heterostructure $MoSe_2$ A2s and B1s

The $MoSe_2$ A2s exciton is expected to fall around the energy of the WSe_2 A1s. However, any Raman signal from the $MoSe_2$ $A_1'(\Gamma)$ phonon in this range in the heterostructures is overwhelmed by signal from the WSe_2 A1s due to its greater oscillator strength. The trio of $MoSe_2$ 2s associated peaks were observed at 480.0, 530.7 and 582.2 cm^{-1} in this 57° twist heterostructure as shown in Figure 4.29. The shifts of these peaks are indicated on the figure with arrows and Raman signal is observed following the A2s outgoing resonance, marked with a dashed red line. A small amount of signal is observed at the incoming resonance for the two higher shift of these peaks. However, the signal is not intense enough to produce resonance profiles that can be fitted accurately with two-state scattering models as was done for the same peaks in the monolayer case. Here, Lorentzian peaks were used to fit the most intense part of the profiles which followed the outgoing resonance. These fits are shown in Figure 4.30. The phonon energies, from the Raman shifts of the peaks, were then subtracted from the fitted energies to give three independent values of the energy of the $MoSe_2$ A2s exciton. These are presented alongside the widths from these fits in Table 4.8. The energies determined from the

three fits are agree to within 1 meV of 1.754 eV which shows as expected that the three peaks are all resonant with the same excitonic state. The energy difference of 134 meV between the 1s and 2s excitons is smaller than the value from $MoSe_2$ monolayer of 153 meV. This is examined in more detail in section 4.3. Whilst the widths from the first two profiles agree to within the errors from the fit, the width from the 582.2 cm^{-1} peak is significantly larger. This reflects the fact that, as with the monolayer case, there is a contribution to the profile from a double resonance with the $MoSe_2$ A2s and the much broader B1s exciton. The true width of the $MoSe_2$ A2s exciton in this case is thus most likely closer to 5.4 meV, the average of the narrower two values.

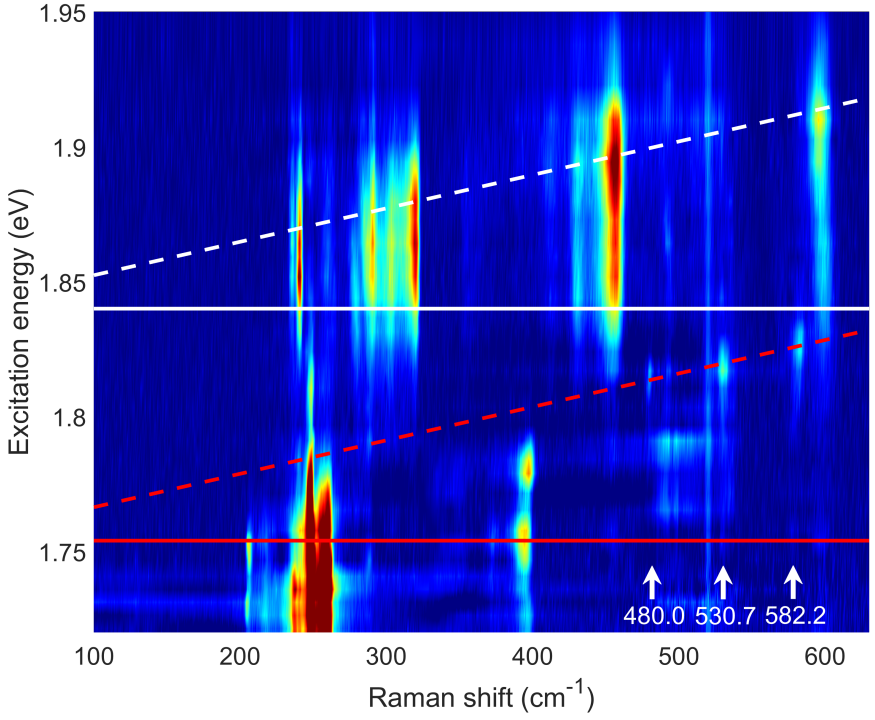

FIGURE 4.29: A colour-map of the resonance Raman spectra of the hBN encapsulated 57° twist $MoSe_2/WSe_2$ heterostructure sample for an energy range from 1.72 - 1.95 eV. The intensity of the Raman scattering is indicated by the colour, with dark blue showing minimum intensity and red corresponding to maximum. The colour scale is logarithmic, which aids examination of the less intense Raman peaks. The white lines indicate the energies of associated with the $MoSe_2$ B1s exciton, with the solid and dashed lines corresponding to the incoming and outgoing resonances respectively. The red lines similarly indicated the $MoSe_2$ A2s exciton resonance energies.

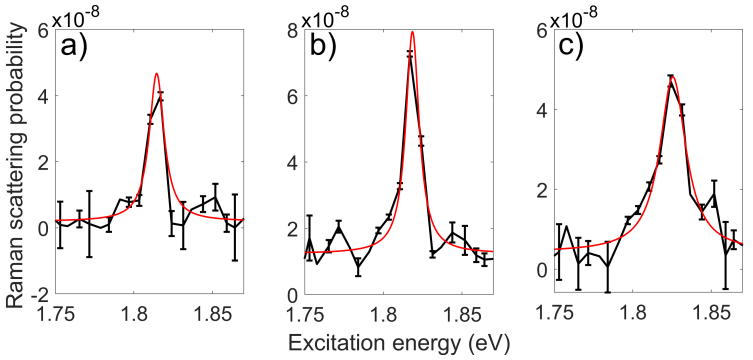

FIGURE 4.30: Resonance Raman profiles of the 2s associated Raman peaks observed in the the 57° twist $MoSe_2/WSe_2$ heterostructure sample across the $MoSe_2$ A2s exciton energy range. Resonance profile of the a) 480.0 cm^{-1} peak. b) 530.7 cm^{-1} peak. c) 582.2 cm^{-1} peak. The fits to a Lorentzian peak are shown in red for each case. The error bars on the data points are standard deviations of the amplitudes of the peaks determined by the spectra fitting process.

Raman shift (cm^{-1})	Energy (eV)	Width (meV)
480.0	1.754 ± 0.0005	5.7 ± 2.2
530.7	1.753 ± 0.001	5.1 ± 1.1
582.2	1.754 ± 0.001	10.14 ± 1.7

TABLE 4.8: Coefficients for fitting resonance Raman profiles of the $MoSe_2$ 2s Raman peaks to Lorentzians at the $MoSe_2$ A2s outgoing resonance for the 57° twist $MoSe_2/WSe_2$ heterostructure sample.

The Raman signal at higher energies in Figure 4.29 is from the $MoSe_2$ B1s exciton, with the incoming and outgoing resonance energies indicated in white. A resonance profile of the main $A_1'(\Gamma)$ phonon peak at 240.0 cm^{-1} was extracted from the data and is shown in Figure 4.31. A single state resonance model was used to fit the data which is shown on the figure in red. A sign of a small shoulder around 1.9 eV is visible in the profile but there is no other evidence of the presence of another $MoSe_2$ excitonic state in that energy range. The fit in Figure 4.31 yielded an energy of 1.839 ± 0.001 eV, width of 23 ± 1.5 meV and an amplitude of 57 ± 10 $\times 10^{-15}$ eV^4. This gives a ratio of the amplitudes of the B1s to the A1s of 6.1 ± 1.2 which overlaps with the value of 4.8 ± 1.5 for the monolayer. The width of the $MoSe_2$ B2s in this case is also significantly broader than the A1s, as in the monolayer case. The rest of the Raman peaks observed at this resonance do not show distinctly different behaviour from the monolayer case. The Moiré zone folded $A_1'(\Gamma)$ phonon peak observed at the $MoSe_2$ A1s in this heterostructure (Figure 4.25) is also observed here at the $MoSe_2$ B1s with a frequency of 234.9 cm^{-1}.

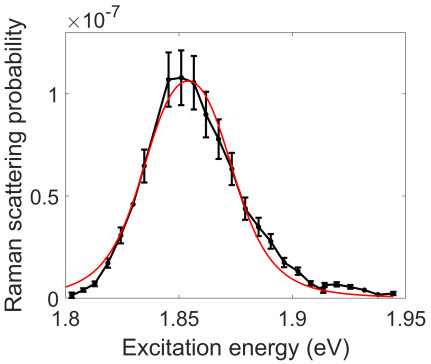

FIGURE 4.31: Resonance Raman profiles of the $A_1'(\Gamma)$ phonon peak observed in the the 57° twist $MoSe_2/WSe_2$ heterostructure sample across the $MoSe_2$ B1s exciton energy range. The profile was fit to a single state resonance model shown in red. The error bars on the data points are standard deviations of the amplitudes of the Raman peak determined by the spectra fitting process.

4.2.4.4 57° Twist Heterostructure WSe_2 A2s

Figure 4.32 shows a colour-map of the $MoSe_2$ B1s exciton in HS57, which has the incoming and outgoing resonance energies marked in white. Within this energy range, the only signal from the WSe_2 $A_1'(\Gamma)/E'(\Gamma)$ phonon peak is the weak tail of the WSe_2 A1s outgoing resonance, present at the bottom of the figure. However, the WSe_2 A2s associated Raman peak, observed in the monolayer, is also found here at 494.4 cm^{-1}. This signal, marked with an arrow indicating its frequency in Figure 4.32, does show distinct incoming and outgoing resonances which do not follow the $MoSe_2$ B1s. A resonance profile of this peak is shown in Figure 4.33. The low intensity of the signal from this peak resulted in a noisy profile with relatively large uncertainties.

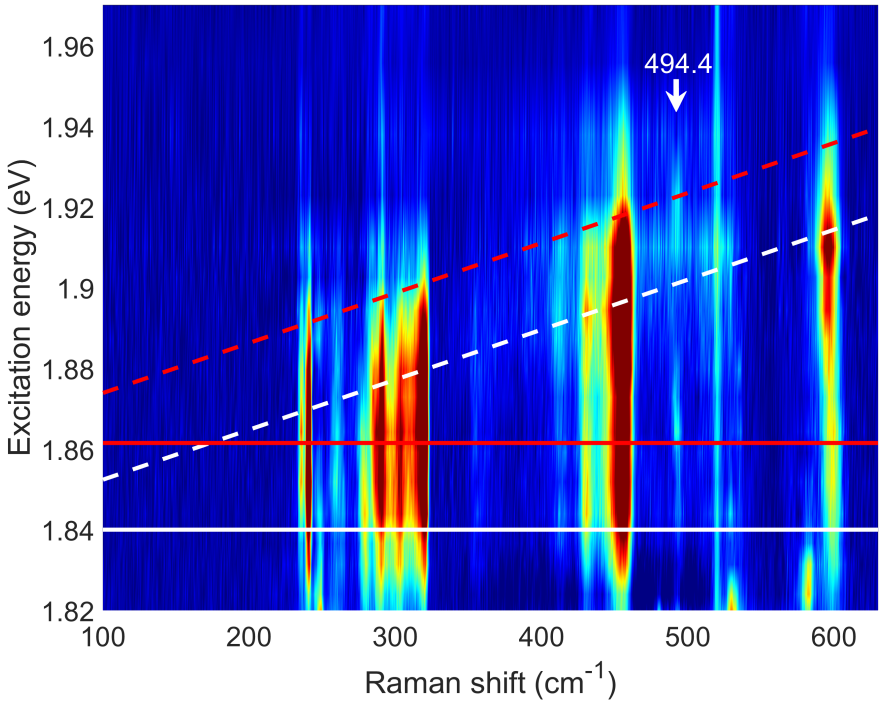

FIGURE 4.32: A colour-map of the resonance Raman spectra of the hBN encapsulated 57° twist $MoSe_2/WSe_2$ heterostructure sample for an energy range from 1.82 - 1.97 eV. The intensity of the Raman scattering is indicated by the colour, with dark blue showing minimum intensity and red corresponding to maximum. The colour scale is logarithmic, which aids examination of the less intense Raman peaks. The white lines indicate the energies of associated with the $MoSe_2$ B1s exciton, with the solid and dashed lines corresponding to the incoming and outgoing resonances respectively. The WSe_2 A2s energies are marked similarly in red.

The profile was fitted to a single state Raman scattering model with a linear background added. Whilst the asymmetry and noisy data impact the quality of the fit, the presence of two resonance peaks in the profile separated by the phonon energy clearly indicates the presence of an excitonic state. The shift of the Raman peak matches that of a peak associated with the WSe_2 A2s in monolayer and so the excitonic state is assigned as the WSe_2 A2s. The fit yields an energy of 1.862 ± 0.003 eV which falls 124 meV above the WSe_2 A1s. This is 7 meV less than the 131 meV of the monolayer WSe_2 case. This small reduction in A1s-A2s splitting is expected from the reduction in exciton binding energy in the heterostructure, and is discussed in more detail in section 4.3. The fitted amplitude is 1.1 ± 0.5 $\times 10^{-15}$ eV^4, which is ≈ two orders of magnitude less than the A1s in this sample. The same is also true for the monolayer case, which strengthens the assignment of this excitonic state to the WSe_2 A2s.

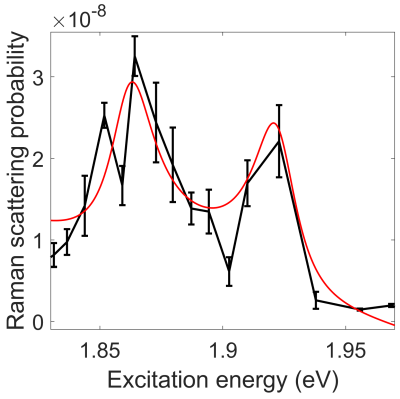

FIGURE 4.33: Resonance Raman profile of the WSe_2 A2s associated Raman peak observed in the the 57° twist $MoSe_2/WSe_2$. The fit to a single state resonance model is shown in red. The error bars on the data points are standard deviations of the amplitudes of the peaks determined by the spectra fitting process.

4.2.4.5 57° Twist Heterostructure $MoSe_2$ B2s

Above the $MoSe_2$ B1s, the B2s is also observed in this heterostructure. A colour-map of the resonance Raman spectra shown in Figure 4.34, with the tails of the lower energy B1s resonance are present at the lowest energies at the bottom of the figure. Towards higher energy, the tails of the WSe_2 B1s are also observed. At 520 cm^{-1}, the Si Raman peak is clearly observed across the whole energy range shown. The more intense two of the three $MoSe_2$ 2s associated Raman peaks marked with arrows showing their fitted Raman shift in cm^{-1}. Some Raman signal around 480 cm^{-1} is present but it is much less intense than that from the two marked peaks, being very difficult to distinguish from noise. Similarly to the monolayer case, the intensity of these peaks drops off more rapidly towards higher energy than towards lower energy.

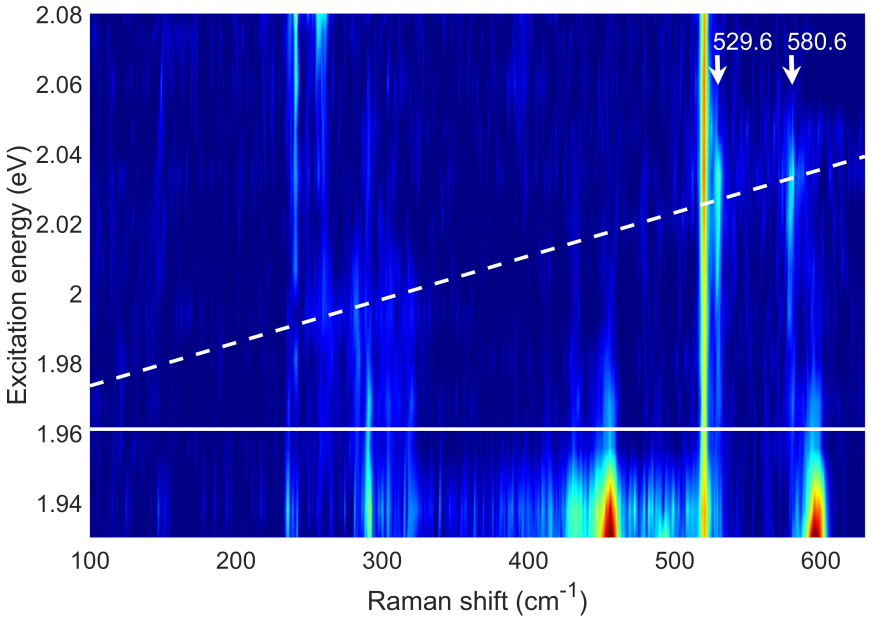

FIGURE 4.34: A colour-map of the resonance Raman spectra of the hBN encapsulated 57° twist $MoSe_2/WSe_2$ heterostructure sample for an energy range from 1.93 - 2.08 eV. The intensity of the Raman scattering is indicated by the colour, with dark blue showing minimum intensity and red corresponding to maximum. The colour scale is logarithmic, which aids examination of the less intense Raman peaks. The white lines indicate the energies of associated with the $MoSe_2$ B2s exciton, with the solid and dashed lines corresponding to the incoming and outgoing resonances respectively.

The resonance profiles for these peaks are shown in Figure 4.35. The profiles were fitted to Lorentzian lineshapes with a linear background added to capture the signal present below the peak of the resonance. The coefficients for these fits are given in Table 4.9. A mean value of 18 meV was found for the widths for this excitonic state and, similarly to the monolayer case, the width of the B2s is narrower than the B1s. The mean value of the two energies falls within the errors of both values, at 1.956 ± 0.003 eV. This gives a B1s-B2s separation of 117 ± 4 meV which is significantly smaller than the 158 ± 2 meV for the monolayer case. This is expected from the drop in exciton binding energy when going from monolayer to a heterostructure due to the additional screening of the exciton by charges in the other layer.

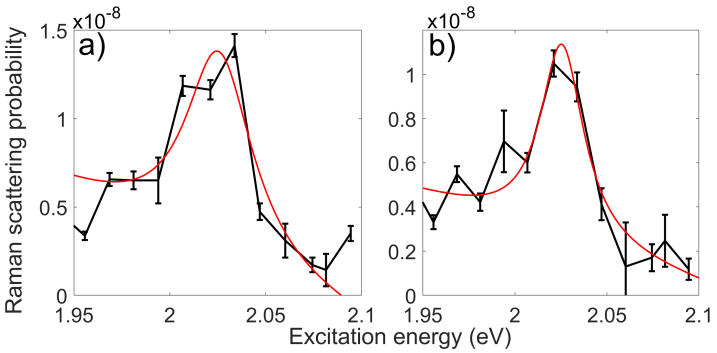

FIGURE 4.35: Resonance Raman profiles of the 2s associated Raman peaks observed in the the 57° twist $MoSe_2/WSe_2$ heterostructure sample across the $MoSe_2$ B2s exciton energy range. Resonance profile of the a) 479.8 cm^{-1} peak. b) 529.6 cm^{-1} peak. c) 580.6 cm^{-1} peak. The fits to a Lorentzian peak are shown in red for each case. The error bars on the data points are standard deviations of the amplitudes of the peaks determined by the spectra fitting process.

Raman shift (cm^{-1})	Energy (eV)	Width (meV)
529.6	1.959 ± 0.005	22 ± 12
580.6	1.953 ± 0.003	14 ± 6

TABLE 4.9: Coefficients for fitting resonance Raman profiles of the $MoSe_2$ 2s Raman peaks to Lorentzians at the $MoSe_2$ B2s outgoing resonance, presented in Figure 4.35 for the 57° twist $MoSe_2/WSe_2$ heterostructure sample.

4.2.4.6 57° Twist Heterostructure WSe_2 B1s

Figure 4.36 shows the highest energy range measured for this sample of 2.05 - 2.26 eV. Whilst only the WSe_2 B1s exciton was observed in the monolayer case, this heterostructure presented more interesting behaviour. The Raman peaks which were observed in the WSe_2 monolayer at this energy range are also observed here. The $A_1'(\Gamma)/E'(\Gamma)$ phonon peak was the most intense, at present at 249.1 cm^{-1} with the adjacent broader feature at 256.6 cm^{-1}. The 396.4 cm^{-1} peak is also observed in this heterostructure with similar resonance behaviour. The regions of highest intensity for these peaks all fall within the white lines marking the incoming (solid) and outgoing (dashed) resonance of the WSe_2 B1s exciton. In addition to these, four more peaks were observed which were not present in the monolayer case and also show distinctly different resonance behaviour to the WSe_2 peaks. These had Raman shifts of 240.5, 291.0, 309.2 and 353.7 cm^{-1}. The first of these has a frequency suggestive of the $MoSe_2$ $A_1'(\Gamma)$ phonon peak.

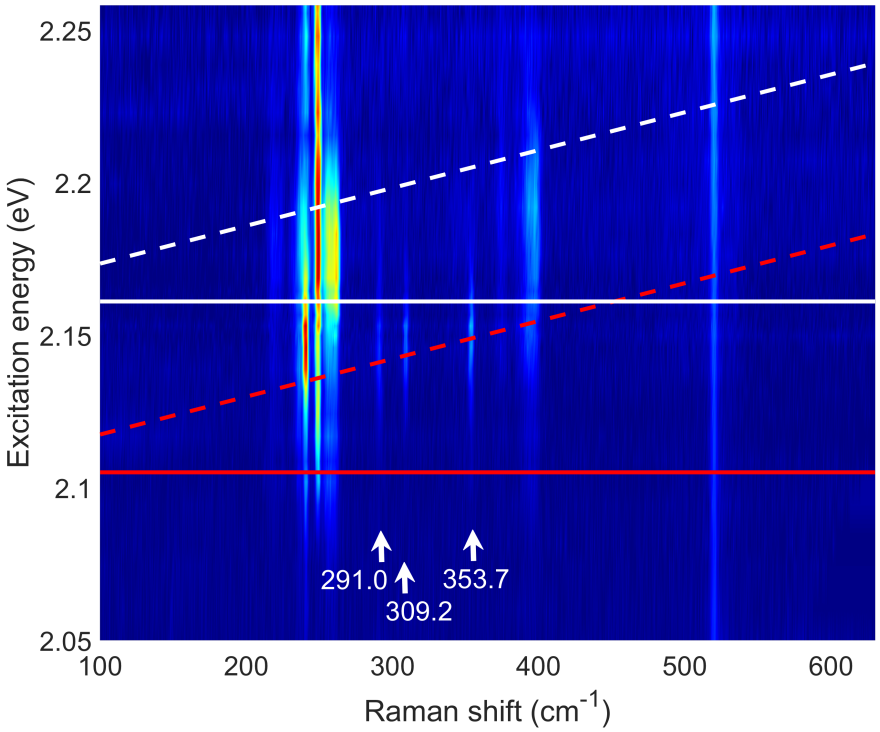

FIGURE 4.36: A colour-map of the resonance Raman spectra of the hBN encapsulated 57° twist $MoSe_2/WSe_2$ heterostructure sample for an energy range from 2.05 - 2.26 eV. The intensity of the Raman scattering is indicated by the colour, with dark blue showing minimum intensity and red corresponding to maximum. The colour scale is logarithmic, which aids examination of the less intense Raman peaks. The white lines indicate the energies of associated with the WSe_2 B1s exciton, with the solid and dashed lines corresponding to the incoming and outgoing resonances respectively.

The resonance profiles of these peaks are presented in Figure 4.37, where b) and f) are profiles of the peaks also observed in monolayer WSe_2. Two state scattering models were fitted to the profiles and these all matched the data closely. The parameters from these fits are given in Table 4.10. The fitted energies for the two states show two distinct values, with 5/6 of the energies agreeing with the mean values of 2.110 and 2.165 eV to within the errors on the fits in both cases. These two states come from hybridisation [16, 86, 97] between the WSe_2 B1s and a bright interlayer exciton with an electron in the lower WSe_2 conduction band and a hole in the upper $MoSe_2$ valence band. This is discussed in more detail alongside theoretical models of these hybrid excitonic states in our paper [98].

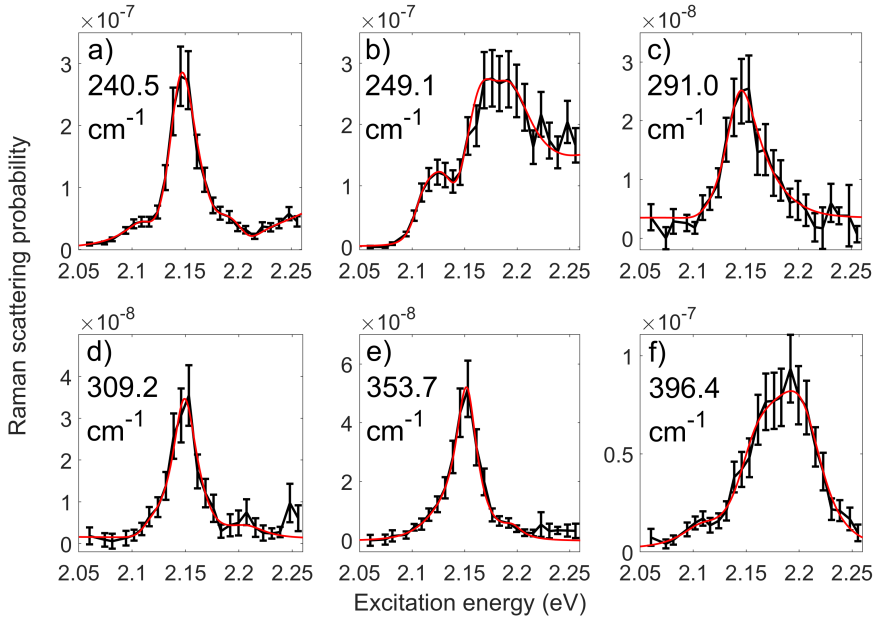

FIGURE 4.37: Resonance Raman profiles of the WSe_2 Raman peaks observed in the the 57° twist $MoSe_2/WSe_2$ heterostructure with Raman shifts of a) 240.5 b) 249.1 c) 291.0 d) 309.2 e) 353.7 and f) 396.4 cm^{-1}. The fits to two state resonance models is shown in red. An additional background signal was added to the fits shown in a) and b) to account for the increasing signal at the highest energy side of the profiles. The error bars on the data points are standard deviations of the amplitudes of the peaks determined by the spectra fitting process.

Shift (cm^{-1})	A_{IX^*} ($10^{-15}\ eV^4$)	A_{B1s} ($10^{-15}\ eV^4$)	A_{I-S} ($10^{-15}\ eV^4$)	Γ_{IX^*} (meV)	Γ_{B1s} (meV)	E_{IX^*} (eV)	E_{B1s} (eV)
240.5	772 ± 81	41 ± 2	152 ± 14	17 ± 2	17 ± 12	2.115 ± 0.003	2.178 ± 0.013
249.1	271 ± 22	61.8 ± 9.6	11.1 ± 2.7	15 ± 10	24 ± 14	2.105 ± 0.016	2.161 ± 0.007
291	3 ± 4	0.3 ± 0.6	11.3 ± 9.9	19 ± 8	39 ± 13	2.106 ± 0.009	2.168 ± 0.012
309.2	8.3 ± 50	5.4 ± 5.8	28.4 ± 11.8	14 ± 3	24 ± 13	2.110 ± 0.003	2.172 ± 0.012
353.7	94 ± 11	5.7 ± 2.7	31 ± 10	33 ± 16	12 ± 2	2.118 ± 0.009	2.152 ± 0.012
396.4	6.1 ± 4.8	175 ± 10	1.7 ± 04.6	25 ± 12	30 ± 3	2.107 ± 0.008	2.160 ± 0.001

TABLE 4.10: Coefficients for fitting the two state scattering model to the resonance Raman profiles of the Raman peaks in Figure 4.37. Here, A is the scattering amplitude for each scattering channel, where A_{I-S} corresponds to interstate scattering. IX^* is the inter-layer exciton and $B1s$ is the WSe_2 B1s exciton. Γ is the width of the state and E is the energy of the state.

For this 57° heterostructure sample, the $MoSe_2$ A1s, A2s, B1s and B2s excitons have been identified and their energies measured by resonance Raman. The WSe_2 A1s, A2s and B1s excitons were also observed in the same way. A WSe_2 A1s positively charged trion was also observed just below the A1s exciton. A pair of hybridised excitonic states were observed at the WSe_2 B1s exciton involving the WSe_2 B1s intralayer exciton and

a dark interlayer exciton. Further analysis of the energies of the excitonic states is given after examining the second heterostructure.

4.2.4.7 20° Twist Heterostructure $MoSe_2$ A1s

Moving on to the hBN encapsulated 20 degree heterostructure sample, resonance Raman measurements were performed over the same energy range as the previous samples. The lowest energy feature observed in this sample is associated with the $MoSe_2$ A1s. Figure 4.38 shows a colour-map of the resonance Raman spectra taken with excitation energies covering this exciton. The top of the figure the WSe_2 A1s is present, marked in red. The white and black lines mark the resonance energies associated with the $MoSe_2$ A1s exciton (black) and A1s trion (white). The Raman peaks observed here are the same as those observed in the $MoSe_2$ monolayer. However, the resonance behaviour here is distinctly different. Additional Raman signal is present at the outgoing resonance that is absent in the HS57 and monolayer cases. This is true of all of the Raman peaks but is most clearly identifiable for the multi-phonon peaks which have Raman shifts greater than 250 cm^{-1}.

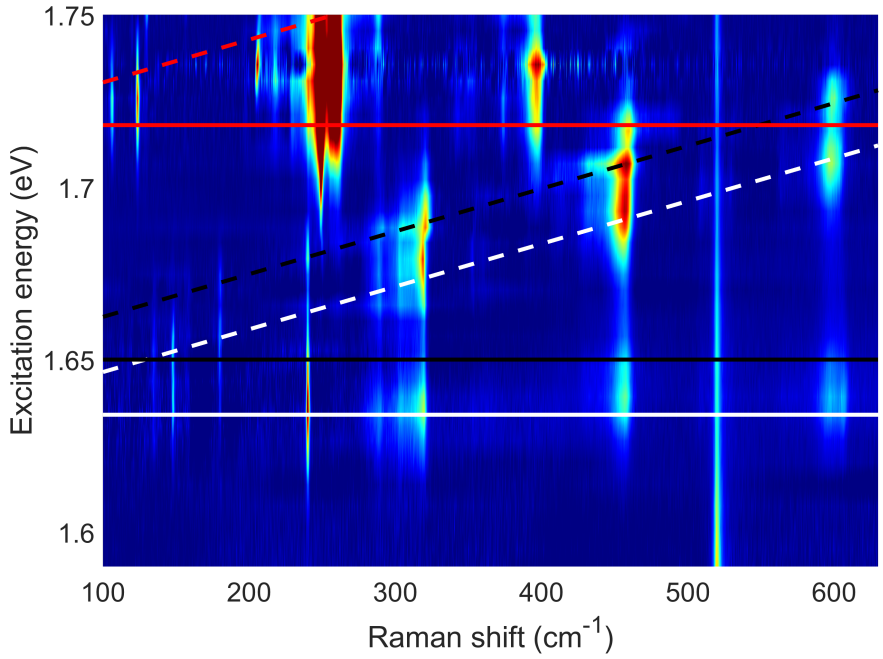

FIGURE 4.38: A colour-map of the resonance Raman spectra of the hBN encapsulated 20° twist $MoSe_2/WSe_2$ heterostructure sample for an energy range from 1.59 - 1.75 eV. The intensity of the Raman scattering is indicated by the colour, with dark blue showing minimum intensity and red corresponding to maximum. The colour scale is logarithmic, which aids examination of the less intense Raman peaks. The white lines indicate the energies of associated with the $MoSe_2$ A1s trion, with the solid and dashed lines corresponding to the incoming and outgoing resonances respectively. The black lines correspond to the $MoSe_2$ A1s exciton and the red corresponds to the WSe_2 A1s exciton.

Resonance Raman profiles for the Raman peaks with shifts of 147.7, 240.4, 319.6 and 456.3 cm^{-1} are presented in Figure 4.39. All of these resonance profiles show significant asymmetry which cannot be explained by a single state resonance fit. The fits shown in red are all two-state scattering models and they generally fit the data well, with the most significant deviation from the data present for the 240.4 cm^{-1} $A_1'(\Gamma)$ phonon mode presented in b). The measured resonance Raman signal increases above the fitted model from 1.7 eV towards higher energy. This increase is a result of the tail end of the intense Raman scattering from the WSe_2 A2s resonance which is picked up while fitting the Raman spectra. As this signal is not from the $MoSe_2$ phonon, the deviation of the resonance profile from the fit above 1.7 eV can be ignored. The energies and widths from these two state fits are shown in Table 4.11. The fits yielded energies which clustered around two distinct mean energies of 1.634 and 1.652 eV, with all of the energies falling within twice the errors from the fit. The fitted widths were similarly close to their mean values of 9.0 and 9.3 meV. The most obvious assignment for these two energies is the lower energy as the trion and the higher energy as the A1s exciton. The separation between these energies of 18 meV is smaller than the value of 24 - 28 meV reported for trions or exciton-polarons in gated measurements of hBN encapsulated monolayer $MoSe_2$ in literature [82, 142, 192–194, 200]. However this is expected as the exciton binding energy is reduced in heterostructures compared to monolayers, due to increased screening form charges in the additional layer, and it is also likely that the trion binding energy is similarly reduced. The fact that the trion is observed at this resonance in this heterostructure sample is suggestive of some doping or charge transfer between the two layers. The fact that a feature is observed in the reflectivity spectrum at the trion energy for this sample as shown in Figure 4.7 also suggests the same.

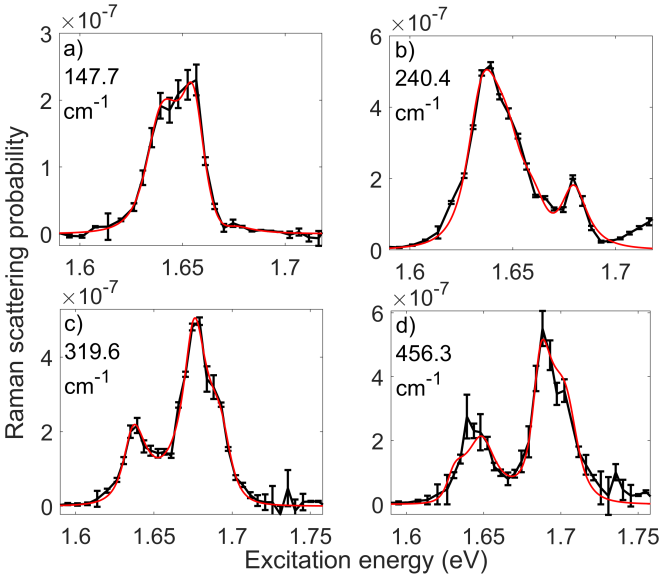

FIGURE 4.39: Resonance Raman profiles of the $MoSe_2$ Raman peaks observed in the the 20° twist $MoSe_2/WSe_2$ heterostrucutre with Raman shifts of a) 147.7 b) 240.4 c) 319.6 and d) 456.3 cm^{-1}. The fits to two state resonance models are shown in red. The error bars on the data points are standard deviations of the amplitudes of the peaks determined by the spectra fitting process.

Raman Shift (cm^{-1})	E_1 (eV)	E_2 (eV)	Γ_1 (meV)	Γ_2 (meV)
147.7	1.637 ± 0.005	1.654 ± 0.009	10 ± 3	8 ± 14
240.4	1.633 ± 0.008	1.650 ± 0.018	10 ± 14	8 ± 21
319.6	1.636 ± 0.002	1.655 ± 0.002	9 ± 1	10 ± 2
456.3	1.629 ± 0.003	1.649 ± 0.003	7 ± 2	11 ± 5

TABLE 4.11: Coefficients for fitting the two state scattering model to the resonance Raman profiles of the Raman peaks in Figure 4.39. Γ is the width of the state and E is the energy of the state.

4.2.4.8 20° Twist Heterostructure WSe_2 A1s

Above the $MoSe_2$ A1s, the WSe_2 A1s exciton is observed. The colour-map of resonance Raman spectra presented in Figure 4.40 shows this with the associated resonance energies marked in red. Similarly to the monolayer WSe_2 case, the only Raman peak which did not show resonance behaviour following the expected resonance energies was the dispersive mode which falls between 205.3 and 207.6 cm^{-1}. This dispersion and different resonance behaviour is suggestive of multi-phonon scattering via dark intermediate excitonic states which requires exciton dispersion relations to model [139].

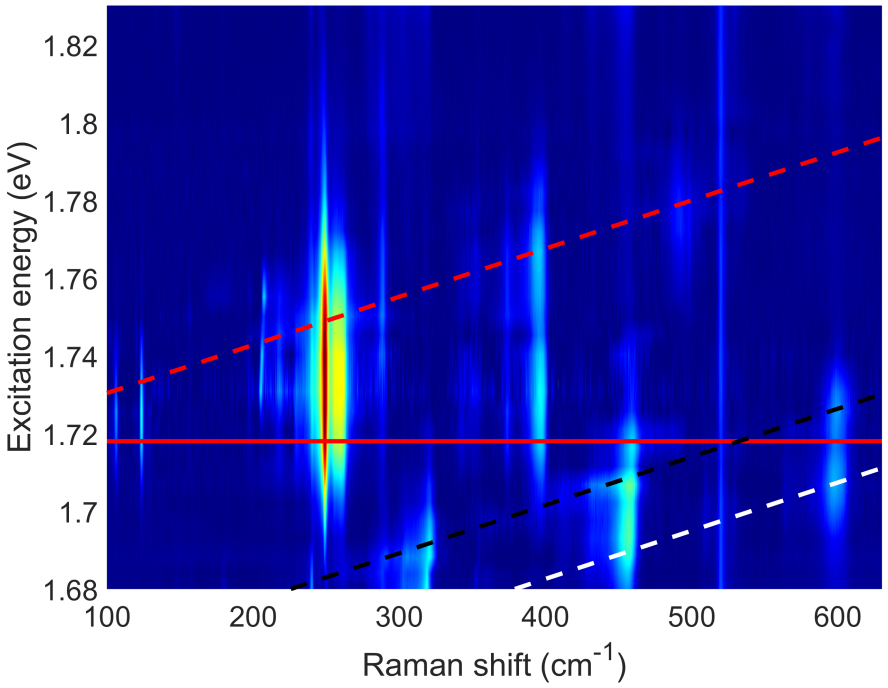

FIGURE 4.40: A colour-map of the resonance Raman spectra of the hBN encapsulated 20° twist $MoSe_2/WSe_2$ heterostructure sample for an energy range from 1.68 - 1.83 eV. The intensity of the Raman scattering is indicated by the colour, with dark blue showing minimum intensity and red corresponding to maximum. The colour scale is logarithmic, which aids examination of the less intense Raman peaks. The red lines indicate the energies of associated with the WSe_2 A1s exciton, with the solid and dashed lines corresponding to the incoming and outgoing resonances respectively. The black and white lines at the lowest energy range shown are from the $MoSe_2$ A1s exciton and trion respectively.

The resonance profile of the 249.0 cm^{-1} $A_1'(\Gamma)/E'(\Gamma)$ phonon Raman peak was fitted to a single state resonance Raman model as shown in Figure 4.41. The model fits the data well, the most apparent deviation around 1.76 eV resulting from only a single data point. This fit gives an amplitude of 276 ± 87 $\times 10^{-15}$ eV^4 with an energy of 1.718 ± 0.002 eV and width of 10.8 ± 0.9 meV for the WSe_2 A1s exciton in this sample. This is broader and lower in energy than the WSe_2 monolayer, which is also true for the 57° heterostructure sample. The increased linewidth is likely a result of reduced lifetime due to the presence of lower energy states in the other layer in the heterostructure as well as additional defects creating lower energy bound states to scatter to.

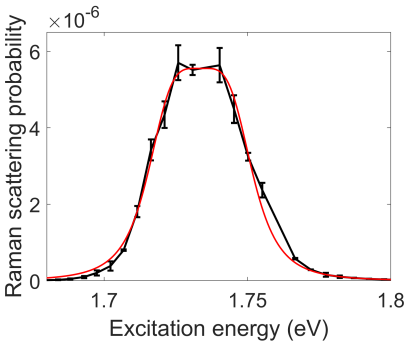

FIGURE 4.41: Resonance Raman profile of the WSe_2 $A_1'(\Gamma)/E'(\Gamma)$ phonon Raman peak observed in the the 20° twist $MoSe_2/WSe_2$ heterostructure at 249.0 cm^{-1}. The fit to a single state resonance models are shown in red. The error bars on the data points are standard deviations of the amplitudes of the peaks determined by the spectra fitting process.

4.2.4.9 20° Twist Heterostructure $MoSe_2$ A2s

Falling between the WSe_2 A1s and $MoSe_2$ B1s, the $MoSe_2$ A2s exciton is observed via the trio of 2s associated $MoSe_2$ Raman peaks. These were observed at the A2s outgoing resonance energy marked with a red dashed line in Figure 4.42. As in the monolayer and HS57 cases, the lowest Raman shift of the three peaks (479.7 cm^{-1}) exhibited by far the least intense Raman scattering. The second at 530.0 cm^{-1} is the clearest of the three, with the peak at 581.8 cm^{-1} overlapping with a peak associated with the higher energy $MoSe_2$ B1s marked with white lines at the top of the plot. The other features in the colour-map at lower energies are from the WSe_2 A1s outgoing resonance. Resonance profiles for these three peaks were extracted and fit to Lorentzian peaks with a linear background added as shown in Figure 4.43. The profile of the lowest energy peak, shown in panel a), was very noisy. However, the two higher shift peak profiles were generally well fit. These fits yielded energies and widths for the $MoSe_2$ A2s exciton given in Table 4.12. The fitted energy increased with the Raman shift of the peak. This is most likely a result of the influence of the B1s exciton on the resonance behaviour. As the A2s outgoing resonance becomes closer to the B1s incoming, the energy is shifted more towards the B2s as a result of double resonance. A two-state model could not be fitted to the data to quantify this as the data was too noisy. The Lorentzian fits resulted in a mean energy of 1.765 ± 0.005 eV with a width of 13 ± 1 meV for this state. Following the outgoing resonance energy for this state once again, with the red dashed line, in Figure 4.42, some enhancement of the peaks at 240 cm^{-1} and 288 cm^{-1} is also observed at this resonance, confirming the assigned energy.

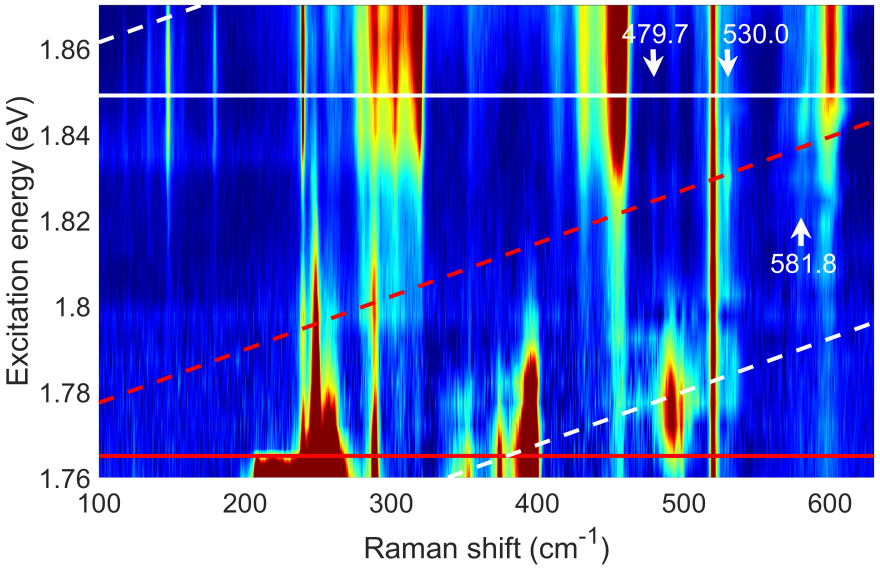

FIGURE 4.42: A colour-map of the resonance Raman spectra of the hBN encapsulated 20° twist $MoSe_2/WSe_2$ heterostructure sample for an energy range from 1.76 - 1.87 eV. The intensity of the Raman scattering is indicated by the colour, with dark blue showing minimum intensity and red corresponding to maximum. The colour scale is logarithmic, which aids examination of the less intense Raman peaks. The red lines indicate the energies of associated with the $MoSe_2$ A2s exciton, with the solid and dashed lines corresponding to the incoming and outgoing resonances respectively. The white lines are from the $MoSe_2$ B1s exciton at the higher energies and WSe_2 A1s at the bottom of the plot.

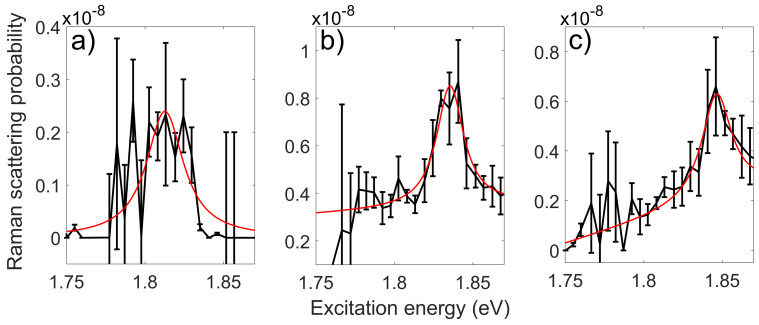

FIGURE 4.43: Resonance Raman profile of the $MoSe_2$ 2s associated phonon Raman peaks observed in the the 20° twist $MoSe_2/WSe_2$ heterostructure at the A2s. The fits to Lorentzian peaks at the outgoing resonance are shown in red. The error bars on the data points are standard deviations of the amplitudes of the peaks determined by the spectra fitting process.

Raman shift (cm^{-1})	Energy (eV)	Width (meV)
479.7	1.754 ± 0.003	12 ± 2
530.0	1.765 ± 0.004	17 ± 3
581.8	1.774 ± 0.001	11 ± 2

TABLE 4.12: Coefficients for fitting resonance Raman profiles of the $MoSe_2$ 2s Raman peaks to Lorentzians at the $MoSe_2$ A2s outgoing resonance, presented in Figure 4.43 for the 20° twist $MoSe_2/WSe_2$ heterostructure sample.

4.2.4.10 20° Twist Heterostructure $MoSe_2$ B1s

Above the $MoSe_2$ A2s, the stronger B1s state, marked here in white, is present as shown in the resonance Raman colour-map in Figure 4.44. This state shows similar behaviour in this heterostructure sample to both HS57 and the monolayer $MoSe_2$ sample. The resonance profile of the $A_1'(\Gamma)$ phonon peak at 239.3 cm^{-1} was fit to a single state resonance model as shown in Figure 4.45. The fit yielded an energy and width of the B1s of 1.849 ± 0.001 eV and 31 ± 2 meV respectively. The fitted amplitude was 30 ± 16 $\times 10^{-15}$ eV^4 which for this sample gives a ratio of B1s/A1s amplitude of 3 ± 2 which overlaps with the errors of the value for the monolayer (5 ± 1) and HS57 (6 ± 1).

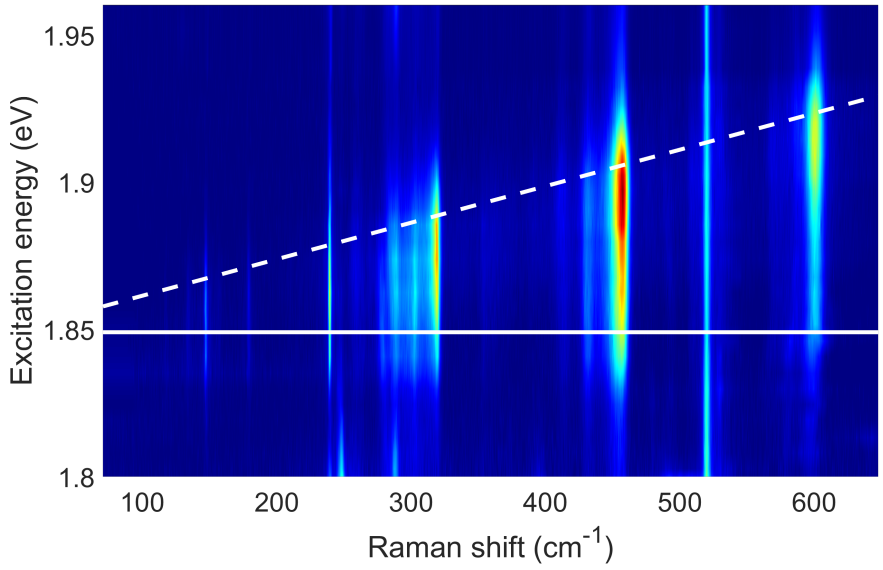

FIGURE 4.44: A colour-map of the resonance Raman spectra of the hBN encapsulated 20° twist $MoSe_2/WSe_2$ heterostructure sample for an energy range from 1.80 - 1.96 eV. The intensity of the Raman scattering is indicated by the colour, with dark blue showing minimum intensity and red corresponding to maximum. The colour scale is logarithmic, which aids examination of the less intense Raman peaks. The white lines indicate the energies of associated with the $MoSe_2$ B1s exciton, with the solid and dashed lines corresponding to the incoming and outgoing resonances respectively.

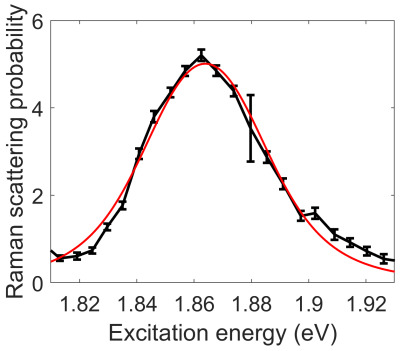

FIGURE 4.45: Resonance Raman profile of the $MoSe_2$ 239.3 cm^{-1} $A_1'(\Gamma)$ Raman peak observed in the the 20° twist $MoSe_2/WSe_2$ heterostructure. The fit to a single state resonance model is shown in red. The error bars on the data points are standard deviations of the amplitudes of the peaks determined by the spectra fitting process.

4.2.4.11 20° Twist Heterostructure WSe_2 A2s

Just below the energy of the $MoSe_2$ B1s, the much weaker WSe_2 A2s was also observed in this 20° twist sample. Figure 4.46 shows a colour-map of the resonance Raman data covering this state, with the white lines indicating the more intense $MoSe_2$ B1s. Here, as in the HS57 case, the WSe_2 2s associated peak around 494.1 cm^{-1} is present. Also similarly to the other heterostructure, no clear signal of the WSe_2 $A_1'(\Gamma)/E'(\Gamma)$ Raman peak near 250 cm^{-1} was observed. The resonance profile of the 2s associated peak is shown in Figure 4.47, fitted to a single state resonance model. This gave an energy of 1.835 ± 0.004 eV and a width of 39 ± 14 meV for the WSe_2 A2s exciton. This corresponds to an A1s-A2s separation of 117 ± 4 meV which, like the HS57 case, is smaller than the WSe_2 monolayer value of 131 ± 1 meV. This reduction in A1s-A2s splitting results from the reduced exciton binding energy in the heterostructure, and is discussed further in section 4.3.

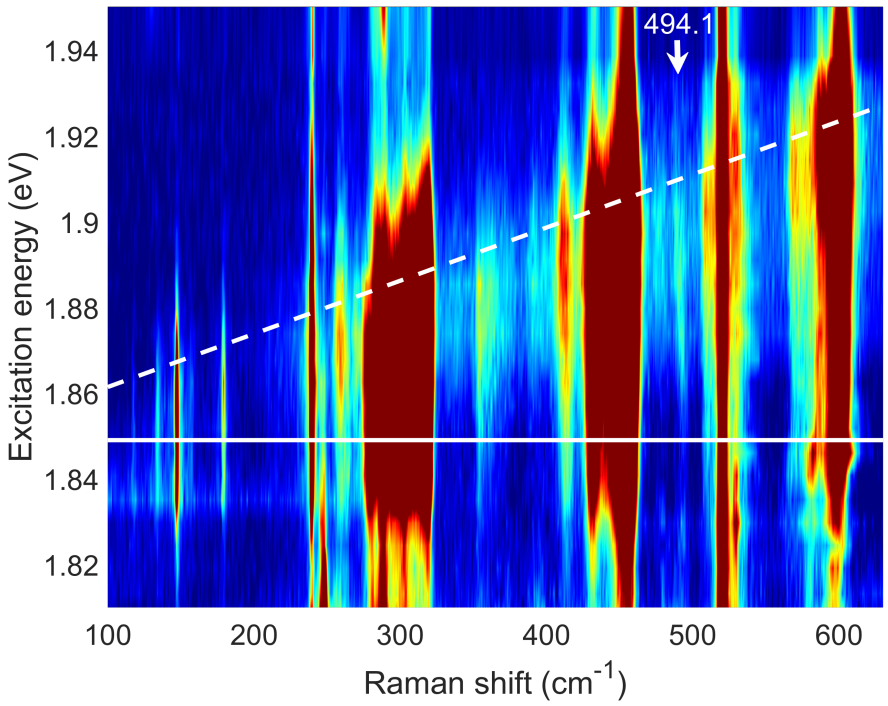

FIGURE 4.46: A colour-map of the resonance Raman spectra of the hBN encapsulated 20° twist $MoSe_2/WSe_2$ heterostructure sample for an energy range from 1.81 - 1.95 eV. The intensity of the Raman scattering is indicated by the colour, with dark blue showing minimum intensity and red corresponding to maximum. The colour scale is logarithmic, which aids examination of the less intense Raman peaks. The white lines indicate the energies associated with the $MoSe_2$ B1s exciton, with the solid and dashed lines corresponding to the incoming and outgoing resonances respectively.

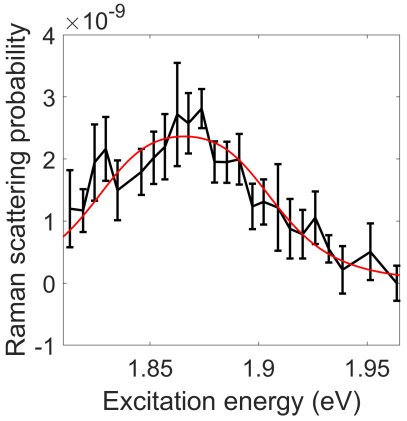

FIGURE 4.47: Resonance Raman profile of the WSe_2 A2s associated phonon Raman peak observed in the the 20° twist $MoSe_2/WSe_2$ heterostructure at 494.1 cm^{-1}. The fit to a single state resonance models are shown in red. The error bars on the data points are standard deviations of the amplitudes of the peaks determined by the spectra fitting process.

4.2.4.12 20° Twist Heterostructure $MoSe_2$ B2s

A colour-map of the resonance Raman data across the $MoSe_2$ B2s exciton energy range is presented in Figure 4.48. As in the monolayer case, the (240.0 cm^{-1}) $MoSe_2$ $A_1'(\Gamma)$ phonon is present as well as an intense peak at 289.4 cm^{-1} and the three 2s associated Raman peaks at 479.7, 529.6 and 581.6 cm^{-1}. These are the same peaks that were observed in the monolayer $MoSe_2$ B2s case. The 240.0 cm^{-1} appears to show more signal towards higher energy than the 289.4 cm^{-1} peak. However, much of this signal is from the lower energy tail of a the resonance of a peak at the same Raman shift at the WSe_2 B1s exciton energy. Similar signal is not present at the frequencies of the other 4 peaks. A dispersive peak was observed adjacent to the 581.6 cm^{-1} peak which shifted toward higher frequency with increasing excitation energy. Resonance profiles of these peaks are presented in Figure 4.49. A single state resonance model was used to fit the 289.4 cm^{-1} peak in panel a). Other than the additional signal at the lower energy side of the resonance profile from the tail of the $MoSe_2$ B1s exciton, the profile does not show any asymmetry. The three 2s associated peak profiles are too narrow to be fit well by a single state resonance model and, like the $MoSe_2$ A2s case, only the outgoing resonance is intense enough to be observed. Therefore the profiles of these Raman peaks, shown in Figure 4.49b)-d), were fitted to a Lorentzian peak to extract energies for the outgoing resonance. The photon energy was subtracted to give values for the exciton energy which are presented in Table 4.13. This results in a mean energy of 1.974 ± 0.008 eV for the B2s exciton in this heterostructure, which gives a spacing between the B1s - B2s excitonic states of 125 ± 5 meV which similarly to the 57 degree twist heterostructure is smaller than the monolayer value of 158 ± 2 meV.

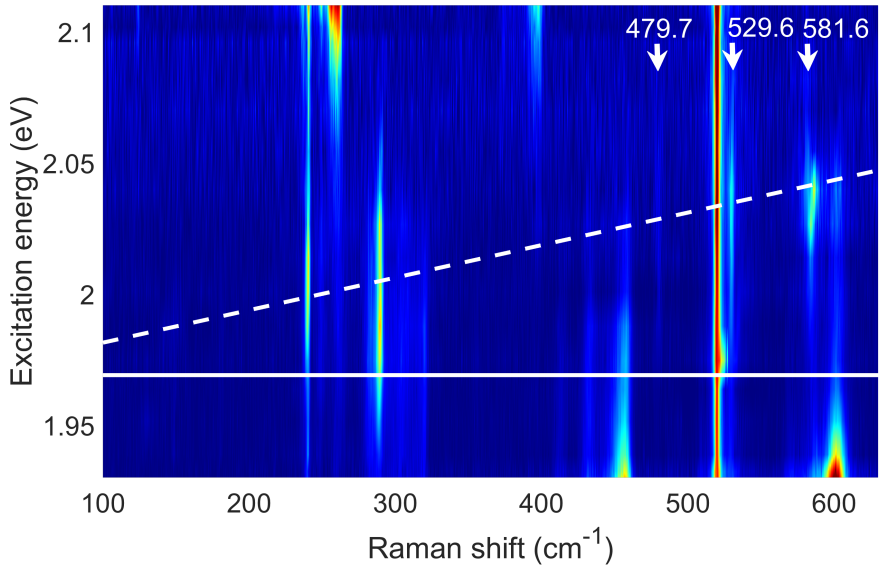

FIGURE 4.48: A colour-map of the resonance Raman spectra of the hBN encapsulated 20° twist $MoSe_2/WSe_2$ heterostructure sample for an energy range from 1.93 - 2.11 eV. The intensity of the Raman scattering is indicated by the colour, with dark blue showing minimum intensity and red corresponding to maximum. The colour scale is logarithmic, which aids examination of the less intense Raman peaks. The white lines indicate the energies of associated with the $MoSe_2$ B2s exciton, with the solid and dashed lines corresponding to the incoming and outgoing resonances respectively.

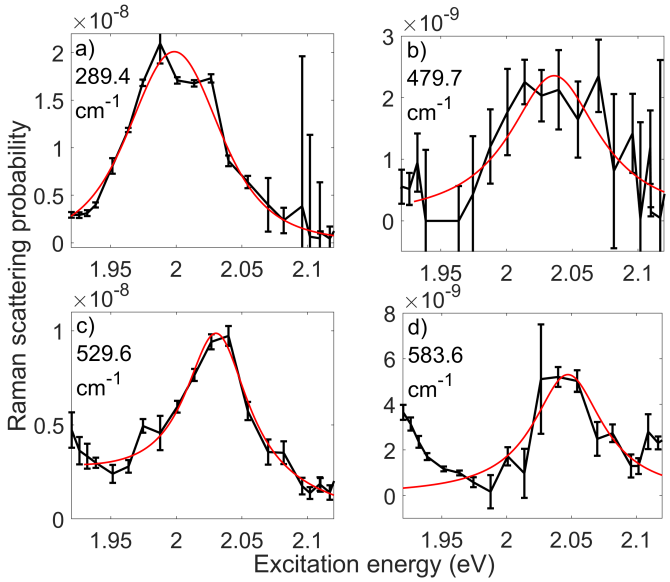

FIGURE 4.49: Resonance Raman profiles of peaks observed in the the 20° twist $MoSe_2/WSe_2$ heterostructure sample across the $MoSe_2$ B2s exciton energy range with a shift of a) 289.4, b) 479.7, c) 529.6 and d) 581.6 cm^{-1}. The profile in a) was fitted to a single state resonance Raman scattering model. The profiles in b)-d) were fitted to a Lorentzian peak, shown in red for the each case. The error bars on the data points are standard deviations of the amplitudes of the peaks determined by the spectra fitting process.

Raman shift (cm^{-1})	Energy (eV)	Width (meV)
289.4	1.981 ± 0.003	55 ± 5
479.7	1.976 ± 0.006	42 ± 10
529.6	1.965 ± 0.002	29 ± 4
581.6	1.975 ± 0.005	32 ± 17

TABLE 4.13: Coefficients for fitting resonance Raman profiles of the $MoSe_2$ Raman peaks at the B2s outgoing resonance, presented in Figure 4.49 for the 20° twist $MoSe_2/WSe_2$ heterostructure sample.

4.2.4.13 20° Twist Heterostructure WSe_2 B1s

The highest energy excitonic state measured via resonance Raman in this heterostructure was the WSe_2 B1s. A colour-map of the resonance Raman data across this state is given in Figure 4.50. Unlike the 57° sample, for which an additional hybridised state was observed, the behaviour of this sample follows that of the WSe_2 monolayer. The only exception to this is the additional peaks observed at 106.4 and 124.0 cm^{-1}. These are be assigned to the $TA(K)$ and $ZA(K)$ K point acoustic phonons using monolayer phonon dispersion relations from literature [113]. These peaks are allowed only in the presence of defects in the crystal lattice which remove the momentum conservation constraint which prevents observation samples with few defects.

The WSe_2 $A_1'(\Gamma)/E'(\Gamma)$ Raman peak is the most intense feature observed at this resonance. It falls at a Raman shift of 249.2 cm^{-1}. The resonance profile of the peak is shown in Figure 4.51. The scattering from this peak does not go to zero at the highest energy range. This is most likely a result of the higher energy C exciton, for which strong resonance Raman signal has been reported to in monolayer WSe_2 in literature [137]. A two state resonance model was used to fit this profile with the additional state accounting for the background added with a fixed energy of 2.3 eV and width of 50 meV. The fitted curve matches the data very well, with the curve still falling within the uncertainties on the two data points at the top of the peak which deviate most. This fit gives an energy 2.164 ± 0.001 eV and a width of 28.8 ± 11 meV for the WSe_2 B1s in this sample.

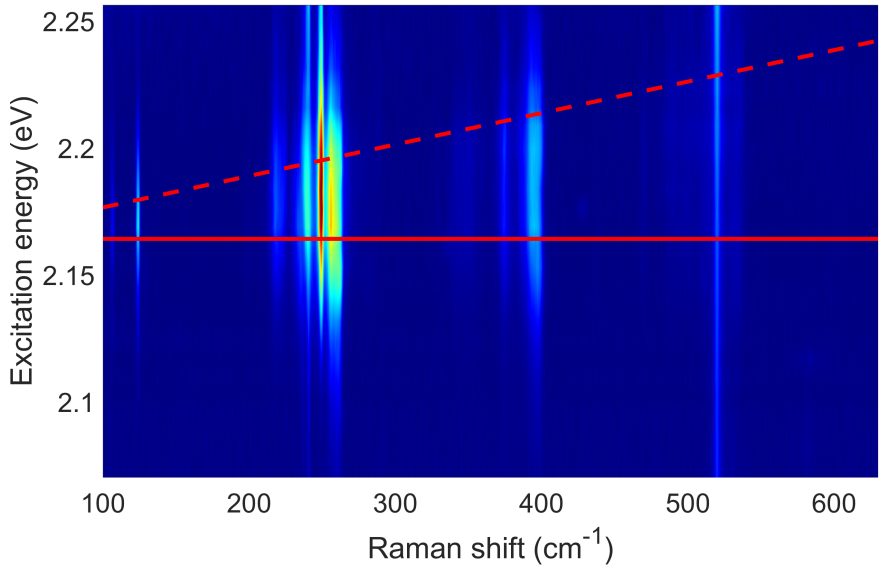

FIGURE 4.50: A colour-map of the resonance Raman spectra of the hBN encapsulated 20° twist $MoSe_2/WSe_2$ heterostructure sample for an energy range from 2.07 - 2.26 eV. The intensity of the Raman scattering is indicated by the colour, with dark blue showing minimum intensity and red corresponding to maximum. The colour scale is logarithmic, which aids examination of the less intense Raman peaks. The red lines indicate the energies of associated with the WSe_2 B1s exciton, with the solid and dashed lines corresponding to the incoming and outgoing resonances respectively.

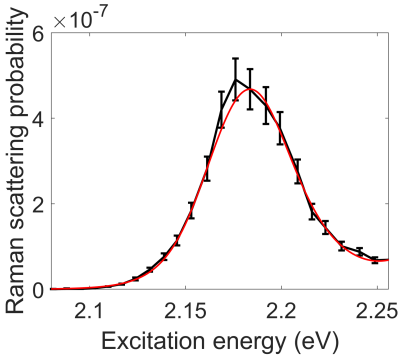

FIGURE 4.51: Resonance Raman profile of the $A_1'(\Gamma)/E'(\Gamma)$ phonon Raman peak observed in the the 20° twist $MoSe_2/WSe_2$ heterostructure at 249.2 cm^{-1} at the B1s exciton resonance. The fit to a single state resonance model are shown in red. The error bars on the data points are standard deviations of the amplitudes of the peaks determined by the spectra fitting process.

4.2.4.14 Summary of Exciton Energies

The energies determined from the resonance Raman measurements for all of the excitons discussed in the previous sections are summarised in Table 4.14. Where trions and excitons were present, only the exciton energy is given. In the 57° heterostructure case, where hybridisation of the WSe_2 B1s was observed, only the lower energy of the two

observed excitonic states is given. This was closer to the energy of the B1s in the other heterostructure and was the state where the WSe_2 associated Raman peaks were more strongly resonant, whereas the higher energy state showed $MoSe_2$ associated peaks and its energy is more associated with the interlayer exciton. Generally, for each of the states, the exciton energies in the heterostructures fell below the corresponding energies in the monolayers. The only exception to this was the $MoSe_2$ A1s in HS20 which shows a small increase. This behaviour is likely a result of the significant charging of this sample which also resulted in observation of scattering with trions in the associated Raman and reflectivity measurements. A drop in exciton energy is suggestive of either a increase in exciton binding energy in the heterostructures or a reduction in the single particle band gap. The exciton binding energy can be estimated by examining the A1s-A2s splitting [180, 201] and it is reduced in the heterostructure case. This means that a significant reduction in the single particle band gap, larger in magnitude than the decrease in exciton binding energy was present. In the next sections, this 1s-2s energy splitting is examined in more detail for the monolayers and heterostructures, and is used to validate theoretical calculations of the exciton binding energies.

		Measured Exciton Energies (eV)		
Material	Exciton	Monolayer	HS57°	HS20°
$MoSe_2$	A1s	1.648 ± 0.001	1.620 ± 0.001	1.652 ± 0.004
$MoSe_2$	A2s	1.800 ± 0.002	1.754 ± 0.001	1.765 ± 0.002
$MoSe_2$	B1s	1.858 ± 0.001	1.839 ± 0.001	1.849 ± 0.001
$MoSe_2$	B2s	2.016 ± 0.001	1.961 ± 0.016	1.971 ± 0.008
WSe_2	A1s	1.740 ± 0.001	1.728 ± 0.002	1.718 ± 0.002
WSe_2	A2s	1.871 ± 0.001	1.857 ± 0.003	1.835 ± 0.004
WSe_2	B1s	2.166 ± 0.001	2.161 ± 0.007	2.164 ± 0.001

TABLE 4.14: Summary table of the exciton energies determined from the resonance Raman profiles.

4.3 Comparison with Theoretically Calculated Exciton Binding Energies

The theoretical calculations of the binding energies of the A, s exciton Rydberg series presented for comparison in this section for the monolayer and heterostructure samples were performed by David A. Ruiz-Tijerina [202]. The key aspects of the model are outlined here and the calculated exciton energy separations are compared with the measured values.

4.3.1 Theoretical Model

For the monolayer case, the layer is modelled as an infinite plane of 0 thickness, with known dielectric polarizability κ_λ which is in-plane only. This layer is in a dielectric environment defined by the encapsulating hBN which is extends infinitely in all directions. In the heterostructure case, an additional infinite plane with known in-plane polarizability is introduced parallel to the first with a separation d. The (intralayer) exciton is modelled as an electron and hole in the same layer separated by an in-plane distance ρ. The excitonic states are the solutions $\psi(\boldsymbol{\rho})$ to the Mott-Wannier Schrödinger equation for an electron-hole system [203]:

$$\left[\frac{\hbar^2}{2\mu^\lambda}{\nabla_{\boldsymbol{\rho}}}^2 + U_\lambda(\rho)\right]\psi(\boldsymbol{\rho}) = E_b\psi(\boldsymbol{\rho}) \tag{4.2}$$

Were $\hbar$ is the reduced Planck constant, $\boldsymbol{\rho} = \mathbf{r}_e - \mathbf{r}_h$ is the relative position vector from the hole to the electron with $\rho \equiv |\boldsymbol{\rho}|$. $\mu^\lambda = m_e^\lambda m_h^\lambda/(m_e^\lambda + m_h^\lambda)$ is the electron-hole reduced mass in material $\lambda = \mathrm{MoSe_2}$ or $\mathrm{WSe_2}$. E_b is the exciton binding energy and $U_\lambda(\rho)$ is the electron-hole interaction potential within the layer for material λ.

In the monolayer case, this takes the form of the Rytova-Keldysh potential [7, 51, 58, 59], which describes the interaction of two point charges in a semiconductor thin film. This uses the assumption that the permittivity of the TMD layer is greater than that of the encapsulating hBN and that the layer thickness is small in comparison to the electron-hole spacing in the exciton.

$$U_\lambda(\rho) = -\frac{\pi e^2}{2r_*^\lambda}\left[H_0\left(\frac{\rho}{r_*^\lambda}\right) - Y_0\left(\frac{\rho}{r_*^\lambda}\right)\right] \tag{4.3}$$

Where $r_*^\lambda = 2\pi\kappa_\lambda/\sqrt{\varepsilon_\parallel\varepsilon_\perp}$ is the the screening length for excitons in the material λ. This is defined by the in-plane polarizability of the TMD layer κ_λ. As the layer is thin, the electric field associated with the exciton exists entirely in the hBN environment. Therefore, the screening length is normalised by the geometric average of the permittivity of the hBN in the directions parallel and perpendicular to the TMD layer ($\varepsilon_\parallel$ and $\varepsilon_\perp$ respectively). H_0 is the zeroth Struve function and Y_0 is the zeroth Bessel function of the second kind. Figure 4.52 shows a plot of this potential as a function of the electron-hole distance. As ρ becomes large, $U_\lambda(\rho)$ tends to the standard $1/\rho$ behaviour of the Coulomb potential for an electron in hBN. This reflects the fact that at larger separations, more of the electric field that matters is in the hBN, so the effects from the TMD layer are minimal. At smaller ρ, the Rytova-Keldysh potential falls below the Coulomb potential as the screening becomes more significant.

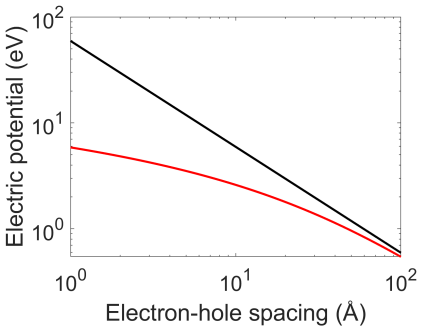

FIGURE 4.52: A log-log plot of the Coulomb (black) and Rytova-Keldysh potential (red) for the WSe_2 monolayer for a range of electron-hole spacings ρ.

For the heterostructures, additional screening from the other layer is present resulting in a more complex potential. This is given in Fourier space as there is no closed-form expression as a function of ρ [59]. As a function of wavevector q, we instead have:

$$U_{WSe_2/MoSe_2}(q) = \frac{2\pi}{q\sqrt{\varepsilon_\parallel \varepsilon_\perp}} \frac{1 + r_*^{MoSe_2/WoSe_2} q(1 - e^{-2q\tilde{d}})}{1 + q(r_*^{WSe_2} + r_*^{MoSe_2}) + q^2 r_*^{WSe_2} r_*^{MoSe_2}(1 - e^{-2q\tilde{d}})} \tag{4.4}$$

In this case $\tilde{d} = d\sqrt{\frac{\varepsilon_\parallel}{\varepsilon_\perp}}$, the renormalised interlayer distance is used to account for the permittivity of the encapsulating hBN. An inverse Fourier transform of this equation was then required to find the potential in real space. Due to the rotational symmetry, this is equivalent to the Hankel transform. In the large exciton limit (small $q\tilde{d}$), the equation can be simplified and then Hankel transformed to the same form as the Keldysh potential (Equation 4.3), but with an effective screening length of $(r_*^{WSe_2} + r_*^{MoSe_2})$. This can be thought of intuitively as most of the significant electric field outside the two layers and they act as a single layer with the screening from both. This of course also goes to the Coulomb potential in the very large q limit. It is even simpler for small exciton radii (large $q\tilde{d}$), as the second layer becomes irrelevant and the potential is the same as in the monolayer case. Here, the electric field from the exciton does not reach to the second layer. Assuming the exciton radius at which the second layer effects become dominant is where $q\tilde{d} < 1$, the value of ρ at this limit is >6 nm in real space, using $\rho = 2\pi/q$. This is larger than the 2 nm A1s exciton radii reported in literature for TMD monolayers and on the order of the 5-8 nm reported for the A2s [60, 141]. Therefore, the addition of the second layer is expected to have a larger relative effect on the binding energy of the 2s excitons than the 1s.

In order to determine the exciton binding energies, the eigenvalue problem of Equation 4.2 was solved numerically [202] with the monolayer and heterostructure potentials using the parameters given in Table 4.15. Values for the majority of these were determined from literature, with only the two polarizability values chosen to minimise the mean difference between the predicted exciton energy differences and experimental data

from these Raman measurements as well as reported values for the WSe_2 monolayer A3s and A4s [60, 61, 191].

Parameter	Symbol	Value	Source
In plane hBN permittivity	$\varepsilon_{\parallel}$	6.9	[204, 205]
Out of plane hBN permittivity	$\varepsilon_{\perp}$	3.7	[204, 205]
Heterostructure layer spacing	d	6.47 Å	[206, 207]
WSe_2 electron mass	$m_e^{WSe_2}$	0.50	[208]
$MoSe_2$ electron mass	$m_e^{MoSe_2}$	0.80	[209]
WSe_2 hole mass	$m_h^{WSe_2}$	0.42	[208]
$MoSe_2$ hole mass	$m_h^{MoSe_2}$	0.50	[209]
WSe_2 in-plane polarizability	κ_{WSe_2}	30.83 Å	Fitted
$MoSe_2$ in-plane polarizability	κ_{MoSe_2}	29.43 Å	Fitted

TABLE 4.15: Parameters used in the model to calculate the binding energies of the exciton Rydberg series in the monolayers and heterostructures. Literature sources for the fixed values used are given and the two fitted parameters are given at the bottom.

4.3.2 Energy Comparison

The energy differences between the 1s and 2s states from measured energies given in Table 4.14 are given alongside the differences in exciton binding energy for the 1s and 2s determined from the theory calculations in Table 4.16. The theory shows excellent agreement with the measured values for the two monolayers, in both cases falling within the experimental errors. In addition to the monolayer measurements here, the A1s-A3s and A1s-A4s splitting of monolayer WSe_2 from literature are available [60, 61, 191] and in both cases they agree with the model to within 2%. The theory value of 138.2 meV for the $MoSe_2$ A1s-A2s splitting in the heterostructure case falls within only 4.2 meV of the 57° twist heterostructure value. The 20° heterostructure value of 113 meV is significantly lower. However, the cause of this was likely the significant charging of this sample, which also caused the $MoSe_2$ A1s trion to appear dominant in the reflectivity measurements over the neutral exciton. For the WSe_2 heterostructure A1s-A2s, the predicted value falls within two standard deviations of the measured values for both twist angles, and within 0.6 meV of the mean of 123 meV. With only 2 free parameters, this model which does not include layer twist effects produces energy splittings which are in reasonable agreement with 3 of the 4 measured values for the heterostructures. In addition, it gives excellent agreement with both of the monolayer measured values A1s-A2s here and also with two additional WSe_2 energy differences determined from measurements in literature[60, 61, 191].

		Exciton Energy Spacing (meV)				
		Monolayer		Heterostructures		
Material	Excitons	Experiment	Theory	57°	20°	Theory
$MoSe_2$	A1s-A2s	152 ± 3	152.3	134 ± 2	113 ± 6	138.2
$MoSe_2$	B1s-B2s	158 ± 2	—	122 ± 17	122 ± 3	—
$MoSe_2$	A1s-B1s	210 ± 2	—	219 ± 2	197 ± 4	—
WSe_2	A1s-A2s	131 ± 1	130.2	129 ± 4	117 ± 4	122.4
WSe_2	A1s-B1s	426 ± 2	—	433 ± 8	446 ± 3	—

TABLE 4.16: The difference in exciton energy between the 1s and 2s excitonic states determined from resonance Raman measurements and the differences in theoretically calculated exciton binding energy for the A1s and A2s excitons.

This model gives a reduction in binding energy of the A1s exciton of 8 ± 0.5 meV when going from monolayer WSe_2 to the heterostructure and a reduction of 19 ± 1 meV for $MoSe_2$ monolayer versus heterostructure. In addition, the absolute A1s energy change when going from monolayer to heterostructure was found to be -17 meV and -12 meV for WSe_2 and $MoSe_2$ respectively, using the mean value for the two heterostructures. This means the single particle band gap was reduced by 25 meV for the WSe_2 layer and 31 meV for the $MoSe_2$ layer on formation of the heterostructure.

4.4 Conclusions

In conclusion, a high resolution resonance Raman study of two hBN encapsulated $WSe_2/MoSe_2$ TMD heterostructure samples has been performed alongside measurements of hBN encapsulated WSe_2 and $MoSe_2$ monolayers. This data was used in combination with photoluminescence and reflectivity measurements to identify the WSe_2 and $MoSe_2$ A1s A2s B1s and $MoSe_2$ B2s excitons in the monolayers and heterostructures. Raman peaks from scattering involving two gamma point phonons that are only present at the 2s resonances were observed. The resonance behaviour of these peaks was used to unambiguously identify the 2s excitonic states in heterostructures for the first time and measure their energies. This is likely also applicable to other heterostructures containing WSe_2 or $MoSe_2$ and it is also possible that equivalent Raman peaks are present in other monolayers. A theoretical model of the exciton binding energies [59, 202] was validated using the A1s-A2s exciton energy separation for the monolayers and heterostructures. The binding energies were found to be smaller for the heterostructures as a result of the additional screening of the electric field by charge carriers in the second layer. The change in single particle band gap was also determined and was found to be reduced on formation of the heterostructure.

Chapter 5

Resonance Raman Spectroscopy of Hyperbolic Phonon Polaritons in hBN Encapsulated TMDs

5.1 Literature Review

Intense Raman peaks above 700 cm^{-1} in spectra of hBN encapsulated WSe_2 monolayers were first reported by Chen et al. in 2016 [195]. These features are shown in Figure 5.1 reproduced from this paper and have full-width at half maximum (FWHM) of 54 and 49 cm^{-1}. This is much broader than typical TMD phonon peaks with FWHM around 2 cm^{-1}. These also appear at a higher Raman shift than any previously observed peaks associated with single or multi-phonon Raman processes in TMDs, falling around 800 and 1050 cm^{-1}. Additionally, these spectral features were orders of magnitude more intense than TMD Raman. This first report suggests these features are hBN ZO phonon scattering and hBN ZO + WSe_2 $A_1'(\Gamma)$ phonon scattering from electronic states in the WSe_2. Figure 5.1 also shows an equivalent spectrum of hBN on Si which shows that these features are not Raman active in pure hBN.

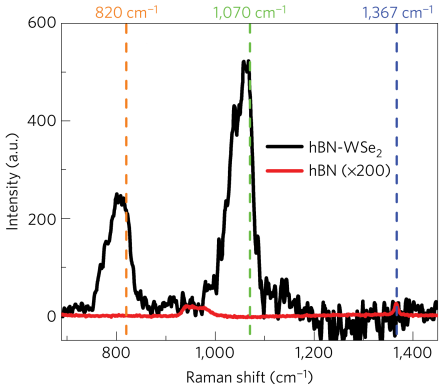

FIGURE 5.1: Reproduced from [195]. Raman spectrum of a WSe_2 layer on top of hBN taken at 77 K with an excitation energy of 1.849 eV. Shown in red is an equivalent spectrum of bare hBN. The sharp high shift edges of the Raman features are marked at 820 and 1070 cm^{-1}. A hBN Raman peak is also marked at 1367 cm^{-1} for the bare hBN sample spectrum.

Later reports confirm that these features are only observed in samples where hBN is the encapsulating material [188] and identify the WSe_2 electronic states involved in the scattering as the A1s and A2s excitons [188]. The high intensity of the features is a result of the strong exciton phonon coupling between the WSe_2 and hBN layers. This is a result of double resonance with the A1s and A2s excitonic states in WSe_2. [171]. In addition to the literature on WSe_2, there has been one report of these hBN modes at the same wavenumber ranges in hBN encapsulated WS_2 but with much less intensity [196]. This paper identifies the hBN associated modes as hyperbolic phonon polaritons (HPPs), which had previously been observed in hBN via near field scattering experiments [114]. Whilst the features have been identified, no one has yet tried to explain the observed lineshape.

5.2 Results

Raman spectra at 4 K were taken of the hBN encapsulated WSe_2 and $MoSe_2$ monolayers which extended up to higher Raman shifts (1200 cm^{-1}) than the spectra shown in the previous chapter. The broad hBN associated Raman features around 815 and 1050 cm^{-1} were observed in these spectra and the resonance behaviour and lineshapes were extracted. The following sections explore the behaviour of these Raman features in the two monolayers.

5.2.1 hBN Modes Identification

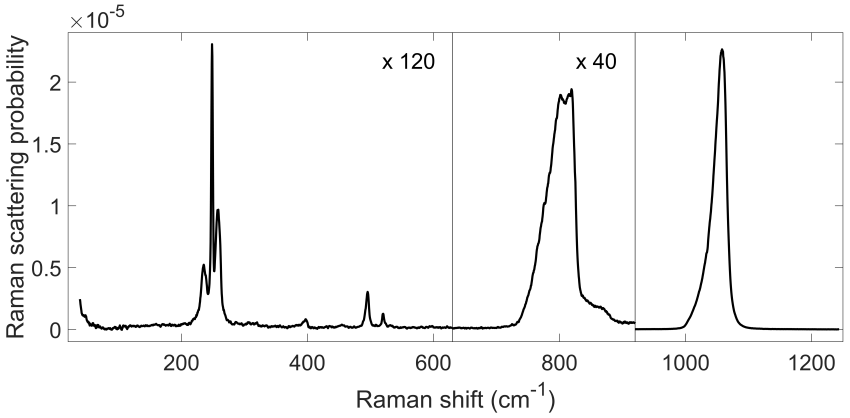

FIGURE 5.2: A WSe_2 monolayer Raman spectrum with an excitation energy of 1.866 eV. The intensity has been scaled up by a factor of 120x for the lowest shift section of the spectrum and by 40x for the middle section for clarity.

A Raman spectrum of the hBN encapsulated WSe_2 monolayer area is presented in Figure 5.2. This spectrum was taken with an excitation energy of 1.866 eV which is close to the incoming resonance of the A2s exciton. As discussed in the previous chapter, the lower frequency section of the spectrum features single phonon WSe_2 Raman peaks with the strongest at 240 cm^{-1}. Near to the Si 520 cm^{-1} peak, the 495 cm^{-1} peak associated with the A2s transition is present and additional weaker multi-phonon peaks are also observed near 400 and 600 cm^{-1}. The middle section of the spectrum in the figure, which is scaled up be a factor of 40, shows the first broad hBN associated feature. This broad peak has a shallow slope on the lower wavenumber side and a steeper cut-off on the higher shift side. Above this cut-off, a weak shoulder is present. The third section of the spectrum in Figure 5.2 contains by far the most intense Raman feature, centred around 1050 cm^{-1}. This is two orders of magnitude stronger than the WSe_2 scattering and over 40x more intense than the feature at 815 cm^{-1}. This also features the shallow slope on the low shift side and high-shift cut-off which are observed in the 815 cm^{-1} peak. However, the flatter top of the 815 cm^{-1} peak is not shared.

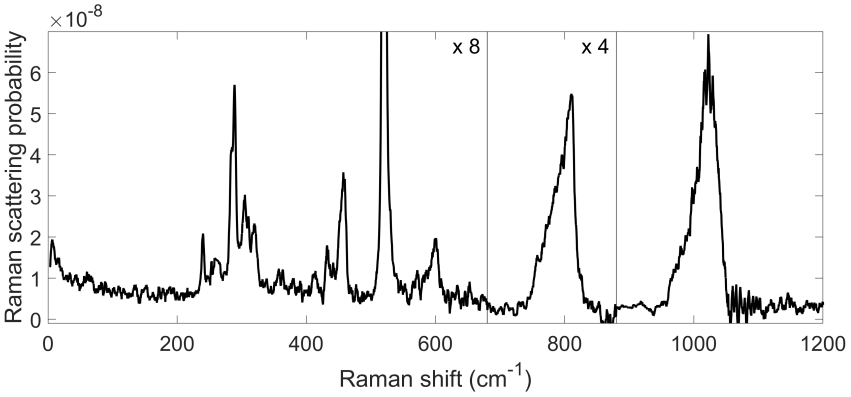

FIGURE 5.3: A $MoSe_2$ monolayer Raman spectrum with an excitation energy of 1.782 eV. The intensity was scaled up by a factor of 8x for the lowest shift section of the spectrum and by 4x for the middle section for clarity.

A Raman spectrum was also taken just below the A2s incoming resonance of the $MoSe_2$ monolayer sample at 1.782 eV and is shown in Figure 5.3. The observed signal was significantly weaker at this resonance in this sample. The $MoSe_2$ phonon associated Raman peaks, which appear in the spectrum below 630 cm^{-1}, were all weaker than the 520 cm^{-1} Si peak which extends off the top of the spectrum shown. As in the WSe_2 case, a broad feature is observed at 815 cm^{-1} with a shallow slope on the lower energy side and a sharp cut-off on the high Raman shift side of the peak. Similarly to the WSe_2 spectrum, an additional peak is observed at 1050 cm^{-1} with a similar lineshape and greater scattering intensity. As well as frequency and overall shape, the FWHM of the 800 cm^{-1} peak in both the WSe_2 and $MoSe_2$ samples, 52 and 48 cm^{-1} respectively, are also similar to the 54 cm^{-1} value from the 800 cm^{-1} peak in literature. This is the first observation of these hBN associated peaks in a Mo based TMD monolayer.

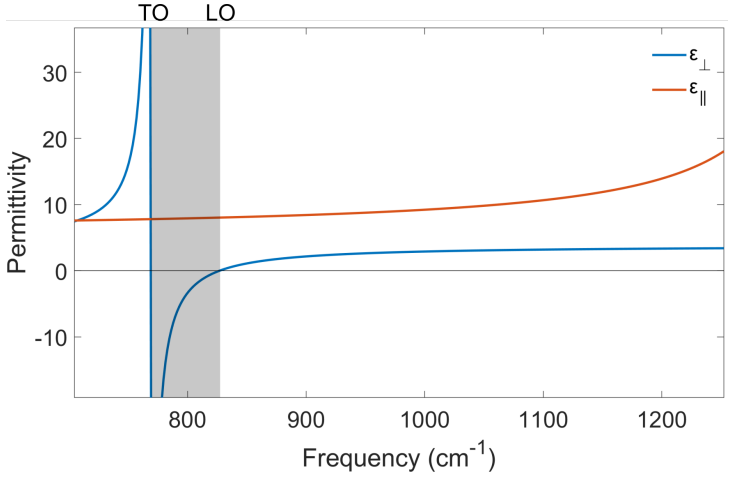

FIGURE 5.4: The real part of the relative dielectric permittivity of hBN plotted against energy for the in plane ($\varepsilon_{\parallel}$) and out of plane ($\varepsilon_{\perp}$) directions. This is plotted over the infrared range which is observed in the Raman spectra. The lower reststrahlen band is highlighted in grey.

hBN is a hyperbolic material in the infrared range, with two distinct reststrahlen bands, where the permittivity is negative in one direction and positive in the other, as shown in Figure 5.4. The lower of these two bands is of most interest as it overlaps in energy with the 800 cm^{-1} broad Raman feature. The upper band falls above 1350 cm^{-1} and whilst Raman scattering may be possible, no evidence of strong broadband modes in that band was observed in the few Raman spectra of that shift range. The TO and LO frequencies which correspond to the edges of the lower reststrahlen band are reported in literature to fall in the ranges of 750 - 768 cm^{-1} and 819 - 825 cm^{-1} respectively [114, 204, 210, 211]. Within the reststrahlen band, hyperbolic phonon polaritons (HPPs) can exist in the hBN. Comparing this to the Raman features in both the WSe_2 and $MoSe_2$ samples in Figure 5.5a) & c) and Figure 5.6a) & c), the reststrahlen band covers the majority of the spectral weight of the peak in all cases. This combined with the distinctly broader width of these features than typical phonon modes means that they can be confidently assigned to hBN HPPs as in [196]. This is an interlayer scattering process where the exciton in the TMD creates a HPP in the hBN layer.

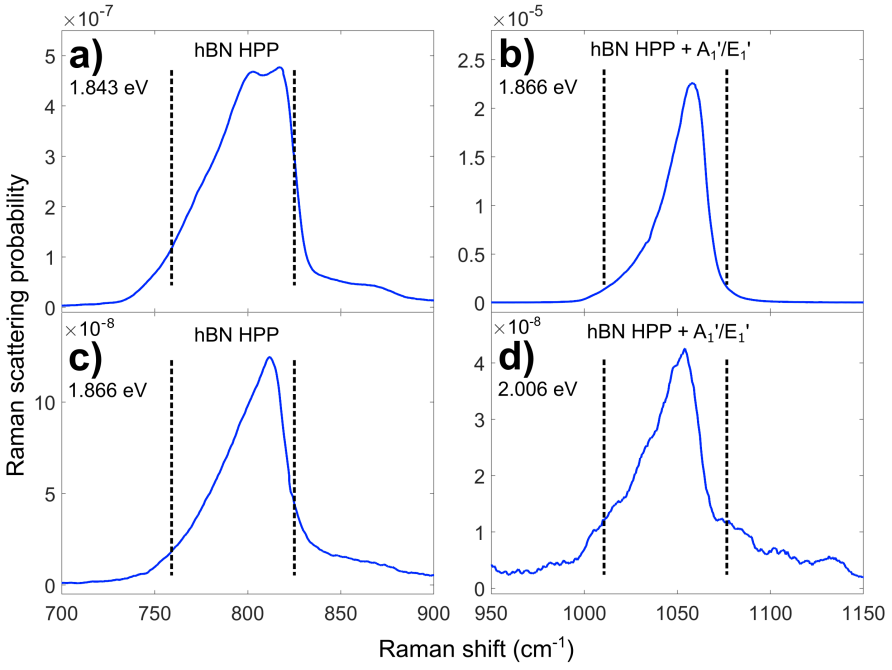

FIGURE 5.5: WSe_2 monolayer Raman spectra showing the two hBN features under different resonance conditions. a) 800 cm^{-1} peak at the A1s exciton outgoing resonance. b) 1050 cm^{-1} at the A1s outgoing/A2s incoming double resonance. c) 800 cm^{-1} peak at the A2s incoming resonance. d) 1050 cm^{-1} peak at the A2s outgoing resonance.

In the case of the 1050 cm^{-1} feature in Figure 5.5b) and d), what is shown is the reststrahlen band frequencies plus the shift of the main WSe_2 $A_1'(\Gamma)$ phonon peak. This feature is assigned to a scattering process involving a hBN HPP and one phonon i.e. HPP + $A_1'(\Gamma)$ as reported previously in the literature [188, 195]. It is important to note that the $E'_{TO/LO}(\Gamma)$ is degenerate with the $A_1'(\Gamma)$ and so it is possible that both phonons contribute.

Raman spectra of the hBN HPP features from the $MoSe_2$ monolayer are shown in Figure 5.6 with the reststrahlen band marked. The hBN HPP case shows the same behaviour as in the WSe_2 sample. However, in $MoSe_2$, the $A_1'(\Gamma)$ and $E'_{TO/LO}(\Gamma)$ phonons are not degenerate in energy. This causes two overlapping higher shift HPP + phonon combination modes to appear. These form a feature that is broader than the lower shift 815 cm^{-1} modes. This is most evident in Figure 5.6d) where a peak is present in the feature where the reststrahlen bands overlap. Whilst the literature reports for WSe_2 samples suggest that the 1050 cm^{-1} mode is from the HPP + $A_1'(\Gamma)$ combination [188, 195], the most significant part of the signal observed in these $MoSe_2$ spectra came from the range of frequencies expected from the HPP + $E'_{TO/LO}(\Gamma)$ combination. This shows that the HPP + $E'_{TO/LO}(\Gamma)$ combination mode must not be neglected.

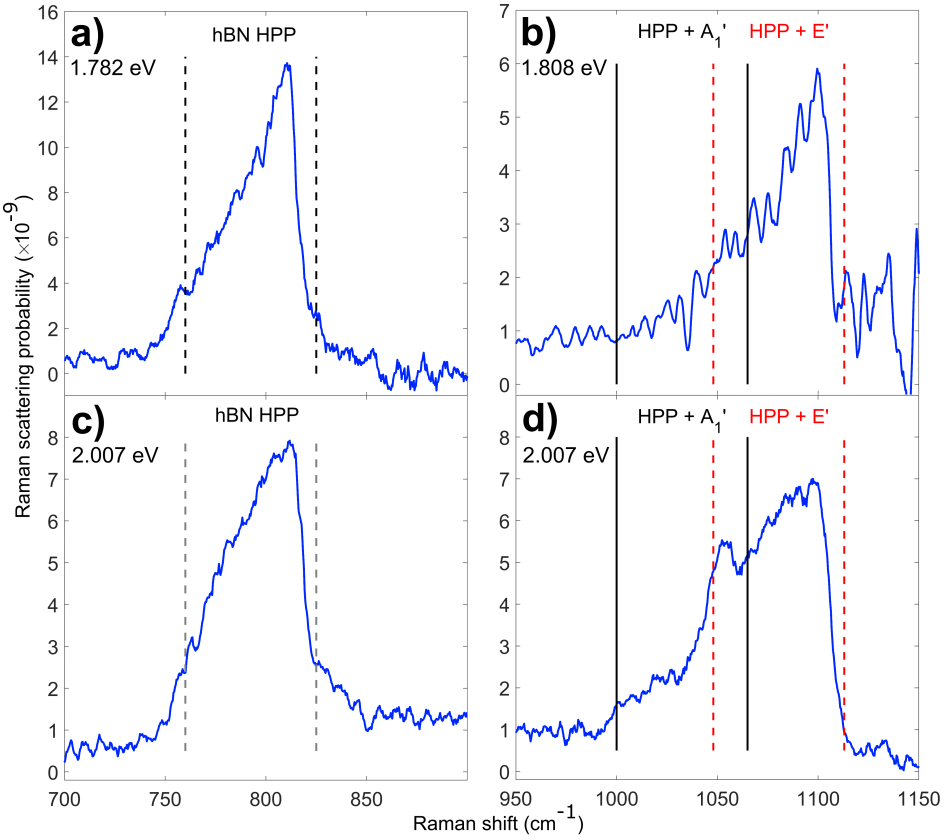

FIGURE 5.6: $MoSe_2$ monolayer Raman spectra showing the hBN HPP feature (a), c)) and combination phonon + hBN HPP peak (b), d)). Excitation energies for a) and b) fall between the A1s and A2s. For c) and d) the excitation energies were between the B1s and B2s.

5.2.2 WSe_2 hBN Resonance Behaviour

In addition to the Raman spectra shown in the previous section, further spectra were taken with excitation energies in the range 1.73 - 2.03 eV, covering the A excitons. A total of 94 spectra were taken and are shown in a colour-map in Figure 5.7. Both the

WSe_2 Raman peaks below 700 and the broad hBN HPP features at 800 cm^{-1} and 1050 cm^{-1} are present.

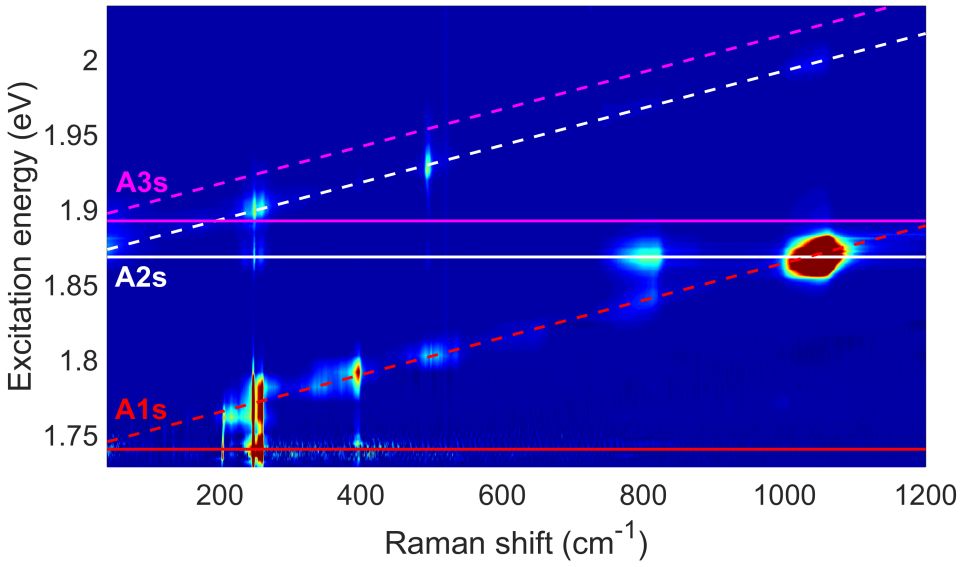

FIGURE 5.7: Colour-map of the WSe_2 monolayer Raman spectra covering the A exciton resonances with Raman shifts up to 1200 cm^{-1}. The colours follow a log scale where blue is minimal scattering and dark red is most intense Raman scattering. Red, white and pink lines respectively mark the A1s, A2s and A3s exciton resonance energies with solid lines corresponding to the incoming resonances and dashed marking the outgoing.

The strongest feature is the 1050 cm^{-1} peak at the WSe_2 A1s outgoing / A2s incoming double resonance. A much weaker resonance is also observed at the A2s outgoing for this peak. The 800 cm^{-1} feature is most intense at the A2s incoming resonance, with signal observed at the A1s outgoing as reported in literature.

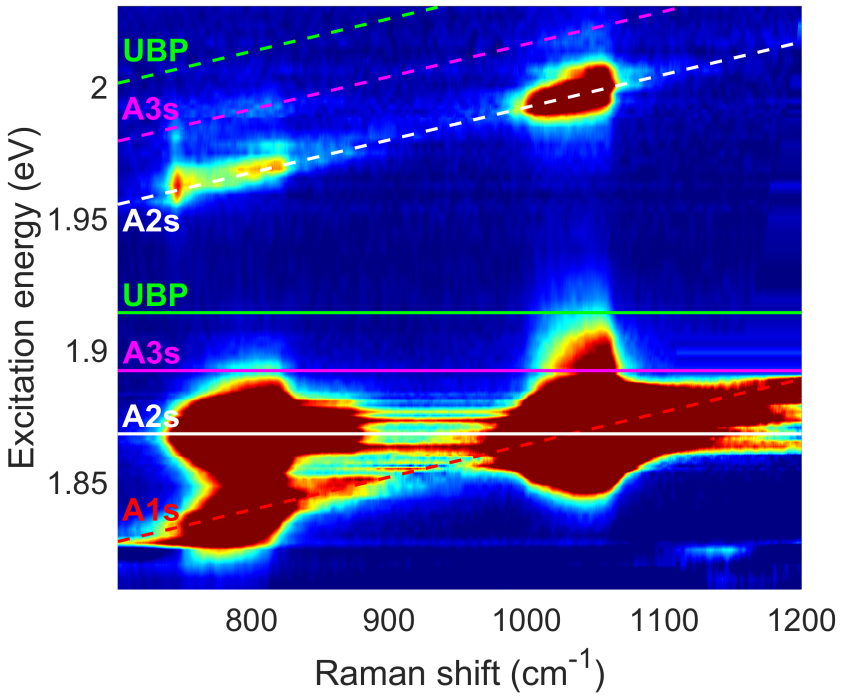

FIGURE 5.8: Scaled subsection of the colour-map of the WSe_2 monolayer Raman spectra in Figure 5.7. In addition to the A1s, A2s and A3s, the resonance energies associated with the unbound electron-hole pair (UBP) are marked in green.

In Figure 5.8, the same data from Figure 5.7 is presented with a different scale to more clearly show the weaker signal. This highlights signal at the A2s outgoing from the two hBN features which extends towards the A3s outgoing. Notably, the HPP peaks all follow the diagonal lines marking the outgoing resonance energies. This shows that rather than being made up of a broad distinct oscillator, the HPPs are made up of a continuum of modes that have independent resonance conditions.

To enable the fitting of the resonance behaviour of the 800 cm^{-1} hBN mode, the intensity of the Raman signal was averaged over a 5 cm^{-1} wide window centred on 815 cm^{-1}. The resonance profiles obtained in this way are shown with blue dots on Figure 5.9. This process was repeated at 775 and 750 cm^{-1}, shown respectively in red and green, to capture any changes in resonance behaviour across the width of the hBN HPP. For all of these profiles, A1s outgoing resonances are observed around 1.84 eV. The most intense peak observed is from the A2s incoming near 1.87 eV. Two weaker peaks are also observed near 1.97 and 1.99 eV, as shown in the scaled sub-plot in the top right corner of the figure. These are from the A2s and A3s outgoing resonances respectively. This is the first measurement of Raman scattering from a TMD A3s exciton. As expected, the energies of the outgoing resonance peaks are dependent upon the chosen centre Raman shift. This is the same effect as the angled lines of the outgoing resonances in the colour-maps, confirming the multi-mode nature of the HPP scattering. The resonance profiles were each fitted to three state (A1s, A2s, A3s) resonance Raman models which are the

solid curves on Figure 5.9. As shown in the figure, each of the fits were reasonable and captured the resonances observed in the profiles.

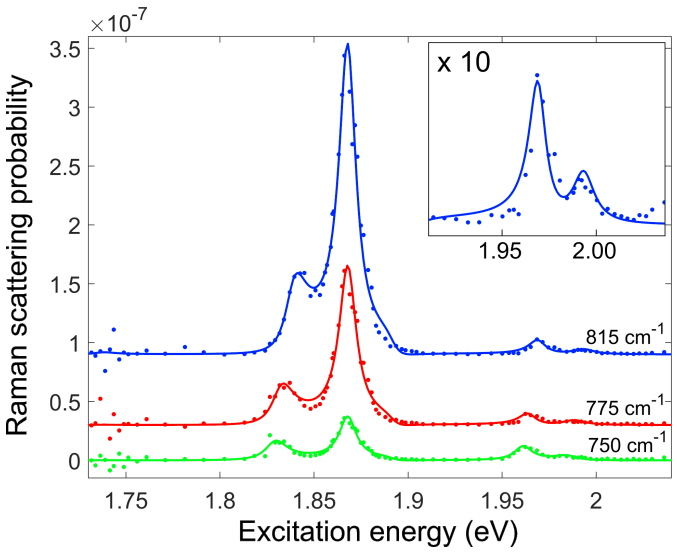

FIGURE 5.9: Resonance profiles of the intensity of the hBN HPP feature at different Raman shifts in the WSe_2 monolayer. The profiles are fitted with 3 state models, where the states are the A1s, A2s and A3s excitons.

Equivalent resonance profiles were also extracted and fitted to three state models for the 1050 cm^{-1} peak. In this case the double resonance dominates the profiles, and the A2s outgoing peak is clearly visible in the scaled sub-plot. The A3s however, is not clearly separable. The only evidence of its presence is a slight shoulder on the higher energy side of the A2s outgoing peak.

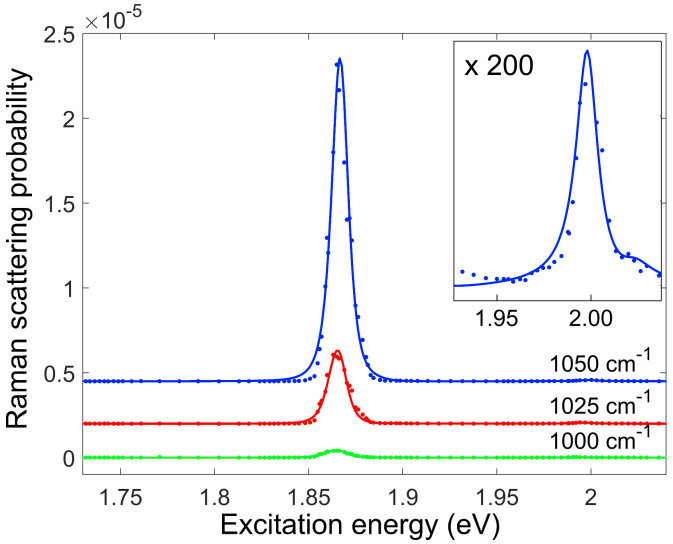

FIGURE 5.10: Resonance profiles of the intensity of the 1050 cm^{-1} hBN HPP + WSe_2 phonon Raman features in the WSe_2 monolayer covering the A1s, A2s and A3s exciton resonances. The profiles are fitted with 3 state models.

It is worth noting that there is no statistically significant Raman scattering from the hBN HPPs at the A1s incoming resonance. However, the significant additional noise due to the strong A1s luminescence means the upper limit on any scattering at these laser energies is comparable with the strength of the Raman scattering at the highest energy resonances. In some ways it is not surprising to observe less scattering at this resonance because the A1s incoming is far in energy from any other resonances and therefore has no double resonance enhancement. One additional factor which will further decrease the scattering at the A1s is that the A1s exciton has a smaller in-plane dipole which couples more weakly to an in-plane electric field of the HPPs.

The best fit parameters from these resonance profiles are given in Table 5.1. The multiple interstate scattering channels leads to relatively large uncertainties on the best fit amplitudes. However, the fitted widths and energies are more tightly constrained, with the widths for each state falling within 2 standard deviations of each other and only 1 in 18 of the energies falling outside this. Since the 800 cm^{-1} fits have a clearer A3s peak, the energies from those were averaged, which places the WSe_2 A3s at 1.891 ± 0.002 eV which is 23 meV above the mean A2s energy (1.868 eV). This A2s-A3s spacing is within the 21-25 meV range from published values for hBN encapsulated monolayer WSe_2 measured by photoluminescence which further bolsters the confidence of the assignment to the A3s.

	Scattering	Sampled Raman shift (cm^{-1})					
	Channel	750	775	815	1000	1025	1050
Absolute	A1s - A1s	2.29±0.95	7.4±1.2	32±3	189.5±8.4	60.6±43	81±2400
Raman	A1s - A2s	9.55±0.02	40.5±0.12	70.0±0.14	17.65±0.16	56.2±0.3	986±13
scattering	A1s - A3s	3.10±0.36	50.4±0.67	69±1	7.3±1.1	300±17	100±960
probability	A2s - A2s	0.062±3.9	0.13±23	97±2.7	409±83	350±780	1000±66000
($x10^{-16}$)	A2s - A3s	16.6±1.3	13±19	19.1±2.0	71.6±45	1820±370	0±22000
	A3s - A3s	6.1±2.7	15±34	99±7.1	756±21	560±250	1300±3400
Energy	A1s	1736±1	1736±5	1738±1	1734±1	1732±1	1736±1
(meV)	A2s	1868±1	1867±1	1867±1	1869±1	1869±1	1.865±3
	A3s	1891±3	1890±7	1892±1	1895±17	1894±3	1897±5
Width	A1s	6.0±1.1	6.4±0.4	6.5±0.8	8.7±1.1	5.9±0.3	7.9±1.1
(meV)	A2s	6.0±0.5	5.6±0.3	5.3±0.2	7.0±0.7	6.9±0.4	7.0±0.1
	A3s	10.0±7.0	10.8±1.1	10.5±1.4	8±14	4.8±2.0	4.2±2.0

TABLE 5.1: Fitting parameters obtained from the best fits for the 3 state resonance models to the profiles of the WSe_2 hBN HPP features from Figure 5.9 and Figure 5.10.

In addition to the resonance behaviour of these hBN modes, the changes in lineshape at different resonance conditions were also examined. For the 800 cm^{-1} mode, Figure 5.11 shows the spectrum when exciting below resonance (blue), on resonance (green) and above resonance (red). In a), at the A1s outgoing, the below resonance spectrum has

more spectral weight towards low shift and the above resonance spectrum has more weight towards higher shifts. The Raman scattering from different HPPs that make up the overall feature is going into and out of resonance at different excitation energies. This is a result of the outgoing resonance energy varying with the Raman shift across the HPP. The effect is even stronger in c) at A2s the outgoing resonance. This is because the exciton linewidth of the A2s is narrower (3.5 meV = 28 cm^{-1}) than the A1s (5.6 meV = 45 cm^{-1}) and so the part of the spectrum which is enhanced at the same excitation energy is narrower. The effect of this on the incoming resonances is much less, as shown in b), as the whole spectrum is resonantly enhanced at the same energy. The spectra in a) and b) all feature peaks with a shallow ramp-up in intensity from the low energy side which begins below the bottom of the reststrahlen band. A sharp drop-off in Raman intensity is also observed in these at the high energy side of the reststrahlen band.

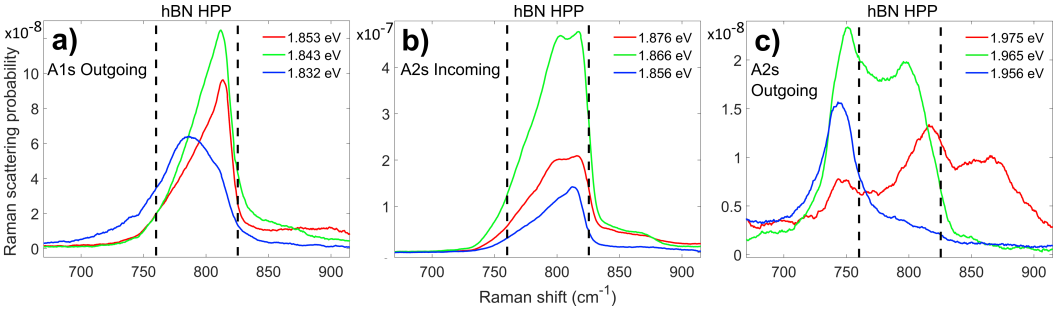

FIGURE 5.11: WSe_2 monolayer Raman spectra showing the hBN HPP feature at various excitation energies around a) The A1s outgoing and B1s incoming double resonance. b) The A2s outgoing resonance. c) The A3s outgoing resonance. For each of these the spectrum is shown with the excitation energy on resonance (green) above resonance (red) and below resonance (blue).

The spectra at the A2s outgoing shown in Figure 5.11 c) are different from the other two resonance conditions in that there is a strong peak in the spectrum at 750 cm^{-1}, just below the reststrahlen band. This is narrow enough to be associated with a multi-phonon peak rather than hBN HPP and the fact that it falls at three times the strong 250 cm^{-1} WSe_2 peak frequency suggests it is a result of a combination mode involving the emission of a total of 3 $A_1'(\Gamma)$ or $E'_{TO/LO}(\Gamma)$ phonons. The fact this is not observed at the lower energy resonances can be explained by this peak being the result of sequential phonon scattering, where the intermediate states between the 3 phonon emissions are all resonant with the lower energy states, enhancing the intensity of the peak only at this A2s outgoing resonance. In a), b) and c), a shoulder is present which extends above the 825 cm^{-1} LO frequency and starts dropping off around 875 cm^{-1}. The shoulder is strongest in c) at an energy above resonance but it is also clearly visible in the on-resonance spectra in a) and b).

The 1050 cm^{-1} peak is shown at a range of resonance conditions in Figure 5.12. This shows the similar ramp and sharp cut-off as the 800 cm^{-1} peak with some differences. The cut-off at the high energy LO frequency is generally less sharp in this higher energy

HPP + WSe_2 phonon feature than the HPP at 800 cm^{-1}. One factor that can explain this is the addition of the width of the WSe_2 phonon. Additionally the degenerate $A_1'(\Gamma)$ and $E'_{TO/LO}(\Gamma)$ phonons may both contribute to the feature, as observed in the $MoSe_2$ case where the difference in the phonon energies is significant.

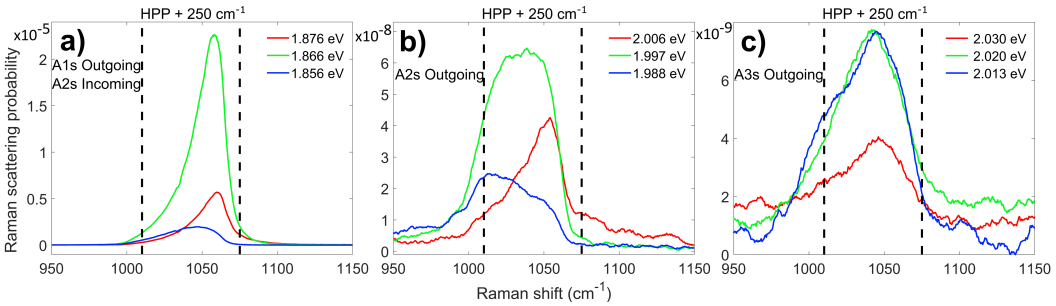

FIGURE 5.12: WSe_2 monolayer Raman spectra showing the combination phonon + hBN HPP feature with excitation energies set around a) The A1s outgoing resonance. b) The A2s incoming resonance. c) The A2s outgoing resonance. For each of these the spectrum is shown with the excitation energy on resonance (green) above resonance (red) and below resonance (blue).

The peak shown in Figure 5.12 a) is much more intense than at any other resonance conditions. Also, the peaks shown in red and blue, taken with excitation energies 10 meV above and below the peak of the resonance, are reduced in intensity by a greater factor than the equivalent spectra in any of the other panels of this figure or the previous figure. This is because the A1s outgoing and A2s incoming resonances fall at the same energy, as the two excitonic states are separated by 131 meV (1057 cm^{-1}). This results in a double resonant enhancement of the Raman signal which is the reason why the intensity of this peak is so great. This also causes the peak to be more sensitive to excitation energy.

In order to better understand the lineshapes, the fitted resonance model was used to attempt to reverse the effects of the different resonance conditions, and determine an underlying lineshape for the features. The results of this are shown in Figure 5.13 for different spectra around the A1s outgoing resonance. These are the same spectra from Figure 5.11a), with the below and above resonance spectra modified to simulate the 1.843 eV condition. The adjusted spectra in Figure 5.13b) match quite well, with the most significant change effecting the 1.832 eV spectrum. Before the correction the peak is much closer to being symmetrical. After, the peak shows the characteristic asymmetric shape of the other two spectra. The fact that the lineshapes match after the correction shows that the differences in lineshape between spectra at different excitation energies is mostly a resonance effect. The most significant difference between the corrected spectra is the intensity of the shoulder above 825 cm^{-1}. This can be neglected as is a result of the calculation amplifying noise which resulted in a more intense shoulder in the spectra with a weaker signal.

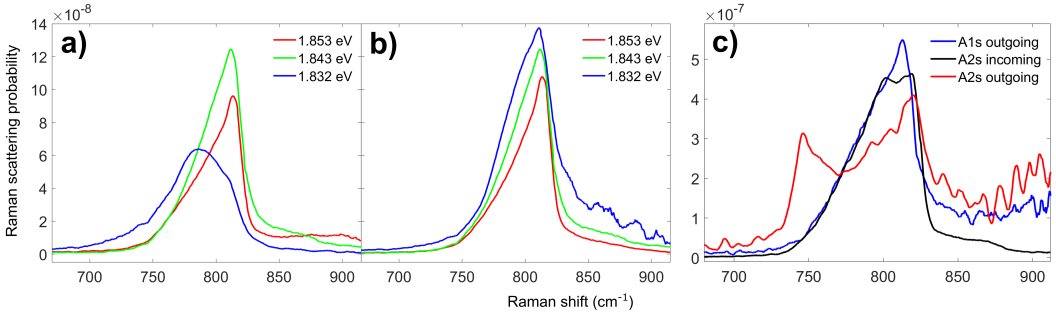

FIGURE 5.13: a) Three spectra at different energies near the A1s outgoing, reproduced from Figure 5.11a). b) Calculated lineshapes determined using the three state resonance model to remove the effects of the resonance enhancement from the spectra in a). c) Three spectra at different resonances, with excitation energies of 1.843, 1.866 and 1.965 eV. The resonance effects have been corrected to match the A2s incoming at 1.866 eV.

The spectra do not match as well when applying the same method to spectra taken at different resonances, as shown in Figure 5.13c), with the altered A1s and A2s outgoing resonances shown alongside the unchanged A2s incoming. The most striking difference is the strong 3 phonon peak at the A2s outgoing resonance near 750 cm^{-1} which is not present in the other two spectra. The Raman signal is also weak in this spectrum which leads to the noisy background signal above 825 cm^{-1}. The A1s outgoing more closely follows the A2s incoming resonance with the single or double peak at the top distinguishing the two. Whilst an underlying lineshape was not quantitatively extracted that can be applied to all of the resonances, it is clear that the HPPs share some common features:

- A shallow ramp up which starts below the reststrahlen band and increases to the peak.
- A comparatively sharp cut off at the high energy side of the reststrahlen band.
- A weak shoulder which extends up to 875 cm^{-1}.

As discussed in the final part it is surprising to observe any Raman scattering from the ramp-up extending below the TO frequency. This is discussed in more depth and compared to a theoretical model of HPPs in the final section of this chapter.

5.2.3 $MoSe_2$ hBN Resonance Behaviour

Now that the WSe_2 case is understood, the the hBN encapsulated $MoSe_2$ monolayer is examined. A colour-map comprised of 117 Raman spectra with excitation energies from 1.60 to 2.24 eV is shown in Figure 5.14. In this case, the hBN features are weaker than the TMD Raman. Resonances of the 800 cm^{-1} HPP are present in between the 1s outgoing and the 2s incoming resonances for both the A and B excitons. The same is

also true of the 1050 cm^{-1} feature. However, residual photoluminescence signal from the A1s outgoing resonance makes this more difficult to observe below 1.8 eV.

Unlike the WSe_2 case, the 1050 cm^{-1} peak is the weaker of the two. The is a result of the different A1s-A2s spacing in this material. In the WSe_2 case, the 1050 cm^{-1} shift of the peak exactly matches the 131 meV A1s-A2s spacing, leading to double resonance condition. Whereas in this $MoSe_2$ sample, the A1s-A2s spacing is 152 meV.

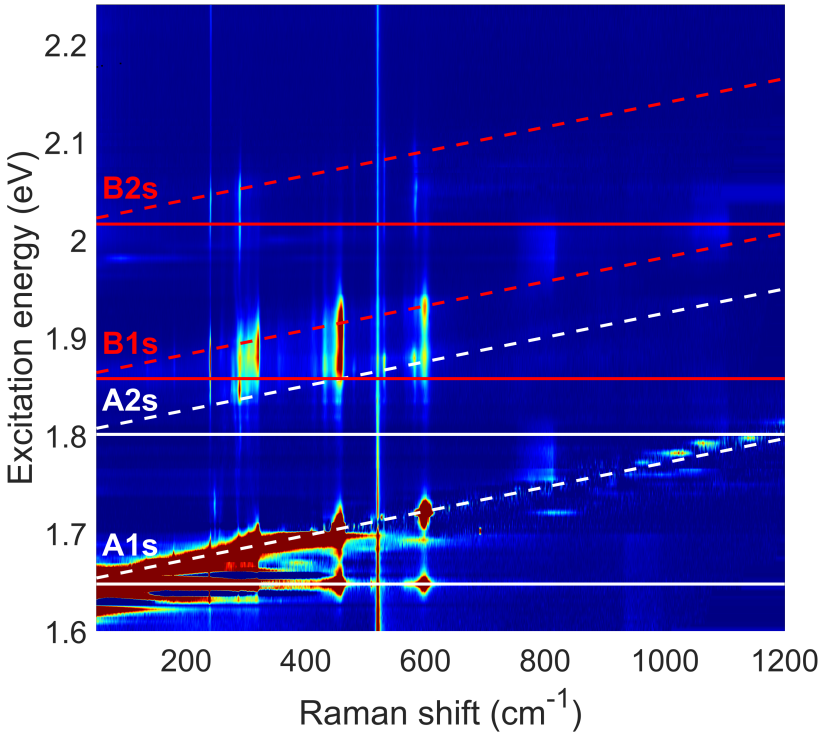

FIGURE 5.14: Colour-map of the $MoSe_2$ monolayer Raman spectra covering the A and B exciton resonances with Raman shifts up to 1200 cm^{-1}. The colours follow a log scale where blue is minimal scattering and dark red is most intense Raman scattering. Red and white lines respectively mark the A and B exciton resonance energies with solid lines corresponding to the incoming resonances and dashed marking the outgoing.

Due to the broader linewidth of the A2s exciton in this $MoSe_2$ sample of 12 ± 3 meV, compared to the 3.5 ± 0.2 meV in the WSe_2, the lineshapes of the hBN modes are not as significantly affected by the resonance conditions. This is because the 12 meV exciton linewidth corresponds to 97 cm^{-1}, which is significantly broader than the 65 cm^{-1} of the reststrahlen band responsible for the hBN modes. This also means that a resonance profile produced by averaging the intensity of a range of pixels in the spectrum, as was done for WSe_2 in the previous section, will be less sensitive to the chosen centre Raman shift. Figure 5.15 shows a resonance profile of the hBN HPP feature produced by taking the mean signal between 797.5 - 802.5 cm^{-1}. The highest signal parts of the profile near 1.8 and 2.0 eV are double resonance conditions where the lower energy is the A1s-A2s and higher is the B1s-B2s. The complex shape of the resonance profile with a multitude

of peaks reflects the fact that all four excitonic states (A1s, A2s, B1s, B2s) contribute both incoming and outgoing resonances to the profile.

The resonance profile was fitted to a four state resonance model with all interstate scattering terms included which is shown in red on the figure. Considering the noisy data around 1.75 eV, the fit of the model is remarkably good. The model shows reasonable agreement with the resonance data, with some caveats. The double peaks in the data around 1.9 eV which correspond to the B1s incoming and A2s outgoing resonances are not fit well and there is some signal from the onset of the broad C exciton above 2.2 eV.

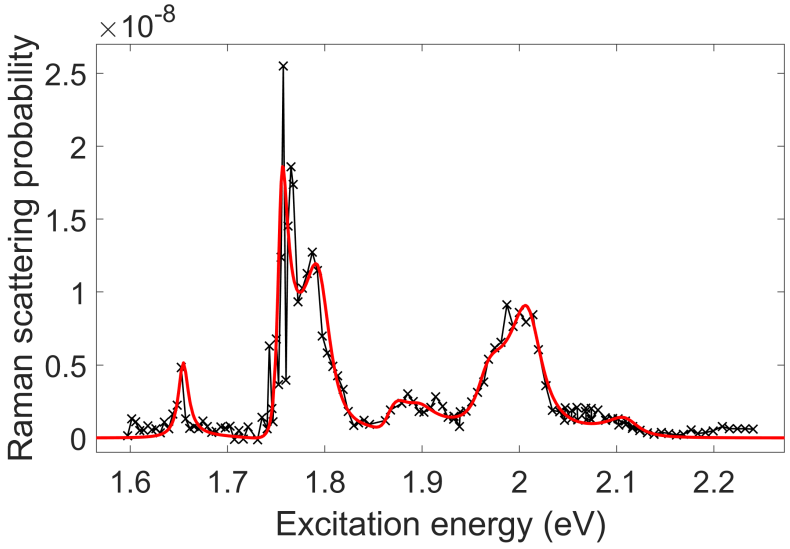

FIGURE 5.15: Resonance profile of the intensity of the 815 cm^{-1} hBN HPP in the $MoSe_2$ monolayer covering the A and B exciton resonances. The profile is fitted to a 4 state model shown in red.

The model makes it difficult for the data to constrain the amplitudes, this is because in addition to the four single state scattering terms, 6 inter-state scatterings are possible, each with an associated phase difference between them. The different phases mean that the amplitudes can combine in both addition and subtraction. For example, the A2s incoming resonance peak around 1.8 eV has significant contributions from the A1s-A2s scattering channel as well as A2s-A2s. This meant finding a well constrained fit of these parameters was not possible in this case. The fact that the over-fitting problem does not effect the energy and width parameters can also be understood by examining the parameter correlation matrix. In order to do this, the Jacobian matrix $\mathbf{J}$ was extracted for the fit, following:

$$\mathbf{J}_{ij} = \frac{\partial f_j}{\partial x_i} \tag{5.1}$$

This is the differential of the fit function at the jth data point f_j with respect to the ith parameter x_j. This matrix is then used to estimate the covariance $\mathbf{C}$, by:

$$\mathbf{C} \approx \frac{\mathbf{r}^T\mathbf{r}}{DOF}(\mathbf{C}^T\mathbf{C})^{-1} \tag{5.2}$$

Where **r** are the residuals from the fit, and *DOF* is the number of degrees of freedom in the fit. Finally we determine the parameter correlation matrix **R** as:

$$\mathbf{R}_{ij} = \frac{\mathbf{C}_{ij}}{\sqrt{\mathbf{C}_{ii}\mathbf{C}_{jj}}} \tag{5.3}$$

The parameter correlation matrix is visualised in Figure 5.16. The diagonal elements are all 1. The 10x10 block in the top left of the figure are the correlations between the amplitude coefficients. These show a higher correlation. The same is also true of the amplitude-phase correlation which forms a 10x9 block in the top right/bottom left and the 9x9 block of phases in the bottom right. The energy and linewidth terms however, do not show such a correlation with each other, nor do they with the amplitudes or phases. This creates the blue "+", and shows that the values from the fit are not problematic.

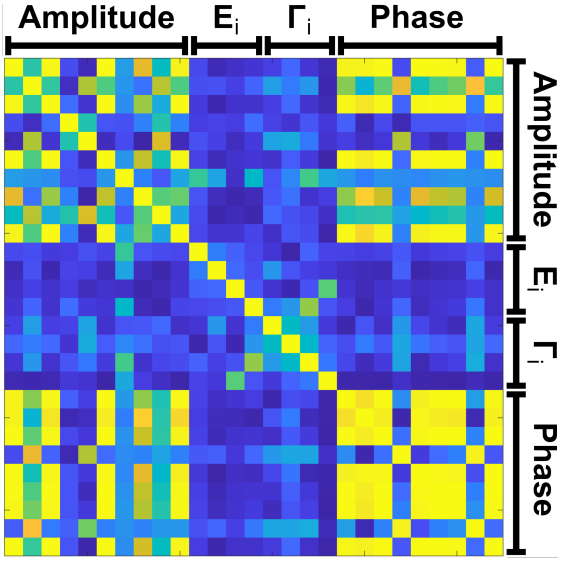

FIGURE 5.16: Visualisation of the parameter correlation matrix for the parameters obtained from fitting the resonance profile of the 815 cm^{-1} hBN associated Raman peak observed in the encapsulated $MoSe_2$ monolayer. Light yellow corresponds to higher correlation between parameters (± 1) and dark blue corresponds to minimal correlation (0). The parameters are labelled where E_i are the exciton energies and Γ_i are their corresponding line widths, equivalent to one over their lifetime.

The best fit energies and widths from the resonance profile are given in Table 5.2. The uncertainties from the fit of the amplitudes were too large for the them to be usable. Despite this, the energy and width parameters could be determined with reasonable errors. The table has, for comparison, the energies determined for the excitonic states from the main $MoSe_2$ gamma point phonon peak resonance data. The 6 of the 8 hBN fitted values fell within one standard deviation of those from the $A_1'(\Gamma)$ and all of them fall within two standard deviations. The good agreement of the energies obtained by this fit with previously determined energies is strong evidence that, as expected, the excitonic states involved in the hBN HPP scattering are the same as those involved in the TMD Raman.

	Fitted energy (eV)		Fitted width (meV)	
Exciton	$A_1'(\Gamma)$ phonon	hBN HPP	$A_1'(\Gamma)$ phonon	hBN HPP
A1s	1.648 ± 0.001	1.654 ± 0.003	3.0 ± 0.1	6.2 ± 3.3
A2s	1.804 ± 0.001	1.796 ± 0.013	8.2 ± 1.7	17.0 ± 7.5
B1s	1.858 ± 0.001	1.860 ± 0.020	18.9 ± 1.3	17.1 ± 15.2
B2s	2.016 ± 0.001	2.012 ± 0.010	9.4 ± 0.7	21.5 ± 14.0

TABLE 5.2: Best fit parameters from the 4 state fit to the resonance profile of the 800 cm^{-1} hBN HPP peak in $MoSe_2$.

Despite not being able to get fitted values for the amplitude terms, some conclusions can still be drawn about the different amplitudes of the scattering channels. The fact that the signal is much smaller at the 1s incoming and 2s outgoing than at the 1s outgoing / 2s incoming suggests that the inter-state scattering between these states is more significant than the single state scattering. This is true for both the A and the B excitons. This is further backed up by the fact that omitting the inter-state scattering terms from the model results in a curve which does not fit the data well.

5.2.4 T-Matrix Modelling of HPPs

Despite previous literature suggesting that these hBN features are from HPPs, none have considered the observed lineshape in detail. Fully modelling the Raman lineshape would require calculating the HPP dispersion relation and lifetimes, as well knowing the coupling constant between the HPP and the excitons, which requires a good model for the exciton wavefunction. Calculating all of this is challenging. Despite this, a lot can be learned from just calculating the dispersion relation of the HPP.

A T-matrix model of the electric field in stacked structures published by Passler et al. [212] was used to model the WSe_2 monolayer sample. This includes the substrate and encapsulating layers with thicknesses determined from atomic force microscopy (AFM) and the fitted reflectivity spectra from the previous chapter. The permittivity values of the graphite [213], SiO_2 [214] and Si [212] used for the model were determined from literature sources. The dielectric function of the hBN used the model from Caldwell et al. [114], with the TO and LO frequencies determined from a range of literature values [204, 210, 211]. A constant refractive index was used for the WSe_2 layer of 2 in plane and 4 out of plane. The HPP are electromagnetic waves taking the form of guided modes of the structure. The first three orders of these modes are shown in Figure 5.17. For a set energy, the wavevector increases with increasing the order of the modes.

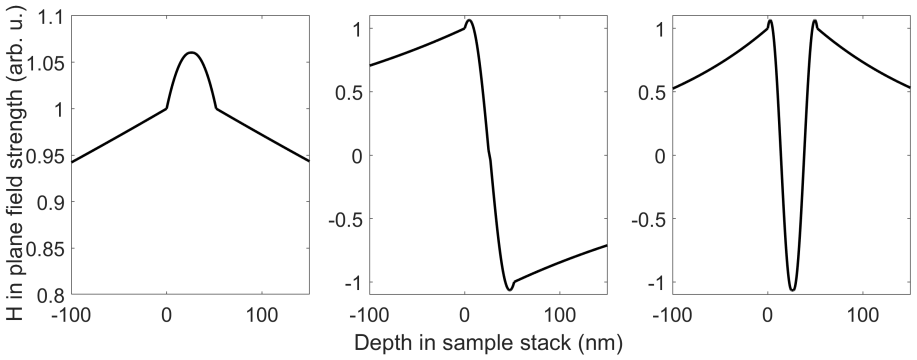

FIGURE 5.17: Plots of the in plane (x) H field strength across the depth of the sample. The first three modes are plotted from left to right.

To predict the dispersion relation of the HPP, the T-matrix model was used. This gave a series of predicted IR absorption spectra as measured in an Otto configuration as a function of wavevector. The spectra were fitted to extract the energy of the HPP at each wavevector value and thus find the dispersion relation as shown in Figure 5.18. The plot of dispersion relation shows a series of branches where the lowest wavevector of these branches corresponds to the first order mode. For each higher branch the order of the modes increases and there is one additional node in the electromagnetic field. The maximum momentum shown is 200,000 cm^{-1} however, in principle, HPPs can have wavevectors which go arbitrarily high (provided the sample is infinite with no losses) [215]. This also shows that HPPs cannot exist outside the reststrahlen band.

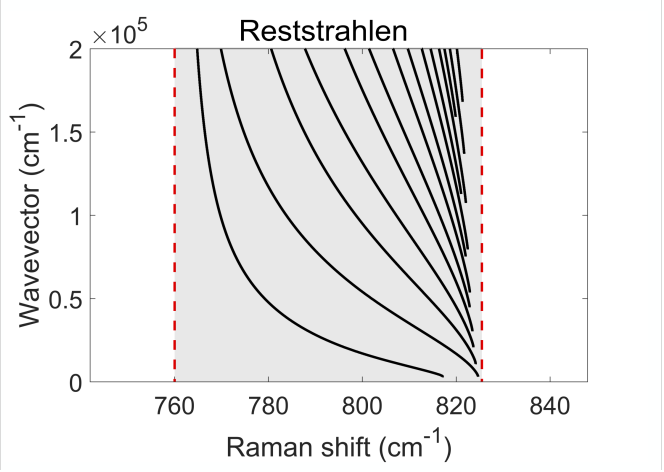

FIGURE 5.18: Simulated dispersion relation of hBN HPPs in the WSe_2 sample over the lower reststrahlen band. The TO and LO frequencies are marked with red dashed lines.

Considering the geometry of the Raman measurement, with a 0.50 NA microscope objective incident normal to the surface of the sample, it is expected from the range of possible angles of incidence (below 30 degrees) of the exciting laser that the available in-plane momentum from an incoming photon at the A2s energy is around 15000 cm^{-1}.

This is indicated on Figure 5.19a) with the blue solid line. Following this restriction, there is only enough momentum to scatter to HPPs between 800 and 825 cm^{-1}. Relaxing momentum conservation by a factor of 5 (75000 cm^{-1}, marked with a dashed line) allows scattering from 770 - 825 cm^{-1} which is much closer to covering the bulk of the signal from the HPP feature. It seems unlikely that the lineshape observed can be explained without some breakdown in conservation of momentum, the reason for which is unknown.

The dispersion relation is shown again, alongside a measured Raman spectrum of the 800 cm^{-1} hBN HPP feature observed in the sample in Figure 5.19b). Considering a higher momentum limit on the dispersion relation in Figure 5.19, few states are available up at lower Raman shifts and more become available as the energy (Raman shift) increases up to the LO frequency. This is an attractive explanation for the slow ramping-up of the intensity from low to high shift observed in the Raman spectra of the HPP feature. This also provides an explanation for the sharp cut-off observed at the high shift side of the feature in the Raman spectra as the large number of available states suddenly become inaccessible as the Raman shift increases beyond the LO frequency.

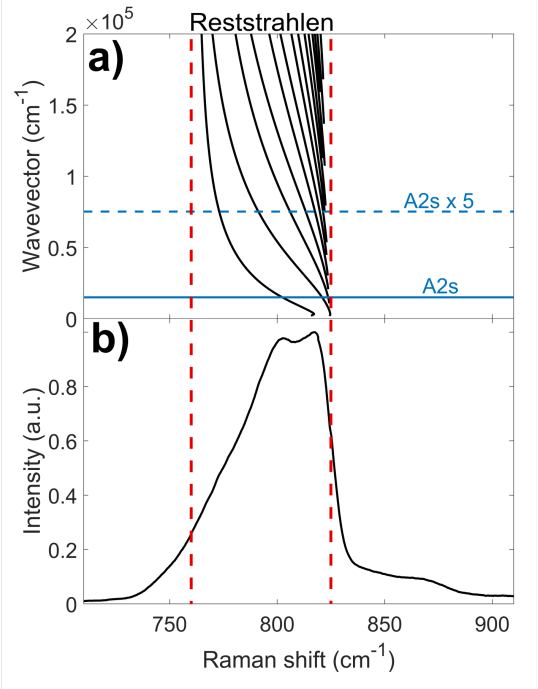

FIGURE 5.19: a) Simulated dispersion relation of hBN HPPs in the WSe_2 sample showing the accessible wavevectors in the lower reststrahlen band. b) Raman spectrum showing the hBN HPP feature observed in the WSe_2 sample.

Two things can clearly not be explained by this HPP model. Firstly, there is the weak shoulder above the TO frequency which extends up to around 875 cm^{-1}. This cannot be explained by simple scattering to a HPP only. This however, could be the result of a combination mode with scattering to a HPP and a low frequency acoustic Raman mode.

Additionally, the signal starts ramping up at 735 cm^{-1}, which is before the expected 760 cm^{-1} TO frequency. This could be explained by the TO frequency being lower than the published values however multiple independent literature measurements and theoretical values suggest otherwise [114, 204, 210, 211], putting the value between 750 and 768 cm^{-1}. Subtractive combination modes also cannot explain the lower energy side as the thermal energy available for these measurements is 4 K which corresponds to 2.8 cm^{-1}. This is unlikely to not be associated with the scattering from the bulk of the HPP as it is observed at multiple energies and resonance conditions.

5.3 Conclusions

Until these measurements, the two hBN HPP modes were always associated with double resonance between the A1s and A2s. The results here have shown that, as may be expected, they can be observed at other resonances, such as the A2s outgoing and A3s. This also constitutes the first observation of Raman scattering from a 3s exciton in TMDs. These modes have also now been observed $MoSe_2$, which is the first time these have been observed in a Mo based TMD and the first observation of these resonant with a B exciton. In addition, the measurements on $MoSe_2$ clearly show that, at least in $MoSe_2$, the higher shift combination HPP + TMD phonon mode is not just a HPP + $A_1'(\Gamma)$ combination, but additionally a HPP + $E'_{TO/LO}(\Gamma)$ mode. As the two phonons are degenerate in WSe_2, this also suggests that the same is also likely to be true of WSe_2.

Despite previous reports identifying these modes as hBN HPPs, none attempted to explain the lineshape beyond this. The comparison of the lineshape of the HPP mode with a theoretical model of HPPs in the sample leads to remarkable conclusions. Firstly, with the limited momentum available from the exciting laser, momentum conservation should restrict the width of the HPP to the upper 25 cm^{-1} of the reststrahlen band. In order to access the full band, at least 5 times that momentum is required. The source of this additional momentum is not known but it suggests that resonant Raman scattering with a TMD exciton may allow access to probe higher wavevector states in other layered heterostructures such as a TMD on Silicon carbide. Additionally, scattering was observed below the bottom of the reststrahlen band which was clearly associated with the HPP feature. This is clearly not possible with current models of HPPs as they must be restricted entirely to the band. The HPP model can explain many features of the HPP lineshape, such as the shallower lower shift ramp up and sharp drop-off at the top of the reststrahlen band but it is highly likely that both momentum conservation breaking and a change in the model of the HPPs will be required to explain them fully.

Chapter 6

Conclusions

The aim of this thesis has been to use resonance Raman spectroscopy to understand the excitonic states in TMD monolayers and van der Waals heterostructures made from stacked TMD layers. Resonance Raman measurements combined with reflectivity and photoluminescence allowed for confident assignment of the A 1s and 2s excitons in both monolayers and heterostructures. This enabled the calculation of changes in the exciton binding energy and the single particle band gaps between monolayers and heterostructures. Resonance Raman measurements and modelling also revealed more about hyperbolic phonon polaritons in hBN which were excited via a range of excitonic states in the adjacent TMDs.

Resonance Raman measurements with exciting photon energies between 1.597 and 2.256 eV were performed on high quality hBN encapsulated TMD monolayers. These measurements revealed three clear resonances in WSe_2 monolayer, corresponding to the A1s, A2s and B1s excitonic states and four resonances in $MoSe_2$ corresponding to the A1s, A2s, B1s and B2s excitons. All of these states apart from the $MoSe_2$ B2s were also observed in reflectivity measurements of the same samples, confirming their assignment. In only the Raman spectra that were resonant with the WSe_2 A2s exciton, an intense Raman peak was observed at 495 cm^{-1}. This peak was more intense at the outgoing resonance than the incoming resonance, due to the presence of higher energy states in the Rydberg series (3s, 4s). At the A2s outgoing resonance energy, the peak split into 3 peaks which all shifted differently with excitation energy. The peak was assigned to three possible 2-phonon combinations: $2A_1'(\Gamma)$, $A_1'(\Gamma) + E'_{TO/LO}(\Gamma)$, and $2E'_{TO/LO}(\Gamma)$. An equivalent set of peaks were also observed in the $MoSe_2$ case where the $A_1'(\Gamma)$ and $E'_{TO/LO}(\Gamma)$ are no longer degenerate in energy, assigned to the same 2-phonon combinations. This trio of Raman peaks also had a similar association with the 2s excitons, showing no signal at the A1s. The reason that peaks were only present at the A2s was due to resonant enhancement from scattering to intermediate lower energy states at higher wavevector.

Resonance Raman measurements over the same excitation energy ranges as the monolayer measurements were also performed on hBN encapsulated heterostructures made from $WSe_2/MoSe_2$. Measurements of two different heterostructures were shown, with twist angles of 57° and 20° between crystal lattices in the two TMD layers. In this case, the reflectivity and PL measurements could not identify the 2s excitonic states due to increased linewidth and overlapping energies with states with greater oscillator strengths. Analysis of resonance Raman profiles of the 2s associated Raman peaks in the heterostructures gave mean energies of 1.760 eV and 1.846 eV for the A2s in $MoSe_2$ and WSe_2 respectively which are comparatively lower than the monolayer values of 1.800 and 1.871 eV respectively. This represents the first measurement of both of these energies. A model of the excitons in the monolayers and heterostructures based on the Keldysh potential was used to fit the energy separations for the monolayers and heterostructures using the in-plane polarizabaility of the two layers as the only free parameters. The model had good agreement with the measured energies and showed that the reduction in exciton binding energy for the A1s on forming the heterostructure is 8 meV for WSe_2 and 19 meV for $MoSe_2$ with a drop in single particle band gap of 25 and 31 meV for WSe_2 and $MoSe_2$.

Resonance Raman measurements of the broad hBN HPP features around 800 and 1050 cm^{-1} were also performed on the hBN encapsulated TMD monolayers with excitation energies covering the A excitonic states for WSe_2 and the A and B excitons of $MoSe_2$. The hBN HPP features were observed, as previously reported, at the WSe_2 A1s outgoing and A2s incoming resonances with the very intense Raman signal observed due to double resonance. Additionally, these features were also observed at the A2s and A3s outgoing resonances. The hBN HPP were also observed in encapsulated monolayer $MoSe_2$ at the double resonance conditions at the A1s outgoing / A2s incoming and the B1s outgoing / A2s incoming resonances. The lineshape and Raman shifts of the upper feature in the encapsulated $MoSe_2$ spectra were consistent with a combination of two 2-phonon scattering processes, one from the 800 cm^{-1} HPP feature + the $A_1'(\Gamma)$ phonon and another from the HPP + the $E'_{TO/LO}(\Gamma)$ phonon. Since these two phonons are degenerate in energy for monolayer WSe_2, it is also possible to conclude that both of these could be contributing to the signal observed at 1050 cm^{-1} from the encapsulated WSe_2 sample.

The lineshapes of the hBN HPPs at different resonance conditions differed significantly. However, the majority of this change was found to be due to resonant enhancement of different parts of the continuum of HPPs dependant on excitation energy, which follows the standard resonance Raman scattering model. Transfer matrix modelling of a hBN encapsulated WSe_2 monolayer was used to predict the dispersion relation of the HPP in the hBN. Comparisons of this dispersion relation with the observed lineshape in the Raman measurement revealed some significant details. Firstly, the Raman signal from the HPPs extended below the hBN reststrahlen band, which cannot be explained by the model, suggesting new HPP physics. Additionally, the HPP spanned the full

energy range reststrahlen band, and the momentum required by the model for this is much greater than what can be provided by optical photons. This shows that there is most likely breaking of momentum conservation in the photon to exciton to HPP scattering process. Whilst complete modelling the Raman lineshape would also require knowledge of the HPP lifetimes and exciton-HPP coupling, the results here suggest that resonance Raman scattering measurements can be used to probe large wavevector states via scattering with excitons.

6.1 Perspectives and Outlook

The goal of this thesis was to understand the electronic and vibrational states in TMD monolayers and heterostructures and how they interact. The results presented here have contribute significantly to this understanding and they have also revealed new physics. It is useful to consider where this research fits into the wider literature and how this work may be extended.

The simplest extension to these measurements would be to perform similar experiments on W and Mo disulphides. This could reveal equivalents to the 2s associated Raman peaks observed in $MoSe_2$ and WSe_2 which could be of use to others in the field. The different exciton energies would also provide more opportunities to observe effects such as hybridisation of states [98] or reveal more moiré effects.

A more interesting extension would be examining TMD heterostructures with a larger range of twist angles. It is clear that the twist angles have a significant effect on the excitonic states through reconstruction [94], and hybridisation [16, 97, 98]. Direct changes in the Raman spectrum are also expected, such as the observation of moiré phonons [13, 96]. Measurement of the effect of twist angle on interlayer excitons [216] would also be of interest. However, the very low oscillator strength means resonant Raman measurements at the interlayer exciton are unlikely to yield results.

Another natural extension to this work would be gated measurements. These would allow observation of Raman scattering from trions and other multi-particle states. Of particular interest are 2s trions which show stronger polaronic effects due to a greater sensitivity to the Fermi sea than 1s states [82]. This may also allow for the observation of strongly correlated electronic states, which have been observed in TMD bilayers [86, 217, 218].

Not all of the peaks in the Raman spectra have been unambiguously assigned to the various vibrational modes in literature. This is particularly true of the multi-phonon peaks at higher Raman shifts. Measurements of TMD monolayers under varying strain could allow more of the peaks to be identified as it would break the symmetry and also tune the shifts of different vibrational modes by different amounts. Full polarisation

measurements of the Stokes parameters combined with analysis of the selection rules of all the combination modes based on the symmetries could also allow for confident identification of more Raman peaks. Strained measurements are also interesting as they have shown shifts in the excitonic states [219–222] and shown strain induced moiré potentials [223].

Considering the longer term future of TMDs, the production of the highest quality monolayers still relies on mechanical exfoliation which is not ideal for commercial devices [29]. The recent improvements in TMD quality from deposition techniques like molecular beam epitaxy [224] and chemical vapour deposition [225] represent a step towards commercialisation. Better understanding of the processes involved in the loss of valley coherence could lead to the use of TMDs for valleytronics [11, 48]. As phonon mediated processes contribute to valley depolarisation, Raman measurements are a natural candidate to aid in this understanding. Just as the earlier 2D material, graphene, has seen successful commercialisation due to it's mechanical strength and electrical properties, it is most probable that TMDs also become increasingly relevant thanks to their diversity of interesting physics.

References

[1] K. S. Novoselov, *"Electric Field Effect in Atomically Thin Carbon Films,"* Science **306**, 666 (2004).

[2] L. Li, Y. Yu, G. J. Ye, Q. Ge, X. Ou, H. Wu, D. Feng, X. H. Chen, and Y. Zhang, *"Black phosphorus field-effect transistors,"* Nature Nanotechnology **9**, 372 (2014).

[3] W. Q. Han, L. Wu, Y. Zhu, K. Watanabe, and T. Taniguchi, *"Structure of chemically derived mono- and few-atomic-layer boron nitride sheets,"* Applied Physics Letters **93**, 1 (2008).

[4] K. F. Mak, C. Lee, J. Hone, J. Shan, and T. F. Heinz, *"Atomically Thin MoS2: A New Direct-Gap Semiconductor,"* Physical Review Letters **105**, 2 (2010).

[5] L. Wang, Z. Wang, H. Y. Wang, G. Grinblat, Y. L. Huang, D. Wang, X. H. Ye, X. B. Li, Q. Bao, A. S. Wee, S. A. Maier, Q. D. Chen, M. L. Zhong, C. W. Qiu, and H. B. Sun, *"Slow cooling and efficient extraction of C-exciton hot carriers in MoS2 monolayer,"* Nature Communications **8** (2017), 10.1038/ncomms13906.

[6] A. Carvalho, R. M. Ribeiro, and A. H. Castro Neto, *"Band nesting and the optical response of two-dimensional semiconducting transition metal dichalcogenides,"* Physical Review B - Condensed Matter and Materials Physics **88**, 1 (2013), arXiv:1305.6672 .

[7] L. V. Keldysh, *"Coulomb interaction in thin semiconductor and semimetal films,"* Soviet Journal of Experimental and Theoretical Physics Letters **29**, 658 (1979).

[8] P. Cudazzo, I. V. Tokatly, and A. Rubio, *"Dielectric screening in two-dimensional insulators: Implications for excitonic and impurity states in graphane,"* Physical Review B - Condensed Matter and Materials Physics **84**, 085406 (2011), arXiv:1104.3346 .

[9] W. Yao, D. Xiao, and Q. Niu, *"Valley-dependent optoelectronics from inversion symmetry breaking,"* Physical Review B - Condensed Matter and Materials Physics **77**, 1 (2008), arXiv:0705.4683 .

[10] K. F. Mak, K. He, J. Shan, and T. F. Heinz, *"Control of valley polarization in monolayer MoS2 by optical helicity,"* Nature Nanotechnology **7**, 494 (2012), arXiv:1205.1822 .

[11] J. R. Schaibley, H. Yu, G. Clark, P. Rivera, J. S. Ross, K. L. Seyler, W. Yao, and X. Xu, *"Valleytronics in 2D materials,"* Nature Reviews Materials **1** (2016), 10.1038/natrevmats.2016.55.

[12] P. J. Zomer, M. H. Guimarães, J. C. Brant, N. Tombros, and B. J. Van Wees, *"Fast pick up technique for high quality heterostructures of bilayer graphene and hexagonal boron nitride,"* Applied Physics Letters **105**, 013101 (2014), arXiv:1403.0399 .

[13] M. L. Lin, Q. H. Tan, J. B. Wu, X. S. Chen, J. H. Wang, Y. H. Pan, X. Zhang, X. Cong, J. Zhang, W. Ji, P. A. Hu, K. H. Liu, and P. H. Tan, *"Moiré phonons in twisted bilayer MoS2,"* ACS Nano **12**, 8770 (2018).

[14] L. P. McDonnell, J. J. S. Viner, P. Rivera, A. Cammarata, H. S. Sen, X. Xu, and D. C. Smith, *"Experimental realisation of Dual Periodicity Moiré Superlattice in a MoSe2/WSe2 Heterobilayer,"* arXiv (2020), 2009.07676, arXiv:2009.07676 .

[15] X. Huang, T. Wang, S. Miao, C. Wang, Z. Li, Z. Lian, T. Taniguchi, K. Watanabe, S. Okamoto, D. Xiao, S.-F. Shi, and Y.-T. Cui, *"Correlated insulating states at fractional fillings of the WS2/WSe2 moiré lattice,"* Nature Physics (2021), 10.1038/s41567-021-01171-w, arXiv:2007.11155 .

[16] D. A. Ruiz-Tijerina and V. I. Fal'Ko, *"Interlayer hybridization and moiré superlattice minibands for electrons and excitons in heterobilayers of transition-metal dichalcogenides,"* Physical Review B **99**, 30 (2019).

[17] K. L. Seyler, P. Rivera, H. Yu, N. P. Wilson, E. L. Ray, D. G. Mandrus, J. Yan, W. Yao, and X. Xu, *"Signatures of moire-trapped valley excitons in MoSe2/WSe2 heterobilayers,"* Nature **567**, 66 (2019), arXiv:1809.04562 .

[18] R. B. Murray and A. D. Yoffe, *"The band structures of some transition metal dichalcogenides: Band structures of the titanium dichalcogenides,"* Journal of Physics C: Solid State Physics **5**, 3038 (1972).

[19] S. Jiménez Sandoval, D. Yang, R. F. Frindt, and J. C. Irwin, *"Raman study and lattice dynamics of single molecular layers of MoS2,"* Physical Review B **44**, 3955 (1991).

[20] Z. Y. Zhu, Y. C. Cheng, and U. Schwingenschlögl, *"Giant spin-orbit-induced spin splitting in two-dimensional transition-metal dichalcogenide semiconductors,"* Physical Review B - Condensed Matter and Materials Physics **84**, 153402 (2011).

[21] J. van Baren, G. Ye, J. A. Yan, Z. Ye, P. Rezaie, P. Yu, Z. Liu, R. He, and C. H. Lui, *"Stacking-Dependent Interlayer Phonons in 3R and 2H MoS2,"* arXiv , 0 (2019).

[22] A. R. Beal, J. C. Knights, and W. Y. Liang, *"Transmission spectra of some transition metal dichalcogenides. I. Group IVA: Octahedral coordination,"* Journal of Physics C: Solid State Physics **5**, 3531 (1972).

[23] C. Ataca, H. Şahin, and S. Ciraci, *"Stable, single-layer MX 2 transition-metal oxides and dichalcogenides in a honeycomb-like structure,"* Journal of Physical Chemistry C **116**, 8983 (2012).

[24] R. Lv, J. A. Robinson, R. E. Schaak, D. Sun, Y. Sun, T. E. Mallouk, and M. Terrones, *"Transition metal dichalcogenides and beyond: Synthesis, properties, and applications of single- and few-layer nanosheets,"* Accounts of Chemical Research **48**, 56 (2015).

[25] N. Lu, H. Guo, L. Li, J. Dai, L. Wang, W. N. Mei, X. Wu, and X. C. Zeng, *"MoS2/MX2 heterobilayers: Bandgap engineering via tensile strain or external electrical field,"* Nanoscale **6**, 2879 (2014).

[26] R. J. Smith, P. J. King, M. Lotya, C. Wirtz, U. Khan, S. De, A. O'Neill, G. S. Duesberg, J. C. Grunlan, G. Moriarty, J. Chen, J. Wang, A. I. Minett, V. Nicolosi, and J. N. Coleman, *"Large-scale exfoliation of inorganic layered compounds in aqueous surfactant solutions,"* Advanced Materials **23**, 3944 (2011).

[27] K. S. Novoselov, D. Jiang, F. Schedin, T. J. Booth, V. V. Khotkevich, S. V. Morozov, and A. K. Geim, *"Two-dimensional atomic crystals,"* Proceedings of the National Academy of Sciences of the United States of America **102**, 10451 (2005).

[28] H. Zeng, J. Dai, W. Yao, D. Xiao, and X. Cui, *"Valley polarization in MoS2 monolayers by optical pumping,"* Nature Nanotechnology **7**, 490 (2012), arXiv:1202.1592 .

[29] Z. Cai, B. Liu, X. Zou, and H. M. Cheng, *"Chemical Vapor Deposition Growth and Applications of Two-Dimensional Materials and Their Heterostructures,"* Chemical Reviews **118**, 6091 (2018).

[30] M. M. Benameur, B. Radisavljevic, J. S. Héron, S. Sahoo, H. Berger, and A. Kis, *"Visibility of dichalcogenide nanolayers,"* Nanotechnology **22** (2011), 10.1088/0957-4484/22/12/125706.

[31] N. Kumar, S. Najmaei, Q. Cui, F. Ceballos, P. M. Ajayan, J. Lou, and H. Zhao, *"Second harmonic microscopy of monolayer MoS2,"* Physical Review B - Condensed Matter and Materials Physics **87**, 1 (2013), arXiv:1302.3935 .

[32] Y. Li, Y. Rao, K. F. Mak, Y. You, S. Wang, C. R. Dean, and T. F. Heinz, *"Probing Symmetry Properties of Few-Layer MoS 2 and h-BN by Optical Second-Harmonic Generation,"* Nano Letters **13**, 3329 (2013).

[33] L. M. Malard, T. V. Alencar, A. P. M. Barboza, K. F. Mak, and A. M. De Paula, *"Observation of intense second harmonic generation from MoS2 atomic crystals,"* Physical Review B - Condensed Matter and Materials Physics **87**, 1 (2013).

[34] T. Jiang, H. Liu, D. Huang, S. Zhang, Y. Li, X. Gong, Y. R. Shen, W. T. Liu, and S. Wu, *"Valley and band structure engineering of folded MoS2 bilayers,"* Nature Nanotechnology **9**, 825 (2014).

[35] L. M. Schneider, J. Kuhnert, S. Schmitt, W. Heimbrodt, U. Huttner, L. Meckbach, T. Stroucken, S. W. Koch, S. Fu, X. Wang, K. Kang, E. H. Yang, and A. Rahimi-Iman, *"Spin-Layer and Spin-Valley Locking in CVD-Grown AA'- and AB-Stacked Tungsten-Disulfide Bilayers,"* Journal of Physical Chemistry C **123**, 21813 (2019), arXiv:1905.02814 .

[36] T. Cheiwchanchamnangij and W. R. Lambrecht, *"Quasiparticle band structure calculation of monolayer, bilayer, and bulk MoS2,"* Physical Review B - Condensed Matter and Materials Physics **85**, 1 (2012).

[37] K. Komider, J. W. González, and J. Fernández-Rossier, *"Large spin splitting in the conduction band of transition metal dichalcogenide monolayers,"* Physical Review B - Condensed Matter and Materials Physics **88**, 1 (2013), arXiv:1311.0049 .

[38] E. S. Kadantsev and P. Hawrylak, *"Electronic structure of a single MoS 2 monolayer,"* Solid State Communications **152**, 909 (2012).

[39] W. Jin, P. C. Yeh, N. Zaki, D. Zhang, J. T. Sadowski, A. Al-Mahboob, A. M. Van Der Zande, D. A. Chenet, J. I. Dadap, I. P. Herman, P. Sutter, J. Hone, and R. M. Osgood, *"Direct measurement of the thickness-dependent electronic band structure of MoS2 using angle-resolved photoemission spectroscopy,"* Physical Review Letters **111**, 1 (2013).

[40] N. R. Wilson, P. V. Nguyen, K. Seyler, P. Rivera, A. J. Marsden, Z. P. Laker, G. C. Constantinescu, V. Kandyba, A. Barinov, N. D. Hine, X. Xu, and D. H. Cobden, *"Determination of band offsets, hybridization, and exciton binding in 2D semiconductor heterostructures,"* Science Advances **3**, 1 (2017).

[41] S. Park, N. Mutz, T. Schultz, S. Blumstengel, A. Han, A. Aljarb, L.-J. J. Li, E. J. W. List-Kratochvil, P. Amsalem, N. Koch, T. Schultz, N. Mutz, S. Park, N. Koch, E. J. W. List-Kratochvil, A. Aljarb, S. Blumstengel, L.-J. J. Li, A. Han, N. Mutz, T. Schultz, S. Blumstengel, A. Han, A. Aljarb, L.-J. J. Li, E. J. W. List-Kratochvil, P. Amsalem, and N. Koch, *"Direct determination of monolayer*

MoS2 and WSe2 exciton binding energies on insulating and metallic substrates," 2D Materials **5**, 025003 (2018).

[42] N. P. Wilson, H. Yu, P. Rivera, W. Yao, X. Xu, and K. L. Seyler, *"Interlayer valley excitons in heterobilayers of transition metal dichalcogenides,"* Nature Nanotechnology **13**, 1004 (2018).

[43] G. B. Liu, W. Y. Shan, Y. Yao, W. Yao, and D. Xiao, *"Three-band tight-binding model for monolayers of group-VIB transition metal dichalcogenides,"* Physical Review B - Condensed Matter and Materials Physics **88**, 1 (2013), arXiv:1305.6089 .

[44] A. Splendiani, L. Sun, Y. Zhang, T. Li, J. Kim, C. Y. Chim, G. Galli, and F. Wang, *"Emerging photoluminescence in monolayer MoS2,"* Nano Letters **10**, 1271 (2010), arXiv:1308.1834 [cond-mat.mtrl-sci] .

[45] D. Xiao, G.-B. Liu, W. Feng, X. Xu, and W. Yao, *"Coupled Spin and Valley Physics in Monolayers of MoS2 and Other Group-VI Dichalcogenides,"* Phys. Rev. Lett. **108**, 196802 (2012), arXiv:1112.3144 .

[46] Z. Jin, X. Li, J. T. Mullen, and K. W. Kim, *"Intrinsic transport properties of electrons and holes in monolayer transition-metal dichalcogenides,"* Physical Review B **90**, 045422 (2014).

[47] S. Wu, J. S. Ross, G. B. Liu, G. Aivazian, A. Jones, Z. Fei, W. Zhu, D. Xiao, W. Yao, D. Cobden, and X. Xu, *"Electrical tuning of valley magnetic moment through symmetry control in bilayer MoS 2,"* Nature Physics **9**, 149 (2013).

[48] A. M. Jones, H. Yu, N. J. Ghimire, S. Wu, G. Aivazian, J. S. Ross, B. Zhao, J. Yan, D. G. Mandrus, D. Xiao, W. Yao, and X. Xu, *"Optical generation of excitonic valley coherence in monolayer WSe 2,"* Nature Nanotechnology **8**, 634 (2013).

[49] C. Mai, A. Barrette, Y. Yu, Y. G. Semenov, K. W. Kim, L. Cao, and K. Gundogdu, *"Many-Body Effects in Valleytronics: Direct Measurement of Valley Lifetimes in Single-Layer MoS 2,"* Nano Letters **14**, 202 (2014).

[50] N. W. Ashcroft and N. D. Mermin, *Solid State Physics*, college ed. (Saunders College Publishing, 1976) p. 826.

[51] A. Chernikov, T. C. Berkelbach, H. M. Hill, A. Rigosi, Y. Li, O. B. Aslan, D. R. Reichman, M. S. Hybertsen, and T. F. Heinz, *"Exciton Binding Energy and Nonhydrogenic Rydberg Series in Monolayer WS2,"* Physical Review Letters **113**, 076802 (2014).

[52] M. A. Green, *"Improved value for the silicon free exciton binding energy,"* AIP Advances **3** (2013), 10.1063/1.4828730.

[53] Z. Ye, T. Cao, K. O'Brien, H. Zhu, X. Yin, Y. Wang, S. G. Louie, and X. Zhang, *"Probing excitonic dark states in single-layer tungsten disulphide,"* Nature **513**, 214 (2014), arXiv:1403.5568 .

[54] X. L. Yang, S. H. Guo, F. T. Chan, K. W. Wong, and W. Y. Ching, *"Analytic solution of a two-dimensional hydrogen atom. I. Nonrelativistic theory,"* Physical Review A **43**, 1186 (1991).

[55] B. L. Evans and P. A. Young, *"Exciton spectra in thin crystals: The diamagnetic effect,"* Proceedings of the Physical Society **91**, 475 (1967).

[56] K. He, N. Kumar, L. Zhao, Z. Wang, K. F. Mak, H. Zhao, and J. Shan, *"Tightly bound excitons in monolayer WSe2,"* Physical Review Letters **113**, 1 (2014).

[57] H. M. Hill, A. F. Rigosi, C. Roquelet, A. Chernikov, T. C. Berkelbach, D. R. Reichman, M. S. Hybertsen, L. E. Brus, and T. F. Heinz, *"Observation of excitonic rydberg states in monolayer MoS2 and WS2 by photoluminescence excitation spectroscopy,"* Nano Letters **15**, 2992 (2015).

[58] N. S. Rytova, A. Chernikov, and M. M. Glazov, *"Screened potential of a point charge in a thin film,"* Moscow University Physics Bulletin **3**, 30 (1967), arXiv:1806.00976 .

[59] M. Danovich, D. A. Ruiz-Tijerina, R. J. Hunt, M. Szyniszewski, N. D. Drummond, and V. I. Fal'Ko, *"Localized interlayer complexes in heterobilayer transition metal dichalcogenides,"* Physical Review B **97**, 195452 (2018), arXiv:1802.06005 .

[60] E. Liu, J. Van Baren, T. Taniguchi, K. Watanabe, Y. C. Chang, and C. H. Lui, *"Magnetophotoluminescence of exciton Rydberg states in monolayer WSe2,"* Physical Review B **99**, 205420 (2019), arXiv:1901.11044 .

[61] a. V. Stier, N. P. Wilson, K. a. Velizhanin, J. Kono, X. Xu, and S. a. Crooker, *"Magnetooptics of Exciton Rydberg States in a Monolayer Semiconductor,"* Physical Review Letters **120**, 057405 (2018), arXiv:1709.00123 .

[62] C. Robert, M. A. Semina, F. Cadiz, M. Manca, E. Courtade, T. Taniguchi, K. Watanabe, H. Cai, S. Tongay, B. Lassagne, P. Renucci, T. Amand, X. Marie, M. M. Glazov, and B. Urbaszek, *"Optical spectroscopy of excited exciton states in MoS2 monolayers in van der Waals heterostructures,"* Physical Review Materials **2**, 011001 (2018), arXiv:1712.01548 .

[63] L. P. McDonnell, J. Viner, P. Rivera, X. Xu, and D. C. Smith, *"Observation of Intravalley Phonon Scattering of 2s Excitons in MoSe2 and WSe2 Monolayers,"* 2D Materials **7**, 045008 (2020), arXiv:2006.05912 .

[64] M. Palummo, M. Bernardi, and J. C. Grossman, *"Exciton radiative lifetimes in two-dimensional transition metal dichalcogenides,"* Nano Letters **15**, 2794 (2015).

[65] S. Brem, J. Zipfel, M. Selig, A. Raja, L. Waldecker, J. D. Ziegler, T. Taniguchi, K. Watanabe, A. Chernikov, and E. Malic, *"Intrinsic lifetime of higher excitonic states in tungsten diselenide monolayers,"* Nanoscale **11**, 12381 (2019), arXiv:1904.04729 .

[66] E. Malic, M. Selig, M. Feierabend, S. Brem, D. Christiansen, F. Wendler, A. Knorr, and G. Berghäuser, *"Dark excitons in transition metal dichalcogenides,"* Physical Review Materials **2**, 014002 (2018).

[67] T. Korn, S. Heydrich, M. Hirmer, J. Schmutzler, and C. Schller, *"Low-temperature photocarrier dynamics in monolayer MoS2,"* Applied Physics Letters **99**, 2 (2011), arXiv:1106.2951 .

[68] A. Ramasubramaniam, *"Large excitonic effects in monolayers of molybdenum and tungsten dichalcogenides,"* Physical Review B - Condensed Matter and Materials Physics **86**, 1 (2012).

[69] M. Selig, G. Berghäuser, A. Raja, P. Nagler, C. Schüller, T. F. Heinz, T. Korn, A. Chernikov, E. Malic, and A. Knorr, *"Excitonic linewidth and coherence lifetime in monolayer transition metal dichalcogenides,"* Nature Communications **7** (2016), 10.1038/ncomms13279, arXiv:1605.03359 .

[70] E. Liu, J. van Baren, T. Taniguchi, K. Watanabe, Y.-C. Chang, and C. H. Lui, *"Valley-selective chiral phonon replicas of dark excitons and trions in monolayer WSe2,"* Physical Review Research **1**, 1 (2019).

[71] L. P. McDonnell, C. C. Huang, Q. Cui, D. W. Hewak, and D. C. Smith, *"Probing Excitons, Trions, and Dark Excitons in Monolayer WS2 Using Resonance Raman Spectroscopy,"* Nano Letters **18**, 1428 (2018).

[72] X. X. Zhang, Y. You, S. Y. F. Zhao, and T. F. Heinz, *"Experimental Evidence for Dark Excitons in Monolayer WSe2,"* Physical Review Letters **115**, 1 (2015).

[73] K. F. Mak, K. He, C. Lee, G. H. Lee, J. Hone, T. F. Heinz, and J. Shan, *"Tightly bound trions in monolayer MoS2,"* Nature Materials **12**, 207 (2013).

[74] J. S. Ross, S. Wu, H. Yu, N. J. Ghimire, A. M. Jones, G. Aivazian, J. Yan, D. G. Mandrus, D. Xiao, W. Yao, and X. Xu, *"Electrical control of neutral and charged excitons in a monolayer semiconductor,"* Nature communications **4**, 1474 (2013).

[75] M. Drüppel, T. Deilmann, P. Krüger, and M. Rohlfing, *"Diversity of trion states and substrate effects in the optical properties of an MoS2 monolayer,"* Nature Communications **8**, 2117 (2017).

[76] G. Plechinger, P. Nagler, A. Arora, R. Schmidt, A. Chernikov, A. G. Del Águila, P. C. Christianen, R. Bratschitsch, C. Schüller, and T. Korn, *"Trion fine structure and coupled spin-valley dynamics in monolayer tungsten disulfide,"* Nature Communications **7**, 1 (2016), arXiv:1803.06405 .

[77] Y. You, X. X. Zhang, T. C. Berkelbach, M. S. Hybertsen, D. R. Reichman, and T. F. Heinz, *"Observation of biexcitons in monolayer WSe 2,"* Nature Physics **11**, 477 (2015).

[78] T. Taniguchi, S. Tongay, H. Li, M. Atatüre, A. C. Ferrari, A. R. Cadore, E. Mostaani, B. Pingault, D. De Fazio, A. R.-P. Montblanch, M. Barbone, B. Chen, K. Watanabe, G. Wang, D. M. Kara, and C. Palacios-Berraquero, *"Charge-tuneable biexciton complexes in monolayer WSe2,"* Nature Communications **9** (2018), 10.1038/s41467-018-05632-4.

[79] Z. Ye, L. Waldecker, E. Y. Ma, D. Rhodes, A. Antony, B. Kim, X. X. Zhang, M. Deng, Y. Jiang, Z. Lu, D. Smirnov, K. Watanabe, T. Taniguchi, J. Hone, and T. F. Heinz, *"Efficient generation of neutral and charged biexcitons in encapsulated WSe2 monolayers,"* Nature Communications **9**, 6 (2018).

[80] Z. Li, T. Wang, Z. Lu, C. Jin, Y. Chen, Y. Meng, Z. Lian, T. Taniguchi, K. Watanabe, S. Zhang, D. Smirnov, and S. F. Shi, *"Revealing the biexciton and trion-exciton complexes in BN encapsulated WSe2,"* Nature Communications **9**, 1 (2018).

[81] A. Arora, T. Deilmann, T. Reichenauer, J. Kern, S. Michaelis De Vasconcellos, M. Rohlfing, and R. Bratschitsch, *"Excited-State Trions in Monolayer WS2,"* Physical Review Letters **123**, 167401 (2019).

[82] T. Goldstein, Y.-C. C. Wu, S.-Y. Y. Chen, T. Taniguchi, K. Watanabe, K. Varga, and J. Yan, *"Ground and excited state exciton polarons in monolayer MoSe2,"* The Journal of Chemical Physics **153**, 071101 (2020), arXiv:2005.05829 .

[83] D. K. Efimkin and A. H. MacDonald, *"Many-body theory of trion absorption features in two-dimensional semiconductors,"* Physical Review B **95**, 1 (2017), arXiv:1609.06329 .

[84] M. Sidler, P. Back, O. Cotlet, A. Srivastava, T. Fink, M. Kroner, E. Demler, and A. Imamoglu, *"Fermi polaron-polaritons in charge-tunable atomically thin semiconductors,"* Nature Physics **13**, 255 (2017), arXiv:1603.09215 .

[85] K. Wagner, E. Wietek, J. D. Ziegler, M. A. Semina, T. Taniguchi, K. Watanabe, J. Zipfel, M. M. Glazov, and A. Chernikov, *"Autoionization and Dressing of Excited Excitons by Free Carriers in Monolayer WSe2,"* Physical Review Letters **125**, 267401 (2020), arXiv:2007.05396 .

[86] Y. Shimazaki, I. Schwartz, K. Watanabe, T. Taniguchi, M. Kroner, and A. Imamoğlu, *"Strongly correlated electrons and hybrid excitons in a moiré heterostructure,"* Nature **580**, 472 (2020).

[87] I. C. Gerber, E. Courtade, S. Shree, C. Robert, T. Taniguchi, K. Watanabe, A. Balocchi, P. Renucci, D. Lagarde, X. Marie, and B. Urbaszek, *"Interlayer excitons in bilayer MoS2 with strong oscillator strength up to room temperature,"* Physical Review B **99**, 1 (2019), arXiv:1811.06469 .

[88] A. T. Hanbicki, H. J. Chuang, M. R. Rosenberger, C. S. Hellberg, S. V. Sivaram, K. M. McCreary, I. I. Mazin, and B. T. Jonker, *"Double Indirect Interlayer Exciton in a MoSe2/WSe2 van der Waals Heterostructure,"* ACS Nano **12**, 4719 (2018), arXiv:1802.05310 .

[89] P. Rivera, J. R. Schaibley, A. M. Jones, J. S. Ross, S. Wu, G. Aivazian, P. Klement, K. Seyler, G. Clark, N. J. Ghimire, J. Yan, D. G. Mandrus, W. Yao, and X. Xu, *"Observation of long-lived interlayer excitons in monolayer MoSe 2-WSe 2 heterostructures,"* Nature Communications **6**, 4 (2015), arXiv:1403.4985 .

[90] F. Ceballos, M. Z. Bellus, H. Y. Chiu, and H. Zhao, *"Probing charge transfer excitons in a MoSe2-WS2 van der Waals heterostructure,"* Nanoscale **7**, 17523 (2015).

[91] K. L. Seyler, P. Rivera, H. Yu, N. P. Wilson, E. L. Ray, D. G. Mandrus, J. Yan, W. Yao, and X. Xu, *"Signatures of moiré-trapped valley excitons in MoSe2/WSe2 heterobilayers,"* Nature **567**, 66 (2019).

[92] C. Jin, E. C. Regan, A. Yan, M. Iqbal Bakti Utama, D. Wang, S. Zhao, Y. Qin, S. Yang, Z. Zheng, S. Shi, K. Watanabe, T. Taniguchi, S. Tongay, A. Zettl, and F. Wang, *"Observation of moiré excitons in WSe2/WS2 heterostructure superlattices,"* Nature **567**, 76 (2019), arXiv:1812.09815 .

[93] A. a. Puretzky, L. Liang, X. Li, K. Xiao, B. G. Sumpter, V. Meunier, and D. B. Geohegan, *"Twisted MoSe2 Bilayers with Variable Local Stacking and Interlayer Coupling Revealed by Low-Frequency Raman Spectroscopy,"* ACS Nano **10**, 2736 (2016).

[94] A. Weston, Y. Zou, V. Enaldiev, A. Summerfield, N. Clark, V. Zólyomi, A. Graham, C. Yelgel, S. Magorrian, M. Zhou, J. Zultak, D. Hopkinson, A. Barinov, T. H. Bointon, A. Kretinin, N. R. Wilson, P. H. Beton, V. I. Fal'ko, S. J. Haigh, and R. Gorbachev, *"Atomic reconstruction in twisted bilayers of transition metal dichalcogenides,"* Nature Nanotechnology **15**, 592 (2020), arXiv:1911.12664 .

[95] V. V. Enaldiev, V. Zólyomi, C. Yelgel, S. J. Magorrian, and V. I. Fal'ko, *"Stacking Domains and Dislocation Networks in Marginally Twisted Bilayers of Transition Metal Dichalcogenides,"* Physical Review Letters **124**, 206101 (2020), arXiv:1911.12804 .

[96] J. Quan, L. Linhart, M. L. Lin, D. Lee, J. Zhu, C. Y. Wang, W. T. Hsu, J. Choi, J. Embley, C. Young, T. Taniguchi, K. Watanabe, C. K. Shih, K. Lai,

A. H. MacDonald, P. H. Tan, F. Libisch, and X. Li, *"Phonon renormalization in reconstructed MoS2 moiré superlattices,"* Nature Materials **20**, 1100 (2021), arXiv:2009.10650 .

[97] E. M. Alexeev, D. A. Ruiz-Tijerina, M. Danovich, M. J. Hamer, D. J. Terry, P. K. Nayak, S. Ahn, S. Pak, J. Lee, J. I. Sohn, M. R. Molas, M. Koperski, K. Watanabe, T. Taniguchi, K. S. Novoselov, R. V. Gorbachev, H. S. Shin, V. I. Fal'ko, and A. I. Tartakovskii, *"Resonantly hybridized excitons in moiré superlattices in van der Waals heterostructures,"* Nature **567**, 81 (2019), arXiv:1904.06214 .

[98] L. P. McDonnell, J. J. S. Viner, D. A. Ruiz-Tijerina, P. Rivera, X. Xu, V. I. Fal'ko, and D. C. Smith, *"Superposition of intra- and inter-layer excitons in twistronic MoSe2/WSe2 bilayers probed by resonant Raman scattering,"* 2D Materials **8**, 035009 (2021), arXiv:2010.02112 .

[99] W. Jaegermann and D. Schmeisser, *"Reactivity of layer type transition metal chalcogenides towards oxidation,"* Surface Science **165**, 143 (1986).

[100] G. Cassabois, P. Valvin, and B. Gil, *"Hexagonal boron nitride is an indirect bandgap semiconductor,"* Nature Photonics **10**, 262 (2016), arXiv:1512.02962 .

[101] E. W. Martin, J. Horng, H. G. Ruth, E. Paik, M. H. Wentzel, H. Deng, and S. T. Cundiff, *"Encapsulation narrows and preserves the excitonic homogeneous linewidth of exfoliated monolayer MoSe2,"* Physical Review Applied **14**, 1 (2020).

[102] E. Courtade, B. Han, S. Nakhaie, C. Robert, X. Marie, P. Renucci, T. Taniguchi, K. Watanabe, L. Geelhaar, J. M. Lopes, and B. Urbaszek, *"Spectrally narrow exciton luminescence from monolayer MoS2 and MoSe2 exfoliated onto epitaxially grown hexagonal BN,"* Applied Physics Letters **113** (2018), 10.1063/1.5033554, arXiv:1804.06623 .

[103] J. Wierzbowski, J. Klein, F. Sigger, C. Straubinger, M. Kremser, T. Taniguchi, K. Watanabe, U. Wurstbauer, A. W. Holleitner, M. Kaniber, K. Müller, and J. J. Finley, *"Direct exciton emission from atomically thin transition metal dichalcogenide heterostructures near the lifetime limit,"* Scientific Reports **7**, 7 (2017), arXiv:1705.00348 .

[104] M. Cardona and R. Merlin, in *Topics in Applied Physics*, Vol. 8 (Springer-Verlag Berlin Heidelberg GmbH, 1975) pp. 1–14.

[105] Y. Y. Peter and C. Manuel, *Fundamentals of Semiconductors* (Springer Heidelberg Dordrecht London New York, 2010) p. 775.

[106] H. Kuzmany, *Solid-State Spectroscopy - An Introduction* (Springer Berlin Heidelberg, Berlin, Heidelberg, 2009) pp. 185–200, arXiv:arXiv:1011.1669v3 .

[107] X. Zhang, X.-F. Qiao, W. Shi, J.-B. Wu, D.-S. Jiang, and P.-H. Tan, *"Phonon and Raman scattering of two-dimensional transition metal dichalcogenides from monolayer, multilayer to bulk material,"* Chemical Society Reviews **44**, 2757 (2015), arXiv:1502.00701 .

[108] C. Lee, H. Yan, L. E. Brus, T. F. Heinz, J. Hone, and S. Ryu, *"Anomalous lattice vibrations of single- and few-layer MoS2,"* ACS Nano **4**, 2695 (2010).

[109] R. A. Bromley, *"The lattice vibrations of the MoS2 structure,"* Philosophical Magazine **23**, 1417 (1971).

[110] I. Bilgin, A. S. Raeliarijaona, M. C. Lucking, S. C. Hodge, A. D. Mohite, A. De Luna Bugallo, H. Terrones, and S. Kar, *"Resonant Raman and Exciton Coupling in High-Quality Single Crystals of Atomically Thin Molybdenum Diselenide Grown by Vapor-Phase Chalcogenization,"* ACS Nano **12**, 740 (2018).

[111] M. De Luca, X. Cartoixà, J. Martín-Sánchez, M. López-Suárez, R. Trotta, R. Rurali, and I. Zardo, *"New insights in the lattice dynamics of monolayers, bilayers, and trilayers of WSe2 and unambiguous determination of few-layer-flakes' thickness,"* 2D Materials **7** (2020), 10.1088/2053-1583/ab5dec.

[112] A. Molina-Sánchez and L. Wirtz, *"Phonons in single-layer and few-layer MoS2 and WS2,"* Physical Review B - Condensed Matter and Materials Physics **84**, 1 (2011).

[113] H. Terrones, E. Del Corro, S. Feng, J. M. Poumirol, D. Rhodes, D. Smirnov, N. R. Pradhan, Z. Lin, M. A. Nguyen, A. L. Elías, T. E. Mallouk, L. Balicas, M. A. Pimenta, and M. Terrones, *"New First Order Raman-active Modes in Few Layered Transition Metal Dichalcogenides,"* Scientific Reports **4**, 4215 (2014).

[114] J. D. Caldwell, A. V. Kretinin, Y. Chen, V. Giannini, M. M. Fogler, Y. Francescato, C. T. Ellis, J. G. Tischler, C. R. Woods, A. J. Giles, M. Hong, K. Watanabe, T. Taniguchi, S. A. Maier, and K. S. Novoselov, *"Sub-diffractional volume-confined polaritons in the natural hyperbolic material hexagonal boron nitride,"* Nature Communications **5**, 5221 (2014).

[115] P. Li, M. Lewin, A. V. Kretinin, J. D. Caldwell, K. S. Novoselov, T. Taniguchi, K. Watanabe, F. Gaussmann, and T. Taubner, *"Hyperbolic phonon-polaritons in boron nitride for near-field optical imaging and focusing,"* Nature Communications **6**, 7507 (2015).

[116] I. H. Lee, M. He, X. Zhang, Y. Luo, S. Liu, J. H. Edgar, K. Wang, P. Avouris, T. Low, J. D. Caldwell, and S. H. Oh, *"Image polaritons in boron nitride for extreme polariton confinement with low losses,"* Nature Communications **11**, 3649 (2020).

[117] S. Dai, Q. Ma, T. Andersen, A. S. McLeod, Z. Fei, M. K. Liu, M. Wagner, K. Watanabe, T. Taniguchi, M. Thiemens, F. Keilmann, P. Jarillo-Herrero, M. M. Fogler, and D. N. Basov, *"Subdiffractional focusing and guiding of polaritonic rays in a natural hyperbolic material,"* Nature Communications **6**, 6963 (2015).

[118] N. C. Passler, C. R. Gubbin, T. G. Folland, I. Razdolski, D. S. Katzer, D. F. Storm, M. Wolf, S. De Liberato, J. D. Caldwell, and A. Paarmann, *"Strong Coupling of Epsilon-Near-Zero Phonon Polaritons in Polar Dielectric Heterostructures,"* Nano Letters **18**, 4285 (2018), arXiv:1811.05754 .

[119] I. Razdolski, Y. Chen, A. J. Giles, S. Gewinner, W. Schöllkopf, M. Hong, M. Wolf, V. Giannini, J. D. Caldwell, S. A. Maier, and A. Paarmann, *"Resonant Enhancement of Second-Harmonic Generation in the Mid-Infrared Using Localized Surface Phonon Polaritons in Subdiffractional Nanostructures,"* Nano Letters **16**, 6954 (2016).

[120] A. Paarmann, I. Razdolski, A. Melnikov, S. Gewinner, W. Schöllkopf, and M. Wolf, *"Second harmonic generation spectroscopy in the Reststrahl band of SiC using an infrared free-electron laser,"* Applied Physics Letters **107**, 081101 (2015).

[121] N. C. Passler, I. Razdolski, S. Gewinner, W. Schöllkopf, M. Wolf, and A. Paarmann, *"Second-Harmonic Generation from Critically Coupled Surface Phonon Polaritons,"* ACS Photonics **4**, 1048 (2017), arXiv:1702.03705 .

[122] T. G. Folland, L. Nordin, D. Wasserman, and J. D. Caldwell, *"Probing polaritons in the mid- to far-infrared,"* Journal of Applied Physics **125**, 191102 (2019).

[123] T. G. Folland, A. Fali, S. T. White, J. R. Matson, S. Liu, N. A. Aghamiri, J. H. Edgar, R. F. Haglund, Y. Abate, and J. D. Caldwell, *"Reconfigurable infrared hyperbolic metasurfaces using phase change materials,"* Nature Communications **9**, 4371 (2018).

[124] J. Chen, M. Badioli, P. Alonso-González, S. Thongrattanasiri, F. Huth, J. Osmond, M. Spasenović, A. Centeno, A. Pesquera, P. Godignon, A. Zurutuza Elorza, N. Camara, F. J. García, R. Hillenbrand, and F. H. Koppens, *"Optical nano-imaging of gate-tunable graphene plasmons,"* Nature **487**, 77 (2012).

[125] S. Dai, Z. Fei, Q. Ma, A. S. Rodin, M. Wagner, A. S. McLeod, M. K. Liu, W. Gannett, W. Regan, K. Watanabe, T. Taniguchi, M. Thiemens, G. Dominguez, A. H. Castro Neto, A. Zettl, F. Keilmann, P. Jarillo-Herrero, M. M. Fogler, and D. N. Basov, *"Tunable phonon polaritons in atomically thin van der Waals crystals of boron nitride,"* Science **343**, 1125 (2014).

[126] Z. Fei, A. S. Rodin, G. O. Andreev, W. Bao, A. S. McLeod, M. Wagner, L. M. Zhang, Z. Zhao, M. Thiemens, G. Dominguez, M. M. Fogler, A. H. Castro Neto,

C. N. Lau, F. Keilmann, and D. N. Basov, *"Gate-tuning of graphene plasmons revealed by infrared nano-imaging,"* Nature **487**, 82 (2012).

[127] L. Liang, J. Zhang, B. G. Sumpter, Q. H. Tan, P. H. Tan, and V. Meunier, *"Low-Frequency Shear and Layer-Breathing Modes in Raman Scattering of Two-Dimensional Materials,"* ACS Nano **11**, 11777 (2017).

[128] C. Neumann, S. Reichardt, P. Venezuela, M. Drögeler, L. Banszerus, M. Schmitz, K. Watanabe, T. Taniguchi, F. Mauri, B. Beschoten, S. V. Rotkin, and C. Stampfer, *"Raman spectroscopy as probe of nanometre-scale strain variations in graphene,"* Nature Communications **6**, 1 (2015), arXiv:1406.7771 .

[129] J. T. Mlack, P. Masih Das, G. Danda, Y. C. Chou, C. H. Naylor, Z. Lin, N. P. López, T. Zhang, M. Terrones, A. T. Johnson, and M. Drndic, *"Transfer of monolayer TMD WS 2 and Raman study of substrate effects,"* Scientific Reports **7**, 1 (2017).

[130] W. Shi, M. L. Lin, Q. H. Tan, X. F. Qiao, J. Zhang, and P. H. Tan, *"Raman and photoluminescence spectra of two-dimensional nanocrystallites of monolayer WS2 and WSe2,"* 2D Materials **3** (2016), 10.1088/2053-1583/3/2/025016.

[131] C. Lee, H. Yan, L. E. Brus, T. F. Heinz, J. Hone, and S. Ryu, *"Anomalous lattice vibrations of single- and few-layer MoS2,"* ACS Nano **4**, 2695 (2010).

[132] H. Li, Q. Zhang, C. C. R. Yap, B. K. Tay, T. H. T. Edwin, A. Olivier, and D. Baillargeat, *"From bulk to monolayer MoS 2: Evolution of Raman scattering,"* Advanced Functional Materials **22**, 1385 (2012).

[133] A. Berkdemir, H. R. Gutiérrez, A. R. Botello-Méndez, N. Perea-López, A. L. Elías, C.-I. Chia, B. Wang, V. H. Crespi, F. López-Urías, J.-C. Charlier, H. Terrones, and M. Terrones, *"Identification of individual and few layers of WS2 using Raman Spectroscopy,"* Scientific Reports **3**, 1755 (2013).

[134] W. Zhao, Z. Ghorannevis, K. K. Amara, J. R. Pang, M. Toh, X. Zhang, C. Kloc, P. H. Tan, and G. Eda, *"Lattice dynamics in mono- and few-layer sheets of WS2 and WSe2,"* Nanoscale **5**, 9677 (2013), arXiv:1304.0911 .

[135] R. Loudon, *"The Raman effect in crystals,"* Advances in Physics **13**, 423 (1964).

[136] B. R. Carvalho, L. M. Malard, J. M. Alves, C. Fantini, and M. a. Pimenta, *"Symmetry-dependent exciton-phonon coupling in 2D and bulk MoS2 observed by resonance Raman scattering,"* Physical Review Letters **114**, 1 (2015).

[137] E. Del Corro, A. Botello-Méndez, Y. Gillet, A. L. Elias, H. Terrones, S. Feng, C. Fantini, D. Rhodes, N. Pradhan, L. Balicas, X. Gonze, J. C. Charlier, M. Terrones, and M. A. Pimenta, *"Atypical Exciton-Phonon Interactions in WS2 and*

WSe2 Monolayers Revealed by Resonance Raman Spectroscopy," Nano Letters **16**, 2363 (2016).

[138] P. Soubelet, a. E. Bruchhausen, A. Fainstein, K. Nogajewski, and C. Faugeras, *"Resonance effects in the Raman scattering of monolayer and few-layer MoSe2,"* Physical Review B **93**, 155407 (2016).

[139] M. a. Pimenta, V. H. Crespi, L. M. Malard, Y. Wang, B. R. Carvalho, S. Mignuzzi, D. Roy, M. Terrones, and C. Fantini, *"Intervalley scattering by acoustic phonons in two-dimensional MoS2 revealed by double-resonance Raman spectroscopy,"* Nature Communications **8**, 14670 (2017).

[140] E. Del Corro, H. Terrones, A. Elias, C. Fantini, S. Feng, M. A. Nguyen, T. E. Mallouk, M. Terrones, and M. a. Pimenta, *"Excited Excitonic States in 1L, 2L, 3L, and Bulk WSe2 Observed by Resonant Raman Spectroscopy,"* ACS Nano **8**, 9629 (2014).

[141] J. Zipfel, J. Holler, A. A. Mitioglu, M. V. Ballottin, P. Nagler, A. V. Stier, T. Taniguchi, K. Watanabe, S. A. Crooker, P. C. Christianen, T. Korn, and A. Chernikov, *"Spatial extent of the excited exciton states in WS2 monolayers from diamagnetic shifts,"* Physical Review B **98**, 1 (2018), arXiv:1808.07786 .

[142] J. Kutrowska-Girzycka, P. Kapuściński, L. Bryja, A. Wójs, J. Jadczak, and Y. S. Huang, *"Probing of free and localized excitons and trions in atomically thin WSe2, WS2, MoSe2 and MoS2 in photoluminescence and reflectivity experiments,"* Nanotechnology **28**, 395702 (2017).

[143] B. Han, C. Robert, E. Courtade, M. Manca, S. Shree, T. Amand, P. Renucci, T. Taniguchi, K. Watanabe, X. Marie, L. E. Golub, M. M. Glazov, and B. Urbaszek, *"Exciton States in Monolayer MoSe2 and MoTe2 Probed by Upconversion Spectroscopy,"* Physical Review X **8**, 031073 (2018), arXiv:1805.04440 .

[144] Y. Li, A. Chernikov, X. Zhang, A. Rigosi, H. M. Hill, A. M. van der Zande, D. A. Chenet, E.-M. Shih, J. Hone, and T. F. Heinz, *"Measurement of the optical dielectric function of monolayer transition-metal dichalcogenides: MoS2, MoSe2, WS2, and WSe2,"* Physical Review B **90**, 205422 (2014).

[145] M. R. Molas, A. O. Slobodeniuk, K. Nogajewski, M. Bartos, Bala, A. Babiński, K. Watanabe, T. Taniguchi, C. Faugeras, and M. Potemski, *"Energy Spectrum of Two-Dimensional Excitons in a Nonuniform Dielectric Medium,"* Physical Review Letters **123** (2019), 10.1103/PhysRevLett.123.136801, arXiv:1902.03962 .

[146] C. Zhu, B. Liu, P. Tan, H. Ye, J. Shi, E. Wang, T. Cao, G. Wang, Q. Niu, W. Han, and J. Feng, *"Valley-selective circular dichroism of monolayer molybdenum disulphide,"* Nature Communications **3**, 885 (2012).

[147] K. M. McCreary, A. T. Hanbicki, S. V. Sivaram, and B. T. Jonker, *"A- and B-exciton photoluminescence intensity ratio as a measure of sample quality for transition metal dichalcogenide monolayers,"* APL Materials **6** (2018), 10.1063/1.5053699.

[148] P. Blake, E. W. Hill, A. H. Castro Neto, K. S. Novoselov, D. Jiang, R. Yang, T. J. Booth, and A. K. Geim, *"Making graphene visible,"* Applied Physics Letters **91** (2007), 10.1063/1.2768624, arXiv:0705.0259 .

[149] K. L. Seyler, J. R. Schaibley, P. Gong, P. Rivera, A. M. Jones, S. Wu, J. Yan, D. G. Mandrus, W. Yao, and X. Xu, *"Electrical control of second-harmonic generation in a WSe2 monolayer transistor,"* Nature Nanotechnology **10**, 407 (2015).

[150] G. Wang, X. Marie, I. Gerber, T. Amand, D. Lagarde, L. Bouet, M. Vidal, A. Balocchi, and B. Urbaszek, *"Giant Enhancement of the Optical Second-Harmonic Emission of WSe2 Monolayers by Laser Excitation at Exciton Resonances,"* Physical Review Letters **114**, 097403 (2015).

[151] M. Lafrentz, D. Brunne, A. V. Rodina, V. V. Pavlov, R. V. Pisarev, D. R. Yakovlev, A. Bakin, and M. Bayer, *"Second-harmonic generation spectroscopy of excitons in ZnO,"* Physical Review B - Condensed Matter and Materials Physics **88**, 1 (2013).

[152] W. T. Hsu, Z. A. Zhao, L. J. Li, C. H. Chen, M. H. Chiu, P. S. Chang, Y. C. Chou, and W. H. Chang, *"Second harmonic generation from artificially stacked transition metal dichalcogenide twisted bilayers,"* ACS Nano **8**, 2951 (2014).

[153] J. R. Schaibley, P. Rivera, H. Yu, K. L. Seyler, J. Yan, D. G. Mandrus, T. Taniguchi, K. Watanabe, W. Yao, and X. Xu, *"Directional interlayer spin-valley transfer in two-dimensional heterostructures,"* Nature Communications **7**, 1 (2016).

[154] M. Bougouma, A. Batan, B. Guel, T. Segato, J. B. Legma, F. Reniers, M. P. Delplancke-Ogletree, C. Buess-Herman, and T. Doneux, *"Growth and characterization of large, high quality MoSe2 single crystals,"* Journal of Crystal Growth **363**, 122 (2013).

[155] X. Zhang, F. Lou, C. Li, X. Zhang, N. Jia, T. Yu, J. He, B. Zhang, H. Xia, S. Wang, and X. Tao, *"Flux method growth of bulk MoS2 single crystals and their application as a saturable absorber,"* CrystEngComm **17**, 4026 (2015).

[156] A. Roy, H. C. Movva, B. Satpati, K. Kim, R. Dey, A. Rai, T. Pramanik, S. Guchhait, E. Tutuc, and S. K. Banerjee, *"Structural and Electrical Properties of MoTe2 and MoSe2 Grown by Molecular Beam Epitaxy,"* ACS Applied Materials and Interfaces **8**, 7396 (2016).

[157] M. W. Chen, D. Ovchinnikov, S. Lazar, M. Pizzochero, M. B. Whitwick, A. Surrente, M. Baranowski, O. L. Sanchez, P. Gillet, P. Plochocka, O. V. Yazyev, and A. Kis, *"Highly Oriented Atomically Thin Ambipolar MoSe2 Grown by Molecular Beam Epitaxy,"* ACS Nano **11**, 6355 (2017).

[158] R. Yue, Y. Nie, L. A. Walsh, R. Addou, C. Liang, N. Lu, A. T. Barton, H. Zhu, Z. Che, D. Barrera, L. Cheng, P. R. Cha, Y. J. Chabal, J. W. Hsu, J. Kim, M. J. Kim, L. Colombo, R. M. Wallace, K. Cho, and C. L. Hinkle, *"Nucleation and growth of WSe2: enabling large grain transition metal dichalcogenides,"* 2D Materials **4** (2017), 10.1088/2053-1583/aa8ab5.

[159] C. Cong, J. Shang, X. Wu, B. Cao, N. Peimyoo, C. Qiu, L. Sun, and T. Yu, *"Synthesis and optical properties of large-area single-crystalline 2D semiconductor WS2 monolayer from chemical vapor deposition,"* Advanced Optical Materials **2**, 131 (2014).

[160] A. Nourbakhsh, A. Zubair, M. S. Dresselhaus, and T. Palacios, *"Transport properties of a MoS2/WSe2 heterojunction transistor and its potential for application,"* Nano Letters **16**, 1359 (2016).

[161] V. Orsi Gordo, M. A. Balanta, Y. Galvão Gobato, F. S. Covre, H. V. Galeti, F. Iikawa, O. D. Couto, F. Qu, M. Henini, D. W. Hewak, and C. C. Huang, *"Revealing the nature of low-temperature photoluminescence peaks by laser treatment in van der Waals epitaxially grown WS2 monolayers,"* Nanoscale **10**, 4807 (2018).

[162] F. Cadiz, C. Robert, G. Wang, W. Kong, X. Fan, M. Blei, D. Lagarde, M. Gay, M. Manca, T. Taniguchi, K. Watanabe, T. Amand, X. Marie, P. Renucci, S. Tongay, and B. Urbaszek, *"Ultra-low power threshold for laser induced changes in optical properties of 2D molybdenum dichalcogenides,"* 2D Materials **3**, 045008 (2016), arXiv:1606.09554 .

[163] E. Smith and G. Dent, *Modern Raman Spectroscopy - A Practical Approach* (WILEY, 2005).

[164] J. R. Ferraro, K. Nakamoto, and C. W. Brown, *Introductory Raman Spectroscopy*, 2nd ed., 1 (Elsevier, 2003).

[165] E. Bright Wilson Jr, J. Decius, and P. C. Cross, *Molecular Vibrations: The Theory of Infrared and Raman Vibrational Spectra* (Dover Publications, 1955).

[166] M. Cardona and G. Güntherodt, *Optics and Laser Technology* (Springer Berlin Heidelberg, 1982).

[167] R. Mupparapu, M. Steinert, A. George, Z. Tang, A. Turchanin, T. Pertsch, and I. Staude, *"Facile Resist-Free Nanopatterning of Monolayers of MoS2 by Focused Ion-Beam Milling,"* Advanced Materials Interfaces **7**, 1 (2020).

[168] J. Tao, J. Chai, X. Lu, L. M. Wong, T. I. Wong, J. Pan, Q. Xiong, D. Chi, and S. Wang, *"Growth of wafer-scale MoS2 monolayer by magnetron sputtering,"* Nanoscale **7**, 2497 (2015).

[169] R. L. Aggarwal, L. W. Farrar, S. K. Saikin, A. Aspuru-Guzik, M. Stopa, and D. L. Polla, *"Measurement of the absolute Raman cross section of the optical phonon in silicon,"* Solid State Communications **151**, 553 (2011).

[170] D. Yoon, H. Moon, Y. W. Son, J. S. Choi, B. H. Park, Y. H. Cha, Y. D. Kim, and H. Cheong, *"Interference effect on Raman spectrum of graphene on SiO2 /Si,"* Physical Review B - Condensed Matter and Materials Physics **80**, 125422 (2009).

[171] L. Du, M. Liao, J. Tang, Q. Zhang, H. Yu, R. Yang, K. Watanabe, T. Taniguchi, D. Shi, Q. Zhang, and G. Zhang, *"Strongly enhanced exciton-phonon coupling in two-dimensional WSe2,"* Physical Review B **97**, 235145 (2018).

[172] D. E. Aspnes and A. A. Studna, *"Dielectric functions and optical parameters of Si, Ge, GaP, GaAs, GaSb, InP, InAs, and InSb from 1.5 to 6.0 eV,"* Physical Review B **27**, 985 (1983).

[173] L. Gao, R. Lemarchand, and M. Lequime, *"Refractive index determination of SiO2 layer in the UV/Vis/NIR range: Spectrophotometric reverse engineering on single and bi-layer designs,"* Journal of the European Optical Society **8**, 13010 (2013).

[174] S. Y. Lee, T. Y. Jeong, S. Jung, and K. J. Yee, *"Refractive Index Dispersion of Hexagonal Boron Nitride in the Visible and Near-Infrared,"* Physica Status Solidi (B) Basic Research **256**, 1 (2019).

[175] F. J. Nelson, V. K. Kamineni, T. Zhang, E. S. Comfort, J. U. Lee, and A. C. Diebold, *"Optical properties of large-area polycrystalline chemical vapor deposited graphene by spectroscopic ellipsometry,"* Applied Physics Letters **97**, 1 (2010).

[176] D. Y. Qiu, F. H. Da Jornada, and S. G. Louie, *"Optical spectrum of MoS2: Many-body effects and diversity of exciton states,"* Physical Review Letters **111**, 1 (2013).

[177] J. Marcus, K. Nogajewski, M. Koperski, C. Faugeras, A. Arora, and M. Potemski, *" Excitonic resonances in thin films of WSe 2 : from monolayer to bulk material ,"* Nanoscale **7**, 10421 (2015), arXiv:1503.01682 .

[178] C. Boule, D. Vaclavkova, M. Bartos, K. Nogajewski, L. ZdraŽil, T. Taniguchi, K. Watanabe, M. Potemski, and J. Kasprzak, *"Coherent dynamics and mapping of excitons in single-layer MoSe2 and WSe2 at the homogeneous limit,"* Physical Review Materials **4**, 12 (2020), arXiv:2002.01436 .

[179] T. C. Berkelbach, M. S. Hybertsen, and D. R. Reichman, *"Bright and dark singlet excitons via linear and two-photon spectroscopy in monolayer transition-metal dichalcogenides,"* Physical Review B - Condensed Matter and Materials Physics **92**, 1 (2015), arXiv:1505.07127 .

[180] M. Goryca, J. Li, A. V. Stier, T. Taniguchi, K. Watanabe, E. Courtade, S. Shree, C. Robert, B. Urbaszek, X. Marie, and S. A. Crooker, *"Revealing exciton masses and dielectric properties of monolayer semiconductors with high magnetic fields,"* Nature Communications **10**, 1 (2019), arXiv:1904.03238 .

[181] K. Kim, J. U. Lee, D. Nam, and H. Cheong, *"Davydov Splitting and Excitonic Resonance Effects in Raman Spectra of Few-Layer MoSe2,"* ACS Nano **10**, 8113 (2016).

[182] H. Sahin, S. Tongay, S. Horzum, W. Fan, J. Zhou, J. Li, J. Wu, and F. M. Peeters, *"Anomalous Raman spectra and thickness-dependent electronic properties of WSe2,"* Physical Review B - Condensed Matter and Materials Physics **87**, 1 (2013), arXiv:1303.5861 .

[183] M. De Luca, X. Cartoixa, D. I. Indolese, J. Martín-Sanchez, K. Watanabe, T. Taniguchi, C. Schönenberger, R. Trotta, R. Rurali, and I. Zardo, *"Experimental demonstration of the suppression of optical phonon splitting in 2D materials by Raman spectroscopy,"* 2D Materials **7**, 035017 (2020).

[184] H. Zeng, B. Zhu, K. Liu, J. Fan, X. Cui, and Q. M. Zhang, *"Low-Frequency Raman Modes and Electronic Excitations In Atomically Thin MoS2 Crystals,"* Physical Review B **86**, 241301 (2012), arXiv:1209.1775 .

[185] N. Scheuschner, O. Ochedowski, M. Schleberger, and J. Maultzsch, *"Resonant Raman profiles and μ-photoluminescence of atomically thin layers of molybdenum disulfide,"* Physica Status Solidi (B) Basic Research **249**, 2644 (2012).

[186] M. R. Molas, K. Nogajewski, M. Potemski, and A. Babiński, *"Raman scattering excitation spectroscopy of monolayer WS2,"* Scientific Reports **7**, 1 (2017), arXiv:1703.09175 .

[187] D. Nam, J. U. Lee, and H. Cheong, *"Excitation energy dependent Raman spectrum of MoSe2,"* Scientific Reports **5**, 1 (2015).

[188] C. M. Chow, H. Yu, A. M. Jones, J. Yan, D. G. Mandrus, T. Taniguchi, K. Watanabe, W. Yao, and X. Xu, *"Unusual Exciton-Phonon Interactions at van der Waals Engineered Interfaces,"* Nano Letters **17**, 1194 (2017).

[189] M. Manca, M. M. Glazov, C. Robert, F. Cadiz, T. Taniguchi, K. Watanabe, E. Courtade, T. Amand, P. Renucci, X. Marie, G. Wang, and B. Urbaszek, *"Enabling valley selective exciton scattering in monolayer WSe2 through upconversion,"* Nature Communications **8**, 14927 (2017), arXiv:1701.05800 .

[190] E. Courtade, M. Semina, M. Manca, M. M. Glazov, C. Robert, F. Cadiz, G. Wang, T. Taniguchi, K. Watanabe, M. Pierre, W. Escoffier, E. L. Ivchenko, P. Renucci, X. Marie, T. Amand, and B. Urbaszek, *"Charged excitons in monolayer WSe2: Experiment and theory,"* Physical Review B **96**, 1 (2017).

[191] S. Y. Chen, Z. Lu, T. Goldstein, J. Tong, A. Chaves, J. Kunstmann, L. S. Cavalcante, T. Woźniak, G. Seifert, D. R. Reichman, T. Taniguchi, K. Watanabe, D. Smirnov, and J. Yan, *"Luminescent Emission of Excited Rydberg Excitons from Monolayer WSe2,"* Nano Letters **19**, 2464 (2019).

[192] C. M. Chow, H. Yu, A. M. Jones, J. R. Schaibley, M. Koehler, D. G. Mandrus, R. Merlin, W. Yao, and X. Xu, *"Phonon-assisted oscillatory exciton dynamics in monolayer MoSe2,"* npj 2D Materials and Applications **1** (2017), 10.1038/s41699-017-0035-1.

[193] S. Shree, M. Semina, C. Robert, B. Han, T. Amand, A. Balocchi, M. Manca, E. Courtade, X. Marie, T. Taniguchi, K. Watanabe, M. M. Glazov, and B. Urbaszek, *"Observation of exciton-phonon coupling in MoSe2 monolayers,"* Physical Review B **98**, 1 (2018).

[194] E. Courtade, B. Han, S. Nakhaie, C. Robert, X. Marie, P. Renucci, T. Taniguchi, K. Watanabe, L. Geelhaar, J. M. Lopes, and B. Urbaszek, *"Spectrally narrow exciton luminescence from monolayer MoS2 and MoSe2 exfoliated onto epitaxially grown hexagonal BN,"* Applied Physics Letters **113** (2018), 10.1063/1.5033554, arXiv:1804.06623 .

[195] C. Jin, J. Kim, J. Suh, Z. Shi, B. Chen, X. Fan, M. Kam, K. Watanabe, T. Taniguchi, S. Tongay, A. Zettl, J. Wu, and F. Wang, *"Interlayer electron–phonon coupling in WSe2/hBN heterostructures,"* Nature Physics **13**, 127 (2016).

[196] L. Du, Y. Zhao, Z. Jia, M. Liao, Q. Wang, X. Guo, Z. Shi, R. Yang, K. Watanabe, T. Taniguchi, J. Xiang, D. Shi, Q. Dai, Z. Sun, and G. Zhang, *"Strong and tunable interlayer coupling of infrared-active phonons to excitons in van der Waals heterostructures,"* Physical Review B **99**, 205410 (2019).

[197] J. J. S. Viner, L. P. McDonnell, P. Rivera, X. Xu, and D. C. Smith, *"Insights into hyperbolic phonon polaritons in h-BN using Raman scattering from encapsulated transition metal dichalcogenide layers,"* Physical Review B **104**, 165404 (2021), arXiv:2104.00393 .

[198] P. Tonndorf, R. Schmidt, P. Böttger, X. Zhang, J. Börner, A. Liebig, M. Albrecht, C. Kloc, O. Gordan, D. R. T. Zahn, S. Michaelis de Vasconcellos, and R. Bratschitsch, *"Photoluminescence emission and Raman response of monolayer MoS2, MoSe2, and WSe2,"* Optics Express **21**, 4908 (2013), arXiv:1208.5864 .

[199] S. Kumar and U. Schwingenschlögl, *"Thermoelectric response of bulk and monolayer MoSe2 and WSe2,"* Chemistry of Materials **27**, 1278 (2015).

[200] G. D. Shepard, J. V. Ardelean, O. A. Ajayi, D. Rhodes, X. Zhu, J. C. Hone, and S. Strauf, *"Trion-Species-Resolved Quantum Beats in MoSe2,"* ACS Nano **11**, 11550 (2017).

[201] A. Raja, A. Chaves, J. Yu, G. Arefe, H. M. Hill, A. F. Rigosi, T. C. Berkelbach, P. Nagler, C. Schüller, T. Korn, C. Nuckolls, J. Hone, L. E. Brus, T. F. Heinz, D. R. Reichman, and A. Chernikov, *"Coulomb engineering of the bandgap and excitons in two-dimensional materials,"* Nature Communications **8**, 15251 (2017).

[202] J. J. S. Viner, L. P. McDonnell, D. A. Ruiz-Tijerina, P. Rivera, X. Xu, V. I. Fal'Ko, and D. C. Smith, *"Excited Rydberg states in MoSe2 /WSe2 heterostructures,"* 2D Materials **8**, 035047 (2021), arXiv:2103.09004 .

[203] M. Szyniszewski, E. Mostaani, N. D. Drummond, and V. I. Fal'Ko, *"Binding energies of trions and biexcitons in two-dimensional semiconductors from diffusion quantum Monte Carlo calculations,"* Physical Review B **95**, 1 (2017), arXiv:1701.07407 .

[204] R. Geick, C. H. Perry, and G. Rupprecht, *"Normal modes in hexagonal boron nitride,"* Physical Review **146**, 543 (1966).

[205] A. Laturia, M. L. Van de Put, and W. G. Vandenberghe, *"Dielectric properties of hexagonal boron nitride and transition metal dichalcogenides: from monolayer to bulk,"* npj 2D Materials and Applications **2**, 6 (2018).

[206] A. A. Al-Hilli and B. L. Evans, *"The preparation and properties of transition metal dichalcogenide single crystals,"* Journal of Crystal Growth **15**, 93 (1972).

[207] W. T. Hicks, *"Semiconducting Behavior of Substituted Tungsten Diselenide and Its Analogues,"* Journal of The Electrochemical Society **111**, 1058 (1964).

[208] M. V. Gustafsson, M. Yankowitz, C. Forsythe, D. Rhodes, K. Watanabe, T. Taniguchi, J. Hone, X. Zhu, and C. R. Dean, *"Ambipolar Landau levels and strong band-selective carrier interactions in monolayer WSe2,"* Nature Materials **17**, 411 (2018), arXiv:1707.08083 .

[209] D. A. P. Nguyen, D. N. Ly, D. N. Le, N. T. D. Hoang, and V. H. Le, *"High-accuracy energy spectra of a two-dimensional exciton screened by reduced dimensionality with the presence of a constant magnetic field,"* Physica E: Low-Dimensional Systems and Nanostructures **113**, 152 (2019).

[210] N. Ohba, K. Miwa, N. Nagasako, and A. Fukumoto, *"First-principles study on structural, dielectric, and dynamical properties for three BN polytypes,"* Physical Review B - Condensed Matter and Materials Physics **63**, 1 (2001).

[211] Y. Cai, L. Zhang, Q. Zeng, L. Cheng, and Y. Xu, *"Infrared reflectance spectrum of BN calculated from first principles,"* Solid State Communications **141**, 262 (2007), arXiv:1108.0154 .

[212] N. C. Passler and A. Paarmann, *"Generalized 4 × 4 matrix formalism for light propagation in anisotropic stratified media: study of surface phonon polaritons in polar dielectric heterostructures,"* Journal of the Optical Society of America B **34**, 2128 (2017), arXiv:1707.00462 .

[213] M. R. Querry, in *Soft X-Ray Optics* (SPIE, 1000 20th Street, Bellingham, WA 98227-0010 USA, 1985) pp. 5–22.

[214] G. Cataldo, E. J. Wollack, A. D. Brown, and K. H. Miller, *"Infrared dielectric properties of low-stress silicon oxide,"* Optics Letters **41**, 1364 (2016), arXiv:1603.04815 .

[215] J. D. Caldwell, I. Aharonovich, G. Cassabois, J. H. Edgar, B. Gil, and D. N. Basov, *"Photonics with hexagonal boron nitride,"* Nature Reviews Materials **4**, 552 (2019).

[216] P. K. Nayak, Y. Horbatenko, S. Ahn, G. Kim, J. U. Lee, K. Y. Ma, A. R. Jang, H. Lim, D. Kim, S. Ryu, H. Cheong, N. Park, and H. S. Shin, *"Probing Evolution of Twist-Angle-Dependent Interlayer Excitons in MoSe2/WSe2 van der Waals Heterostructures,"* ACS Nano **11**, 4041 (2017).

[217] Y. Xu, S. Liu, D. A. Rhodes, K. Watanabe, T. Taniguchi, J. Hone, V. Elser, K. F. Mak, and J. Shan, *"Correlated insulating states at fractional fillings of moiré superlattices,"* Nature **587**, 214 (2020).

[218] L. Wang, E. M. Shih, A. Ghiotto, L. Xian, D. A. Rhodes, C. Tan, M. Claassen, D. M. Kennes, Y. Bai, B. Kim, K. Watanabe, T. Taniguchi, X. Zhu, J. Hone, A. Rubio, A. N. Pasupathy, and C. R. Dean, *"Correlated electronic phases in twisted bilayer transition metal dichalcogenides,"* Nature Materials **19**, 861 (2020).

[219] O. B. Aslan, M. Deng, and T. F. Heinz, *"Strain tuning of excitons in monolayer WSe2,"* Physical Review B **98**, 115308 (2018).

[220] I. Niehues, A. Blob, T. Stiehm, S. Michaelis De Vasconcellos, and R. Bratschitsch, *"Interlayer excitons in bilayer MoS2 under uniaxial tensile strain,"* Nanoscale **11**, 12788 (2019).

[221] K. Zollner, P. E. Junior, and J. Fabian, *"Strain-tunable orbital, spin-orbit, and optical properties of monolayer transition-metal dichalcogenides,"* Physical Review B **100**, 195126 (2019), arXiv:1909.10763 .

[222] O. B. Aslan, M. Deng, M. L. Brongersma, and T. F. Heinz, *"Strained bilayer WSe2 with reduced exciton-phonon coupling,"* Physical Review B **101**, 115305 (2020).

[223] Y. Bai, L. Zhou, J. Wang, W. Wu, L. J. McGilly, D. Halbertal, C. F. B. Lo, F. Liu, J. Ardelean, P. Rivera, N. R. Finney, X. C. Yang, D. N. Basov, W. Yao, X. Xu, J. Hone, A. N. Pasupathy, and X. Y. Zhu, *"Excitons in strain-induced one-dimensional moiré potentials at transition metal dichalcogenide heterojunctions,"* Nature Materials **19**, 1068 (2020).

[224] W. Pacuski, M. Grzeszczyk, K. Nogajewski, A. Bogucki, K. Oreszczuk, J. Kucharek, K. E. Połczyńska, B. Seredyński, A. Rodek, R. Bożek, T. Taniguchi, K. Watanabe, S. Kret, J. Sadowski, T. Kazimierczuk, M. Potemski, and P. Kossacki, *"Narrow Excitonic Lines and Large-Scale Homogeneity of Transition-Metal Dichalcogenide Monolayers Grown by Molecular Beam Epitaxy on Hexagonal Boron Nitride,"* Nano Letters **20**, 3058 (2020).

[225] S. Shree, A. George, T. Lehnert, C. Neumann, M. Benelajla, C. Robert, X. Marie, K. Watanabe, T. Taniguchi, U. Kaiser, B. Urbaszek, and A. Turchanin, *"High optical quality of MoS2 monolayers grown by chemical vapor deposition,"* 2D Materials **7** (2020), 10.1088/2053-1583/ab4f1f.